

MAX-PLANCK-INSTITUT FÜR RADIOASTRONOMIE

# Targeted Fast Radio Burst Searches with the Effelsberg 100-m Radio Telescope

Dissertation

zur

Erlangung des Doktorgrades (*Dr. rer. nat.*)

der

Mathematisch-Naturwissenschaftlichen Fakultät

der

Rheinischen Friedrich–Wilhelms–Universität, Bonn

vorgelegt von

Guðjón Henning HILMARSSON

aus

Reykjavík, Island

Bonn 2020

1. Referent: Prof. Dr. Michael Kramer  
2. Referent: Prof. Dr. Norbert Langer  
Tag der Promotion: 26.2.2021  
Erscheinungsjahr: 2021

Angefertigt mit Genehmigung der Mathematisch-Naturwissenschaftlichen Fakultät  
der Rheinischen Friedrich-Wilhelms-Universität Bonn

# Targeted Fast Radio Burst Searches with the Effelsberg 100-m Radio Telescope

## *Abstract*

by G. Henning Hilmarsson

for the degree of

*Doctor rerum naturalium*

Fast radio bursts (FRBs) are bright, energetic, millisecond duration radio bursts of extragalactic origin. The source of FRBs still remains an open problem. Since the discovery of FRBs in 2007, over 100 FRBs have been detected. Most FRBs are single-burst events, while others are observed to be repeating sources. Due to their cosmological origin, FRBs can be used as probes of the intergalactic medium and the medium of their host galaxies.

Roughly ten FRBs have been localised to a host galaxy. Of those, FRB121102 was both the first discovered repeating FRB and the first FRB localised to a host galaxy, and was the primary motivation for the vast majority of the observations performed in this thesis. The FRB121102 bursting source has been proposed to originate from a magnetar within a supernova remnant (SNR), a scenario that can account for repeating bursts, an associated persistent radio source (PRS), and large Faraday rotation measures (RMs).

Large, single-dish telescopes have high sensitivities and small fields of view, making them ideal for targeted and follow-up surveys. This thesis focuses on targeted FRB searches with single-dish telescopes, with the Effelsberg 100-m radio telescope at the forefront. The surveys in this thesis were performed in order to obtain a better understanding of the origin of FRBs, specifically repeating ones, by observing known FRBs and potential hosts of FRB sources, with each scientific chapter being a different approach to that goal.

The commissioning of a phased array feed (PAF) receiver at Effelsberg is presented in Chapter 3. With PAFs, highly customisable beams can be formed on the sky, providing more flexibility than typical multi-beam receivers while also having a larger field of view. PAFs and their use cases are introduced, along with a detailed discussion on the Effelsberg PAF observations at 1.4 GHz. The main observing targets were PRSs associated with galactic disks or star formation regions to search for FRB121102-like bursting sources, and other FRBs such as two of the repeating FRBs, FRB121102 and FRB180814.J0422+73. No bursts were detected, so upper limits (ULs) to the burst rates were calculated based on the observations. The burst rate of FRB121102 was also scaled to each PRS. The scaled rates of five of the eleven PRSs were constrained by the UL rates at the 95% confidence level (CL), rejecting the hypothesis of an FRB121102-like

source associated with those PRSs.

Chapter 4 presents the observations of ten superluminous supernovae (SLSNe) and long gamma-ray bursts (LGRBs) with Effelsberg using the S45-mm receiver at 5.3–9.3 GHz. SLSNe and LGRBs were targeted due to the similarities between their host galaxies and the host galaxy of FRB121102, and were therefore observed to search for FRB121102-like sources. As no bursts were detected, UL burst rates and scaled FRB121102 rates to each target were calculated. None of the scaled rates were constrained by the ULs at the 95% CL. Furthermore, a PRS coincident with the SLSN PTF10hgi was added as a target and observed with the PAF at Effelsberg and the ultra-wideband-low (UWL) receiver at the Parkes 64-m radio telescope in Australia. The FRB121102 rate scaled to PTF10hgi was excluded at the 99% CL. The apparent clustering of bursts from FRB121102 can be explained with a Weibull distribution. For such a distribution, a non-detection probability of 14% and 16% was calculated for the PAF and UWL observations, respectively.

Chapter 5 investigates the temporal RM evolution of FRB121102. Faraday rotation is the rotation of the linearly polarised plane of a signal induced by the line of sight magnetic field. The rate of this rotation across frequency is quantified by the RM. The first RM measurements of FRB121102 was exceptionally high,  $1.46 \times 10^5 \text{ rad m}^{-2}$  in the source reference frame, decreasing down to  $1.33 \times 10^5 \text{ rad m}^{-2}$  in seven months. In Chapter 5, sixteen additional FRB121102 RM measurements are presented from burst detections with the Arecibo 305-m radio telescope, the Effelsberg 100-m radio telescope, and the Karl G. Jansky Very Large Array, showing a continued decreasing trend in RM over time down to  $9.7 \times 10^4 \text{ rad m}^{-2}$  at the most recent epoch of August 2019. Erratic, short-term RM variations of  $\sim 10^3 \text{ rad m}^{-2}$  per week were seen from multiple detections within a 30-day window. The complete RM sample of FRB121102, spanning 2.5 years, was compared to theoretical RM evolution models of magnetars within SNRs. The data were inconsistent with model varieties where the remnant magnetar is surrounded by a constant density interstellar medium. However, the data agree with model varieties where the magnetar is surrounded by a magnetar wind nebula. The age of the FRB121102 bursting source was also estimated based on the RM evolution models and was found to be 6–17 years old at the time of the first FRB121102 RM measurement (at the end of 2016). The RM evolution of FRB121102 is also compared to the Galactic center magnetar, PSR J1745-2900, which has shown a similarly drastic decrease in its absolute RM over time.

To the good people and animals in my life



“When you do things right, people won’t be sure you’ve done anything at all.”

God  
*Futurama, S3E20*

“One of the major difficulties Trillian experienced in her relationship with Zaphod was learning to distinguish between him pretending to be stupid just to get people off their guard, pretending to be stupid because he couldn’t be bothered to think and wanted someone else to do it for him, pretending to be outrageously stupid to hide the fact that he actually didn’t understand what was going on, and really being genuinely stupid. He was renowned for being amazingly clever and quite clearly was so - but not all the time, which obviously worried him, hence, the act. He preferred people to be puzzled rather than contemptuous”

Douglas Adams  
*The Hitchhiker’s Guide to the Galaxy*

/)/)  
(^  
(")(")



# Acknowledgements

During this thesis there have been plenty of people who have made things easier for me or helped guiding my brain towards solutions, or simply just lifted my spirits by being the bee's knees.

First and foremost, I want to thank Michael Kramer for providing me with the opportunity to come working in Bonn. Without you, I wouldn't have met all the fantastic people here. Even with your busy schedule, you still manage to squeeze in time for all the students, providing them with valuable input.

To my day-to-day supervisor, Laura Spitler, thank you. Seemingly at the drop of a hat you manage to make time for your students, and are always ready to listen to and give feedback to questions or any other issues that might arise. Furthermore; thank you for, noticing all my: punctuation mistakes.

For post-docs applying here, it seems there is a strict requirement of being friendly and helpful. Ewan Barr, you are a bottomless pit of wisdom and apparently know everything about everything computer-wise. Especially during the PAF days, you were like a secondary supervisor, and I'm grateful for your help. Plus, it is hilarious how you turn your Scottish accent up to 11 when you celebrate Bacchus. To the post-docs that have at some point had offices in the madhouse that is the ground floor, Gregory Desvignes, Ralph Eatough, Charlie Walker, and the Roberts Main and Wharton, thank you for your various help throughout the years.

I also want to thank my TAC: Ben Stappers, Olaf Wucknitz, Norbert Langer, Laura, and Michael. Thank you for listening to me complaining about all the things that didn't work, and trying to find solutions to my problems. For a long time it really did feel like all my projects were cursed, but at least you guys were there to listen to me.

To the trio that made things so much easier, and to an extent kept me away from the never-ending rabbit hole that is German bureaucracy, thank you. Kira Kühn, Mariya Halvadzheva, and Tuyet-Le Tran, you guys are the treasure of MPIfR.

Of course one can not observe without a telescope. Alex Kraus, the wizard of Effelsberg scheduling, thank you for all your efforts. To the Effelsberg operators, thank you for all your help with observations.

To the people who led me to the path that brought me to Bonn, Vilhelm Sigfús Sigmundsson (Fúsi), Páll Jakobsson, Gunnlaugur Björnsson, and Einar H. Guðmundsson, this is all your fault and I thank you for it.

Where would one be without friends and loved ones? Nataliya Porayko, you are so many things packed into such small space. Sweet, passionate (aggressive?), caring, smart (sometimes tupoj), funny little babuska. I love you. Hans Nguyen, my brother that my mother did not give birth to. I don't want to make these acknowledgements too long, so I'll just say that you are the poster boy of a perfect friend, and people understandably envy our bromance. My MPI mom, Eleni Graikou. You are such a nice person and are also able to completely roast people without any warning, that is a hilariously awesome combination. Marilyn Cruces, meme queen, the greatest office

mate, and all-round great person. I couldn't have asked for a better PhD twin. Arshia Jacob, you somehow understand my weird brain, that's pretty cool. Also, it's creepy. Tilemachos Athanasiadis, bouzouki savant and infectiously joyful. Robert Main, smash and MtG boomer (your words), nicest person ever award winner. Jose Martinez, always down for a good time and a good office mate. Leon Houben, a short Dutch guy (how?) but still a good friend and yet another good office mate. Ralph Eatough, the other half of the basement band rhythm section. Gregory Desvignes, ping pong master with an outrageously strong French accent. Bragi Hilmarsson, fantastic brother and online gaming partner. James McKee, fellow football enthusiast. Alessandro Ridolfi, supportingly laughing at my jokes. Jens and Prajwal of the badminton gang. Felix and Tobias of the MtG drafting gang. All of you, my heartfelt thanks for your company.

Lastly, to my family. I'm an adult and I know how to take care of myself, but I appreciate your concerns for my well-being. Thank you for everything.

# Contents

<b>1</b>	<b>Introduction</b>	<b>3</b>
1.1	Rates and Properties of FRBs . . . . .	4
1.2	Propagation Effects . . . . .	9
1.2.1	Dispersion Measure . . . . .	9
1.2.2	DM Budget and Redshift Estimate of FRBs . . . . .	11
1.2.3	Faraday Rotation . . . . .	12
1.2.4	Scattering . . . . .	14
1.2.5	Scintillation . . . . .	17
1.3	FRB121102 . . . . .	18
1.4	FRB180916.J0158+65 . . . . .	20
1.5	Galactic FRB-like bursts from SGR 1935+2154 . . . . .	21
1.6	Progenitor Theories . . . . .	22
1.6.1	Magnetars in Supernova Remnants . . . . .	22
1.6.2	Active Galactic Nuclei . . . . .	23
1.6.3	Periodicity . . . . .	24
1.6.4	Cataclysmic and Exotic Models . . . . .	24
1.7	FRB Follow-up Across the Electromagnetic Spectrum . . . . .	25
1.7.1	General FRB Follow-up Strategies . . . . .	25
1.7.2	FRB121102 Follow-up . . . . .	26
1.8	FRBs as Astrophysical Tools . . . . .	28
1.9	Thesis Outline . . . . .	29
<b>2</b>	<b>Data Acquisition and Searching</b>	<b>31</b>
2.1	Instrumentation . . . . .	31
2.1.1	Sensitivity and Field of View . . . . .	31
2.1.2	Frontend . . . . .	33
2.1.3	Backend . . . . .	34
2.1.4	Baseband . . . . .	35
2.1.5	Polarimetry . . . . .	35
2.2	Radio Frequency Interference . . . . .	37
2.3	Dedispersion . . . . .	38
2.3.1	Incoherent Dedispersion . . . . .	38
2.3.2	Coherent Dedispersion . . . . .	40
2.3.3	Dispersion Smearing . . . . .	40
2.3.4	DM Step Size . . . . .	41
2.3.5	DM Steps in Practice . . . . .	41
2.4	Single Pulse Searching . . . . .	42
2.5	Measuring Rotation Measure . . . . .	45
2.6	Search Software and Pipelines . . . . .	46

2.6.1	Presto . . . . .	48
2.6.2	Presto Search Pipeline . . . . .	49
2.6.3	Heimdall . . . . .	51
2.6.4	Heimdall Search Pipeline . . . . .	53
<b>3</b>	<b>Phased Array Feeds and Commissioning at Effelsberg</b>	<b>55</b>
3.1	Increasing the FOV and Survey Speed . . . . .	56
3.2	Localisation . . . . .	56
3.3	Mitigating RFI . . . . .	58
3.4	Multi-source Observations . . . . .	59
3.5	PAF at Effelsberg . . . . .	59
3.5.1	PAF Observations . . . . .	60
3.5.2	Test Pulsars and Sensitivity . . . . .	63
3.5.3	Single Pulse Candidates and RFI . . . . .	65
3.5.4	FRBs . . . . .	68
3.5.5	PRSs . . . . .	71
3.5.6	GC Pulsars . . . . .	72
3.5.7	Future Outlook . . . . .	72
<b>4</b>	<b>Observing superluminous supernovae and long gamma ray bursts as potential birthplaces of repeating fast radio bursts</b>	<b>75</b>
4.1	Abstract . . . . .	75
4.2	Introduction . . . . .	76
4.3	Observations . . . . .	78
4.3.1	S45mm receiver . . . . .	79
4.3.2	PAF receiver . . . . .	82
4.3.3	UWL receiver . . . . .	82
4.3.4	Data processing . . . . .	82
4.4	Results & Analysis . . . . .	84
4.4.1	C-band observations of SLSNe/LGRBs . . . . .	85
4.4.2	PAF & UWL observations of PTF10hgi . . . . .	86
4.4.3	Beaming fraction . . . . .	89
4.4.4	Poisson & Weibull distributions . . . . .	90
4.5	Discussion & Conclusions . . . . .	92
<b>5</b>	<b>Rotation Measure Evolution of the Repeating Fast Radio Burst Source FRB 121102</b>	<b>97</b>
5.1	Abstract . . . . .	97
5.2	Introduction . . . . .	98
5.3	Observations . . . . .	99
5.3.1	Effelsberg . . . . .	100
5.3.2	Arecibo . . . . .	101
5.3.3	VLA . . . . .	101
5.4	Observational Results . . . . .	102

5.4.1	Long-term Burst Rate at C-band at Effelsberg . . . . .	102
5.4.2	Burst Properties . . . . .	104
5.4.3	Dispersion and Rotation Measures of FRB 121102 . . . . .	105
5.5	Implications for source scenarios . . . . .	107
5.5.1	Piro & Gaensler (2018) . . . . .	109
5.5.2	Margalit & Metzger (2018) . . . . .	110
5.5.3	Galactic Center Magnetar PSR J1745–2900 . . . . .	115
5.6	Discussion . . . . .	115
5.7	Conclusions . . . . .	120
<b>6</b>	<b>Conclusions</b>	<b>123</b>
6.1	PAF at Effelsberg . . . . .	123
6.2	SLSNe/LGRBs . . . . .	124
6.3	FRB121102 RM . . . . .	125
6.4	Future Outlook . . . . .	126
	<b>Bibliography</b>	<b>127</b>



# List of Figures

1.1	Dispersion sweep of an FRB . . . . .	10
1.2	Illustration of the thin scattering screen approximation . . . . .	15
1.3	Effect of the scattering timescale at different frequencies . . . . .	16
1.4	Downward frequency drift of a burst from FRB121102 . . . . .	20
2.1	Illustration of a telescope beam . . . . .	33
2.2	Polarisation ellipse . . . . .	36
2.3	Dedispersing a burst at correct and incorrect DMs . . . . .	39
2.4	Visualisation of a dedispersion plan . . . . .	43
2.5	Convolution of a time series with a boxcar filter . . . . .	44
2.6	Signal-to-noise as a function of trial boxcar widths . . . . .	45
2.7	Depolarisation fraction as a function of RM . . . . .	47
2.8	PRESTO single pulse search candidate plot . . . . .	50
2.9	Single pulse search pipeline candidate plots . . . . .	52
3.1	Field of view comparison between the PAF and 7-beam receivers at Effelsberg . . . . .	57
3.2	Incoherent and interferometric localisation regions of ASKAP . . . . .	58
3.3	Effelsberg PAF beam configuration . . . . .	62
3.4	SEFD over time of the Effelsberg PAF . . . . .	65
3.5	Test pulsar single pulse candidates from the PAF . . . . .	66
3.6	Effelsberg PAF RFI examples . . . . .	68
3.7	Self-generated PAF RFI single pulse candidates . . . . .	69
3.8	Folding of the test pulsar B0609+37 . . . . .	70
3.9	Active phases of FRB121102 and time of PAF observations . . . . .	70
4.1	FRB121102 burst rate at C-band scaled to observed SLSNe/LGRBs . . . . .	88
4.2	FRB121102 burst rate scaled to PTF10hgi for different receivers . . . . .	89
4.3	Probability of sources beaming towards an observer . . . . .	91
4.4	Probability of non-detection from a Weibull distribution . . . . .	93
4.5	Probability of non-detection from a Weibull distribution for a survey spanning a varying number of observations . . . . .	95
5.1	Dynamic spectra of FRBs detected with Arecibo, Effelsberg, and VLA . . . . .	106
5.2	RMs of FRB 121102 over time . . . . .	108
5.3	Posterior corner plots for parameters of SNR evolution models in Piro & Gaensler (2018) when fitted to FRB 121102 RMs . . . . .	111
5.4	Source frame RM over time for SNR evolution models in Piro & Gaensler (2018) compared to RMs of FRB 121102 . . . . .	113
5.5	Source frame DM versus RM for SNR evolution models in Piro & Gaensler (2018) . . . . .	114

5.6	Posterior corner plots for parameters of SNR evolution models in Margalit & Metzger (2018) when fitted to FRB 121102 RMs . . . . .	117
5.7	Source frame RM over time for SNR evolution models in Margalit & Metzger (2018) compared to RMs of FRB 121102 . . . . .	118

# List of Tables

1.1	FRB121102 follow-up across the EM spectrum . . . . .	27
2.1	Dedispersion plan for Effelsberg 7-beam data . . . . .	42
2.2	Frequency information of receivers commonly used to observe FRB121102	46
3.1	PAF observation summary, April 2018 . . . . .	60
3.2	PAF observation summary, June 2018 . . . . .	61
3.3	PAF observation summary, August 2018 . . . . .	61
3.4	PAF observation summary, March 2019 . . . . .	62
3.5	PAF data properties for each observing run . . . . .	62
3.6	Sources observed with the PAF ordered by project and burst rate calculation results . . . . .	64
3.7	PAF single pulse candidate and excision statistics . . . . .	67
4.1	SLSNe/LGRBs observed and their estimated DMs . . . . .	80
4.2	List of SLSN/LGRB observations . . . . .	81
4.3	Burst rate analysis results of the observed SLSNe/LGRBs . . . . .	87
4.4	FRB121102 burst rate scaled to the observed SLSNe/LGRBs and the UWL receiver at Parkes . . . . .	95
5.1	FRB 121102 burst detections with measured RMs . . . . .	103
5.2	Number of detections and hours observed for FRB 121102 surveys at frequencies between 4–8 GHz . . . . .	104
5.3	Parameters of SNR evolution models in Piro & Gaensler (2018) . . . . .	112
5.4	Parameters of SNR evolution models in Margalit & Metzger (2018) . . . . .	116



## Recurring acronyms

ACM	Array covariance matrix	LoS	Line of sight
ADC	Analog-to-digital converter	NS	Neutron star
AGN	Active galactic nucleus	PA	Polarisation angle
BMF	Beamformer	PAF	Phased array feed
CL	Confidence level	PPA	Polarisation position angle
CPU	Central processing unit	PRS	Persistent radio source
DEC	Declination	PSR	Pulsar
DM	Dispersion measure	RA	Right ascension
EM	Electromagnetic	RFI	Radio frequency interference
FFT	Fast Fourier transform	RHCP	Right-hand circularly polarised
FOV	Field of view	RM	Rotation measure
FRB	Fast radio burst	RRAT	Rotating radio transient
GC	Galactic center	S/N	Signal-to-noise ratio
GPU	Graphics processing unit	SEFD	System equivalent flux density
GRB	Gamma-ray burst	SGR	Soft gamma repeater
HPBW	Half power beam width	SLSN	Superluminous supernova
IGM	Intergalactic medium	SM	Scattering measure
ISM	Interstellar medium	SN	Supernova
LHCP	Left-hand circularly polarised	SVS	Survey speed
LNA	Low-noise amplifier	UL	Upper limit

## Radio telescope acronyms

Arecibo, AO	Arecibo observatory 305-m William E. Gordon radio telescope
ASKAP	Australian square kilometer array pathfinder
CHIME	Canadian hydrogen intensity mapping experiment
DSA-10	Deep synoptic array ten-antenna
Effelsberg, EFF	Effelsberg 100-m radio telescope
EVN	European VLBI network
FAST	Five-hundred-metre aperture spherical radio telescope
GBT	Robert C. Byrd Green Bank Telescope
LOFAR	The low frequency array
MWA	Murchison widefield array
Parkes	Parkes 64-m radio telescope
SRT	Sardinia radio telescope
STARE2	Survey for transient astronomical radio emission 2
UTMOST	Upgraded Molongolo observatory synthesis telescope
VLA	Karl G. Jansky very large array
WSRT	Westerbork synthesis radio telescope



# Introduction

---

The fast radio burst (FRB) branch of astronomy is relatively new, being just over a decade old, with the inaugural FRB discovery made in 2007. The FRB field emerged from pulsar astronomy following the increased interest in single pulse searching for the then-recently discovered (2006) rotating radio transients (RRATs) in the time-frequency domain, instead of the standard pulsar Fourier-domain periodicity search.

FRBs are bright, short-duration radio transients, lasting only a few milliseconds, and have been detected from directions all over the celestial sphere. FRBs originate from extragalactic sources, and from their inferred distances and brightness they are  $\gtrsim 10$  orders of magnitude brighter than canonical pulsars (Pietka et al., 2015), thus requiring vast amounts of energy to produce ( $\sim 10^{39}$  erg). To date there are over 100 published FRBs<sup>1</sup> (Petroff et al., 2016), and their all-sky event rate is estimated to be on the order of  $\sim 10^3$  sky<sup>-1</sup> day<sup>-1</sup> above a 1 Jy ms fluence threshold<sup>2</sup> (Petroff et al., 2019). FRBs have been detected within a relatively wide range of the radio spectrum, from roughly 0.3 GHz to 8 GHz. Some FRBs have been observed to repeat, while others have only occurred once, despite extensive efforts to observe repeat bursts. The origin of FRBs is still an open problem.

The first FRB discovery was made in 2007 at the Parkes Observatory in New South Wales, Australia, while searching in archival pulsar data from 2001 (Lorimer et al., 2007). The first few FRB detections were all made at Parkes (Lorimer et al., 2007; Keane et al., 2012; Thornton et al., 2013; Burke-Spolaor & Bannister, 2014). A new class of FRB-like radio frequency interference (RFI, §2.2), dubbed Perytons, was also discovered at Parkes around the time of the first FRB detections. Luckily, the source of Perytons was quickly discovered. They were found to be RFI generated on-site by a microwave oven, which was promptly put out of commission (Petroff et al., 2015a).

Later on FRBs started to be detected at telescopes all around the world. The earlier FRB surveys were carried out using single-dish telescopes. While successful in finding FRBs, these surveys had the significant drawback of not being able to localise FRBs due to the poor localisation capabilities of single-dish telescopes. Some of the successful single-dish surveys dedicated to finding FRBs include detections from Parkes (Ravi et al., 2015; Petroff et al., 2015b; Champion et al., 2016; Bhandari et al., 2018), the Arecibo Observatory in Puerto Rico (Spitler et al., 2014a), the Green Bank Telescope in the USA (Masui et al., 2015). Conducting surveys with an interferometer enables the localisation of FRBs. The larger field of view also results in more FRBs being detected. Interferometric surveys that have detected FRBs, with some either localising

---

<sup>1</sup>[frbcatalog.org](http://frbcatalog.org)

<sup>2</sup>1 Jy =  $10^{-23}$  erg cm<sup>-2</sup> s<sup>-1</sup> Hz<sup>-1</sup>

or highly constraining the localisation region of FRBs, include the upgraded Molongolo Observatory Synthesis Telescope (UTMOST) in Australia (Farah et al., 2018, 2019), the Australian Square Kilometer Array Pathfinder (ASKAP) (Bannister et al., 2017; Shannon et al., 2018), the Deep Synoptic Array ten-antenna (DSA-10) in the USA (Ravi et al., 2019), and the Canadian Hydrogen Intensity Mapping Experiment (CHIME) using the CHIME/FRB instrument (CHIME/FRB Collaboration et al., 2019a,b).

The landmark re-detection of an FRB, FRB121102 (Spitler et al., 2016), introduced excitement and confusion within the FRB community. The FRB catalog now included a repeating FRB and apparent one-off FRBs, perplexing the radio astronomy community to this day. This initiated important questions which remain unanswered, such as: Is the FRB population split into two distinct classes: cataclysmic and non-cataclysmic events explaining non-repeating and repeating FRBs? Or do all FRBs repeat, but repeat bursts are much weaker than the first burst, resulting in them not being detected? As of writing there are currently around 20 repeating FRBs published in the literature. FRB121102 (Spitler et al., 2014a) and FRB180916.J0158+65 (CHIME/FRB Collaboration et al., 2019a) are repeating FRBs of special interest, and are discussed further in §1.3 and §1.4, respectively. Additionally, FRB-like bursts have been detected from the Galactic magnetar SGR 1935+2154, which are further examined in §1.5.

The naming convention of FRBs is rather straightforward, starting with “FRB”, followed by six digits indicating the date of the detection in a “YYMMDD” format. FRB121102 was therefore discovered on November 2nd, 2012. With highly successful FRB detection telescopes like CHIME, multiple bursts can be detected at the same date, requiring an extension of the current standard. The solution, inspired by the naming convention of pulsars, was to append the J2000 coordinates of the detection to the standard name, e.g. FRB180916.J0158+65<sup>3</sup>.

## 1.1 Rates and Properties of FRBs

Observed FRB rates can be used to predict results of future surveys, as well as comparing to the rates of possible FRB-generating sources. The properties of FRBs can help deciphering the unanswered question of how, and what, generates FRBs.

Before discussing rates and properties of FRBs, it is important to first introduce the units of flux density and fluence. In radio astronomy it is more common to use units of flux density and fluence instead of flux. Flux density,  $S$ , is measured in Janskys, which has an SI unit of  $10^{-26} \text{ W m}^{-2} \text{ Hz}^{-1}$ , or  $10^{-23} \text{ erg s}^{-1} \text{ cm}^{-2} \text{ Hz}^{-1}$  in cgs units. Fluence,  $\mathcal{F} = S \times W$ , is in Jy ms, where  $W$  is the burst width in milliseconds. Flux density and fluence are easily interchangeable, and it is good practice to pay attention to which is being used at each time in the literature to avoid confusion.

<sup>3</sup> The FRB community discussed the best solution to expand the naming convention during the annual FRB conference in Amsterdam, 2019. Strong opinions for and against various conventions arose, and the discussion seemed to be barreling towards another “Great Debate”, as the one in 1995 where the GRB community debated over cosmological and Galactic origin of GRBs, before the moderators ended the discussion abruptly due to time constraints. At that point CHIME FRBs had already been named using the J2000 solution, resulting in the community accepting it as the tentative standard.

The all-sky burst event rate of an FRB survey can be calculated simply from the number of FRBs detected ( $N_{\text{FRB}}$ ), the survey observing time ( $T_{\text{obs}}$ , hours), and the fraction of the sky observed, or sky coverage, of the survey ( $\Omega_{\text{s}}$ ,  $\text{deg}^2$ ) with

$$R_{\text{survey}} = N_{\text{FRB}} \frac{24}{T_{\text{obs}}} \frac{4\pi \times (180/\pi)^2}{\Omega_{\text{s}}} \text{sky}^{-1} \text{day}^{-1}. \quad (1.1)$$

Even though the total number of detected FRBs is fairly low ( $\sim 10^2$ ), survey detections translate to surprisingly high all-sky rates of  $\sim 10^3 - 10^4$  bursts per sky per day (e.g. Thornton et al., 2013; Champion et al., 2016; Bhandari et al., 2018; Patel et al., 2018). Due to the varying sensitivity between telescopes and receivers, burst rates are expressed as the rate above the minimum fluence detection threshold of each survey, which in general lies between  $\sim 0.1 - 30$  Jy ms.

The FRB sky-rate can be converted to a volumetric rate, which is often done in order to compare the FRB event rate to the rate of other transients such as gamma-ray bursts or supernovae. A volumetric rate can be obtained from a daily sky-rate of  $R$  with

$$R_{\text{vol}} = 365 \frac{R}{V_{\text{max}}} \text{Gpc}^{-3} \text{yr}^{-1}, \quad (1.2)$$

where  $V_{\text{max}}$  is the maximum volume to which the survey is sensitive to. The volume is calculated as

$$V_{\text{max}} = \frac{4\pi}{3} d_{\text{max}}^3, \quad (1.3)$$

where  $d_{\text{max}}$  is the maximum distance to which the survey is sensitive to. To estimate  $d_{\text{max}}$  one can use either luminosity distance or co-moving distance (see discussion around Eq. 1.8), both of which can be estimated based on the survey fluence limit. The luminosity distance needs to be converted to co-moving distance to properly describe  $d_{\text{max}}$ . To use luminosity distance, one has to make assumptions about the intrinsic luminosity of FRBs, which is still an open problem. The other way is to estimate a redshift to which a survey is sensitive to, and obtain a co-moving distance from that redshift. An example of this is in Bhandari et al. (2018), where they obtain a sky-rate from Parkes FRBs of  $1.7_{-0.9}^{1.5} \times 10^3 \text{sky}^{-1} \text{day}^{-1}$ , out to a redshift of 1 (co-moving distance of 3.35 Gpc). The volumetric rate obtained from Eq. 1.2 is thus  $2000 - 7000 \text{Gpc}^{-3} \text{yr}^{-1}$ .

A caveat to the observed FRB burst rate is that the bursts may be beamed, meaning that they may not be isotropic. This in turn means that the actual burst rate is higher than the observed one, and by how much depends on the still-unknown FRB beaming fraction.

The observed rate of a survey (Eq. 1.1) can be used to estimate an expected burst rate of another survey. The rate and minimum fluence threshold of a reference survey can be scaled to the fluence threshold of the intended survey as (Connor et al., 2016)

$$R = R_{\text{ref}} \left( \frac{\mathcal{F}_{\text{min}}}{\mathcal{F}_{\text{min,ref}}} \right)^\gamma, \quad (1.4)$$

where the ‘‘ref’’ underscore denotes the reference survey and  $\gamma$  is the FRB brightness distribution power-law index.

The power-law index can be estimated from the FRB source-count distribution, which estimates the number of sources above a specific flux density (or energy/fluence) and is assumed to be a power-law as (Crawford et al., 1970)

$$N(S > S_{\min}) \propto S_{\min}^{\gamma}. \quad (1.5)$$

For uniformly distributed sources in a Euclidean Universe,  $\gamma$  is equal to -1.5. For the Parkes and ASKAP FRB samples, James et al. (2019) find  $\gamma$  to be  $-1.18 \pm 0.24$  and  $-2.20 \pm 0.46$ , respectively, and  $\gamma = -1.52 \pm 0.24$  for the combined sample. They find this result incompatible with a single power-law, implying a steepening in the FRB source-count distribution in the fluence range 5–40 Jy ms.

A flux density function power-law index can also be determined for single sources. For FRB121102,  $\gamma$  has been estimated from a number of surveys. Combining results from multiple telescopes at multiple frequencies, James (2019) obtain a value of  $\gamma = -0.9 \pm 0.2$ . FRB121102 surveys using the Westerbork Synthesis Radio Telescope (WSRT) (Oostrum et al., 2020) and Arecibo (Gourdji et al., 2019) have yielded a  $\gamma$  of  $-1.7 \pm 0.6$  and  $-1.8 \pm 0.3$ , respectively.

Another way to estimate the FRB distribution is with a Schechter luminosity function, which is generally used to estimate the distribution of stars or galaxies per luminosity interval (Schechter, 1976). The source count distribution is

$$\phi(\log L) = \left(\frac{L}{L_*}\right)^{\gamma'+1} \exp\left(-\frac{L}{L_*}\right), \quad (1.6)$$

where  $L_*$  is a cut-off luminosity. Luo et al. (2018) find  $L_* \sim 5 \times 10^{10} L_{\odot}$  and  $-1.8 < \gamma' < -1.2$ , consistent with power-law indices of pulsar giant pulses at low frequencies (Karuppusamy et al., 2012), pulsars (Han et al., 2016; Jankowski et al., 2018), short and long gamma-ray bursts (Sun et al., 2015; Pescalli et al., 2016), and compact binary mergers (Cao et al., 2018).

The observed widths of FRBs lie in the range of  $\sim 0.1 - 40$  ms (Petroff et al., 2016). The widths between bursts of repeating FRB sources also vary, with FRB121102 having bursts widths between 0.1–14 ms (Hessels et al., 2019; Gourdji et al., 2019), and FRB180916.J0158+65 with widths of 0.5–9 ms (The CHIME/FRB Collaboration et al., 2020a). At higher radio frequencies (4–8 GHz), FRB121102 seems to consistently have burst widths  $\lesssim 1$  ms (Michilli et al., 2018a; Zhang et al., 2018).

The majority of FRB observations have been carried out at frequencies centered around 1.4 GHz. Other common central frequencies include 0.6, 5, and 6 GHz. For the lower observing frequencies ( $< 2$  GHz), observing bandwidths are generally 300–400 MHz (e.g. CHIME, Effelsberg L-band, Arecibo L-band) or less, while the higher observing frequencies the bandwidths are in the range of 1–4 GHz (e.g. Effelsberg C-band, Arecibo C-band, VLA C-band). The lowest frequency detection of FRBs is 300 MHz, where multiple bursts from FRB180916.J0158+65 were detected in both the 298–362 MHz band of the Sardinia radio telescope (SRT, Pilia et al., 2020) and the 300–400 MHz band of the Robert C. Byrd Green Bank Telescope (GBT, Chawla et al., 2020a). On the other hand, the highest frequency FRB detection is 8 GHz, where

bursts from FRB121102 were detected in the 4–8 GHz band of the GBT (Gajjar et al., 2018; Zhang et al., 2018).

Attempts have been made to describe the frequency dependency of FRB brightness, or flux density, as a power-law with a spectral index,  $\alpha$ , where

$$S_f \propto f^\alpha. \quad (1.7)$$

The spectral index is poorly constrained due to small observing bandwidths and lack of simultaneous detections over a wide range of bandwidths. From simultaneous FRB121102 observations using Effelsberg at 1.4 GHz and the low frequency array (LOFAR) at 150 MHz, Houben et al. (2019) obtain a spectral index lower limit of  $-1.2 \pm 0.4$  based on Effelsberg detections and LOFAR non-detections. Macquart et al. (2019) calculate  $\alpha$  on a burst-by-burst basis from 23 ASKAP FRBs and obtain a mean spectral index of  $\alpha = -1.6^{+0.3}_{-0.2}$ , which is consistent with the Galactic pulsar spectral index of  $\sim -1.6$  (Jankowski et al., 2018). From a simultaneous detection of FRB121102 using the Karl G. Jansky Very Large Array (VLA) at 3 GHz and Arecibo at 1.4 GHz, Law et al. (2017) find  $\alpha = 2.1$ , which is in stark contrast to the aforementioned results, and argue that burst spectra of FRBs are not well described by a power-law.

Polarisation properties (linear/circular polarisation, rotation measure) have only been measured for  $\sim 20$  different FRB sources (Petroff et al., 2016). Linear polarisation fractions have been measured between  $\sim 0 - 100\%$ , and in five cases circular polarisation has been measured (3 – 30%). The majority of observed rotation measures (RMs) lie in the absolute value range of  $\lesssim 20 \text{ rad m}^{-2}$ , while some have RMs of  $\sim 10^2 \text{ rad m}^{-2}$ , exceeding the expected Galactic and intergalactic contribution, suggesting a dense magneto-ionic environment local to the bursting source. Two of the observed FRB RMs are particularly interesting: FRB110523 (Masui et al., 2015), which has an RM value consistent with propagation through a host galaxy disk, and FRB121102, whose bursts exhibit monumentally large RMs (Michilli et al., 2018a). Polarisation properties of FRBs and how they are extracted from data are explained in §1.2.3 and §2.5, and are discussed in more detail with regards to FRB121102 and FRB180916.J0158+65 in §1.3 and §1.4, respectively.

The redshift of an FRB bursting source can be estimated from the DM (§1.2.1). Converting from redshift to a physical distance requires an assumption of a model for the expansion of the Universe. Generally, a flat  $\Lambda$ CDM universe is assumed. Cosmological distances can be derived from redshift, namely co-moving distance ( $D_c$ ), angular diameter distance ( $D_A$ ), and luminosity distance ( $D_L$ ). One can use online calculators to obtain these distances<sup>4</sup> (e.g. Wright, 2006). The co-moving distance can be viewed as the physical distance to a source, as it does not change in time and takes the expansion of the Universe into account. Angular distance is defined as the proper size of an object divided by its angular size viewed by an observer. Luminosity distance is the distance based on the measured flux,  $F$ , and the intrinsic luminosity,  $L$ , of an object and can be expressed using the inverse square law as

$$D_L^2 = \frac{L}{4\pi F}, \quad (1.8)$$

<sup>4</sup>[astro.ucla.edu/~wright/CosmoCalc.html](http://astro.ucla.edu/~wright/CosmoCalc.html)

where  $F$  is in units of  $W \text{ m}^{-2}$  and  $L$  in units of  $W$ .

Luminosity distance can be used to calculate the energy of a burst (Petroff et al., 2019)

$$E_{\text{FRB}} \approx \left( \frac{D_L^2}{\text{Gpc}} \right) \left( \frac{\mathcal{F}}{0.1 \text{ Jy ms}} \right) \left( \frac{\Delta f_{\text{FRB}}}{\text{GHz}} \right) \left( \frac{\delta\Omega}{4\pi} \right) 10^{38} \text{ erg}, \quad (1.9)$$

where  $D_L$  is the luminosity distance,  $\mathcal{F}$  is the fluence,  $\Delta f_{\text{FRB}}$  is the burst emission bandwidth, and  $\delta\Omega$  is the emission solid angle in steradians. An observer does not necessarily have the complete information on  $\Delta f_{\text{FRB}}$  as the burst bandwidth is rarely completely contained within the observing bandwidth. Therefore the bandwidth term in Eq. 1.9 is replaced by the blueshifted observing bandwidth,  $\Delta f_{\text{obs}}(1+z)^{-1}$ . The emission mechanism of FRBs is still unknown, so one can assume isotropic emission ( $\delta\Omega \sim 4\pi$ ) and obtain upper limits, or assume some beaming solid angle, e.g. one steradian (Thornton et al., 2013). FRBs have been found to have energies in the range of  $\sim 10^{37} - 10^{41}$  erg (Keane & Petroff, 2015; Petroff et al., 2016; Gourdjji et al., 2019).

An important property of FRB emission is brightness temperature,  $T_b$ , which can help explaining the FRB emission process. Brightness temperature is the blackbody temperature radiating in the Rayleigh-Jeans portion of the Planck spectrum,

$$I_f = \frac{2kT_b}{\lambda^2}, \quad (1.10)$$

where  $I_f$  is the spectral intensity,  $k$  is the Boltzmann constant, and  $\lambda$  is the wavelength. The specific intensity of a burst of duration  $W$  and peak flux density  $S_{\text{peak}}$  is (Cordes & Chatterjee, 2019)

$$I_f \sim \frac{S_{\text{peak}}}{\delta\Omega}. \quad (1.11)$$

The light travel time across the source defines its maximum size (Lorimer & Kramer, 2012),

$$r < cW, \quad (1.12)$$

which in tandem with angular diameter distance,  $D_A$ , enables one to write  $\delta\Omega$  as

$$\delta\Omega \sim \left( \frac{cW}{D_A} \right)^2. \quad (1.13)$$

By combining Eqs 1.10–1.13 the brightness temperature can be written as

$$T_b \simeq \left( \frac{S_{\text{peak}}}{\text{Jy}} \right) \left( \frac{D_L}{\text{Gpc}} \right)^2 \left( \frac{f}{\text{GHz}} \right)^{-2} \left( \frac{W}{\text{ms}} \right)^{-2} (1+z)^{-4} 10^{36} \text{ K}, \quad (1.14)$$

where  $f$  is the central observed frequency and the conversion between angular and luminosity distance  $D_A = D_L(1+z)^{-2}$  is utilized (Macquart & Ekers, 2018). The brightness temperature of FRBs is  $T_b \sim 10^{35}$  K. Such high brightness temperatures require coherent emission, as brightness temperatures of  $T_b \geq 10^{12}$  K cannot be produced by incoherent emission (Readhead, 1994). Coherent radiation is when photons or waves are emitted in phase. An electron bunch consisting of  $N$  electrons, with all electrons radiating in phase, results in radiated power being proportional to  $N^2$  instead of  $N$  (Lyne & Graham-Smith, 2012). Lasers and masers are also sources of coherent emission.

## 1.2 Propagation Effects

FRBs travel long distances from its source before it reaches an observer on Earth. The FRB signal does not travel unaffected as it would in vacuum, as the space between stars in the galaxies and the space between galaxies themselves is filled with ionised medium.

Being a broad-band signal, FRBs will undergo frequency-dependant changes during its propagation through cold plasma. These changes have an effect on how a signal looks like to an observer compared to the original emitted signal, and in some cases the changes can be so dramatic that a signal is undetectable by an observer. The main propagation effects of FRBs, namely dispersion measure, rotation measure, scattering, and scintillation will be addressed in the following sections.

FRBs originate at cosmological distances, so redshift effects of radiation propagation and time will occur. These effects will be discussed when applicable.

### 1.2.1 Dispersion Measure

Electromagnetic (EM) radiation from FRB sources travels through the intergalactic medium (IGM) and the interstellar media (ISM) of both the host galaxy and the Milky Way before reaching an observer on Earth. The IGM and ISM are both composed of cold plasma, and will therefore have a frequency dependent effect on the group velocity,  $v_g$ , of traversing EM radiation. The group velocity of an EM wave traversing such media is (Lorimer & Kramer, 2012)

$$v_g(f) = c\sqrt{1 - \left(\frac{f_p}{f}\right)^2}, \quad (1.15)$$

where  $c$  is the speed of light,  $f$  is the frequency of the wave, and  $f_p$  is the plasma frequency, given by (Cordes, 2002)

$$f_p = \sqrt{\frac{e^2 n_e}{\pi m_e}} \simeq 8.5 \left(\frac{n_e}{\text{cm}^{-3}}\right)^{1/2} \text{ kHz}, \quad (1.16)$$

where  $e$  is the electron charge,  $n_e$  is the free electron number density, and  $m_e$  is the electron mass. One can make several deductions based on Eq. 1.15. First, a frequency lower than  $f_p$  is unable to pass through the plasma. Second, as  $f$  approaches infinity, the group velocity approaches  $c$  and an EM wave travels through the medium as it would in vacuum. Third, and most relevant to the study of FRBs, is that each frequency has a different group velocity so the higher frequencies of the signal travel faster than the lower. This means that for a broad-band signal where all frequencies are emitted simultaneously, the higher frequencies of the signal arrive earlier at the telescope, and the full extent of the signal is spread over time. This phenomenon is referred to as dispersion.

The arrival time difference between the frequency boundaries of a broad-band signal can be calculated by integrating the electron number density along the line of sight

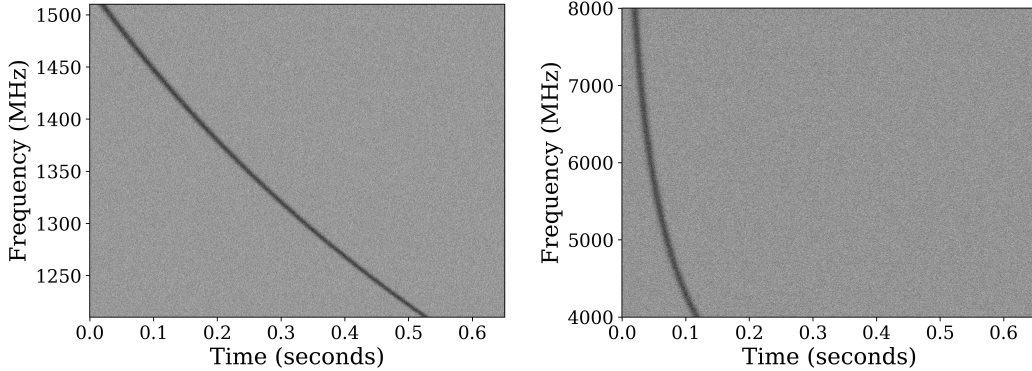


Figure 1.1: Dynamic spectrum of a simulated FRB with a DM of  $500 \text{ pc cm}^{-3}$  at different frequency ranges. *Left panel:* 7-beam receiver frequency range. *Right panel:* CX receiver frequency range.

(LoS) to the emitting source, resulting in

$$\Delta t = \mathcal{D} \text{ DM} \left( \frac{1}{f_b^2} - \frac{1}{f_t^2} \right) \text{ s}, \quad (1.17)$$

where  $f_b$  and  $f_t$  are the bottom and top frequencies of the signal respectively,  $\mathcal{D}$  is the dispersion constant, defined as

$$\mathcal{D} \equiv \frac{e^2}{2\pi m_e c} \simeq 4.15 \times 10^3 \text{ MHz}^2 \text{ pc}^{-1} \text{ cm}^3 \text{ s}, \quad (1.18)$$

and DM is the dispersion measure of a signal which has traveled a distance  $d$ , given by

$$\text{DM} = \int_0^d n_e \text{ dl } \text{ pc cm}^{-3}. \quad (1.19)$$

The DM of an astrophysical signal can be directly measured from the arrival time difference between the signal's frequencies. The arrival time difference between the frequency boundaries is referred to as the DM sweep, and can be used to crudely estimate the DM of a signal through Eq. 1.17. More appropriate methods used to determine DM are discussed in §2.3.

Figure 1.1 shows the dynamic spectrum (frequency versus time) of a simulated FRB with a DM of  $500 \text{ pc cm}^{-3}$ , exhibiting the difference of the DM sweep between two different frequency ranges. These ranges are the bandwidths of two commonly used receivers at the Effelsberg 100-m radio telescope, the P217mm (commonly known as the 7-beam) receiver, which has a bandwidth of 300 MHz between 1.21–1.51 GHz, and the S45mm (commonly known as the CX) receiver, which has a bandwidth of 4000 MHz between 4–8 GHz. The DM time delay of this signal across the bandwidths of these receivers can be calculated using Eq. 1.17, and is 0.51 and 0.10 seconds in the frequency bands of the 7-beam and CX receivers, respectively.

As Eq. 1.19 shows, DM is simply the integrated free electron column density along the line of sight, and can thus be used as a proxy for distance. In order to estimate the distance, models of the electron content for both the IGM and ISM are needed.

### 1.2.2 DM Budget and Redshift Estimate of FRBs

To estimate the distance to an FRB based on its DM, one first needs to account for each contributing factor of the total DM. The total DM of an FRB can be written as

$$\text{DM} = \text{DM}_{\text{MW}} + \text{DM}_{\text{MW,halo}} + \text{DM}_{\text{IGM}} + \text{DM}_{\text{host}}, \quad (1.20)$$

where the contributions are:  $\text{DM}_{\text{MW}}$  from the Galaxy,  $\text{DM}_{\text{MW,halo}}$  from the Galactic halo,  $\text{DM}_{\text{IGM}}$  from the IGM and possible intervening halos, and  $\text{DM}_{\text{host}}$  from the host galaxy, its halo, and the local environment of the FRB. The distance a signal travels within our Galaxy and its host galaxy is negligible compared to the cosmological distances it travels through the IGM, thus the distance to the bursting source can then be estimated from a relation between  $\text{DM}_{\text{IGM}}$  and redshift, once the other DM factors have been accounted for.

The two main models used to estimate the Galactic free electron content (and thus  $\text{DM}_{\text{MW}}$ ) are NE2001 (Cordes & Lazio, 2002) and YMW16 (Yao et al., 2017). The NE2001 model estimates the Galactic free electron content based on DMs of Galactic pulsars and contains several electron density distribution components such as the spiral arms, the local arm, and overdense components representing small scale structures. As the name suggests, the model is based on the measurements available at the end of the year 2001, but it still remained as the de facto standard in pulsar and FRB astronomy until the release of YMW16. The YMW16 model incorporates numerous additional pulsar DM measurements from more recent results. Like NE2001, YMW16 takes into account contributions from various Galactic components, and extends to the Magellanic clouds as well. For FRBs, these models are used to calculate the Galactic DM contribution along the line of sight to the source.  $\text{DM}_{\text{MW}}$  typically does not exceed  $100 \text{ pc cm}^{-3}$  for LoSs away from the Galactic plane.

Prochaska & Zheng (2019) estimate  $\text{DM}_{\text{MW,halo}}$  to be  $50\text{--}80 \text{ pc cm}^{-3}$ . Their estimation is based on DM contributions from nearby ionised and neutral high velocity clouds and highly ionised oxygen ions in the Galactic halo.

In a flat  $\Lambda$ CDM universe,  $\text{DM}_{\text{IGM}}$  is related to redshift,  $z$ , through (Deng & Zhang, 2014)

$$\text{DM}_{\text{IGM}} = \frac{3cH_0\Omega_b f_{\text{IGM}}}{8\pi G m_p} \int_0^z \frac{\chi(z)(1+z)dz}{[\Omega_m(1+z)^3 + \Omega_\Lambda]^{1/2}}, \quad (1.21)$$

where  $H_0$  is the Hubble constant,  $f_{\text{IGM}}$  is the fraction of baryons in the IGM,  $G$  is the gravitational constant,  $m_p$  is the proton mass,  $\chi$  is the free electron number per baryon in the Universe, and  $\Omega_b$ ,  $\Omega_m$ , and  $\Omega_\Lambda$  are the baryon, matter, and dark energy density parameters, respectively. By adopting the Planck results for the cosmological parameters (Planck Collaboration et al., 2016), Zhang (2018a) obtains an estimate of Eq. 1.21, assuming  $f_{\text{IGM}} = 0.83$  and  $\chi = 7/8$ , for  $z < 3$  of

$$z \sim \text{DM}_{\text{IGM}}/855 \text{ pc cm}^{-3}. \quad (1.22)$$

This relation has been found to be in agreement with DM measurements of localised FRBs (Ravi et al., 2019; Bannister et al., 2019). An important note is that LoS variations due to intervening haloes as high as  $1000 \text{ pc cm}^{-3}$  in  $\text{DM}_{\text{IGM}}$  for redshifts up

to 1 might occur depending on halo gas profile models of ionised baryons (McQuinn, 2014).

$DM_{\text{host}}$  in Eq. 1.20 is the DM value in the reference frame of the observer. Electromagnetic phase deviation in cold plasma can be written as (Rickett, 1990)

$$\phi = -\lambda r_e DM, \quad (1.23)$$

where  $\lambda$  is the wavelength and  $r_e$  is the electron radius. The redshift relation between observed and emitted wavelengths,

$$1 + z = \frac{\lambda_{\text{observed}}}{\lambda_{\text{emitted}}}, \quad (1.24)$$

and that the electromagnetic phase is invariant (Jackson, 1962), can be used along with Eq. 1.23 to show that the observed  $DM_{\text{host}}$  from a galaxy at a redshift  $z$  is  $DM_{\text{host}} \times (1 + z)$  in the source reference frame.

Estimating  $DM_{\text{host}}$  of FRBs depends on whether they have been localised to a host galaxy or not. The difference lies in how the remainder of the DM budget is handled after subtracting  $DM_{\text{MW}}$  and  $DM_{\text{MW,halo}}$ . For non-localised FRBs this is a non-trivial task, as it depends on numerous factors: FRB progenitor model, local environment, host galaxy type and orientation, and the LoS through the host (Walker et al., 2018). This can be handled by either ignoring  $DM_{\text{host}}$  and obtaining the redshift upper limit to the burst using Eq. 1.22, or by making assumptions about  $DM_{\text{host}}$  to obtain  $DM_{\text{IGM}}$  from which a redshift is obtained. On the other hand, this becomes a manageable endeavor for localised FRBs. Their host has a determined redshift which can be used to estimate  $DM_{\text{IGM}}$  with Eq. 1.22. The DM remainder can then be attributed to  $DM_{\text{host}}$ .

### 1.2.3 Faraday Rotation

As discussed in §1.2.1, an EM wave traversing cold plasma will be affected by dispersion. If the plasma is magnetised along the LoS, the wave is also subject to another effect, called Faraday rotation. Faraday rotation is the rotation of the linearly polarised plane of a signal, induced by the magnetic field parallel to the direction of its propagation.

Any polarisation can be written as a combination of left-hand circularly polarised (LHCP) and right-hand circularly polarised (RHCP) waves. The LHCP and RHCP waves have different phase velocities, and it is from that difference where Faraday rotation arises. The phase velocity is (e.g. Suresh & Cordes, 2019)

$$v_p(f) = \frac{2\pi f}{k}, \quad (1.25)$$

where  $k = 2\pi f/c$  is the wave number in a vacuum. In cold, magnetised plasma the wave number also contains a term for a frequency dependent refraction index,  $\mu(f)$ , i.e. (e.g. Lorimer & Kramer, 2012)

$$k(f) = \frac{2\pi f \mu(f)}{c} = \frac{2\pi f}{c} \sqrt{1 - \frac{f_p^2}{f^2} \mp \frac{f_p^2 f_B}{f^3}}, \quad (1.26)$$

with  $f_B$  being the cyclotron frequency

$$f_B = \frac{eB_{\parallel}}{2\pi m_e c} \simeq \frac{B_{\parallel}}{\text{G}} \times 3 \text{ MHz}, \quad (1.27)$$

where  $B_{\parallel}$  is the magnetic field along the line of sight in gauss. The  $\mp$  sign in Eq. 1.26 refers to the different propagation speeds of the RHCP (“−” sign) and LHCP (“+” sign) waves in a magnetised medium. The phase rotation difference between the RHCP and LHCP waves is expressed as

$$\Delta\Psi_{\text{Faraday}}(f) = \int_0^d (k_{\text{RHCP}} - k_{\text{LHCP}}) dl, \quad (1.28)$$

where  $d$  is the distance that the waves have traveled through magnetised medium. By inserting the expressions for  $k_{\text{RHCP}}$  and  $k_{\text{LHCP}}$  from Eq. 1.26 into Eq. 1.28, and assuming that  $f \gg f_p$  and  $f \gg f_B$ , the phase rotation difference becomes (Lorimer & Kramer, 2012)

$$\Delta\Psi_{\text{Faraday}}(f) = \frac{e^3}{\pi m_e^2 c^2 f^2} \int_0^d n_e B_{\parallel} dl. \quad (1.29)$$

This differential phase rotation is periodic in phase on  $2\pi$ . Faraday rotation however exhibits itself as the rotation of the polarisation position angle (PPA) on the linear polarisation plane and is therefore periodic on  $\pi$  (e.g. Everett & Weisberg, 2001). The change in PPA is then

$$\Delta\Psi_{\text{PPA}} = \frac{\Delta\Psi_{\text{Faraday}}}{2} \equiv \left(\frac{c}{f}\right)^2 \text{ RM}, \quad (1.30)$$

where the rotation measure (RM) is

$$\text{RM} = \frac{e^3}{2\pi m_e^2 c^4} \int_0^d n_e B_{\parallel} dl \text{ rad m}^{-2}. \quad (1.31)$$

The intensity of the Faraday rotation effect is thus measured through RM. RM can be either positive or negative depending on the direction of the magnetic field. If positive, the magnetic field is directed towards the observer, and if negative, the direction is away from the observer.

RM can also be used in tandem with DM to gauge the average magnetic field strength through the LoS of a signal (ignoring any variations along the LoS) by using Eqs. 1.19 and 1.31 to obtain (e.g. Mitra et al., 2003):

$$\langle B_{\parallel} \rangle = 1.232 \left( \frac{\text{RM}}{\text{rad m}^{-2}} \right) \left( \frac{\text{DM}}{\text{pc cm}^{-3}} \right)^{-1} \mu\text{G}. \quad (1.32)$$

Due to the cosmological origins of FRBs, redshift effects on the RM must be taken into account. Through Eqs. 1.24 and 2.8 one can obtain the following relation,

$$\text{RM}_{\text{obs}} = \frac{\text{RM}_{\text{source}}}{(1+z)^2}, \quad (1.33)$$

where  $\text{RM}_{\text{obs}}$  is the observed RM, and  $\text{RM}_{\text{source}}$  is the RM in the source frame.

However,  $\text{RM}_{\text{obs}}$  can not be solely attributed to the source, as magnetic fields in the IGM and ISM also contribute to Faraday rotation. Out to the maximum redshifts of observed FRBs,  $z \sim 1$ , the maximum absolute RM value expected from the IGM is  $\text{RM}_{\text{IGM}} \sim 10 \text{ rad m}^{-2}$  (Akhori et al., 2016; Hackstein et al., 2019). To estimate the Galactic ISM RM contribution, one can use either of the Galactic electron content models, NE2001 or YMW16, along with a model of the Galactic magnetic field (e.g. JF12, Jansson & Farrar, 2012).  $\text{RM}_{\text{IGM}}$  will vary depending on the LoS, but generally does not exceed  $\sim$  tens of  $\text{rad m}^{-2}$ .

### 1.2.4 Scattering

The ionised electrons in the cold plasma of the IGM and ISM are not homogeneously distributed. This will cause variations in the refractive index,  $\mu$ , introduced in Eq. 1.26 due to the dependency on electron number density in the plasma frequency (Eq. 1.16). As  $\mu$  is frequency dependent, it will in turn have a frequency dependent effect on the group velocity of a propagating wave,

$$v_g = c \mu. \quad (1.34)$$

A broad-band signal will therefore undergo a multi-path propagation. This phenomenon is known as scattering.

A fairly simple model that can reproduce basic properties of observed scattering in the ISM from pulsars is the so-called thin screen approximation (Williamson, 1972), where a thin scattering screen with a different refractive index than the rest of the ISM/IGM is placed approximately midway between the source and the observer. A simple illustration of this setup is shown in Fig. 1.2. A signal travelling through plasma within this model experiences phase variations due to the angular deflection of light,  $\theta_0$ , producing a broadened image of the source with an angular radius  $\theta_d$ . If the distance to the source is  $d$ , and the thickness of the scattering screen is  $a$ , the angular radius is (Lorimer & Kramer, 2012)

$$\theta_d = \frac{\theta_0}{2} \approx \frac{e^2}{2\pi m_e} \frac{\Delta n_e}{\sqrt{a}} \frac{\sqrt{d}}{f^2}, \quad (1.35)$$

where  $\Delta n_e$  is the electron density perturbation caused by the scattering screen. A signal received at an angle  $\theta_d$  will arrive later than a non-scattered signal. This time difference scales strongly with frequency and is known as the scattering timescale, given by

$$\tau_s = \frac{\theta_d^2 d}{c} \propto f^{-4}. \quad (1.36)$$

For a Kolmogorov turbulence spectrum of the ISM, the scattering timescale scales with frequency as  $\tau_s \propto f^{-4.4}$ .

Scattering manifests itself as an asymmetric broadening of a signal as a function of geometric time delay,  $\Delta t(\theta)$ , which is calculated using Eq. 1.36 by replacing  $\theta_d$  with  $\theta$ . This broadening is a time-dependent intensity known as a scattering tail and appears

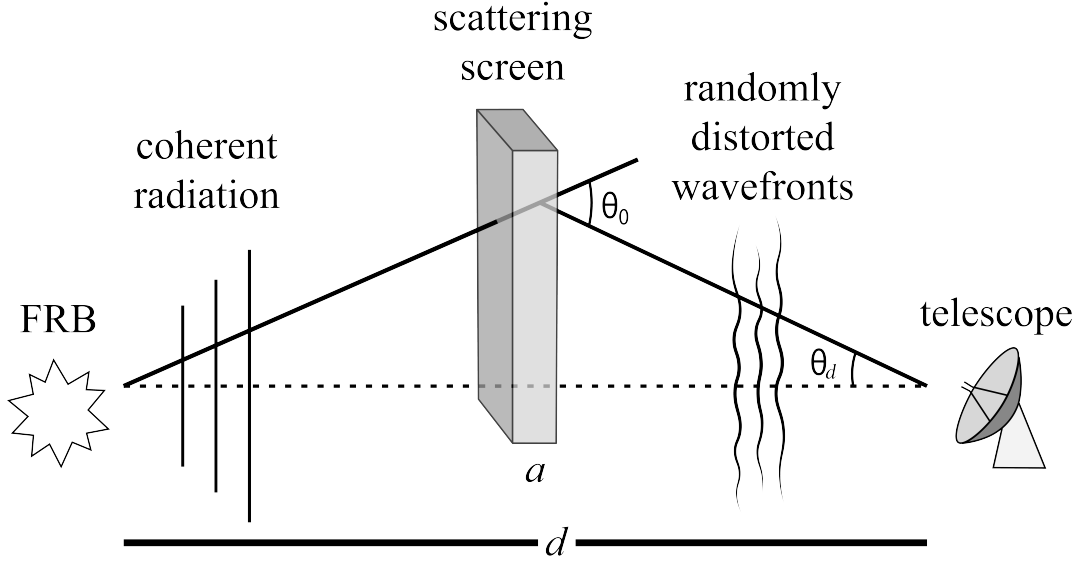


Figure 1.2: A geometrical illustration of a thin scattering screen placed halfway between an FRB source and an observer. The distance between the source and observer is  $d$ , and the thickness of the scattering screen is  $a$ . A signal experiences an angular deflection of  $\theta_0$  due to the scattering screen, producing a broadened image with an angular radius  $\theta_d$ . At the source, the radiation is spatially coherent, but becomes distorted as it travels through the screen, causing scintillation. The figure is adapted from Cordes (2002).

on the observed pulse shape,  $I_{\text{obs}}(t)$ , as the convolution of a one-sided exponential and the intrinsic pulse shape,  $I_{\text{int}}(t)$ , as (Lorimer & Kramer, 2012)

$$I_{\text{obs}}(t) = I_{\text{int}}(t) * e^{-\Delta t/\tau_s}, \quad (1.37)$$

where the intrinsic pulse shape is assumed to be a Gaussian. This effect is displayed in Fig. 1.3, showing how a pulse at 5.5 GHz with  $\tau_s = 1$  ms would look like at lower frequencies due to the strong scaling of  $\tau_s$  with frequency. When searching for single pulses (see Chapter 2), strong scattering can lead to a burst not being detected by conventional searching methods.

For extragalactic sources, like FRBs, the scattering timescale in Eq. 1.36 needs to be expanded to include the cosmological distances of the scattering screen and source. Abandoning the assumption of a scattering screen having to be located halfway between the source and observer, the cosmological analogue to Eq. 1.36 becomes (Macquart & Koay, 2013)

$$\tau = \frac{D_{\text{Sc}} D_{\text{ScSo}}}{D_{\text{So}}} \frac{\lambda_0^2}{4\pi^2 c r_{\text{diff}}^2}, \quad (1.38)$$

where  $D_{\text{Sc}}$  and  $D_{\text{So}}$  are the angular diameter distance to the scattering screen and burst source, respectively,  $D_{\text{ScSo}}$  is the angular diameter distance between the scattering screen and source,  $\lambda_0$  is the observing wavelength, and  $r_{\text{diff}}$  is the diffractive scale length. The diffractive scale length is the scale over which the scattering medium induces one

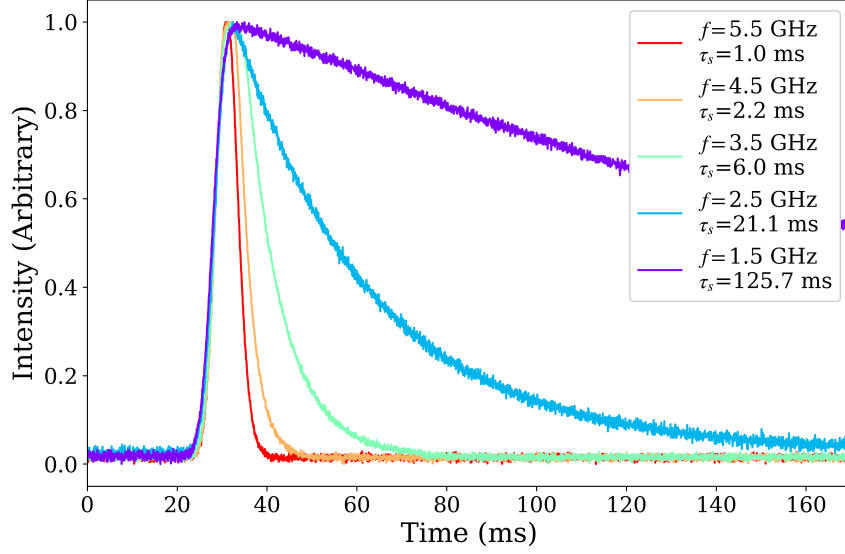


Figure 1.3: De-dispersed time series (see §2) of simulated bursts at different central frequencies with different scattering timescales,  $\tau_s$ , using the thin screen approximation. Each frequency band has 500 MHz of bandwidth, and  $\tau_s$  is scaled with respect to  $\tau_s$  at the top frequency (1 ms) following  $\tau_s \propto f^{-4.4}$ .

radian of phase difference to a signal and can be expressed as (Xu & Zhang, 2016)

$$r_{\text{diff}} \sim \begin{cases} \left[ \frac{\pi r_e^2 \lambda_0^2}{(1+z_{\text{Sc}})^2} \text{SM} l_0^{\beta-4} \right]^{-1/2} & , r_{\text{diff}} < l_0 \\ \left[ \frac{\pi r_e^2 \lambda_0^2}{(1+z_{\text{Sc}})^2} \text{SM} \right]^{1/(2-\beta)} & , r_{\text{diff}} > l_0, \end{cases} \quad (1.39)$$

where  $r_e$  is the electron radius,  $z_{\text{Sc}}$  is the redshift to the scattering screen,  $\beta$  is the turbulence spectral index,  $l_0$  is the turbulence inner scale, and SM is the scattering measure. SM is the integral of the turbulence power spectrum through the scattering region, and scales with redshift as (Macquart & Koay, 2013)

$$\text{SM} \propto \begin{cases} z & , z < 1 \\ (1+z)^{5/2} & , z > 1. \end{cases} \quad (1.40)$$

Through Eqs. 1.38–1.39 one can obtain a numerical expression for cosmological scattering, assuming a Kolmogorov turbulence ( $\beta = 11/3$ ), (Macquart & Koay, 2013)

$$\tau = (1+z_{\text{Sc}})^{-1} \left( \frac{D_{\text{eff}}}{1 \text{ Gpc}} \right) \left( \frac{\text{SM}}{10^{12} \text{ m}^{-17/3}} \right) \times \begin{cases} 4.1 \times 10^{-2} \left( \frac{\lambda_0}{1 \text{ m}} \right)^4 \left( \frac{l_0}{1 \text{ AU}} \right)^{-1/3} \text{ ms} & , r_{\text{diff}} < l_0 \\ 1.9 \times 10^{-1} \left( \frac{\lambda_0}{1 \text{ m}} \right)^{22/5} \text{ ms} & , r_{\text{diff}} > l_0, \end{cases} \quad (1.41)$$

where  $D_{\text{eff}}$  is the distance factor in Eq. 1.38, defined as the effective scattering distance,  $D_{\text{eff}} \equiv D_{\text{Sc}} D_{\text{ScSo}} / D_{\text{So}}$ .

The scattering timescale can be scrutinised further with respect to redshift and the location of the scattering screen. The scattering screen can either be located within the host galaxy of the bursting source, or in the IGM. If the screen is located in the host galaxy, one can assume that  $D_{\text{Sc}} = D_{\text{So}}$ , resulting in  $D_{\text{eff}} = D_{\text{ScSo}}$  and  $z_{\text{Sc}} = z_{\text{So}}$ , where  $z_{\text{So}}$  is the source redshift. For a scattering screen located in the host galaxy, the SM can be considered to represent intrinsic properties of host galaxy environments, and assumed to not change with redshift. Continuing to assume a Kolmogorov turbulence ( $\beta = 11/3$ ), the scattering within the host galaxy results in a scattering timescale of

$$\tau_{\text{host}} = D_{\text{ScSo}} \frac{\lambda_0^2}{4\pi^2 c r_{\text{diff}}^2} \propto \begin{cases} (1 + z_{\text{Sc}})^{-3} & , r_{\text{diff}} < l_0 \\ (1 + z_{\text{Sc}})^{-3.4} & , r_{\text{diff}} > l_0. \end{cases} \quad (1.42)$$

For the case where the scattering screen is in the IGM, the redshift scaling of  $D_{\text{eff}}$  needs to be taken into account. Macquart & Koay (2013) find that  $D_{\text{eff}}$  scales linearly with redshift up to  $z = 1$ , where it plateaus and starts decreasing with  $(1 + z_{\text{So}})^{-(1-1.3)}$ , depending on the fraction of  $z_{\text{Sc}}/z_{\text{So}}$ . They also argue that observed FRBs support the case where the diffractive scale is less than the inner turbulence scale, so the case of  $r_{\text{diff}} > l_0$  will not be explored here. With this information at hand, along with the SM redshift scaling in Eq. 1.40, the redshift scaling of scattering from a scattering screen in the IGM becomes

$$\tau_{\text{IGM}} \propto \begin{cases} z_{\text{So}}^2 & , z_{\text{So}} \lesssim 1 \\ (1 + z_{\text{So}})^{1.2-1.5} & , z_{\text{So}} \gtrsim 1. \end{cases} \quad (1.43)$$

### 1.2.5 Scintillation

Another effect of the inhomogeneities in the IGM and ISM plasma is scintillation. Scintillation causes intensity fluctuations in the frequency spectrum of a signal, known as scintles. This is caused by frequency-dependent phase differences as a signal undergoes its multi-path propagation through the aforementioned scattering screen, leading to constructive and destructive interference patterns, as previously depicted in Fig. 1.2. The phase difference of signals received over  $\tau_s$  is (Rickett, 1977)

$$\delta\Phi \sim 2\pi f \tau_s. \quad (1.44)$$

If the waves differ by more than roughly one radian, the interference becomes decorrelated. The frequency of interfering waves is limited to a bandwidth, with frequencies outside this bandwidth not contributing to the interference. This bandwidth is the scintillation bandwidth, or decorrelation bandwidth, and the condition for interference is thus (Lorimer & Kramer, 2012)

$$2\pi\Delta f \tau_s \sim 1, \quad (1.45)$$

where  $\Delta f$  is the scintillation bandwidth. For a Kolmogorov spectrum this relation becomes  $2\pi\Delta f \tau_s \sim 1.16$ .

Scintillation can be split into two branches, strong and weak. Whether weak or strong scintillation occurs depends on the scintillation strength, defined as (Rickett, 1990)

$$u \equiv \sqrt{\frac{f}{\Delta f}} \propto d^{1.1} f^{-1.7}, \quad (1.46)$$

where strong scintillation occurs when  $u > 1$  and weak when  $u < 1$ . The transition frequency between strong and weak scintillation,  $f_c$ , is when  $u = 1$ , and is obtained from Eqs. 1.45–1.46 as

$$f_c = \Delta f = \frac{1.16}{2\pi\tau_s}. \quad (1.47)$$

As the name suggests, weak scintillation results in minor interference modulations. Eq. 1.46 shows that the scintillation strength is proportional to distance, and inversely proportional to frequency. Weak scintillations are therefore generally observed from nearby sources or at high frequencies.

Strong scintillation can be either diffractive or refractive. Refractive scintillation occurs when a scattering structure incoherently changes the total amount of light reaching an observer. The intensity variations are long-term (hours to days), and results in an observed signal being uniformly brighter or fainter across the observing frequency. Diffractive scintillation is the interference (constructive and destructive) of the multi-path propagation of a signal through a scattering structure, resulting in short-term intensity variations (seconds to minutes). The way diffractive scintillation appears in data depends on the observing frequency bandwidth,  $\Delta f_{\text{obs}}$ , and the scintillation bandwidth,  $\Delta f$ . Multiple scintles can be present in a signal if  $\Delta f_{\text{obs}} > \Delta f$ , appearing as intensity modulations in parts of the observing bandwidth. If  $\Delta f_{\text{obs}} < \Delta f$ , only one scintle is sampled at any instant, and modulations between observations can be up to 100% (Lorimer & Kramer, 2012). This can be detrimental to FRB observations, as it could make a burst completely undetectable due to scintillation.

### 1.3 FRB121102

The detection of FRB121102 (Spitler et al., 2014a) with the Arecibo Observatory in Puerto Rico was the first FRB detection with a different telescope than the Parkes radio telescope in Australia. FRB121102 was detected towards the anti-center of the Galaxy with a DM of  $557 \text{ pc cm}^{-3}$ , three times the expected Galactic DM contribution according to the NE2001 model, which strongly suggested an extragalactic origin.

In May and June of 2015, 10 more bursts were detected from FRB121102 at Arecibo (Spitler et al., 2016). The additional bursts had DMs and sky positions consistent with the original burst, clearly confirming that FRB121102 was indeed the first repeating FRB. To date FRB121102 has been detected by a plethora of radio telescopes around the world, including (but not limited to) Arecibo (e.g. Scholz et al., 2016; Hessels et al., 2019), Effelsberg (e.g. Spitler et al., 2018; Houben et al., 2019; Hilmarsson et al., 2020a), CHIME (Josephy et al., 2019), VLA (e.g. Chatterjee et al., 2017; Hilmarsson et al., 2020a), GBT (e.g. Gajjar et al., 2018), and MeerKAT (Caleb et al., 2019).

Being the only known repeating FRB, FRB121102 was an ideal candidate for a campaign in order to localise it to a host galaxy. This became a reality when FRB121102 was detected with the Karl G. Jansky Very Large Array (VLA), enabling a sub-arcsecond localisation (Chatterjee et al., 2017). The J2000 position of the bursting source has a right ascension (RA) of  $05^{\text{h}}31^{\text{m}}58.70^{\text{s}}$  and declination (DEC) of  $+33^{\circ}08'52.5''$  with an uncertainty of  $\sim 0.1''$ . The host galaxy was identified as a low-mass, low-metallicity dwarf galaxy at a redshift of  $z = 0.1927$  (Tendulkar et al., 2017). The stellar mass of the host is  $\sim 1.3 \times 10^8 M_{\odot}$ , and the bursting source of FRB121102 is located within a star-forming region of the host galaxy (Bassa et al., 2017b).

The localisation of FRB121102 also revealed a faint ( $180 \mu\text{Jy}$ ), persistent radio source (PRS) coincident with it (Chatterjee et al., 2017). Using the European VLBI Network (EVN) and Arecibo, Marcote et al. (2017) were able to see the FRB121102 bursting source and the PRS on a milliarcsecond angular scale, both of which are offset from the optical center of the host galaxy. They found that the projected size of the PRS is  $\lesssim 0.7$  pc and that it is co-located with FRB121102 within  $\lesssim 40$  pc.

Bursts from FRB121102 have exhibited extremely high RMs. The first RM measurement of FRB121102 was  $\sim 100300 \text{ rad m}^{-2}$ , made on December 25, 2016 (Michilli et al., 2018a). The RM was observed to decrease to  $\sim 94000 \text{ rad m}^{-2}$  over the following seven months (Michilli et al., 2018a; Gajjar et al., 2018). The RM of FRB121102 has been observed to be decreasing even further, down to  $\sim 68000 \text{ rad m}^{-2}$  (Hilmarsson et al., 2020a, Chapter 5). The vast majority of the RM is thought to originate local to the bursting source (local environment and host galaxy), as the combined Galactic and IGM RM contribution is expected to be  $\lesssim 10^2 \text{ rad m}^{-2}$  (Michilli et al., 2018a). Bursts from FRB121102 are consistently  $\sim 100\%$  linearly polarised and the polarisation angles (PAs) are flat across the burst envelopes (Michilli et al., 2018a; Gajjar et al., 2018; Hilmarsson et al., 2020a).

While the RM of FRB121102 has changed drastically over time, the DM has undergone only minor changes. The initial DM was  $557 \text{ pc cm}^{-3}$  (Spitler et al., 2014a) and has subsequently been measured to be  $559 \text{ pc cm}^{-3}$  (Michilli et al., 2018a) and  $564 \text{ pc cm}^{-3}$  (Hilmarsson et al., 2020a), which averages to an increase of roughly  $1 \text{ pc cm}^{-3}$  per year. The Galactic and IGM contribution to the DM is estimated to be  $\sim 370 \text{ pc cm}^{-3}$  (Michilli et al., 2018a), meaning that the local environment of FRB121102 contributes  $\sim 190 \text{ pc cm}^{-3}$  to the observed DM.

A study on the time-frequency structure of FRB121102 bursts has shown that they exhibit a downward drift in frequency, as well as showing a variety of sub-components. (Hessels et al., 2019; Gourdji et al., 2019). The downward drifting phenomenon exhibits itself as burst envelopes shifting towards later times inversely with frequency, shown in Fig. 1.4. This has changed the standard of dedispersing (§2.3) bursts from maximising the signal-to-noise ratio to maximising the burst structure. Downward drifting has also been seen in bursts of other repeating FRBs (CHIME/FRB Collaboration et al., 2019a,c; Fonseca et al., 2020a). However, this downward drift is not ubiquitous across all bursts of repeating FRBs.

Simultaneous and follow-up observations of FRB121102 at other parts of the EM

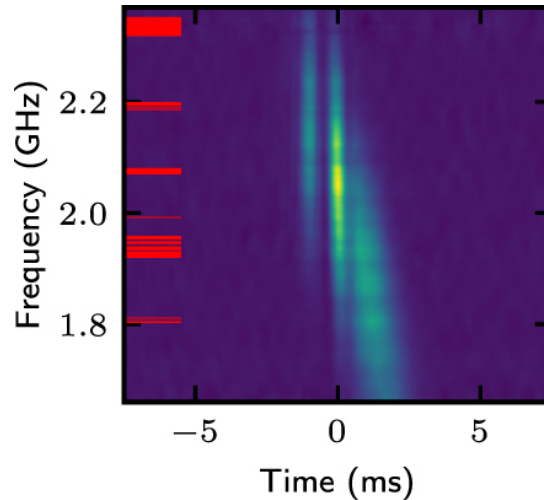


Figure 1.4: Dedispersed dynamic spectrum of one of the FRB121102 bursts in Hessels et al. (2019), exhibiting a clear downward drift towards lower frequencies.

spectrum have been performed but without any detection of a counterpart. This topic will be covered in more detail in §1.7.

Burst activity of FRB121102 seems to go through phases of activity and inactivity. By analyzing burst arrival times, Oppermann et al. (2018) find that the burst distribution is not Poissonian, but rather follows a Weibull distribution, which takes event clustering into account (see Chapter 4). Using detections from their survey with the 76-m Lovell telescope, along with detections in the literature, Rajwade et al. (2020a) find an apparent period of 157 days, where FRB121102 remains inactive for a contiguous 44% of the time within each cycle.

## 1.4 FRB180916.J0158+65

One of the first repeating FRBs detected at CHIME was FRB180916.J0158+65 (CHIME/FRB Collaboration et al., 2019c). The initial positional uncertainty of  $7'$  in RA and  $11'$  in DEC made it impossible to associate the bursting source with a host galaxy. Later on, Marcote et al. (2020) localised FRB180916.J0158+65 to the J2000 position of RA =  $01^{\text{h}}58^{\text{m}}00.7502^{\text{s}} \pm 2.3$  mas and DEC =  $65^{\circ}43'00.3152'' \pm 2.3$  mas using the EVN with the Effelsberg-100 m telescope at the forefront. The EVN observations consisted of data from eight telescopes, where the data from Effelsberg were used to search for single pulses. Four single pulses were detected, and data from the EVN telescopes were cross-correlated to produce radio interferometric images at the burst arrival times, enabling the aforementioned localisation.

The localisation of FRB180916.J0158+65 revealed a vastly different host galaxy than the one of FRB121102. The host is a spiral galaxy at a redshift of  $z = 0.0337$ , a solar neighbourhood metallicity and a stellar mass of  $\sim 10^{10} M_{\odot}$ , i.e. 100 times more massive and with five times higher metallicity than the host of FRB121102

(Marcote et al., 2020). There is also no PRS above a limit of  $18 \mu\text{Jy}$  coincident with FRB180916.J0158+65. Similar to FRB121102 though, FRB180916.J0158+65 resides within a star forming region of its host galaxy.

The DM of FRB180916.J0158+65 is  $349 \text{ pc cm}^{-3}$ , of which  $\lesssim 70 \text{ pc cm}^{-3}$  is attributed to  $\text{DM}_{\text{host}}$ . Its bursts are  $\sim 100\%$  linearly polarised, and its absolute RM is  $\sim 10^2 \text{ rad m}^{-2}$ , three orders of magnitude less than FRB121102.

Observations of FRB180916.J0158+65 have revealed an underlying four day bursting phase window with a  $16.35 \pm 0.18$  day periodicity (The CHIME/FRB Collaboration et al., 2020a). Each cycle does not exhibit the same level of activity, as some cycles are void of bursts, while others have one or multiple bursts.

## 1.5 Galactic FRB-like bursts from SGR 1935+2154

The soft gamma repeater (SGR) SGR 1935+2154 is a Galactic magnetar that has until April 2020 only been detected in the X-ray regime. On April 27th 2020, the *Swift* Burst Alert Telescope (BAT) detected multiple X-ray bursts from SGR 1935+2154 (Palmer & BAT Team, 2020). A bright, FRB-like burst was detected on April 28th 2020 with both CHIME (The CHIME/FRB Collaboration et al., 2020b) and the Survey for Transient Astronomical Radio Emission 2 (STARE2, Bochenek et al., 2020). An X-ray burst temporally coincident with the radio burst was detected with the X-ray/gamma-ray satellite AGILE (Tavani et al., 2020). The burst in the CHIME 400–800 MHz bandwidth was double peaked, and the estimated fluence and energy from the components combined were  $\sim 700 \text{ kJy ms}$  and  $\sim 3 \times 10^{34} \text{ erg}$ , respectively (The CHIME/FRB Collaboration et al., 2020b). STARE2 observes between 1280–1530 MHz, and the detected burst was single peaked, with a fluence of  $1.5 \text{ MJy ms}$  and an energy of  $2.2 \times 10^{35} \text{ erg}$  (Bochenek et al., 2020). On May 3rd 2020, the Five-hundred-metre Aperture Spherical radio telescope (FAST) detected a burst from SGR 1935+2154 (Zhang et al., 2020). The burst detected in the 1–1.5 GHz bandwidth of FAST was less bright than the CHIME/STARE2 burst, with a fluence of  $60 \text{ mJy ms}$ . The burst however had similar attributes to FRB121102, with a nearly fully linearly polarized burst, and a flat PA across the burst. The DM of the CHIME, STARE2, and FAST bursts are all consistent with  $333 \text{ pc cm}^{-3}$ . The maximum estimated Galactic DM contribution from NE2001 is  $540 \text{ pc cm}^{-3}$ . A search for a PRS using the EVN was performed on June 6th 2020 with no radio emission detected above the threshold of  $95 \mu\text{Jy}$  (Nimmo et al., 2020).

Margalit et al. (2020) show that the coincident radio and X-ray bursts of SGR 1935+2154 are consistent with predictions from the synchrotron maser shock model within a supernova remnant (§1.6.1). This claim is reinforced by the fact that SGR 1935+2154 lies within a Galactic supernova remnant (Gaensler, 2014). The STARE2 burst energy is a factor of  $\sim 10^3$  greater than any Galactic radio burst detected, and a factor of 40 less than the lowest-energy FRB detected, placing it outside the general energy limits of both FRBs and pulsars/magnetars. Whether the bursts from SGR 1935+2154 are FRBs, or a phenomenon that bridges the gap between magnetar radio bursts and FRBs remains to be seen.

## 1.6 Progenitor Theories

In the early days of the FRB field, the number of progenitor theories grew faster than the number of new FRB detections. It was not until 2019 that the number of published FRBs surpassed the number of theories. As more observational information on FRBs has been gathered over the years, more FRB theories have been excluded. Comparing the progenitor modelling to the early days of the GRB field, Kulkarni (2018) writes: *“The modus operandi was astonishingly familiar: suggest all possible collisions between comets, asteroids, brown dwarfs, white dwarfs, neutron stars, and black holes, invoke improbable scenarios, and failing all these possibilities invoke string theory.”*

An FRB model needs to take into account the various FRB properties, such as duration, polarisation, time-frequency structure, emission frequency, energetics, and event rate. On top of that the models should specify whether they explain repeating or non-repeating FRBs, or both. Neutron stars (NSs) and other compact objects are the most straightforward candidate as FRB sources due to the small burst emission region (Eq. 1.12) and their capabilities of producing the required FRB energies.

The FRB field has gravitated towards one paradigm: highly magnetized NSs (magnetars) within supernova remnants (SNRs). Active galactic nuclei (AGNs), possibly interacting with NSs, are still considered as a possibility for the isolated case of FRB121102. The discussion here will be focused on these two paradigms, with a brief mention of a few other models. An interested reader is encouraged to browse the FRB theory catalog<sup>5</sup> (Platts et al., 2019) for a summary and references of published models.

### 1.6.1 Magnetars in Supernova Remnants

Within this framework the emphasis has been on trying to explain the repetition and high RM of FRB121102, as well as the coincident PRS. A clear requirement for this model is a supernova (SN) which leaves behind a NS.

Piro (2016) discusses the impact of an SNR on FRBs generated within, without an assumption on how FRBs are generated. The SNR goes through two main stages of expansion: an ejecta dominated stage where the ejecta moves at the velocity set by the SN, and the Sedov-Taylor stage when the ejecta slows down from interaction with the surrounding medium. Considering only regions re-ionised by the reverse shock, both the DM and RM are expected to change with  $\Delta r = r_b - r_r$ , where  $r_b$  is the blastwave radius and  $r_r$  is the reverse shock radius. Observationally, the most important way in which the SNR can impact an FRB is through free-free absorption, where at early times following the SN, the SNR is optically thick at radio frequencies. Piro (2016) finds that free-free absorption dominates the SNR on a timescale of  $\sim 100 - 500$  years at radio frequencies, assuming the SNR is mainly ionized by the reverse shock. By assuming that the SNR is also photoionized from within by the rotationally powered magnetar nebula, the SNR becomes optically thin after a timescale of  $\sim$  years at radio frequencies (Metzger et al., 2017).

---

<sup>5</sup>[frbtheorycat.org](http://frbtheorycat.org)

The host galaxy of FRB121102 shares similarities with those of long-duration gamma-ray bursts (LGRBs) and type-I hydrogen-poor superluminous supernovae (SLSNe-I), i.e. low mass and low metallicity. SLSNe-I are a subclass of supernovae which are hydrogen poor and orders of magnitude more luminous than type-I SN. The additional luminosity is powered by a remnant magnetar (Greiner et al., 2015). Metzger et al. (2017) propose that repeating FRBs originate from young magnetars embedded within a young SNR, thus linking them to SLSNe-I/LGRBs.

Two main avenues exist for the generation of FRBs from within an SNR: pulsar-like emission in the magnetar magnetosphere (Kumar et al., 2017; Yang & Zhang, 2018), and a synchrotron maser mechanism from relativistic shocks in the magnetar circumstellar medium (Lyubarsky, 2014; Beloborodov, 2017). Here the focus is on the maser mechanism, but avid pulsar emission enthusiasts are encouraged to read Cordes & Wasserman (2016), where they model extragalactic FRBs from super-giant pulses from the Crab pulsar.

Another example of the relativistic shock model, which is considered in the work done in Chapter 5, is from Metzger et al. (2019). They propose a model where FRBs originate from a flaring magnetar within an SNR. The magnetar releases an ultra-relativistic shell which collides with a mildly relativistic magnetized ion-electron shell. As the shell decelerates, forward shocks produce coherent radio emission through a synchrotron maser mechanism. Within this scenario, the magnetar wind nebula is responsible for the large and evolving RM, as well as the PRS. A  $\sim 10$  ms timescale gamma-ray afterglow is expected to follow the radio burst. Unfortunately, the afterglow luminosity is below the detection threshold of current telescopes for a source at the distance of FRB121102.

### 1.6.2 Active Galactic Nuclei

The “cosmic comb” is one of the main FRB models involving an AGN and an NS. Zhang (2017) propose that a canonical pulsar, which is undetectable at cosmological distances, can produce FRBs if its magnetosphere is “combed” by a nearby, strong plasma stream. AGNs are not the sole possible companion within this model. Any object that can produce plasma streams is viable (e.g. GRBs, SNe, and stellar flares), as long as the ram pressure of the plasma stream exceeds the magnetic pressure of the pulsar magnetosphere. Zhang (2018b) build upon this to explain the observational data from FRB121102. They use variable outflows of a low-luminosity, accreting super-massive black hole “combing” the magnetosphere of a nearby pulsar to explain various FRB121102 properties such as RM and its variation, polarization, repetition, and burst structures.

Romero et al. (2016) provide a solution requiring only an AGN. In that model, an FRB is the result of the interaction between relativistic jets and plasma condensations (clouds). The jets induce turbulence in the clouds which in turn scatter electrons and produce radiation. The emission becomes coherent in the presence of density inhomogeneities in the jet, giving rise to observable FRBs at cosmological distances.

An AGN model was initially thought unlikely, as AGNs rarely reside within dwarf

galaxies, like the host galaxy of FRB121102. There was also no evidence of an AGN in the FRB121102 host optical spectrum (Tendulkar et al., 2017). More recently it was shown that AGNs can often be found offset from the optical centre of dwarf galaxies (Reines et al., 2020). Also, there are similarities in RM the evolution between FRB121102 and the Galactic centre magnetar, J1745-2900 (Desvignes et al., 2018). As a general FRB progenitor model, AGN models are disfavoured based on localisations of four FRBs with the Australian Square Kilometer Array Pathfinder (ASKAP) telescope, as they were localised to the outskirts of massive galaxies (Bhandari et al., 2020).

### 1.6.3 Periodicity

The apparent periodicity of FRB121102 and FRB180916.J0158+65 has naturally spurred an insurgence in models attempting to explain this. Here I will briefly introduce two of those models.

Ioka & Zhang (2020) make use of the “cosmic comb” model involving an interacting NS binary system to model periodic FRBs. The FRB producing NS is a highly magnetized pulsar, and the binary companion is a massive star or a millisecond pulsar. The FRB production arises from the magnetic field of the FRB pulsar as it is “combed” by the strong wind of the companion. The wind of the FRB pulsar creates a funnel in the wind of its companion, and observable FRBs are emitted from the funnel. The periodicity is explained by orbital period of the binary system, and the active bursting period represents the time window when the funnel is directed towards an observer.

Levin et al. (2020) model periodic FRBs with a precessing flaring magnetar, where the precession arises from the magnetar being deformed. The strong magnetic field of the magnetar is required for both the energy budget of FRBs and in order to deform the magnetar. The periodicity is tied to the precession period, and the active bursting phase arises when the flares of the precessing magnetar are directed towards an observer. This model can be tested with observations, as damping of the precession leads to an increase in the precession period over time.

### 1.6.4 Cataclysmic and Exotic Models

The fact that some FRBs repeat does not necessarily exclude all models involving cataclysmic events, as the FRB population might not all originate from the same type of events. Following is a brief introduction to a few popular picks from the vast collection of published models.

Falcke & Rezzolla (2014) provided one of the most popular cataclysmic FRB theories, involving objects that they call “blitzars”. According to them, a “blitzar” is a supramassive neutron star with mass above the critical mass for non-rotating neutron stars, and is supported from collapse by its rapid rotation. As its spin slows due to magnetic braking, the neutron star will suddenly collapse to a black hole on the order of  $\sim 10^3 - 10^6$  years after its birth once the angular momentum no longer supports it. During the collapse the magnetic field lines snap violently, resulting in an FRB. Most et al. (2018) performed simulations of the gravitational collapse of rotating, magnetized

NSs. Based on their simulations they found that the blitzar scenario is consistent with observed FRB luminosities. The blitzar scenario could therefore still be plausible for non-repeating FRBs.

Many works attempt to model FRBs from binary neutron star mergers (e.g. Totani, 2013; Wang et al., 2016; Yamasaki et al., 2018; Margalit et al., 2019). To name one, Yamasaki et al. (2018) explain both repeating and non-repeating FRBs from binary neutron star mergers. The event of the merger would result in a single FRB. A fraction of the mergers can leave behind a rapidly rotating and stable NS. This remnant NS would then be capable of producing fainter, repeating bursts. The circumstellar environment of the remnant NS is optically thick at radio frequencies following the merger. Repeating bursts would therefore become observable once the environment is optically thin at radio frequencies, which is a timescale of 1–10 years after the merger. If a gravitational wave from a binary NS merger is detected, it can be followed up on this timescale to search for repeating FRBs.

Some more exotic models include exploding black holes (Barrau et al., 2014), superconducting cosmic strings (Yu et al., 2014), and even technomarkers from extragalactic civilizations, where FRBs are the result of powering light sails (Lingam & Loeb, 2017).

## 1.7 FRB Follow-up Across the Electromagnetic Spectrum

A myriad of FRB observations in other parts of the EM spectrum have been performed, both in tandem with radio observations and as follow-up observations. These observations are mainly done in optical, X-ray, and gamma-ray parts of the EM spectrum, in order to search for FRB counterparts. Possible counterparts can be precursors, prompt (contemporaneous), delayed (akin to GRB afterglow), or persistent (long-lived, similar to the PRS of FRB121102). Although no non-radio FRB counterparts have been found, the non-detections can provide upper limits and thus add some constraints to the FRB models. Repeating FRBs have a clear advantage in this area, as radio and other EM spectrum observations can be carried out in tandem during bursting activity, while “one-off” bursts can only be followed up as early as hours–days following the burst. Following is a brief discussion on general counterpart follow-up strategies, as well as a discussion on FRB121102 follow-up.

### 1.7.1 General FRB Follow-up Strategies

There are three general ways which one can do FRB follow-up observations, all of which are applicable to both general FRB searches and observations of repeating FRBs. First is to trigger other telescopes once a burst is detected. Preferably the burst should be detected in real-time so that the trigger can be sent posthaste. This method is suitable for finding delayed counterparts due to the possible long delays between the burst detection and follow-up and is usually performed with optical and high-energy telescopes. Second is to look through archival data of telescopes to see if the location of an FRB was being observed by chance at the time of its occurrence. This is a common procedure for the space-based  $\gamma$ -ray telescopes. Third is to simply observe with other

telescopes simultaneously to the radio observations. This is called s and is common when observing known repeating FRBs. An example of each follow-up type is listed below.

The real-time detection of FRB140514 (Petroff et al., 2015b) with the Parkes radio telescope was the first real-time FRB detection made, providing an unprecedented opportunity to perform rapid follow-up observations. Radio follow-up at other telescopes started seven hours following the burst using the Australia Telescope Compact Array (ATCA) for three hours. Further radio follow-up observations were performed 2–70 days following the burst using Parkes, Effelberg, and the Giant Metrewave Radio Telescope (GMRT). 8.5 hours following the burst, the *Swift* X-ray Telescope (XRT) observed the FRB140514 field for roughly an hour and 15 hours later for another half hour. The Gamma-Ray Burst Optical/Near-Infrared Detector (GROND) followed-up 16 hours and 2.6 days after the burst, with roughly 10 minutes of exposure at each epoch. Optical follow-up was made 16 hours–55 days following the burst using the Swope telescope, the intermediate Palomar Transient Factory (iPTF), the Magellan telescope, the SkyMapper telescope, and the Nordic Optical Telescope (NOT). The extensive follow-up on FRB140514 unfortunately revealed no associated counterpart at any of the observing wavelengths. The non-detection of a counterpart was used to rule out association between this FRB and a nearby SN or a long GRB.

Cunningham et al. (2019) search for high-energy counterparts (X-ray–gamma-ray) of 23 FRBs with the *Fermi* Gamma-ray Burst Monitor (GBM), *Fermi* Large Area Telescope (LAT), and the *Swift* Burst Alert Telescope (BAT). Data from any one of the telescopes were available for only 14 of the FRBs. Cunningham et al. (2019) used the high-energy fluence threshold to place upper limits on the high-energy emission of FRBs ( $< 0.3 \times 10^{-6}$  erg cm $^{-2}$  for a timescale of 0.1 s). They also placed limits of the ratio of radio to gamma-ray fluence of  $> 10^9$  Jy ms erg $^{-1}$  cm $^2$ .

Sokolowski et al. (2018) used the Murchison Widefield Array (MWA) in a campaign to shadow ASKAP. The MWA observes at frequencies between 170 and 200 MHz, while ASKAP observed between 1150–1490 MHz. The aim of the shadowing campaign was to detect FRBs at lower radio frequencies and to investigate the FRB frequency spectrum. Seven FRBs were detected at ASKAP with simultaneous MWA data. No emission was detected in the MWA band, and the non-detection with the MWA suggests a spectral turnover, i.e. a sharp change in the spectral index, at frequencies above 200 MHz.

### 1.7.2 FRB121102 Follow-up

FRB121102 is by far the most studied FRB and has been observed with telescopes all around the world at wavelengths spanning the entire EM spectrum. Aside from its associated PRS, no other counterpart at any wavelength has been detected. There is certainly no dearth of FRB121102 follow-up work in the literature, but it would be quixotic to list them all here. Instead a selected few multi-telescope campaigns and their results are listed in Table 1.1.

Table 1.1: Follow-up surveys of FRB121102 across the electromagnetic spectrum. *From left to right:* Survey reference, telescopes used, part of the electromagnetic spectrum observed, duration of non-radio observations in tandem with radio observations, and number of bursts from FRB121102 detected during the radio observations or the survey upper limits. Abbreviations used are the 305-m William E. Gordon Telescope at the Arecibo Observatory (AO), Effelsberg 100-m radio telescope (EFF), the Robert C. Byrd Green Bank Telescope (GBT), the Karl G. Jansky Very Large Array (VLA), the *Swift* X-ray telescope (XRT), the X-ray Multi-Mirror Mission (XMM) Newton observatory, the *Fermi* Gamma-ray burst monitor (GBM), and the low-frequency array (LOFAR).

Survey ref.	Telescopes	EM spectrum	Obs. dur.	No. FRBs/Upper limits
(1)	AO, EFF, GBT	Radio		12
	XMM Newton, Chandra	X-ray	30 ks 40 ks	$3 \times 10^{-11}$ erg cm <sup>-2</sup> on 0.5–10 keV fluence
	<i>Fermi</i> GBM	$\gamma$ -ray		$4 \times 10^{-9}$ erg cm <sup>-2</sup> on 10–100 keV fluence
(2)	EFF	Radio		13
	ULTRASPEC	Optical	19.6 hrs	0.33 mJy at 767 nm
(3)	AO	Radio		Unpublished
	VERITAS	$\gamma$ -ray	10.8 hrs	$5.2 \times 10^{-12}$ cm <sup>-2</sup> s <sup>-1</sup> TeV <sup>-1</sup> at 0.2 TeV $4.0 \times 10^{-11}$ cm <sup>-2</sup> s <sup>-1</sup> TeV <sup>-1</sup> at 0.15 TeV
(4)	AO	Radio		5
	MAGIC	$\gamma$ -ray	22 hrs	$\sim 10^{-12}$ cm <sup>-2</sup> s <sup>-1</sup> persistent flux
		Optical		$\sim 10^{-7}$ cm <sup>-2</sup> s <sup>-1</sup> ms timescale
				8.6 mJy U-band, 1 ms timescale
(5)	EFF	Radio		9
	LOFAR	Radio (low freq.)	19 hrs	0 FRBs

(1) Scholz et al. (2017), (2) Hardy et al. (2017), (3) Bird & VERITAS Collaboration (2017), (4) MAGIC Collaboration et al. (2018), (5) Houben et al. (2019)

## 1.8 FRBs as Astrophysical Tools

Solving the mystery of how FRBs are created can help deepening the understanding of coherent emission. FRBs can however also be useful without the knowledge of how they are formed, as they can be used as tools for astrophysics. Currently their usefulness is limited, as applications are heavily reliant on the number of FRBs (usually within a certain redshift range), localisation precision and number of localisations, and redshift range of the FRB population. These conditions can feasibly be met in the near future with the current and upcoming observing instruments. Following is a discussion on how FRBs can help answer some of the open problems in modern astrophysics.

FRBs can be used to solve the “missing baryon” problem, where only half of the cosmic baryons in the local universe can be accounted for. The missing baryons reside at densities and temperatures that are difficult to detect through absorption or emission, so their constraints are weak. McQuinn (2014) show that the DM measurement distribution is sensitive to intervening galactic halos. With  $\sim 100$  DM measurements at redshifts  $z \gtrsim 0.5$ , localised within an arcminute, constraints can be placed on baryonic mass profiles surrounding different galaxy types. Macquart et al. (2020) managed to find the “missing baryons” with a sample of five FRBs with arcsecond localisation. By investigating the DM-redshift relation of their FRB sample they find that the missing baryons are present in the ionised IGM, and they derive a cosmic baryon density of  $\Omega_b = 0.051_{-0.025}^{+0.021} h_{70}^{-1}$  with 95% confidence, where  $h_{70}$  is the dimensionless Hubble’s constant,  $h_{70} = H_0 / (70 \text{ km s}^{-1} \text{ Mpc}^{-1})$ .

Zhou et al. (2014) postulate that FRBs can be used as cosmological probes, adding constraints to the dark energy equation of state. Given enough FRBs along different sightlines within a narrow redshift bin (e.g.  $\Delta z \sim 0.05$ ), the mean dispersion measure will not suffer from the inhomogeneities of the IGM. With tens of FRBs in each redshift bin, reaching out to redshifts of  $\geq 3$ , FRBs can help constrain the dark energy equation of state through the IGM DM-redshift relation.

By using DM as a proxy for distance, Masui & Sigurdson (2015) propose that FRBs can be used to study the three-dimensional clustering of matter in the universe without the need for redshift information. The FRBs would therefore not need to be localised, and a clustering signal could be measured with  $\sim 10^3$  FRBs. However, stochasticity in the IGM DM and DM local to the bursting source could increase this number drastically.

FRBs can be used to constrain the mass of photons. The speed of light in vacuum is frequency dependent if photons have a non-zero rest mass. This frequency dependence will be indistinguishable from plasma dispersion, but their contributions vary with redshift. An assumption of how much the IGM contributes to the dispersion delay is required. Bonetti et al. (2017) use the localisation of FRB121102 to constrain the photon mass upper limit to  $< 3.9 \times 10^{-50} \text{ kg}$ .

With measured RMs and DMs, an average magnetic field along the line of sight can be obtained. Vazza et al. (2018) show that for  $\sim 10^2 - 10^3$  RMs and DMs, FRBs can be used to discriminate between scenarios for the origin of cosmic magnetic fields as RM and DM are affected differently between scenarios. This method is independent of

the distance distribution, so no localisations are required.

The time delay of strongly gravitationally lensed FRBs can be measured to high precision due to the short duration of FRBs. Strongly lensed FRBs can thus be used for various cosmological purposes. Li et al. (2018) show that by observing 10 strongly lensed FRBs by intervening galaxies using the upcoming Square Kilometer Array (SKA), the Hubble constant can be constrained within a 0.91% uncertainty, assuming a flat  $\Lambda$ CDM Universe. As the SKA is not yet operational, an optimistic time-frame to achieve this is within 30 years. Liu et al. (2019) show that time delay measurements of strongly lensed FRBs can constrain the dark energy equation of state. By adding 30 such time delays to the cosmic microwave background radiation and type Ia supernovae constraints, Liu et al. (2019) show that the dark energy equation of state constraints can be improved by a factor of two.

## 1.9 Thesis Outline

This thesis focuses on FRB searches with the Effelsberg 100-m radio telescope and is arranged as follows:

- Chapter 2 describes how an astrophysical signal is received by a telescope and how the resulting data are reduced and searched for FRBs. Also described are the search software and search pipelines used in later chapters.
- Chapter 3 introduces phased array feed receivers, their use cases on single-dish telescopes, and the commissioning of such a receiver at Effelsberg. The results from the commissioning observations are interpreted. Potential observing targets and improvements for future observations are also discussed.
- Chapter 4 describes observations of superluminous supernovae and long gamma-ray bursts in search of FRB121102-like sources with Effelsberg. The burst rate of FRB121102 is scaled to each of the observed targets and compared to the upper rate limits obtained from the non-detections of the observations. Also discussed are the effects of a potential beaming fraction and a bursting source following a Weibull distribution.
- Chapter 5 introduces sixteen FRB121102 burst RMs from observations with the Arecibo Observatory 305-m William E. Gordon radio telescope, Effelsberg, and the Karl G. Jansky Very Large Array. The RMs of FRB121102 show a significant decrease over year-timescales and less intense, erratic variations on week-timescales. The long-term RM trend is compared to models of RM evolution from a magnetar within a supernova remnant and the Galactic center magnetar, PSR J1745-2900.
- Chapter 6 summarises the results of the previous chapters, and discusses future prospects for FRB searches with Effelsberg and in general.



# Data Acquisition and Searching

---

Detecting a burst from an FRB is certainly not a trivial task. From a technical standpoint, telescopes with large collecting areas, sophisticated hardware, and dedicated software are required. Building and designing these also comes at a high cost.

The typical radio telescope is a parabolic or spherical reflector, ranging from  $\sim 10$  to 500 meters in diameter. To the uninformed, these large sizes might seem excessive, but they do serve an important purpose. Telescopes can operate as a single unit or in tandem to form an interferometric array.

This chapter will describe how an EM wave from a cosmological FRB is collected by a single-dish telescope, converted to data, subsequently searched using specific software, and finally seen by an astronomer as a figure on a computer monitor, who exclaims: “Aha! That’s a burst!”

## 2.1 Instrumentation

There is more to radio telescopes than the eye can see. While the monumental dishes are impressive, the inner workings are (to some) just as impressive. The purpose of a dish is to collect incoming radiation and focus it to the feed of a receiver. Once at the receiver, an EM wave goes through the inner workings of a telescope, the frontend and the backend, where it is converted and formatted to data in such a way that astronomers can inspect it with dedicated software.

The following sections describe the impact of a telescope’s dish on sensitivity and field of view, the purpose of the frontend and backend, and how a signal is prepared as searchable data.

### 2.1.1 Sensitivity and Field of View

The sensitivity of a telescope is directly related to its diameter. A higher sensitivity means a lower minimum detectable flux density threshold. The sensitivity, or gain, of a telescope can be calculated as (Wilson et al., 2013)

$$G = \eta_a \frac{\pi D^2}{8k_B} \text{ K Jy}^{-1}, \quad (2.1)$$

where  $\eta_a$  is the aperture efficiency,  $D$  is the diameter of the telescope’s collecting area, and  $k_B$  is the Boltzmann constant. The aperture efficiency is the ratio of the area of the telescope that reflects radiation to the feed of a receiver and the geometric area of the telescope.

The sensitivity can also be quantified with the system equivalent flux density (SEFD),

$$\text{SEFD} = \frac{T_{\text{sys}}}{G} \text{ Jy}, \quad (2.2)$$

where  $T_{\text{sys}}$  is the system temperature (in Kelvin), which is the combined added noise to the system from all noise-generating sources, such as the sky, losses in the feed, and electronics.

The minimum detectable flux density of a single burst can be calculated using the radiometer equation (Lorimer & Kramer, 2012),

$$S_{\text{min}} = \beta \frac{\text{SEFD} (S/N)_{\text{min}}}{\sqrt{n_p W f_{\text{BW}}}} \text{ Jy}, \quad (2.3)$$

where  $\beta$  is a signal digitisation degradation constant ( $\gtrsim 1$ ),  $S/N_{\text{min}}$  is the minimum signal-to-noise with which a detection can be made,  $n_p$  is the number of polarisations summed (generally two),  $W$  is the width of a burst, and  $f_{\text{BW}}$  is the bandwidth of the receiver. With a detected width and S/N of a burst, as well as knowledge of the observing system, Eq. 2.3 can be used to calculate the measured flux density of a burst. The gain and system temperature varies between receiver systems on telescopes and are usually listed in the receiver documentation of a telescope<sup>1</sup>. One can then look up those values to use in Eq. 2.3. For pulsars, eq. 2.3 includes a factor of the pulsar's duty cycle, and  $W$  is the integration time.

Like sensitivity, the field of view (FOV) of a telescope is related to the size of the telescope, but inversely. The FOV is also dependent on the receiver used. The FOV of a receiver is called a beam, and its angular power response is described with a Bessel function (Wilson et al., 2013). The main peak is called the main beam or lobe, while the others are called sidelobes. A cross-section representation of a beam pattern is shown in Fig. 2.1. The FOV is estimated from the half power beam width (HPBW) of the main beam, which is the width of the beam at half its maximum level, calculated as

$$\text{HPBW} = \xi \frac{\lambda}{D} \text{ rad}, \quad (2.4)$$

where  $\xi \gtrsim 1$  depends on the maximum aperture efficiency<sup>2</sup>, and  $\lambda$  is the observing wavelength. The FOV is the solid angle covered by the HPBW in steradians, or

$$\begin{aligned} \Omega &\propto \text{HPBW}^2 \text{ sr} \\ &\simeq 3.3 \times 10^3 \text{ HPBW}^2 \text{ deg}^2 \\ &\simeq 1.2 \times 10^7 \text{ HPBW}^2 \text{ arcmin}^2. \end{aligned} \quad (2.5)$$

For single pulse observations (e.g. FRBs) the sensitivity of an observation can be increased by increasing the size of the collecting area or the observing bandwidth, or by using a more sensitive receiver. For pulsar observations the sensitivity can also be

<sup>1</sup>E.g. for Effelsberg:

[eff100mwiki.mpifr-bonn.mpg.de/doku.php?id=information\\_for\\_astronomers:rx\\_list](http://eff100mwiki.mpifr-bonn.mpg.de/doku.php?id=information_for_astronomers:rx_list)

<sup>2</sup>For aperture efficiency of 1,  $\xi = 1.02$

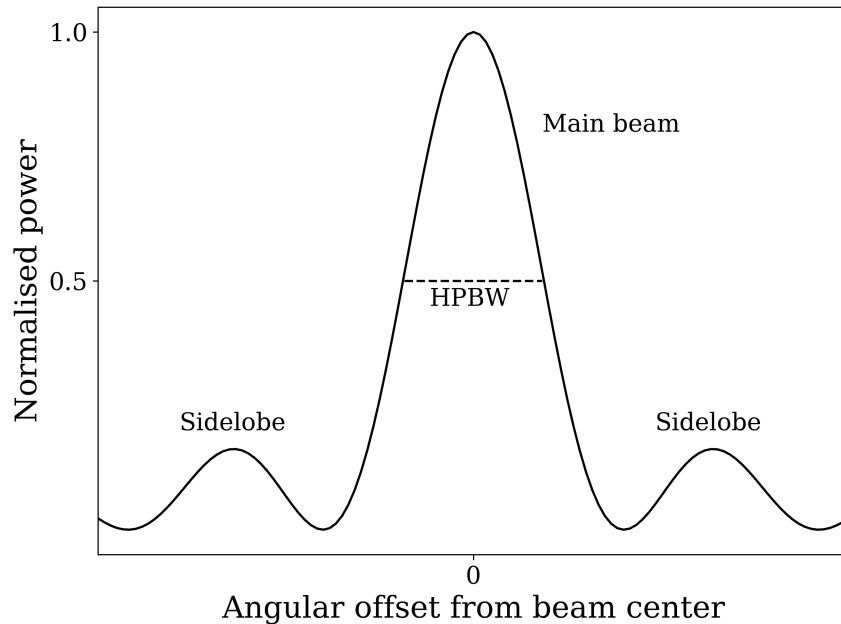


Figure 2.1: A cross-section representation of a beam pattern. Shown are the main beam and the first sidelobes at an arbitrary angular offset from the beam center. The dashed line shows the half power beam width (HPBW).

increased with longer integration times. Increasing the collecting area of already-built telescopes can be difficult to achieve. Therefore, using more sensitive receivers or increasing the observing bandwidth are more desirable ways to increase the sensitivity of observations. Receivers with only a single beam (i.e. one feed) are called single-pixel receivers, and generally have wider bandwidths than multi-beam receivers. On large, sensitive telescopes, single-pixel receivers are well suited for a targeted search (e.g. Chapter 4) or observations of localised radio sources (e.g. FRB121102, Chapter 5). Multi-beam receivers have multiple feeds and can form multiple beams on the sky, resulting in a larger FOV. This type of receiver is better suited than single-pixel receivers to perform surveys of large portions of the sky whilst utilising the high sensitivity of large telescopes. Multi-beam receivers are also useful for targeted searches due to their capability of using their beams to distinguish real astrophysical signals from RFI. A more recent type of multi-beam receivers are phased array feeds (PAFs) that do not have typical feeds, but rather multiple receiver elements, enabling highly customisable beams. PAFs on single dish telescopes will be discussed in Chapter 3.

### 2.1.2 Frontend

The frontend, or receiver, handles an incoming radio signal and converts it to analog voltage data. The receiver is located at either the primary or secondary focus of a telescope. An EM wave collected by a telescope enters the receiver at a feed, where the EM wave is converted to voltages. The feed allows certain frequencies of EM

waves to be converted based on the specifications of the receiver. Signals are typically sampled by two receptors, sampling two orthogonal polarisation states, either dual linear or dual circular. The signal is then amplified by a low-noise amplifier (LNA), which is cryogenically cooled in order to refrain from adding thermal noise to the signal. Following the LNA amplification, it is common for the signal to go through a filter that censors frequencies within the frequency band that are known to contain persistent RFI. Finally, the signal is converted to lower frequencies through heterodyning with a lower frequency signal from a local oscillator. Heterodyning mixes signals in a so-called mixer, creating signals at frequencies at the sum and difference of the incident signal frequency and the local oscillator frequency. The mixer shifts the original signal into a frequency band appropriate for the backend, which is usually at lower frequencies. The conversion to lower frequency reduces signal losses during transmission from the frontend to the backend and reduces technical requirements when the signal is sampled in the backend.

### 2.1.3 Backend

The backend serves to digitise the signal and formats it into a data format usable by search software. Once the signal arrives at the backend from the frontend, it is digitised using an analog-to-digital converter (ADC), and Nyquist sampled. Nyquist sampling converts a continuous signal into a discrete sequence in time with a sampling frequency twice the highest frequency of the signal. This sampling frequency is the minimum required frequency to reconstruct the original signal. The sampled data then goes through a spectrometer, which produces spectra by fast Fourier transforming (FFT) discrete blocks of data. To create  $N$  number of frequency channels, a  $2N$ -point FFT is required. A complex-to-complex FFT can also be used, where two streams that are  $90^\circ$  out of phase are sampled in parallel, resulting in  $N$  channels from an  $N$ -point FFT. This channelisation process is called filterbanking. Spectral leakage occurs during the FFT, where strong signals in the Fourier power spectrum can leak to adjacent Fourier bins. In order to decrease this effect, overlapping blocks of data are weighted with a sinc function ( $\sin(\pi x)/(\pi x)$ ) before the FFT in a process called polyphase filtering. A spectrometer utilising these techniques is called a polyphase filterbank.

As an example, let us use the main instrumentation used in Chapters 4 and 5, i.e. the S45mm (or CX) receiver. The frequency range of the receiver is 4–8 GHz, split into two separate sub-bands. Each sub-band is thus treated as a single 2 GHz wide band. The final data product from each sub-band consists of 1024 frequency channels, with a time resolution of  $131 \mu\text{s}$ . The frontend lowers the frequency of each sub-band to be 0–2 GHz, resulting in a Nyquist sampling frequency of 4 GHz. The data resolution from the polyphase filterbank is therefore  $2048/4 \times 10^9 = 0.512 \mu\text{s}$ . This is a much higher sampling rate than required to detect FRBs, and storing data with such a fine sampling time would require an inordinate amount of disk space. Therefore, spectra from the polyphase filterbank are integrated to obtain larger sampling rates, which in this case is 256 spectra to obtain the final time resolution of  $131 \mu\text{s}$ .

For searching purposes, polarisation information is not always recorded. In that

case, the output from each polarisation channel is summed in quadrature, resulting in total intensity data. Polarisation of data is discussed in §2.1.5.

#### 2.1.4 Baseband

After the Nyquist sampling stage in the backend, the data can be written to disk as baseband data. Baseband data is therefore just sampled voltage data and allows one to exchange time resolution for frequency resolution, and vice versa, as the data do not go through the backend spectrometer. Baseband data contains the phase information (complex values) from the orthogonal receptors and can be dedispersed and Faraday de-rotated to high precision. Baseband data can also reveal minute details in burst structures through its high time-resolution. This flexibility comes at a price though, as baseband data require extreme amounts of disk space to be stored.

To avoid storing excessive amounts of baseband data, real-time searches can be performed where baseband data around the time of arrival of a burst is stored. This method requires a ring buffer in which baseband data is continuously written and usually stores only the previous  $\sim$ tens of seconds of data. The incoming data is searched in real-time, and if the search algorithm finds a burst it will trigger the ring buffer data to be stored on disk in a process called baseband dumping. Alongside this method, standard filterbank data is also written to disk and can be searched offline for bursts missed by the real-time search.

#### 2.1.5 Polarimetry

Polarisation information is obtained through the two frontend receptors that sample two orthogonal polarisation states. The receptors and their resulting signal path are often referred to as polarisation channels. In a Cartesian reference frame, the receptors lie on the  $x - y$  plane, while an incident EM wave arrives at the receiver along the  $z$ -axis, resulting in the EM wave electric field oscillating in the  $x - y$  plane. The electric field traces out an ellipse on the plane of the receptors, described by the polarisation state angle,  $\chi$ , and the polarisation position angle (PPA),  $\psi$ . The polarisation ellipse is shown in Fig. 2.2. The Stokes parameters are used to describe linear and circular polarisation, and their intensities, and can be written in terms of the polarisation ellipse and its amplitude in the  $x$  and  $y$  directions ( $E_x$  and  $E_y$ ) as (Wilson et al., 2013)

$$\begin{aligned} I &= E_x^2 + E_y^2 \\ Q &= Ip \cos(2\chi) \cos(2\psi) \\ U &= Ip \cos(2\chi) \sin(2\psi) \\ V &= Ip \sin(2\chi), \end{aligned} \tag{2.6}$$

where  $I$  is the total intensity,  $Q$  and  $U$  describe linear polarisation,  $V$  describes circular polarisation, and  $p$  is the polarisation fraction, calculated as

$$p = \frac{\sqrt{Q^2 + U^2 + V^2}}{I}. \tag{2.7}$$

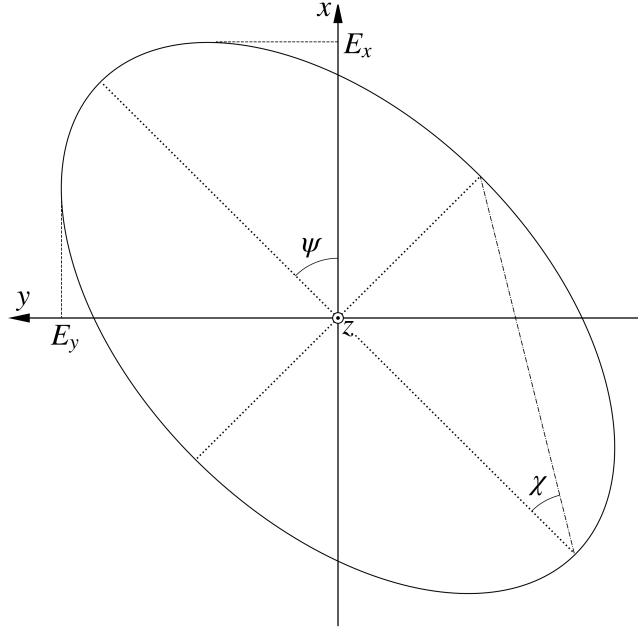


Figure 2.2: Polarisation ellipse. The incoming EM wave travels in the positive  $z$  direction, and its electric field traces out an ellipse in the  $x - y$  plane. The angles  $\chi$  and  $\psi$  are the polarisation state and polarisation position angles, respectively.  $E_x$  and  $E_y$  are the ellipse amplitudes in the  $x$  and  $y$  directions. The figure is adapted from Thompson et al. (2017).

Specific values of  $\chi$  reduce the polarisation ellipse to either a straight line or a circle, resulting in fully linear or circular polarisation states. For  $\chi = 0$ , Stokes  $V$  is zero, and the polarisation is fully linear. For  $\chi = \pm\pi/4$ , Stokes  $Q$  and  $U$  become zero, and the polarisation is fully circular. The PPA is the position angle of the plane of linear polarisation and can be calculated from Stokes  $Q$  and  $U$  as (Thompson et al., 2017)

$$\psi = \frac{1}{2} \arctan \left( \frac{U}{Q} \right). \quad (2.8)$$

The two polarisation channels are Nyquist sampled and thus still retain phase information (i.e. complex values), and the Stokes parameters can be calculated before the data is channelised in the spectrometer. The Stokes parameters can be constructed for a dual-linear feed with polarisation channels  $P_x$  and  $P_y$  as (Lorimer & Kramer, 2012):

$$\begin{aligned} I &= |P_x|^2 + |P_y|^2 \\ Q &= |P_x|^2 - |P_y|^2 \\ U &= 2 \operatorname{Re}(P_x^* P_y) \\ V &= 2 \operatorname{Im}(P_x^* P_y), \end{aligned} \quad (2.9)$$

where  $*$  denotes the complex conjugate. For a dual-circular feed with a left-hand

channel  $P_L$  and a right-hand channel  $P_R$ , the Stokes parameters are calculated as:

$$\begin{aligned}
 I &= |P_L|^2 + |P_R|^2 \\
 Q &= 2 \operatorname{Re}(P_L^* P_R) \\
 U &= 2 \operatorname{Im}(P_L^* P_R) \\
 V &= |P_R|^2 - |P_L|^2.
 \end{aligned}
 \tag{2.10}$$

The polarisation information, i.e. the Stokes parameters, of the resultant data can differ from the actual polarisation information of an incident wave due to instrumental effects. These effects can arise from varying orientations between the receiver and source throughout an observation, power leakage between feeds, and phase differences between polarisation channels due to differences in gain or cable length. Polarisation data thus needs to be calibrated to recover the original Stokes parameters. The most common method is to perform noise diode observations at either the start or end of FRB observations. The noise diode is 100% linearly polarised and equally bright in both feeds and therefore has well defined Stokes parameters. The difference in polarisation of the noise diode data from the two polarisation channels can then be used to calibrate the FRB polarisation data using dedicated software. This method works for both linear and circular feeds.

## 2.2 Radio Frequency Interference

The bane of radio astronomers is most certainly radio frequency interference (RFI). RFI manifests itself as statistical outliers in data, in which noise is typically Gaussian. The manifestation is typically very narrow-banded (tens of MHz) and of short duration increase in data intensity. Numerous other types of RFI exist, e.g. variations of narrow-bandedness, periodic, sinusoidal, or completely sporadic. The RFI environment differs between telescopes and observing frequencies. RFI is detrimental to FRB searches, as it can both mask actual bursts within data, leaving the bursts undetectable by search algorithms, or appear as bursts in data time series, resulting in false positives when searching for bursts.

Electronic and communication devices are the main source of RFI. While most RFI generating sources are extrinsic to the site of telescopes, sources local to telescopes and even telescope components can produce RFI. The mobile communication bands around 800 MHz and 1800 MHz and the aircraft radar band around 1000 MHz are fairly common perpetrators regarding RFI in radio astronomy data around those frequencies. Different observing frequency bands have their own RFI environment where persistent RFI needs to be identified on a band-by-band basis. Luckily, some small parts of the radio spectrum are protected, meaning that specific frequencies are only meant for radio observations. Of the protected bands, the most notable one is for the hydrogen line at 1420 MHz (21 cm), where a few tens of MHz around that frequency are protected for radio observations.

The omnipresence of RFI has forced radio astronomers to develop methods of excising RFI. The RFI situation can vary between receivers of a single telescope, and for

most receivers there are always certain “bad channels” in the data. These bad channels are usually known due to experience of using a certain receiver and can be “zapped” during processing (i.e. ignored by search algorithms). The most standard way of excising RFI is to create an RFI mask, where data is searched for statistical outliers in either frequency or time that get written to the mask. Search algorithms then use the RFI mask to zap these outliers. For arrays of telescopes or multi-beam receivers, RFI can be excised with coincidenting, where if a burst candidate is seen in too many beams to be considered astrophysical, it gets flagged as RFI.

## 2.3 Dedispersion

The propagation effect of dispersion is contained within a signal arriving at a telescope. The dispersion effect must be accounted for, as searching for bursts without doing so is an exercise in futility, because bursts would not be aligned in time across the observing frequencies.

Undoing the effect of dispersion is called dedispersing and can be done by either coherent or incoherent dedispersion. Both methods will be introduced, but all subsequent discussion will be focused on incoherent dedispersion, unless otherwise stated.

### 2.3.1 Incoherent Dedispersion

Channelised filterbank data can only be incoherently dedispersed. To incoherently dedisperse data, one has to calculate the time delay in each frequency channel with respect to a reference frequency, which is usually the top frequency of the observing band, using Eq. 1.17 for a specific DM. Each data frequency channel contains the intensity of each time sample, called channel time series. Each channel time series needs to be shifted in time with respect to the time delay of its frequency and the reference frequency. If dedispersed at the correct DM, a burst will align properly in time in all channels. Dedispersing at the incorrect DM results in the burst becoming broadened and weaker, and if the trial DM is too far from the correct one, the burst will not be visible. Channel time series are rarely inspected when searching the data. An averaged sum of the channel times series is more commonly used as it shows a burst much more clearly. The dispersed and dedispersed dynamic spectra and time series of a burst are shown in Fig. 2.3, where the same burst as shown in the left panel of Fig. 1.1 is used ( $DM=500 \text{ pc cm}^{-3}$ ). The burst is also dedispersed at incorrect DMs to show the broadening effect.

Data can also be dedispersed in sub-bands. Sub-banding data is to divide the data into chunks of frequency channels. The dedispersion is then performed on each sub-band by shifting all the frequency channel in the sub-band in time with respect to the dispersion time delay at the top (or center) of the sub-band. The size of the sub-bands must be chosen with respect to the time delay within a sub-band and the time resolution of the data. If the sub-bands are too large, a burst can get smeared out and might be missed by a search algorithm.

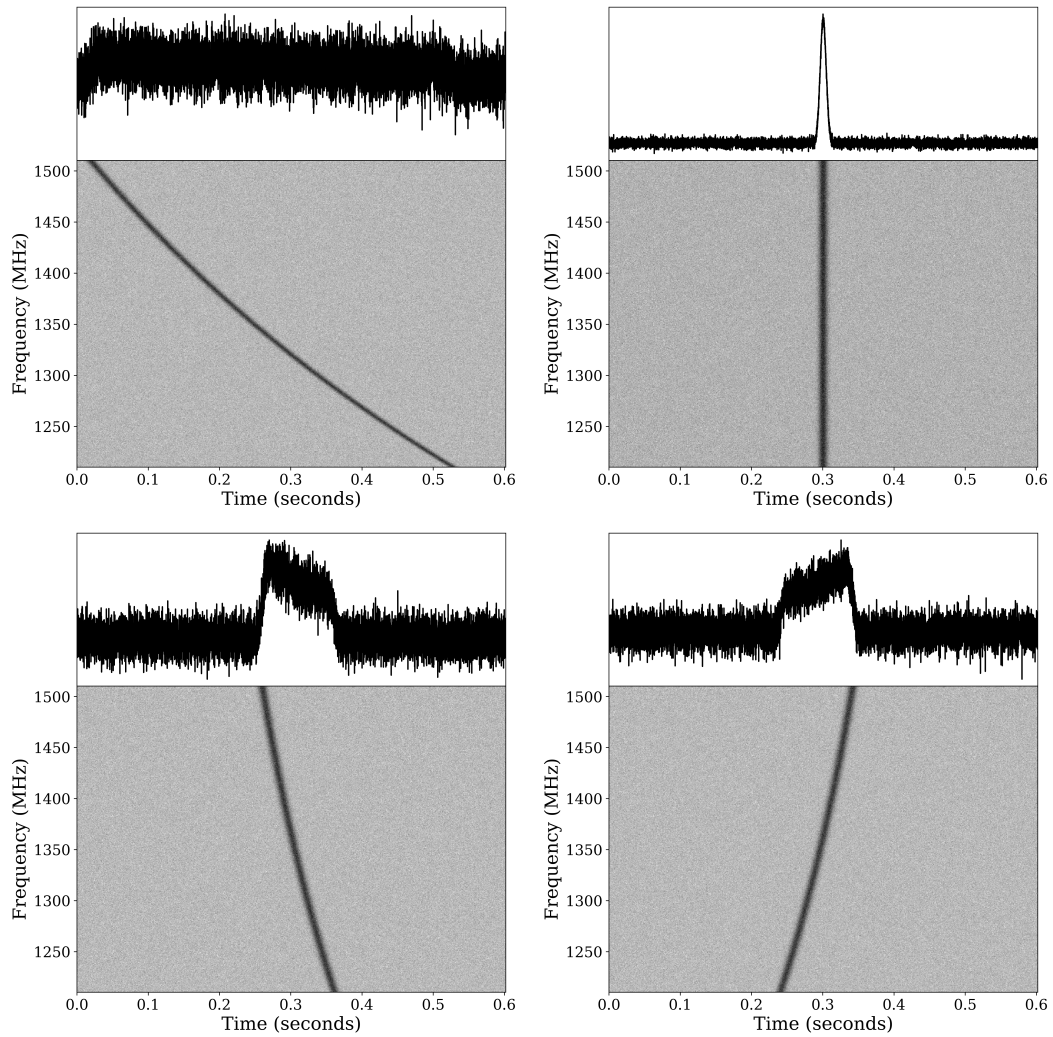


Figure 2.3: A simulated burst with a DM of  $500 \text{ pc cm}^{-3}$  dedispersed at different DMs of  $0 \text{ pc cm}^{-3}$  (upper left),  $500 \text{ pc cm}^{-3}$  (upper right),  $400 \text{ pc cm}^{-3}$  (lower left), and  $600 \text{ pc cm}^{-3}$  (lower right). Each panel shows the dedispersed time series (top) and dynamic spectrum (bottom) at their respective DMs.

### 2.3.2 Coherent Dedispersion

Nyquist-sampled voltage data can be coherently dedispersed. This method can fully recover the original signal, as it does not suffer from the dispersion smearing effect of channelised data (§2.3.3). By applying an FFT to the Nyquist-sampled voltages, a Fourier series of complex voltages containing amplitudes and phases is obtained. To correct for dispersion, each Fourier component phase is de-rotated by an amount corresponding to a specific DM. This is done by applying the inverse of the so-called transfer function (Lorimer & Kramer, 2012),

$$H(f_c + f) = \exp\left(i \frac{2\pi \mathcal{D} f^2}{(f + f_0) f_0^2} \text{DM}\right), \quad (2.11)$$

where  $\mathcal{D}$  is the dispersion constant (see Eq. 1.18),  $f_c$  is the central frequency, and  $f$  goes from  $-f_{\text{BW}}/2 \leq f \leq +f_{\text{BW}}/2$  with  $f_{\text{BW}}$  being the frequency bandwidth. The transfer function only affects the phase of a Fourier component, while leaving its amplitude unchanged, and its application is equivalent to the time delay application of incoherent dedispersion.

Coherent dedispersion is more computationally expensive than incoherent dedispersion and is thus not applicable to every type of observation. When observing sources with DMs previously obtained from incoherent dedispersion (e.g. known pulsars), coherent dedispersion can be applied in the backend, resulting in improved resolution of the pulse profile. Baseband dumps from real-time FRB searching can be coherently dedispersed, revealing the burst structure in tremendous detail (e.g. Farah et al., 2018). Bassa et al. (2017a) have implemented a semi-coherent dedispersion method for searching for pulsars and FRBs at low frequencies ( $\sim 100$  MHz), where bursts can be missed due to smearing when using incoherent dedispersion. They perform multiple coherent dedispersions in parallel at coarsely separated DM trials that are subsequently incoherently dedispersed with finer DM steps.

### 2.3.3 Dispersion Smearing

The observed width of a detected burst,  $W_{\text{obs}}$ , will be different to its intrinsic width,  $W_{\text{int}}$ , due to both instrumental and propagation effects which cause a broadening effect. The observed width can be written as the quadratic sum of the intrinsic width and the broadening effects as

$$W_{\text{obs}} = \left(W_{\text{int}}^2 + t_{\text{samp}}^2 + \Delta t_{\text{DM}}^2 + \Delta t_{\text{DMerr}}^2 + \tau_s^2\right)^{1/2}, \quad (2.12)$$

where  $t_{\text{samp}}$  is the data sampling time,  $\Delta t_{\text{DM}}$  is the dispersion smearing,  $\Delta t_{\text{DMerr}}$  is the smearing due to dedispersing at the incorrect DM, and  $\tau_s$  is the scattering timescale (§1.2.4). The dispersion smearing factor is a time delay caused by intra-channel smearing of a burst due to dispersion across the channel bandwidth,  $\Delta f$ . This factor can be approximated with Eq. 1.17 using the central observing frequency,  $f_c$ , and the channel bandwidth, under the assumption that  $\Delta f \ll f_c$ ,

$$\Delta t_{\text{DM}} \simeq 8.3 \times 10^6 \text{ DM} \left(\frac{\Delta f}{f_c^3}\right) \text{ ms}, \quad (2.13)$$

where the frequencies are in MHz. The smearing error arises from dedispersing at a DM of  $\delta\text{DM}$  away from the true DM, and this factor is written as (Cordes & McLaughlin, 2003)

$$\Delta t_{\text{DMerr}} = \Delta t_{\text{DM}} \left( \frac{\delta\text{DM}}{\text{DM}} \right) \text{ ms.} \quad (2.14)$$

### 2.3.4 DM Step Size

When searching data for FRBs that have not been observed before, a series of DM trials are required. FRBs have been detected with DMs up to  $\sim 2000 \text{ pc cm}^{-3}$ , so searches need to cover a large DM range without being too computationally expensive. A general range for a blind search usually covers DMs from  $0 \text{ pc cm}^{-3}$  to a few thousand  $\text{pc cm}^{-3}$ .

The number of DM trials, or DM steps, needs to be carefully thought out with respect to computational effort and the loss of sensitivity due to smearing. For overly large DM steps a burst which resides between steps will be broadened, thus reducing the sensitivity, and might be missed by search algorithms. If the DM steps are too small a burst will not look any different between neighbouring steps, and computing power (and time) will be wasted. An ideal DM step is when  $\Delta t_{\text{DM}} = t_{\text{samp}}$ , as loss in sensitivity and computing power will be minimal.

To find the size of the DM steps, let us first consider the minimum total smearing. Considering only the broadening terms in Eq. 2.12, the total smearing is (Cordes & McLaughlin, 2003)

$$\Delta t = (t_{\text{samp}}^2 + \Delta t_{\text{DM}}^2 + \Delta t_{\text{DMerr}}^2 + \tau_s^2)^{1/2} \quad (2.15)$$

The minimum dispersion smearing is obtained by setting  $\Delta t_{\text{DMerr}} = 0$ ,  $\Delta t_{\text{DM}} = t_{\text{samp}}$ , and ignoring scattering for simplicity,

$$\Delta t_{\text{min}} = (2 t_{\text{samp}}^2)^{1/2} \quad (2.16)$$

The DM step is then obtained from Eqs. 2.13–2.14 and setting  $\Delta t_{\text{DMerr}}$  as a fraction of the total smearing,  $\varepsilon \Delta t$ ,

$$\delta\text{DM} = \frac{\varepsilon \Delta t f_c^3}{8.3 \times 10^6 \Delta f} \text{ pc cm}^{-3}, \quad (2.17)$$

where the optimal DM step is when  $\Delta t = \Delta t_{\text{min}}$ .

### 2.3.5 DM Steps in Practice

In practice the choice of DM steps depends on the intended search range of DMs and the parameters of the data: data sampling time ( $t_{\text{samp}}$ ), central frequency of observing band ( $f_c$ ), observing bandwidth ( $f_{\text{BW}}$ ), number of data channels ( $n_{\text{chan}}$ ), and channel bandwidth ( $\Delta f = f_{\text{BW}}/n_{\text{chan}}$ ). The choice of  $\delta\text{DM}$  can vary within sub-ranges of the total DM search range. The steps need to be calculated, and the final list of  $\delta\text{DM}$  for each DM sub-range is called a dedispersion plan. While the data sampling

Table 2.1: Dedispersion plan for Effelsberg 7-beam data for a DM search range of 0–2100 pc cm<sup>-3</sup>. *From left to right:* Low and high DMs of each sub-range of the total DM range, DM step size for each sub-range, and the data downsampling of each sub-range.

Low DM ( pc cm <sup>-3</sup> )	High DM ( pc cm <sup>-3</sup> )	$\delta$ DM ( pc cm <sup>-3</sup> )	Downsampling
0	95	0.1	1
95	163	0.2	2
163	346	0.5	4
346	686	1.0	8
686	1368	2.0	16
1368	2100	3.0	32

time is larger than the dispersion smearing per data channel,  $\delta$ DM is chosen so that the smearing of the step size across the bandwidth is roughly equal to  $t_{\text{samp}}$ . As per Eq. 2.13 the smearing rises with DM, meaning that for a large DM search range the smearing will likely at some point exceed  $t_{\text{samp}}$ . When that occurs the data are downsampled to accomodate for the large smearing. Downsampling of data is when adjacent time samples are added together and averaged, and is usually performed by adding powers of two samples together (i.e.  $2^0, 2^1, 2^2, \dots$ ). The data sampling time thus becomes  $t_{\text{samp}} \times \text{DS}$ , where DS is the downsampling factor. Once the data have been downsampled  $\delta$ DM needs to be adjusted accordingly in the same way as described above. The process of downsampling and re-adjusting  $\delta$ DM then continues until the end of the DM search range is reached, and a dedispersion plan is ready.

While creating a dedispersion plan it is common practice to use a set of pre-determined  $\delta$ DM and to use a so-called fudge factor to soften the boundaries in order to simplify the plan and reduce computation cost while only suffering minimal loss in sensitivity. Let us take a look at a dedispersion plan for data taken with the 7-beam receiver at Effelsberg. The data have  $t_{\text{samp}} = 54.6 \mu\text{s}$ ,  $f_c = 1360 \text{ MHz}$ ,  $f_{\text{BW}} = 300 \text{ MHz}$ ,  $n_{\text{chan}} = 512$ , and  $\Delta f = 0.59 \text{ MHz}$ , and the intended DM search range will be 0–2100 pc cm<sup>-3</sup>. By following the process described above, the resulting dedispersion plan is shown in Table 2.1. The dedispersion plan is also plotted in Fig. 2.4 to give a visual feel to the smearing factors.

## 2.4 Single Pulse Searching

To find FRBs in filterbank data one needs to perform single pulse searching on the dedispersed time series. The search is done by matched filtering, which convolves the dedispersed time series with a signal of a known shape. Convolution can be computationally expensive so the known shape used is in most cases a boxcar filter. The convolution can be implemented by computing a running sum for the data with a given boxcar filter size and subtracting it from the data at plus/minus the filter width (Barsdell et al., 2012). Fig. 2.5 shows the convolution process results for time series with

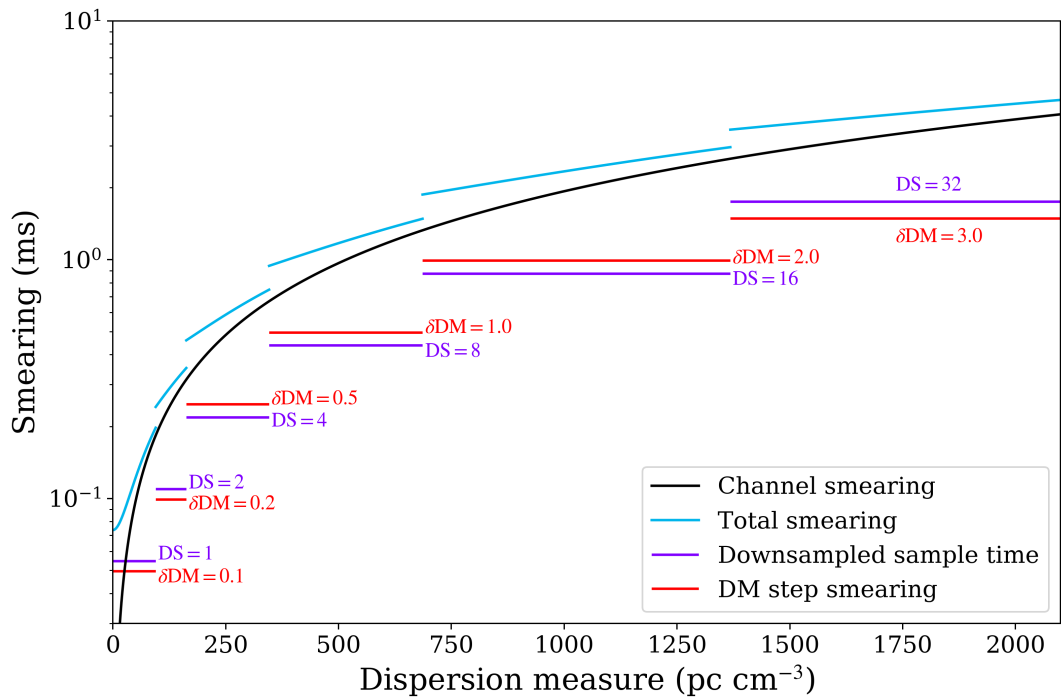


Figure 2.4: Visualisation of the dedispersion plan in Table 2.1 as dispersion smearing as a function of dispersion measure. Shown are the per-channel smearing (black), total smearing (blue), the downsampled sample time per DM search sub-range (purple), and the smearing across the bandwidth for each DM step (red). The downsampling factor (DS) and the DM step size ( $\delta\text{DM}$ ) are written at each of their respective lines.

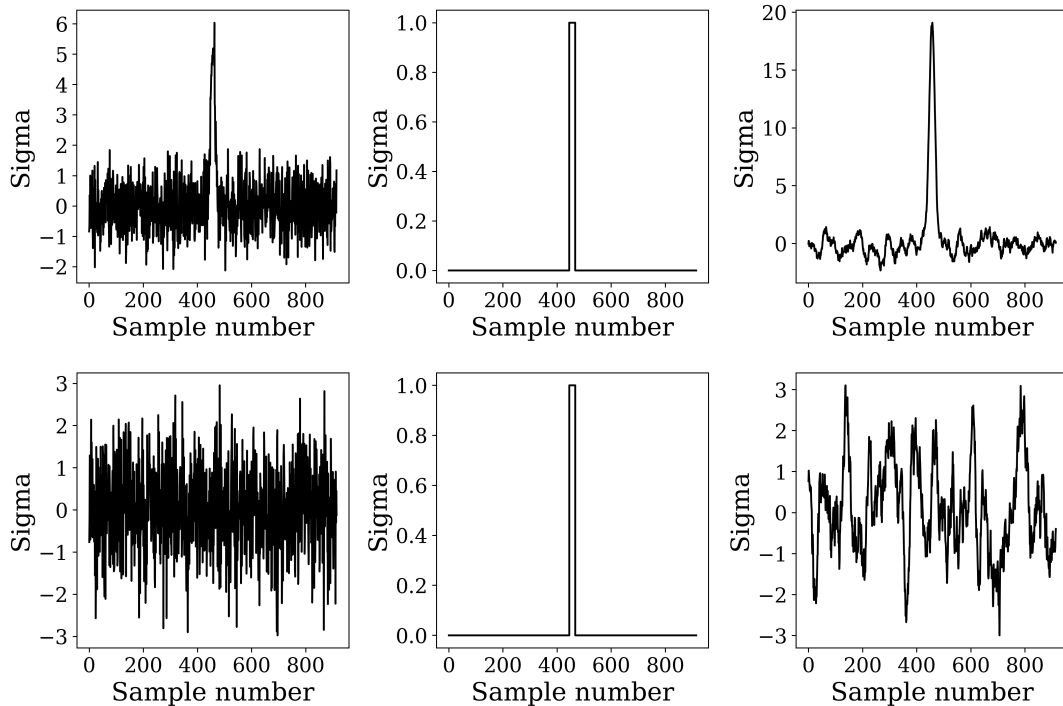


Figure 2.5: Convolution of time series with a boxcar filter. *Left:* Data time series as standard deviation from the median value over time samples. *Center:* Boxcar filter with a signal-to-noise maximising sample width. *Right:* Convolution of the previous two panels as standard deviation from the median value over time samples. The top row shows the convolution for a time series with a simulated burst, dispersed to the DM of the burst, and a boxcar with a width maximising the S/N. The bottom row shows how the convolution process looks for time series without a burst.

and without a burst. Another method is to perform an FFT convolution, utilising that multiplication in the frequency domain corresponds to convolution in the time domain (Smith, 1997). The time series are transformed to the frequency domain with an FFT, multiplied by the filter, and transformed back to the time domain with an inverse FFT. The single pulse search software **PRESTO** (§2.6.1) and **HEIMDALL** (§2.6.3) use FFT convolution and running sum, respectively.

The width of a burst is unknown prior to searching, so various boxcar widths must be tried in order to maximise the signal-to-noise ratio (S/N). Single pulse searching software use boxcar widths in number of time samples, either with a pre-determined list of sample widths or as powers of two samples. The detected S/N of a burst drops as the boxcar width becomes wider or narrower than the burst so it is paramount to get as close to the correct width to maximise the chances of detection. The detected S/N of a burst with a width of 20 time samples as a function of boxcar widths is shown in Fig. 2.6.

Searching for bursts in a filterbank file requires single pulse searching in multiple

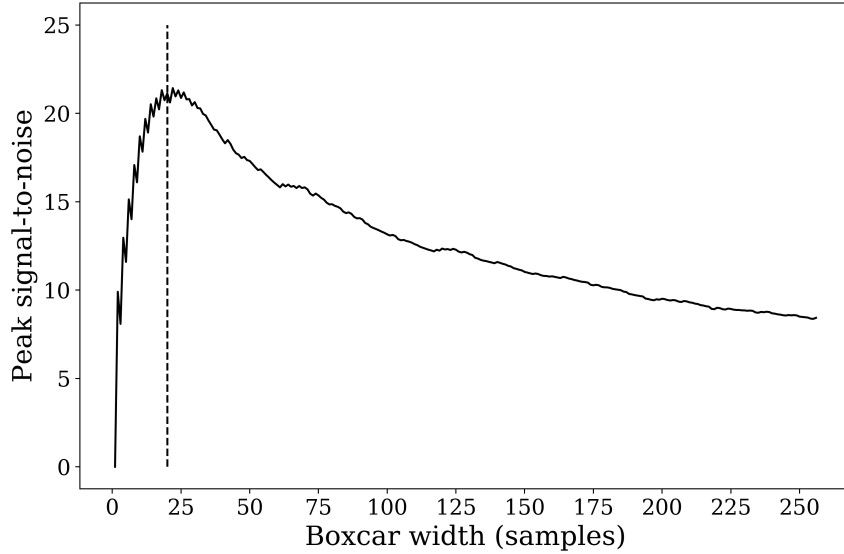


Figure 2.6: Peak signal-to-noise as a function of trial boxcar widths which are convolved with time series containing a 20 sample wide, simulated burst. The time series is dedispersed to the DM of the burst. The vertical dashed line indicates a boxcar width of 20 samples.

dedispersed time series, dedispersed to DMs according to a dedispersion plan. If a burst resides within the data it will be detected with multiple trial widths in each time series and at multiple DMs. As the DMs stray away from the correct one, the bursts will appear wider and will have lower S/Ns, until the DM becomes so incorrect that they will not be detected at all. The burst event will however be detected at the same time in each dedispersed time series, so the event in the time series at the DM which maximises the S/N can be chosen as the burst candidate, as it most likely represents the true properties of the burst.

## 2.5 Measuring Rotation Measure

One of the more common ways to measure the RM of FRBs is by using `rmfit` from the PSRCHIVE<sup>3</sup> software package (Hotan et al., 2004). By giving `rmfit` an input of RM range and number of steps, it will Faraday de-rotate the data at the trial RMs. For each trial RM, the frequency-averaged linear polarisation intensity is calculated,

$$I_{\text{lin}}(\text{RM}_{\text{trial}}) = \sum_i^{n_{\text{chan}}} \sqrt{Q_{\text{RM}_{\text{trial}},i}^2 + U_{\text{RM}_{\text{trial}},i}^2}, \quad (2.18)$$

resulting in a linear polarisation intensity spectrum over trial RMs. The peak of the spectrum is fitted with a Gaussian, whose centroid represents the best-fit RM. To

<sup>3</sup>[psrchive.sourceforge.net](http://psrchive.sourceforge.net)

Table 2.2: Information of receivers commonly used to observe FRB121102. *From left to right:* Telescope, receiver, central frequency ( $f_c$ ), frequency channel bandwidth ( $\Delta f$ ), and observing bandwidth ( $f_{\text{BW}}$ ).

Telescope	Receiver	$f_c$ (GHz)	$\Delta f$ (MHz)	$f_{\text{BW}}$ (GHz)
Arecibo	C-band	4.5	1.56	0.8
CHIME	FRB	0.6	0.39	0.4
Effelsberg	7-beam	1.36	0.59	0.3
Effelsberg	CX	6.0	0.98	4
VLA	S-band	3.0	0.25	2

obtain a reliable RM value, one must first polarise calibrate their data with noise diode observations. This can be done using `pac` from `PSRCHIVE`.

Other methods of determining RM include the RM synthesis technique (Brentjens & de Bruyn, 2005), and a fitting of the Stokes Q and U parameters as a function of wavelength (e.g. Schnitzeler & Lee, 2017)

When measuring RMs, one needs to be aware of the intra-channel Faraday rotation, calculated as

$$\Delta\theta = \frac{\text{RM}c^2\Delta f}{f_c^3} \text{ rad}, \quad (2.19)$$

where  $c$  is the speed of light,  $\Delta f$  is the frequency channel bandwidth, and  $f_c$  is the central observing frequency. If  $\Delta\theta$  becomes too large, channels become depolarised, and the RM can not be accurately measured. The depolarisation fraction is

$$\kappa_{\text{depol}} = 1 - \frac{\sin(2\Delta\theta)}{2\Delta\theta}. \quad (2.20)$$

As  $\kappa_{\text{depol}}$  increases, the accuracy to measure RM decreases. Eq. 2.19 shows that observing at high frequencies and having narrow channel bandwidths enables measurements of high RMs. This is important for polarisation measurements of FRB121102, as lower frequency data with CHIME and Effelsberg are fully depolarised, unless baseband data are recorded. Fig. 2.7 shows  $\kappa_{\text{depol}}$  as a function of RM for commonly used receivers (Table 2.2) that are used to observe FRB121102.

## 2.6 Search Software and Pipelines

The two main publicly available single pulse search software suites used to search for FRBs are `PRESTO`<sup>4</sup> (Ransom, 2011) and `HEIMDALL`<sup>5</sup>. `PRESTO` is designed to be used on central processing units (CPUs), while `HEIMDALL` is designed for graphics processing units (GPUs) in order to increase processing speeds. While both are very useful, they do come with their advantages and drawbacks. The various modules of the search software can be categorised as pre-processing, processing, and post-processing. Processing is

<sup>4</sup>[github.com/scottransom/presto](https://github.com/scottransom/presto)

<sup>5</sup>[sourceforge.net/projects/heimdall-astro](https://sourceforge.net/projects/heimdall-astro)

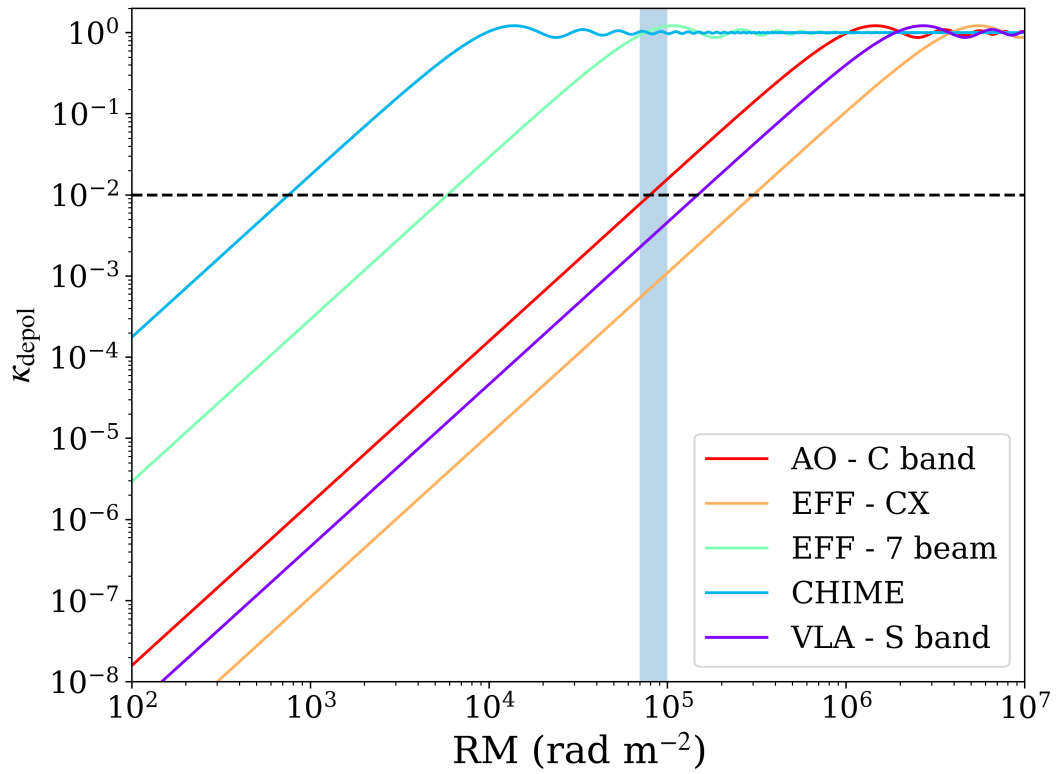


Figure 2.7: Depolarisation fraction,  $\kappa_{\text{depol}}$  (Eq. 2.20), as a function of rotation measure for commonly used receivers used to observe FRB121102. The horizontal dashed line indicates  $\kappa_{\text{depol}} = 1\%$ , and the vertical shaded region shows the range of rotation measures observed from FRB121102. The receiver information is listed in Table 2.2.

defined here as the dedispersion and single pulse search of data. Pre-processing and post-processing are then all processes occurring before and after the processing step, respectively. Following is a description of the search software and the search pipelines used in Chapters 3 and 5. The burst search work in this thesis is done on data in a filterbank format, so the discussion is solely focused on filterbanks.

### 2.6.1 Presto

PRESTO is used to search for single pulses in the time domain as well as periodic signals from pulsars in the Fourier domain. Here the focus will be on the time domain single pulse search.

One of the pre-processing modules of PRESTO is `DDplan.py`, which creates a dedispersion plan based on the data parameters as described in §2.3.5. `DDplan.py` offers the option of sub-banding the data and a maximum time resolution with respect to down-sampling. The dedispersion plan is adjusted accordingly if these optional parameters are used. `DDplan.py` trades a small amount of sensitivity to decrease computing time.

Another pre-processing module of PRESTO is `rfifind`, which identifies potential RFI based on statistical deviations within the data and creates an RFI mask containing the time and frequency locations of RFI in the data. These locations will get zapped during processing, meaning that they get masked with a value of zero. `rfifind` splits the data into equal blocks of time at each frequency channel, where the duration of each block is user defined ( $\sim$  seconds). The statistics calculated by `rfifind` for each block of data are the maximum of the time series Fourier power spectrum, standard deviation, and mean. If any of the calculated statistics for a block deviate too far from the average of all the blocks, the block gets flagged as RFI. The default is 10 standard deviations in time and 4 standard deviations in frequency. By default, if 30% of the time blocks of a channel get flagged, the whole channel is flagged as RFI. Conversely, if 70% of blocks at the same time interval across all channels get flagged, all blocks at that time are flagged as RFI. Users can also input a range of frequency channels and time intervals that will get zapped. This is useful in cases where the user is aware of persistently bad channels in their data.

The dedispersion process can be done in one of two ways in PRESTO with either `prepdata` or `prepsubband`. Both of them perform the same general task, to dedisperse data at a specific DM and write out a dedispersed time series. The more straightforward of the two is `prepdata`, which takes DMs and downsampling factors from `DDplan.py` and an RFI mask from `rfifind` as inputs. As `prepdata` only dedisperses at a single DM, a loop over the DMs from `DDplan.py` is required in order to dedisperse at multiple DMs. The process is somewhat more complex with `prepsubband`, as it performs a sub-banded dedispersion. When sub-banding, the dedispersion plan from `DDplan.py` includes more processing parameters than just the dedispersion step across the desired DM range, which further break down the DM steps with respect to the number of sub-bands. As `prepsubband` dedisperses a range of DMs, one has to loop over the ranges of DMs given by `DDplan.py` in order to cover the desired DM range. Like `prepdata`, `prepsubband` reads in the downsampling factors from the `DDplan.py` dedispersion plan,

and the RFI mask from `rfifind`.

Single pulse searching with PRESTO is done with `single_pulse_search.py`, which performs matched filtering on the dedispersed time series created by `prepdata` or `prepsubband`. Peaks in the matched filtering above a S/N threshold are called single pulse candidates. The candidates are written out for each dedispersed time series, listing for each candidate the DM, S/N, time and sample number within the data, and boxcar width. Optionally one can have `single_pulse_search.py` create a four panel plot showing *i)* a histogram of the candidates' S/Ns, *ii)* a histogram of the candidates' DMs, *iii)* a plot of the S/N versus DM of the candidates, and *iv)* the DM of candidates over time, where the marker size corresponds to the candidate S/N. This plot is shown for a simulated FRB with a DM of  $500 \text{ pc cm}^{-3}$  in Fig. 2.8. There are three important optional input parameters to use in `single_pulse_search.py`. First is the S/N threshold, whose default is 5.0. In practice this threshold is too low and can create a large amount of false positive candidates. The S/N in PRESTO is calculated as

$$S/N_{\text{PRESTO}} = \frac{\sum^{\text{pulse}} (I - B_l)}{\text{RMS} \sqrt{W_{\text{box}}}}, \quad (2.21)$$

where  $I$  is the signal,  $B_l$  is the background level, RMS is the root mean square of the data, and  $W_{\text{box}}$  is the boxcar width. The data is generally normalised by PRESTO such that  $B_l = 0$  and  $\text{RMS} = 1$ . Second parameter is the maximum width in seconds to search, which translates to a range of boxcar templates. In PRESTO there is a pre-determined list of boxcar widths to use<sup>6</sup> that goes to a maximum of 30 samples wide by default. The boxcar widths differ based on the time resolution of the data, so a user-defined maximum width is ideal in order keep search parameters roughly the same across varying data sets. Third is the so-called “no bad-blocks” flag that removes blocks of data that have broad and strong pulse candidates. This can be useful when searching for single pulses from a known pulsar where such pulses are not expected, but can be detrimental when searching for FRBs that have unknown widths and intensities.

## 2.6.2 Presto Search Pipeline

I have written a PRESTO pipeline<sup>7</sup> that is used to search for FRBs in Chapters 4 and 5. It uses all the features of PRESTO described above, as well as having some customised features for RFI exclusion and candidate plotting.

The main inputs of the pipeline are a filterbank file and the edges of the DM search range. To start with, the pipeline creates a dedispersion plan using `DDplan.py`, followed by creating an RFI mask with `rfifind`. By default, it uses `prepdata` to dedisperse the data, but using sub-bands with `prepsubband` is optional, as well as manually inputting the DM steps and downsampling factor. Next, `single_pulse_search.py` is run on the dedispersed time series, which creates separate candidate files for each DM. The pipeline then collects all the candidates above a S/N of 7, sorts them in time in a single

<sup>6</sup> The boxcars are 1, 2, 3, 4, 6, 9, 14, 20, 30, 45, 70, 100, 150, 200, and 300 samples wide.

<sup>7</sup>[github.com/gHENNING/new\\_SPS\\_pipeline](https://github.com/gHENNING/new_SPS_pipeline)

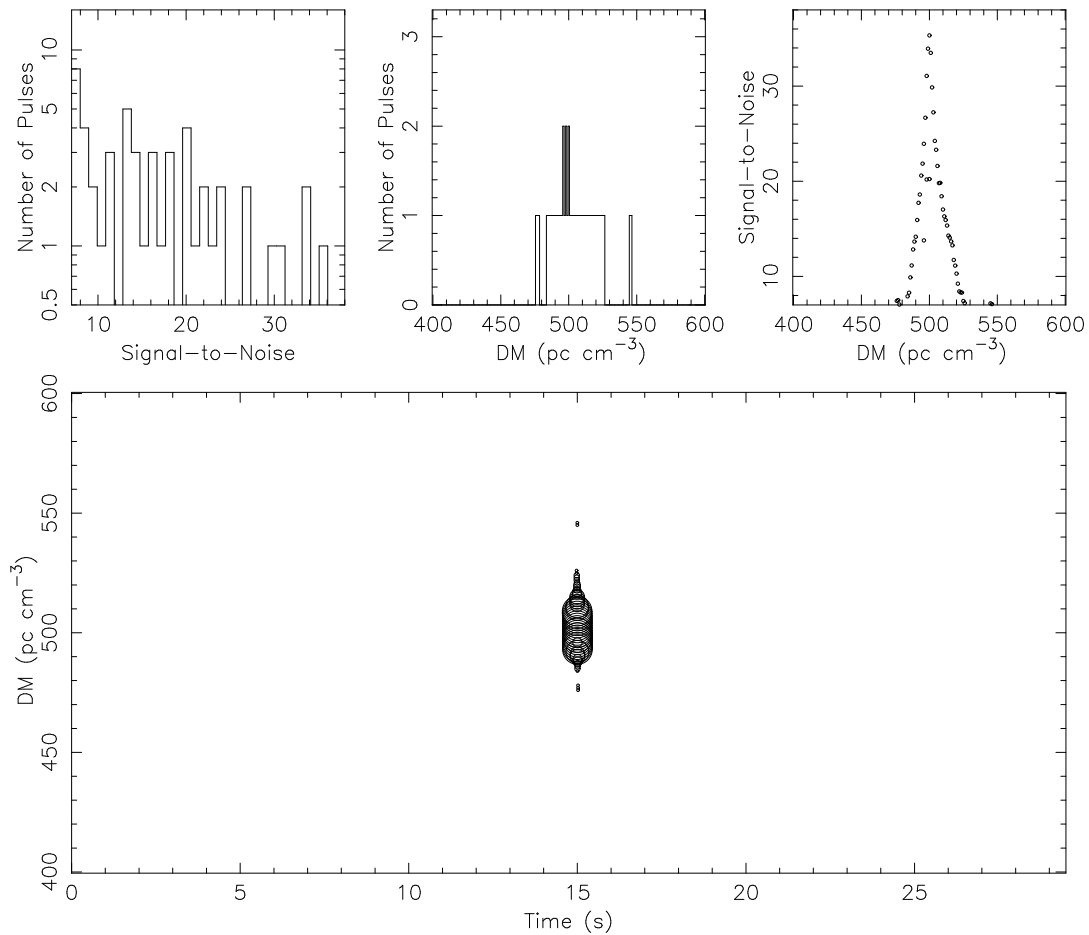


Figure 2.8: Candidate plot from `single_pulse_search.py`. The top row panels show histograms of number of candidates over S/N and DM, and a scatter plot of S/N over DM. The bottom panel shows the candidate DM over time within the data, where the marker sizes increase with S/N. Shown here are the results of a simulated FRB with a DM of  $500 \text{ pc cm}^{-3}$ . A typical sign of a burst is the triangle-like shape centered around the burst DM in the upper right panel, and the increasing and then decreasing marker size with DM around the burst DM at a specific time in the DM versus time plot.

file, and calculates their modulation index,  $m_I$ . The modulation index is an estimation of the fractional variation across the data frequency spectrum, used to discriminate between broad-band signals and narrow-band RFI (Spitler et al., 2012). It is calculated as the normalised standard deviation of intensity across the frequency channels. The modulation index threshold,  $m_{I,\text{thresh}}$ , above which candidates are considered to be RFI, is calculated as

$$m_{I,\text{thresh}} = \frac{\sqrt{n_{\text{chan}}}}{(\text{S/N})_{\text{min}}}, \quad (2.22)$$

where  $n_{\text{chan}}$  is the number of data channels, and  $(\text{S/N})_{\text{min}}$  is the S/N threshold applied to the search. If the modulation of a candidate is below the threshold, the pipeline creates plots showing the dedispersed time series and the dynamic spectrum (dedispersed and non-dedispersed) around the candidate. These plots can be seen in Fig. 2.9, where the dynamic spectra are downsampled by a factor of 16. The plots can optionally be downsampled and sub-banded to desired values. Finally, the pipeline creates a colorised version of Fig. 2.8, which is used to look for promising candidates that can be further inspected with the candidate files and plots.

### 2.6.3 Heimdall

HEIMDALL is a single pulse searching software designed to be ran on GPUs in order to enable real-time searching. HEIMDALL is best suited for multi-beam data, as it handles RFI in post-processing by coinciding candidates. The main inputs of HEIMDALL are a filterbank file, the edges of the intended DM search range, and a S/N detection threshold. If one is familiar with the data, it is possible to input channel ranges to zap. The DM steps are determined by HEIMDALL based on the pulse broadening induced by the step size, resulting in each DM trial being a function of the data properties and the previous DM trial (Levin, 2012). The single pulse searching is performed with a boxcar matched filtering. The boxcar widths are powers of two samples wide, and the default range is  $2^0 - 2^{12}$  samples. Single pulse search candidates that are close in DM and time are grouped together and the highest S/N candidate is listed, so the multiple candidates from the burst in Fig. 2.8 would be grouped together as a single candidate. The HEIMDALL candidate files contain somewhat more information than in PRESTO. The beam number information is written in the candidate file name, and the candidate file itself has the following information:

1. Peak S/N of candidate group.
2. Time sample number of candidate.
3. Time of candidate.
4. Boxcar width power index.
5. DM trial number.
6. Candidate DM.

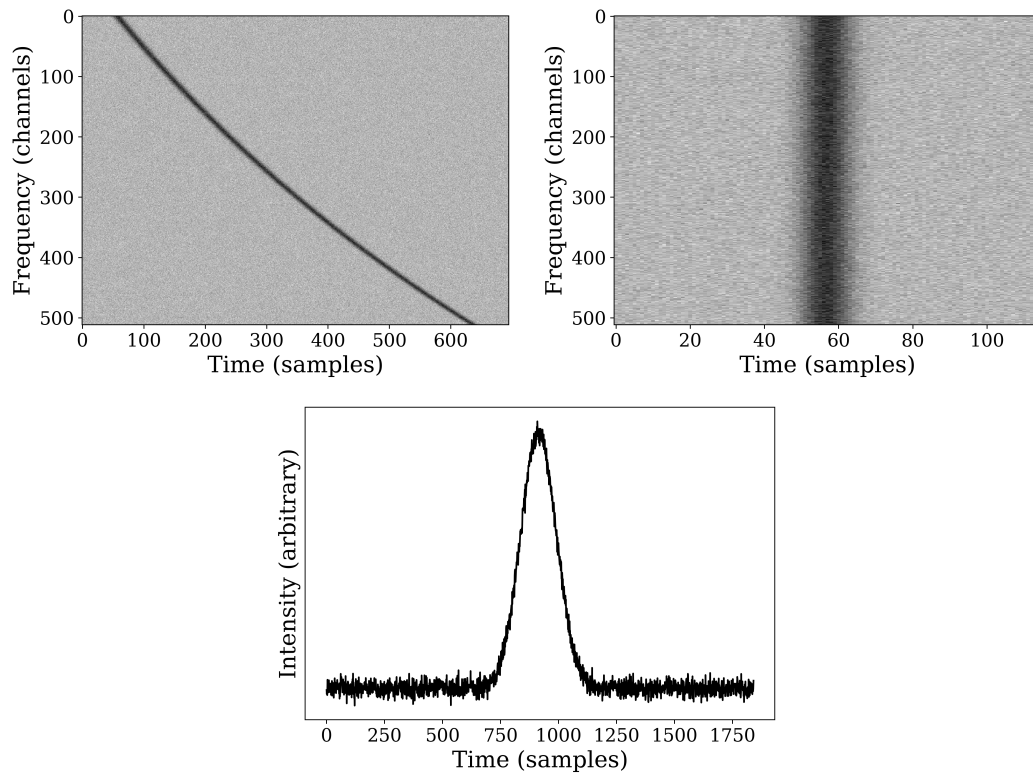


Figure 2.9: Candidate plots from the PRESTO search pipeline for a simulated FRB. The top two panels show the non-dedispersed and dedispersed dynamic spectrum around the candidate, both of which are downsampled by a factor of 16. The bottom panel shows the dedispersed time series of the candidate. The dedispersion is performed at the maximum DM found by `single_pulse_search.py`.

7. Number of candidates in candidate group.
8. Earliest sample number of candidate group.
9. Latest sample number of candidate group.

As mentioned, HEIMDALL performs RFI classification through the post-processing module `coincider`. Coinciding of candidates simply means looking for candidates occurring in multiple beams at the same DM and time. The great distance towards FRB sources means that a burst from an FRB should not be detected in too many beams. If a candidate occurs in more than a few beams, it is highly likely that it is RFI. The exact number of beams depends on the beam arrangement with respect to each other on the sky and has to be estimated on a case-by-case basis. The `coincider` reads the candidate files and outputs a compilation from all of them with the same information, with the addition of:

1. Number of beams in which candidate is seen.
2. Beam mask.
3. Beam in which candidate has the highest S/N.
4. Maximum S/N across all beams.
5. Beam ID of detection.

The beam mask is a binary number displayed as a base-10 number and represents in which beams a candidate is detected. Each beam is represented by a bit in the binary number, with the rightmost bit being the first beam. The bits are 1 for beams in which the candidate is detected, and 0 otherwise. If a candidate is detected in beams number 1, 2, and 5 out of seven beams, the beam mask will be  $0010011_2 = 19_{10}$ .

HEIMDALL does have plotting tools that can produce plots somewhat similar to PRESTO. It is more common though to write one's own plotting software based on one's preference, where the software makes use the candidate information. The beam mask is particularly important in this respect, as it makes the plotting software, and candidate rejection, highly customisable.

#### 2.6.4 Heimdall Search Pipeline

HEIMDALL was used to search the multi-beam data from the Phased Array Feed (PAF) receiver on Effelsberg in Chapters 3 and 4. In their current state, data from the PAF beams are not synchronised, meaning that the start and end times of data from different beams could differ by a small amount ( $\sim$  seconds). This results in the coincider not working appropriately. To resolve this issue, each observation is checked for its earliest start time and latest end time. For beams not starting or ending at these times, Gaussian noise is prepended and appended appropriately using a running mean of the data<sup>8</sup>. Once the data from all the beams of an observation are the same length

<sup>8</sup>[github.com/ghenning/PAFcode](https://github.com/ghenning/PAFcode)

and with the same start and end times, the data are dedispersed and searched with HEIMDALL, and subsequently coincided with the `coincider`.

For post-processing, candidates are sifted further with an increased S/N threshold of 8, minimum DM of 25, maximum boxcar width of 10 (equal to 55 ms for the PAF data), and maximum number of beam detections of 4. The added S/N threshold is due to the PAF data having numerous false positive candidates in the S/N range of 7–8. The remaining candidates are then plotted in the same way as in Fig. 2.9.

# Phased Array Feeds and Commissioning at Effelsberg

---

One of the more recent receiver developments in radio astronomy are phased array feeds (PAFs). Typical receivers have feed horns for each of their receiving elements and beams of multi-beam receivers are thus separated by some distance based on the physical separation of the feed horns. PAFs however are made up of an array of receiver elements without a feed horn, giving a continuous sampling of the focal plane. The inputs from the PAF elements are combined and made to form virtual beams on the sky. PAFs can be used to form multiple beams on the sky, resulting in a greater field of view (FOV) than standard receivers. PAF beams are highly customisable through the process of beamforming that is applied in the backend after the signal from all the elements have been received. The shape, pattern, and distribution of the beams can be controlled, resulting in various practical applications. This versatility provides an advantage over typical multi-beam receivers (e.g. the 7-beam receiver at Effelsberg) which have fixed beam patterns due to their physical feeds.

PAFs have been successful in their relatively recent usage as radio telescope receivers. The most notable use of PAFs is at ASKAP, which is an array of 36 12-m antennas, each equipped with a PAF capable of forming 36 beams. At ASKAP, multiple FRBs have been detected (e.g. Shannon et al., 2018; Bhandari et al., 2019; Qiu et al., 2019) and localised (e.g. Bannister et al., 2019), and its detections have been used to solve the cosmological missing baryon problem (Macquart et al., 2020, see §1.8). The aperture tile in focus (Apertif) is a PAF system recently installed on the Westerbork synthesis radio telescope (WSRT) in the Netherlands. Apertif has been able to detect multiple bursts from FRB121102 (Oostrum et al., 2020) as well as localising an FRB within a narrow  $5'' \times 7'$  ellipse (Connor et al., 2020).

Even though the appeal of PAFs is clear, they suffer from technical challenges. Their system temperature is generally somewhat higher than standard receivers, upwards of 50 K (e.g. Oosterloo et al., 2010; Chippendale et al., 2015; Deng et al., 2018), which results in lowered sensitivity (see Eq. 2.2). To combat this problem, efforts have been made to manufacture cryogenically cooled PAFs. Progress on such PAFs is already underway, where a system temperature (normalised by aperture efficiency) of 25 K has been achieved at GBT (with 19 receiver elements), comparable to the cryogenic single-feed receiver at the telescope (Roshi et al., 2018). Another interesting development in cryogenically cooled PAFs is the so-called “Rocket PAF” that has conical receiving elements resembling a rocket (Dunning et al., 2016), and is being tested at Parkes. This PAF has 32 receiving elements (16 central, 16 edge), and is estimated to achieve

sub-20 K system temperatures.

The following sections will describe the use cases of PAFs, with a focus on single-dish telescopes, followed by a section on the commissioning of a PAF at Effelsberg.

### 3.1 Increasing the FOV and Survey Speed

Large, single-dish telescopes have a high sensitivity, but small FOVs. As seen in Eqs. 2.4–2.5, the FOV of a telescope is inversely proportional to its size, resulting in a slower survey speed (SVS), approximated as (e.g. Fisher et al., 2009)

$$\text{SVS} \propto N_b \Omega_b f_{\text{BW}} \left( \frac{A_{\text{eff}}}{T_{\text{sys}}} \right)^2, \quad (3.1)$$

where  $N_b$  is the number of beams,  $\Omega_b$  is the solid angle covered by each beam,  $f_{\text{BW}}$  is the receiver bandwidth,  $A_{\text{eff}}$  is the effective collecting area of the telescope, and  $T_{\text{sys}}$  is the system temperature.

Multi-beam receivers on large telescopes, such as the 7-beam receiver at Effelsberg, alleviate the FOV and SVS issues to some extent. With 36 beams, the Effelsberg PAF has a FOV five times greater than the 7-beam. Assuming that  $T_{\text{sys,PAF}} = 2 \times T_{\text{sys,7beam}}$ , the PAF has a 30% greater SVS than the 7-beam. If the PAF can be cooled such that  $T_{\text{sys,PAF}} = 1.5 \times T_{\text{sys,7beam}}$ , the SVS would become 130% greater than the 7-beam.

The average number of days to an FRB detection can also be compared between the PAF and 7-beam receivers at Effelsberg. Scaling the all-sky rate from Bhandari et al. (2018) using Eq. 1.4 yields  $3 \times 10^4$  bursts  $\text{sky}^{-1} \text{day}^{-1}$  for the 7-beam receiver and  $1.6 \times 10^4$  bursts  $\text{sky}^{-1} \text{day}^{-1}$  for the PAF (assuming  $T_{\text{sys,PAF}} = 2 \times T_{\text{sys,7beam}}$ ). The FOV of the PAF and 7-beam receivers is  $1 \text{ deg}^2$  and  $0.2 \text{ deg}^2$ , respectively. The average time until detection can then be calculated as

$$T = \left( \text{Rate} \times \frac{\text{FOV}}{41253 \text{ deg}^2} \right)^{-1} \text{ days}, \quad (3.2)$$

resulting in 2.6 days until detection for the PAF and 6.9 days for the 7-beam receiver.

To maximise the FOV of a PAF, the beam pattern should be so that there is no overlap between beams. This is not a common observing mode with PAFs, as the beam pattern is typically such that adjacent beams marginally overlap to provide continuous coverage and to improve localisation. Fig. 3.1 shows the difference in the FOVs of the PAF and 7-beam receivers at Effelsberg, where the beam pattern of the PAF is in a FOV maximising mode.

### 3.2 Localisation

PAFs offer a high localisation flexibility due to their beam customisation capabilities. Depending on the objective, the beam pattern can be adjusted accordingly: For a blind survey, the beams can be set to slightly overlap to provide both localisation capabilities and a large FOV; or the beams can be set to highly overlap in order to increase localisation capabilities of a targeted survey.

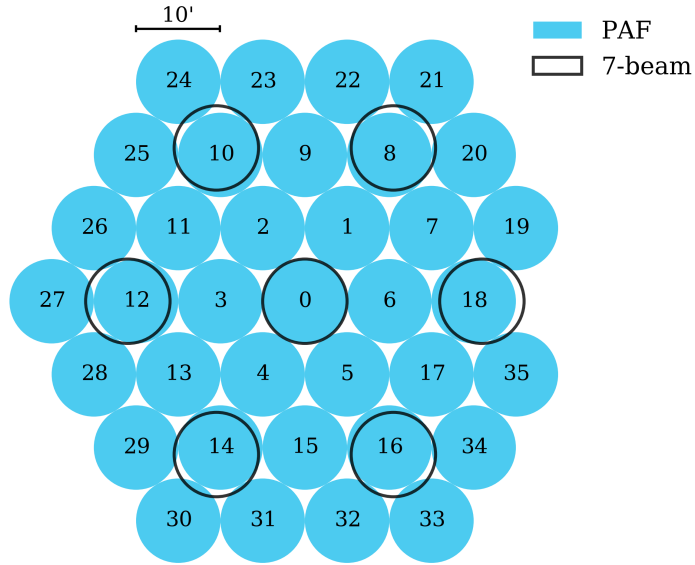


Figure 3.1: Field of view (FOV) comparison between the PAF and 7-beam receivers at Effelsberg. The PAF beam pattern is set to maximise the FOV. The 36 PAF beam numbers are listed at the center of each beam. Each beam width is 10 arcminutes.

If a burst is detected within a PAF beam, it can be incoherently localised based on the detections and limits in adjacent beams. The detections and upper limits in the beams are compared to a model for expected flux density that is a function of intrinsic brightness and sky location, i.e. a beam model. Using ASKAP, Bannister et al. (2017) incoherently localised an FRB detected in a fly’s eye survey (no overlap between antennas and only minor overlap between beams of each antenna) to an  $8' \times 8'$  region using Bayesian inference (see §5.5 for discussion on Bayesian inference). The diameter of the ASKAP antennas is 12 meters, so a single beam is  $\sim 60'$  (see Eq. 2.4). The beam pattern and localisation region are shown in the left panel of Fig. 3.2.

Detecting a burst in real-time and thus triggering a baseband dump can offer even better localisation constraints. The baseband data can be correlated and radio images can be created at high time-resolution to obtain a localisation region. This method has been used at ASKAP to localise FRBs to a host galaxy (e.g. Bannister et al., 2019; Macquart et al., 2020), where ASKAP’s 6 km array baseline yields statistical position errors of  $\sim 10'' \times S/N^{-1}$ . The right panel in Fig. 3.2 shows the localisation region of a burst using both incoherent and interferometric localisation.

Even though PAFs on single-dish telescopes lack the baseline to interferometrically localise FRBs, they can still be useful. For the PAF at Effelsberg the beam width is  $10'$ , so a position error of  $\sim 10' \times S/N^{-1}$  can be achieved. Performing a survey with only marginally overlapping beams, a PAF can still localise an FRB to within a region that can be easily followed up with other receivers or telescopes, as was shown in

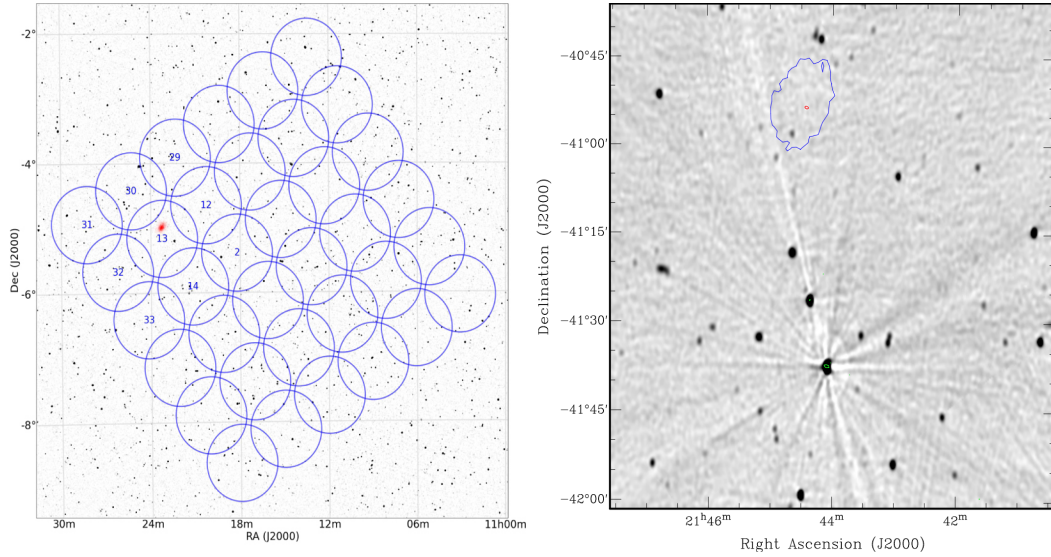


Figure 3.2: ASKAP localisation regions. *Left*: Incoherent localisation of an FRB in a fly’s eye mode. Blue circles are the 36 beams of a single PAF, and the red area is the localisation region. Figure is from Bannister et al. (2017). *Right*: Incoherent and interferometric localisation regions of an FRB. Blue area shows the incoherent localisation region, and the red area shows the interferometric localisation area using baseband data. Figure is from Bannister et al. (2019).

Bannister et al. (2017). The localisation capability of a PAF can be increased by using a more compact beam pattern. This is ideal when following up poorly localised FRBs (e.g. from CHIME) in order to further constrain their localisation region, or to have a high localisation precision while performing a targeted survey.

### 3.3 Mitigating RFI

The digital beamformer in the PAF backend can be used to suppress RFI. The beamformer can be used to calculate beam array covariance matrices (ACMs). The interfering signal subspace can be estimated from the ACM and be used to update the beamformer weights, creating spatial nulls towards RFI (Chippendale & Hellbourg, 2017). During commissioning of the Effelberg PAF at the Parkes radio telescope, Chippendale & Hellbourg (2017) successfully implemented this method to mitigate known RFI at the telescope without reducing the PAF system sensitivity. The cycle of downloading the ACMs and updating the beam weights was two minutes. Chippendale & Hellbourg (2017) state that by refining the software performing these tasks could significantly reduce this cycle time, resulting in improved dynamic RFI mitigation.

### 3.4 Multi-source Observations

The beamforming of PAFs provides an intriguing opportunity for single-dish telescopes to observe multiple spread-out sources at once by placing the PAF beams on the position of several targets simultaneously. Examples of this application could be observing multiple pulsars nearby on the sky, such as the Galactic center (GC) pulsars, localised FRBs, or a combination of all these. If all targets are localised, a single beam can be dedicated to each source and up to 36 sources can be observed simultaneously. On the other hand, if any of the sources are poorly localised, multiple beams in a close-packed formation could be dedicated to those sources in an attempt to localise them. During the commissioning of the Effelsberg PAF at the Parkes radio telescope, Deng et al. (2017) successfully observed three pulsars simultaneously that were within the PAF FOV.

### 3.5 PAF at Effelsberg

The PAF at Effelsberg is an ASKAP Mark II PAF, i.e. the same as are being used at ASKAP but modified for use at Effelsberg (Chippendale et al., 2016). The 188 ( $94 \times 2$  polarisations) receiving elements of the Effelsberg PAF form a chequerboard pattern across a 1.2-m diameter circle. A total of 36 dual-polarisation beams can be formed, resulting in an FOV of  $1 \text{ deg}^2$  at 1.4 GHz in a FOV maximising mode. In comparison, the 7-beam (1.4 GHz) receiver at Effelsberg has an FOV of  $0.2 \text{ deg}^2$ . For both receivers, the beam widths are  $10'$ .

The PAF can operate at three different frequency bands centered at 900, 1350, or 1500 MHz. The outer two bands suffer from vastly higher system temperatures than the central band (Deng et al., 2018), while the lower band also suffered from severe RFI. Only the central band was thus used in the commissioning runs described here.

Due to the size of the PAF frontend, it does not fit in the main focus cabin of the Effelsberg telescope. Therefore it must be mounted to the outside of the cabin, rendering other receivers on the telescope inoperable while the PAF is installed, resulting in infrequent, long-duration ( $\sim$ week) commissioning runs.

Once a signal reaches the backend it gets channelised into 336 channels. The channels are separated by 1 MHz and oversampled by a factor of  $32/27$ , meaning that adjacent channel edges overlap. The oversampling reduces aliasing effects and results in a flatter frequency response across the bandwidth (Tuthill et al., 2012). The oversampled channels then go through the beamformer (BMF) to form the synthesised PAF beams. Next, each oversampled channel goes through a 32-point complex-to-complex FFT, meaning each 1-MHz channel is further channelised into 32 channels. For each 32 fine channels, the first two and last three are cut to remove the overlap due to the oversampling in the coarse channelising stage. Channels at the edges of the band are also removed, as the frequency response drops significantly near the edges, reducing the total bandwidth from 336 MHz down to 303 MHz. The data are then detected (summed in quadrature to obtain total intensity) and integrated in frequency and time

Table 3.1: PAF observation summary from 17 to 19 April 2018. *From left to right:* Source name, right ascension (RA) and declination (DEC) in J2000 coordinates, and total duration of observing each source. At the bottom is shown the total observing time from all the observations.

Source name	RA	DEC	Obs. dur. (min)
FRB121102	05 <sup>h</sup> 31 <sup>m</sup> 02.6 <sup>s</sup>	+33°08′04″	171
J1400-0251	14 <sup>h</sup> 00 <sup>m</sup> 39 <sup>s</sup>	−02°51′23″	60
J1410+0859	14 <sup>h</sup> 10 <sup>m</sup> 44 <sup>s</sup>	+08°59′29.96″	60
J1314+2959	13 <sup>h</sup> 14 <sup>m</sup> 42 <sup>s</sup>	+29°59′59.19″	60
J1419+3940	14 <sup>h</sup> 19 <sup>m</sup> 18.855 <sup>s</sup>	+39°40′36.03″	226
J1622+3212	16 <sup>h</sup> 22 <sup>m</sup> 44.571 <sup>s</sup>	+32°12′59.28″	118
J2353+0758	23 <sup>h</sup> 53 <sup>m</sup> 51.412 <sup>s</sup>	+07°58′35.91″	77
Total			772

to obtain the final data output that is written to disk. For a more detailed description of the technical and computing aspects of the PAF, see Malenta (2018).

### 3.5.1 PAF Observations

While mounted on Effesberg, the PAF underwent engineering operations and science observations. Observational results from four PAF commissioning runs will be described here: 17 April–19 April 2018, 26 June–2 July 2018, 29 August–3 September 2018, and 21 March–27 March 2019. The sources observed and their total observation duration for each run are listed in Tables 3.1–3.4. All the sources were observed at the center of the boresight beam.

The number of beams for which data are recorded is limited by the GPU power in the backend. For the runs in 2018, 16 beams were formed for the observations. In 2019, six more beams could be formed by sacrificing a part of the observing bandwidth. Table 3.5 shows the properties of the total intensity filterbanks and number of beams for each commissioning run. The beams were arranged in the same way for all the runs, where the separation between adjacent beams was 7.2′. The beam configuration for 16, 22, and 36 beams is shown in Fig. 3.3.

The sources observed can be categorised into four distinct groups:

- *Test pulsars (PSRs)*: It is common practice during FRB observations to first observe a pulsar to estimate the system functionality and quality of an observation. During the PAF observations, short test pulsar observations were interwoven with regular observations.
- *FRBs*: The main FRB focus was to attempt to observe repeat bursts from FRB121102. When FRB121102 was not in the observable sky of Effelsberg, so-far one-off FRBs were observed to look for repeat bursts. The FRBs observed were FRB130729 (Champion et al., 2016) and FRB110523 (Masui et al., 2015). During the March 2019 observations the focus was shifted towards FRB180814.J0422+73,

Table 3.2: As Table 3.1 but with PAF observation summary from 26 June to 2 July 2018.

Source name	RA	DEC	Obs. dur. (min)
FRB121102	05 <sup>h</sup> 31 <sup>m</sup> 02.6 <sup>s</sup>	+33°08'04"	774
FRB130729	13 <sup>h</sup> 41 <sup>m</sup> 21 <sup>s</sup>	−05°59'43"	231
J0927-0225	09 <sup>h</sup> 27 <sup>m</sup> 58.282 <sup>s</sup>	−02°25'58.95"	174
J1025+1715	10 <sup>h</sup> 25 <sup>m</sup> 26.189 <sup>s</sup>	+17°15'47.97"	137
J1047+0602	10 <sup>h</sup> 47 <sup>m</sup> 26.693 <sup>s</sup>	+06°02'47.72"	48
J1058+2413	10 <sup>h</sup> 58 <sup>m</sup> 23.641 <sup>s</sup>	+24°13'55.32"	114
J1145+1923	11 <sup>h</sup> 45 <sup>m</sup> 29.346 <sup>s</sup>	+19°23'27.46"	52
J1419+3940	14 <sup>h</sup> 19 <sup>m</sup> 18.855 <sup>s</sup>	+39°40'36.03"	689
J1622+3212	16 <sup>h</sup> 22 <sup>m</sup> 44.571 <sup>s</sup>	+32°12'59.28"	351
J1745-2900	17 <sup>h</sup> 45 <sup>m</sup> 40.1662 <sup>s</sup>	−29°00'29.896"	234
J2353+0758	23 <sup>h</sup> 53 <sup>m</sup> 51.412 <sup>s</sup>	+07°58'35.91"	354
NGC1569	04 <sup>h</sup> 30 <sup>m</sup> 49 <sup>s</sup>	+64°50'53"	354
Total			3512

Table 3.3: As Table 3.1 but with PAF observation summary from 29 August to 3 September 2018.

Source name	RA	DEC	Obs. dur. (min)
B0402+61	04 <sup>h</sup> 06 <sup>m</sup> 30.082 <sup>s</sup>	+61°38'41.04"	20
B0609+37	06 <sup>h</sup> 12 <sup>m</sup> 48.6867 <sup>s</sup>	+37°21'37.36"	203
B1508+55	15 <sup>h</sup> 09 <sup>m</sup> 25.6298 <sup>s</sup>	+55°31'32.394"	14
B1957+20	19 <sup>h</sup> 59 <sup>m</sup> 36.76988 <sup>s</sup>	+20°48'15.1222"	187
FRB110523	21 <sup>h</sup> 45 <sup>m</sup> 12 <sup>s</sup>	−00°09'37"	469
FRB121102	05 <sup>h</sup> 31 <sup>m</sup> 02.6 <sup>s</sup>	+33°08'04"	1027
J1419+3940	14 <sup>h</sup> 19 <sup>m</sup> 18.855 <sup>s</sup>	+39°40'36.03"	583
NGC1569	04 <sup>h</sup> 30 <sup>m</sup> 49 <sup>s</sup>	+64°50'53"	250
SN2018COW	16 <sup>h</sup> 16 <sup>m</sup> 00.22 <sup>s</sup>	+22°16'04.83"	60
Total			2813

Table 3.4: As Table 3.1 but with PAF observation summary from 21 to 27 March 2019.

Source name	RA	DEC	Obs. dur. (min)
B0355+54	03 <sup>h</sup> 58 <sup>m</sup> 53.7238 <sup>s</sup>	+54°13′13.784″	115
B0531+21	05 <sup>h</sup> 34 <sup>m</sup> 32.0 <sup>s</sup>	+22°00′52.1″	55
B1612+07	16 <sup>h</sup> 14 <sup>m</sup> 41.0 <sup>s</sup>	+07°37′31.0″	70
FRB121102	05 <sup>h</sup> 31 <sup>m</sup> 02.6 <sup>s</sup>	+33°08′04″	275
FRB180814	04 <sup>h</sup> 22 <sup>m</sup> 22 <sup>s</sup>	+73°40′00″	1825
.J0422+73			
GRB050826	05 <sup>h</sup> 51 <sup>m</sup> 02.6 <sup>s</sup>	−02°39′28.8″	442
J1419+3940	14 <sup>h</sup> 19 <sup>m</sup> 18.855 <sup>s</sup>	+39°40′36.03″	569
NGC1569	04 <sup>h</sup> 30 <sup>m</sup> 49 <sup>s</sup>	+64°50′53″	99
PTF10hgi	16 <sup>h</sup> 37 <sup>m</sup> 47 <sup>s</sup>	+06°12′32.3″	778
Total			4228

Table 3.5: Properties of the PAF total intensity filterbanks and number of beams for each commissioning run. *From left to right:* Commissioning run date, number of beams, observing bandwidth ( $f_{\text{BW}}$ ), top frequency ( $f_{\text{top}}$ ), channel bandwidth ( $\Delta f$ ), number of channels ( $n_{\text{chan}}$ ), and sample time ( $t_{\text{samp}}$ ).

Date	No. beams	$f_{\text{BW}}$ (MHz)	$f_{\text{top}}$ (MHz)	$\Delta f$ (MHz)	$n_{\text{chan}}$	$t_{\text{samp}}$ ( $\mu\text{s}$ )
April 2018	16	303	1492.2	0.59	512	54
June 2018	16	303	1492.2	0.59	512	54
August 2018	16	303	1492.2	0.59	512	54
March 2019	22	230	1451.7	0.45	512	54

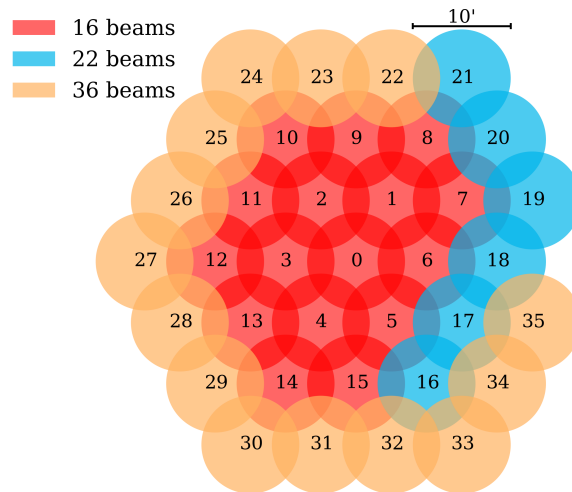


Figure 3.3: Effelsberg PAF beam configuration for 16 (as used in 2018), 22 (as used in 2019), and 36 beams (maximum beam capacity). Each beam width is 10 arcminutes.

which at the time had only recently been detected and was the only other repeating FRB (CHIME/FRB Collaboration et al., 2019a).

- *Persistent radio sources (PRSs)*: Ofek (2017) searched nearby galaxies for PRSs similar to the PRS associated with FRB121102, and found 11 PRSs spatially coincident with galactic disks or star formation regions while having radio luminosities  $> 10\%$  of the FRB121102 PRS. Ofek (2017) notes a reasonable follow-up prioritisation by the inverse galaxy size and association with star-forming regions due to smaller galaxies having a lower probability of chance coincidence with background objects. Of the 11 PRSs, J1419+3940 thus has the highest priority and is also the most luminous among the PRSs with a luminosity of 0.95 times the PRS associated with FRB121102. The flux density of J1419+3940 has faded from 26 mJy in 1993 to 0.4 mJy in 2017 (Law et al., 2018), and has been found to be consistent with the afterglow of a long gamma-ray burst (LGRB, Marcote et al., 2019). Another PRS of great interest is PTF10hgi (Eftekhari et al., 2019). It is coincident with a Type-I superluminous supernova (SLSN) and is the first detection of radio emission coincident with an SLSN. PTF10hgi could be analogous to the PRS of FRB121102, and the connection between FRBs and SLSNe/LGRBs (see §1.6.1 and Chapter 4) would be unambiguously demonstrated if an FRB were to be detected coincident with PTF10hgi.
- *Miscellaneous*: A few extra sources were observed to fill gaps in the observing schedules when the primary sources were off-sky for Effelsberg. These sources were NGC1569, a nearby dwarf galaxy with a high star formation rate, SN2018COW and GRB050826, a supernova and a long gamma-ray burst, which were among the sources observed in §4, and the GC magnetar, PSR J1745-2900 (Desvignes et al., 2018).

The observed sources in Tables 3.1–3.4 are sorted by projects in Table 3.6.

### 3.5.2 Test Pulsars and Sensitivity

The test pulsars observed in August 2018 and March 2019 can be used to estimate the system equivalent flux density (SEFD, see Eq. 2.2) of the PAF. The test pulsars were observed for 5–10 minutes at regular intervals throughout the observations. The pulsar version of the radiometer equation can be used to estimate the SEFD (Lorimer & Kramer, 2012):

$$S = \frac{\text{SEFD } S/N}{\sqrt{n_p t_{\text{int}} f_{\text{BW}}}} \sqrt{\frac{W}{P - W}} \text{ Jy}, \quad (3.3)$$

where  $S$  is the pulse averaged summed flux density of the pulsar,  $S/N$  is the signal to noise ratio,  $n_p = 2$  is the number of polarisations,  $t_{\text{int}}$  is the integration time,  $f_{\text{BW}}$  is the total bandwidth (after RFI zapping),  $W$  is the width of the pulsar (full width at half maximum), and  $P$  is the period of the pulsar. The properties,  $S$  (at 1.4 GHz),  $W$ ,

Table 3.6: Sources from Tables 3.1–3.4 ordered by project. *From left to right:* Test pulsars (PSRs), FRBs, persistent radio sources (PRSs), and miscellaneous sources. The last four columns are the burst rate analysis results from §3.5.4–3.5.5 and show luminosity distance ( $D_L$ ), redshift ( $z$ ), 95% confidence level burst rate upper limits ( $R_{UL}$ ), and the rate of an FRB121102-like source scaled with respect to the PAF and distance ( $R_{sc}$ ). The fluence threshold of the rates is above  $1.9(w_{ms}/ms)^{1/2}$  Jy ms for burst widths of  $w_{ms}$  milliseconds. The distance to Galactic sources, i.e. the test PSRs and J1745-2900, is a DM-based distance estimated from the YMW16 electron density model, and is given in kiloparsecs.

Project	Source	Obs. dur. (min)	$D_L$ (Mpc)	$z$	$R_{UL}$ (bursts/day)	$R_{sc}$ (bursts/day)
Test PSRs	B0355+54	115	1.0 kpc			
	B0402+61	20	4.6 kpc			
	B0609+37	203	0.5 kpc			
	B1508+55	14	2.1 kpc			
	B1957+20	187	1.4 kpc			
	B0531+21	115	2.0 kpc			
	B1612+07	70	1.6 kpc			
Total		724				
FRBs	FRB121102	2247	947.5	0.193	4.1	$2.1 \pm 0.5$
	FRB130729	774			5.6	
	FRB110523	469			9.2	
	FRB180814	1825			2.4	
	.J0422+73					
Total		5315				
PRSs	J1400-0251	60	109.8	0.025	71.9	$39 \pm 15$
	J1410+0859	60	100.8	0.023	71.9	$45 \pm 17$
	J1314+2959	60	100.8	0.023	71.9	$45 \pm 17$
	J1419+3940	2067	87.5	0.020	2.1	$59 \pm 22$
	J1622+3212	469	96.4	0.022	9.2	$50 \pm 19$
	J2353+0758	431	78.6	0.018	10.0	$72 \pm 27$
	J0927-0225	174	100.8	0.023	27.8	$45 \pm 17$
	J1025+1715	137	78.6	0.018	31.5	$72 \pm 27$
	J1047+0602	48	83.1	0.019	89.9	$64 \pm 24$
	J1058+2413	114	91.9	0.021	37.8	$54 \pm 20$
	J1145+1923	52	109.8	0.025	82.3	$39 \pm 15$
PTF10hgi	778	see §4.4.2				
Total		4450				
Misc.	NGC1569	703	2.5	0.00056	6.1	$38000 \pm 14000$
	SN2018COW	60	63.3	0.014	71.9	$106 \pm 40$
	GRB050826	442	1542.3	0.296	9.8	$0.4 \pm 0.1$
	J1745-2900	234	8.3 kpc			
Total		1439				

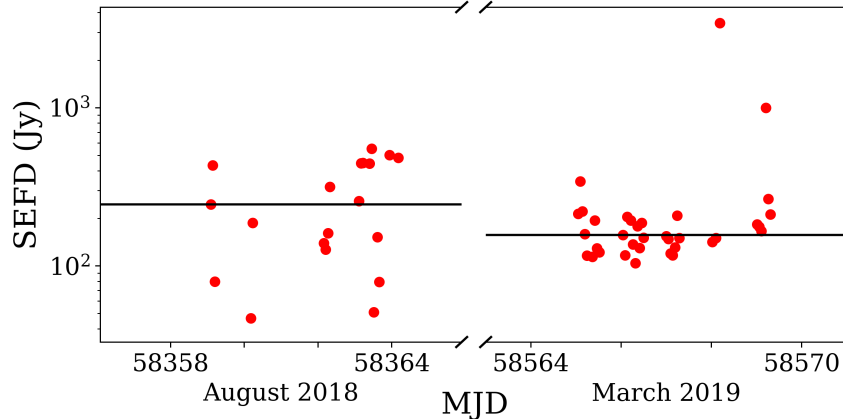


Figure 3.4: The SEFD over time in MJD for the commissioning runs in August 2018 and March 2019. Each point represents a test pulsar observation from which an SEFD was estimated. The horizontal lines show the median SEFD value of each run.

and  $P$  of each pulsar can be obtained from the ATNF pulsar catalogue<sup>1</sup> (Manchester et al., 2005). The other quantities in Eq. 3.3 are obtained from the observations.

The pulsar data were folded, i.e. aggregated over intervals equal to the pulsar period, using `dspsr`<sup>2</sup> (van Straten & Bailes, 2011) and excised of RFI using `pazi` from PSRCHIVE, which was also used to obtain  $S/N$ ,  $t_{\text{int}}$ , and  $f_{\text{BW}}$ . The resulting SEFD over time is shown in Fig. 3.4. The SEFD between pulsar observations was highly erratic in August 2018, while staying much more stable in March 2019. The median SEFD was 245 Jy and 157 Jy in August 2018 and March 2019, respectively.

The scattering timescale of the test pulsars at the observed frequency is on the order of  $10^{-7}$  s, resulting in scintillation bandwidths of  $\sim 1$  MHz (Eq. 1.45) and a total of  $\sim 200$  scintles across the observing band. Scintillation is therefore unlikely to be the primary cause for the highly varying SEFD estimates from August 2018. The scattering timescales are also orders of magnitude less than the periods of the pulsars, so scattering should also not have an effect on the SEFD estimates. The varying SEFD in August 2018 could be linked to self-generated PAF RFI erratically overwhelming the pulsar signals, resulting in varying pulsar  $S/N$ s. The unexpectedly high overall SEFD could be due to underestimated numbers of badly beamformed channels, reducing the effective bandwidth. The PAF RFI and beamforming issues are both discussed further in the following section.

### 3.5.3 Single Pulse Candidates and RFI

The PAF data were searched using the HEIMDALL single pulse search pipeline described in §2.6.4. Unfortunately, no single pulses were detected, except from the test pulsars. Example single pulse candidate plots from the pulsars B0355+54 and B1508+55 can

<sup>1</sup>[atnf.csiro.au/research/pulsar/psrcat](http://atnf.csiro.au/research/pulsar/psrcat)

<sup>2</sup>[dspsr.sourceforge.net](https://dspsr.sourceforge.net)

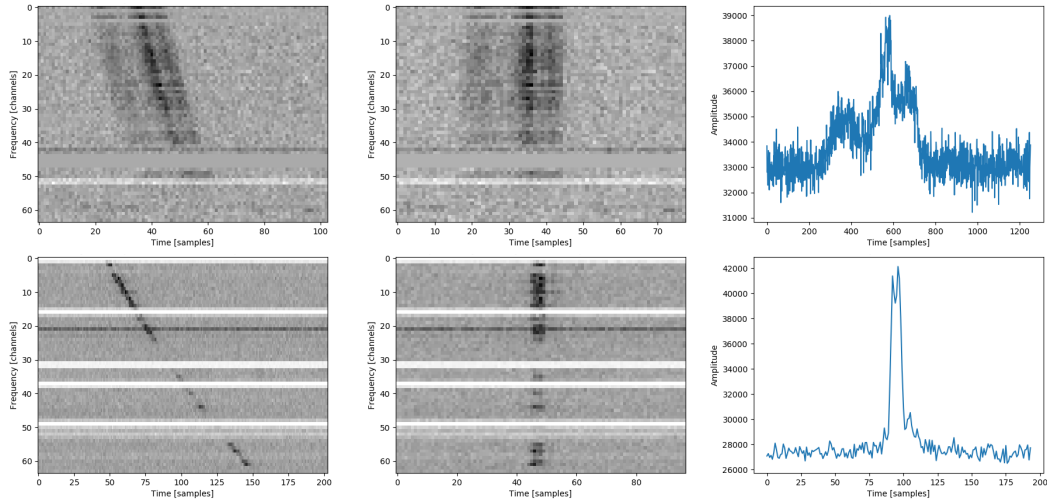


Figure 3.5: Candidate plots of single pulses from B1508+55 from 2 September 2018 (top row, DM of  $20 \text{ pc cm}^{-3}$ ) and B0355+54 from 23 March 2019 (bottom row, DM of  $57 \text{ pc cm}^{-3}$ ). *Left*: Dynamic spectrum. *Center*: Dedispersed dynamic spectrum. *Right*: Dedispersed time series. The dynamic spectra are downsampled by a factor of 16 and subbanded to 64 channels.

be seen in Fig. 3.5. The number of single pulse candidates (ignoring test pulsars) and the number of excised candidates for each commissioning run are shown in Table 3.7. The number of candidates rejected individually by each method is also shown, where the maximum width and beam mask methods were the most effective.

A real, astrophysical signal originates from very far away and thus should only be detected in a single beam, or several adjacent beams depending on how strong it is. Locally originating RFI is usually detected in many or all beams. On top of the rejection methods described in §2.6.4, the beam mask obtained from `Heimdall` can be very useful in rejecting multi-beam RFI single pulse candidates. A very primitive beam mask sifting was used in 2018 where candidates were only rejected if detected in all beams (beam mask of  $2^x$ , where  $x$  is the number of beams). This means that all the candidates rejected by the beam mask sifting were by default also rejected by the number of beams sifting (i.e. detected in fewer than 5 beams). The beam mask sifting method was updated for the observations in 2019. For each candidate the binary representation of a bad beam mask was calculated to contain beams not adjacent to the detection beam. If the candidate’s beam mask shared any binary bits with the “bad beam mask”, it was rejected. This also removed the requirement of using the number of beams sifting.

From the candidate inspection it was evident that the observations were heavily affected by RFI. An example of regularly occurring, detrimental RFI can be seen in Fig. 3.6. The observations in 2018 suffered from a peculiar type of RFI, where string-like signals were apparent in the dynamic spectrum of the data. Example candidates from this RFI are shown in Fig. 3.7. When dedispersed, this RFI could by chance line

Table 3.7: PAF candidates from the four commissioning runs from April 2018 to March 2019. *From left to right:* Observing epoch, total number of candidates, candidates removed due to signal-to-noise threshold, minimum DM, boxcar width, beam mask, and number of beams candidate was seen in, how many candidates remain after removal, percentage of candidates removed, and the number of candidates per minute after false positive rejection. Each rejection method column indicates the number of candidates rejected individually by each method. The beam mask excision was updated in 2019 such that number of beams excision was not needed.

Obs.	Num. cand	S/N	DM	Width	Beam mask	Num. beams	Remaining	% reduction	Cands./min.
April 2018	956586	159137	647223	878268	758075	805625	44597	95%	58
June 2018	2566370	833281	1765553	2434240	2417424	2485481	539884	79%	153
August 2018	2862251	478359	2036076	2641370	2338977	2520754	168837	94%	60
March 2019	3717505	1275441	3029372	3465385	3357856	-	633220	83%	150
Total	10102712	2746218	7478224	9419263	8872332	5811860	1386538	86%	122

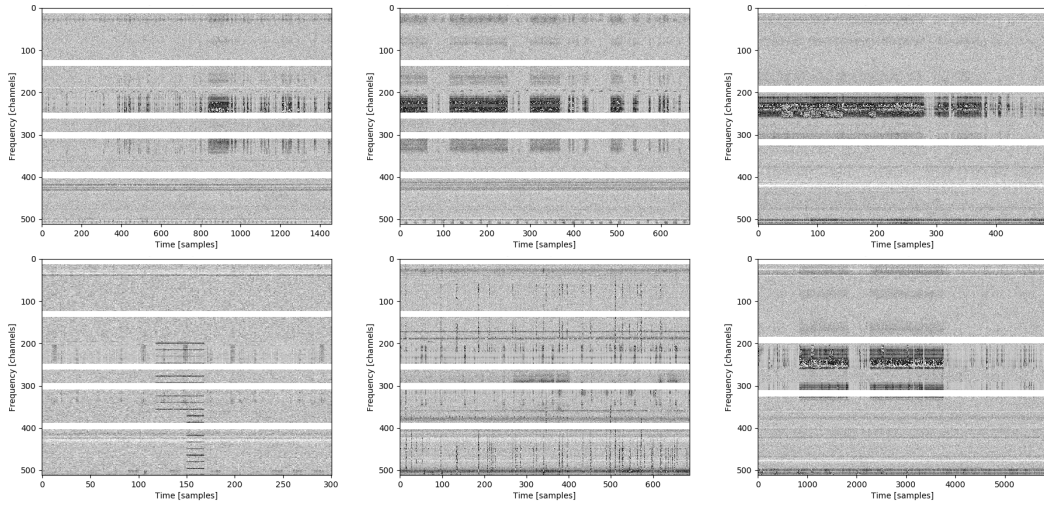


Figure 3.6: Dynamic spectra of PAF data showing various RFI. The white horizontal bars are nulls in the data due to failed data streaming.

up in such a way that it looks like a burst in the dedispersed time series. The source of this RFI turned out to be self-generated by the PAF from its receiver element monitor.

An error in the backend occurred in August 2018, where frequency channels would not be aligned correctly in time. This problem was only noticeable early on during the commissioning run and seems to have been fixed by restarting the backend. This can be seen clearly in the folded profile and dynamic spectrum of the pulsar B0609+37, shown in Fig. 3.8.

In the BMF, the coarse 1 MHz frequency channels are calibrated in groups of 7. If a channel group is affected by RFI stronger than the calibration source, the group will have an undefined pointing position. These are called “badly beamformed” channels and produce incoherent data. Identifying the badly beamformed channels is not always obvious, but suspected channels can be seen in the dynamic spectra of Figs. 3.5 and 3.8 as grey horizontal bars cutting out the pulsar signals. Each time the BMF was started, data streaming of some channel groups did not initialise and as a result have null-values in their channel time-series. During each observing epoch, 4–6 channel groups on average suffered from failed data streaming, resulting in a bandwidth decrease of 28–42 MHz. This effect can be clearly seen as white, horizontal bars in the dynamic spectra shown in Figs. 3.5–3.6.

### 3.5.4 FRBs

During two of the four commissioning runs, FRB121102 was in a state of inactivity based on its apparent periodicity of  $165 \pm 5$  days with a 60% activity window (Cruces et al., 2020). The active phases of FRB121102 and the PAF observing dates are plotted in Fig. 3.9. The observations in April 2018 and March 2019 were near the edge of the suspected activity. However, there are uncertainties on the periodicity and activity window of FRB121102, so whether these observations are during an active phase is

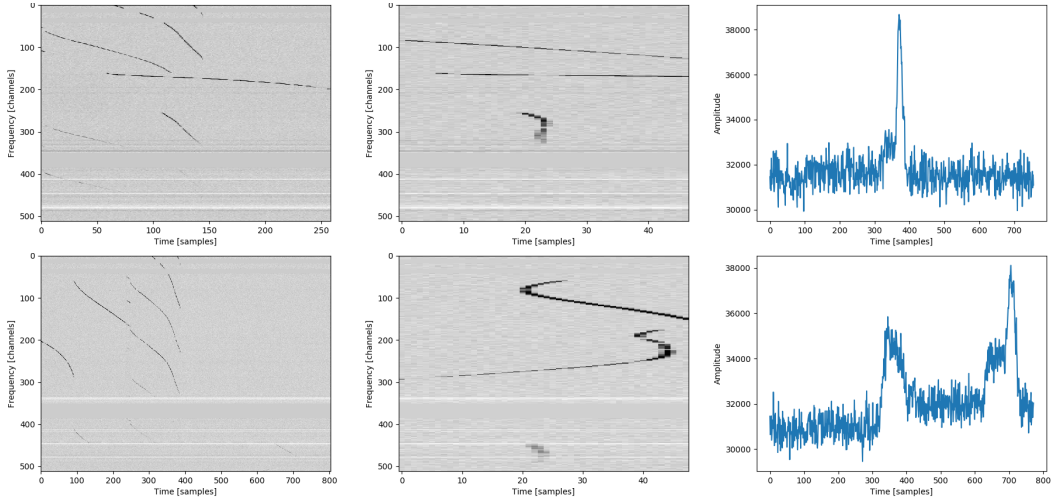


Figure 3.7: Single pulse candidate plots of the string-like, self-generated PAF RFI. *Top row:* Candidate at a DM of  $171 \text{ pc cm}^{-3}$ . *Bottom row:* Candidate at a DM of  $609 \text{ pc cm}^{-3}$ . *Left:* Dynamic spectrum. *Center:* Dedispersed dynamic spectrum. *Right:* Dedispersed time series. The dynamic spectra are downsampled by a factor of 16.

uncertain. Assuming a periodicity of 165 days and a 60% activity window, FRB121102 was observed with the PAF for a total of 1049 minutes while active, i.e. in June 2018 and March 2019.

Following the methods in §4.4, a published burst rate of FRB121102 can be scaled to the sensitivity of the PAF, and an upper limit (UL) to its burst rate can be calculated for the observations within activity windows. Obtaining ULs is useful for further surveys to estimate the time required to obtain more constraining ULs, or to use a model or source with predicted rates to see if the rates are consistent with the ULs. Assuming Poissonian statistics, the rate of FRB121102 during its active phase based on observations with the 7-beam receiver at Effelsberg is  $18 \pm 4$  bursts per day above a fluence of  $0.08(w_{\text{ms}}/\text{ms})^{1/2}$  Jy ms for burst widths of  $w_{\text{ms}}$  milliseconds (Cruces et al., 2020). Scaling this rate to the PAF observations yields  $2.1 \pm 0.5$  bursts per day above a fluence of  $1.9(w_{\text{ms}}/\text{ms})^{1/2}$  Jy ms, assuming an SEFD of 157 Jy and a bandwidth of 210 MHz due to failed data streaming and high volume of RFI during the 2018 observations. Based on this rate, the expected number of bursts on average from the PAF observations is 1–2. Since no bursts were detected, the probability of non-detection can be calculated by assuming Poissonian statistics. The probability of detecting  $X$  bursts is

$$P(X|r, t) = \exp(-rt) \frac{(rt)^X}{X!}, \quad (3.4)$$

where  $r$  is the average rate and  $t$  is the duration of the observations. Alternatively, this probability can be calculated using Eq. 4.11 as a Weibull distribution is reduced to a Poissonian one when the Weibull shape parameter is equal to one. The probability of non-detection from FRB121102 is 22%. Based on the PAF observations, the 95%

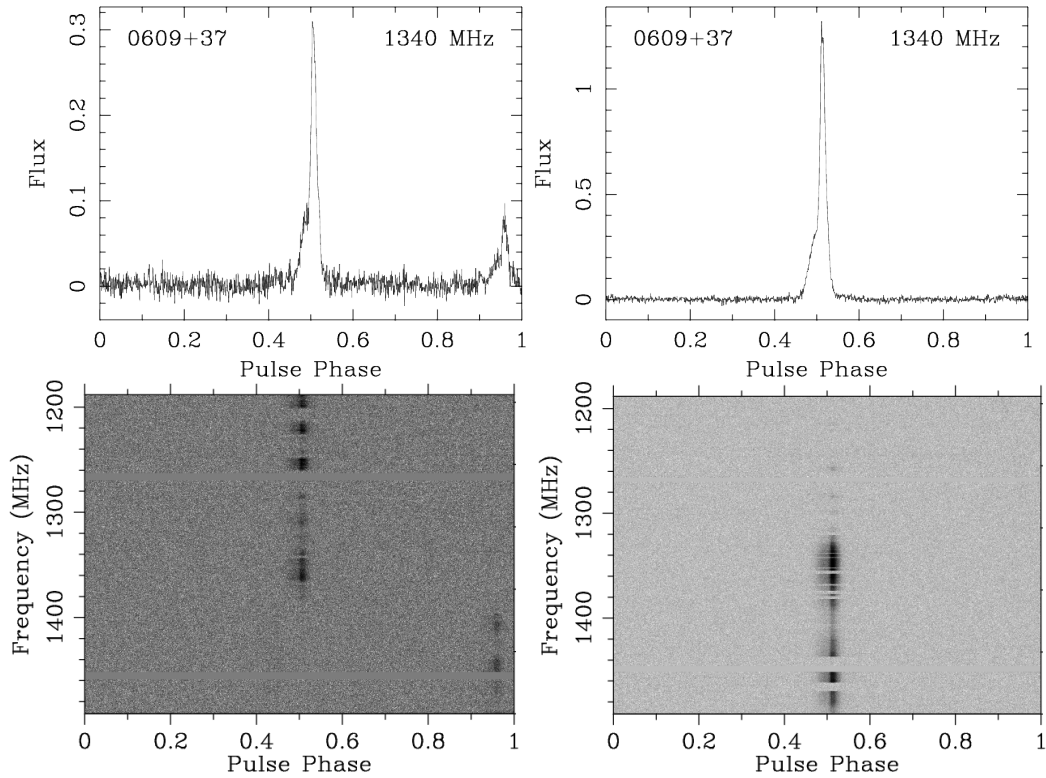


Figure 3.8: Folding of B0609+37 from observations at August 29th 2018 (left) and August 30th 2018 (right). *Top*: Folded profile. *Bottom*: Dedispersed dynamic spectrum. The left panels show a frequency misalignment in time. The right panels show the channels properly aligned in time after restarting the PAF backend.

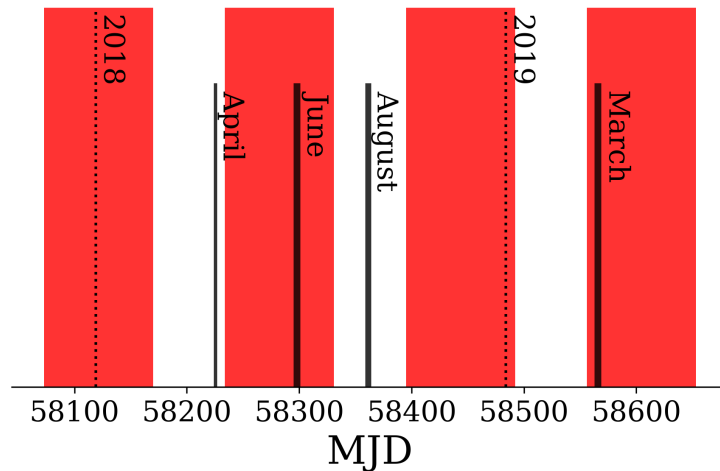


Figure 3.9: Active phases (red columns) of FRB121102 and the time of each PAF commissioning run (black lines, Tables 3.1–3.4) in MJD. Each run is labeled with the month it occurred. The dotted lines indicate the start of a calendar year.

confidence level (CL) FRB121102 burst rate UL is 4.1 bursts per day, and thus does not constrain the scaled rate. For the other FRB observations, the 95% CL burst rate ULs are calculated in the same way. All the FRB burst rate estimates are listed in Table 3.6.

On 29 March 2019, only a few days after the PAF observations, a burst from FRB180814.J0422+73 with an S/N of 11.7 was detected with CHIME<sup>3</sup>. This S/N can be translated to a PAF S/N using the radiometer equation (Eq. 2.3). The difference in observing frequencies between the PAF and CHIME also requires an assumption of an FRB spectral index (Eq. 1.7). Two spectral indices will be assumed here: similar to pulsars, i.e.  $\alpha = -1.5$  as well as a flat spectral index. An estimate of the sensitivity of CHIME is also required. Using CHIME detections from CHIME/FRB Collaboration et al. (2019c), the CHIME SEFD can be estimated to be roughly 80 Jy. The resulting PAF S/N is 1.3 for a spectral index of  $-1.5$ , and 4.4 for a flat spectral index. Both values lie well beneath the S/N threshold of the PAF single pulse search, meaning this burst could not have been detected with the PAF.

### 3.5.5 PRSs

For the PRSs, the analysis in §4.4 can be repeated, where two rates can be inferred from the PAF observations: a 95% CL burst rate UL based on the non-detections and a rate of an FRB121102-like source located at the observed target, scaled with respect to distance and receiver sensitivity difference. This analysis is done for the PAF observations of PTF10hgi in §4.4.2, where 4–7 bursts are expected on average from the observations and the scaled FRB121102 rate is excluded at the 99% CL. Analysis of the other PRSs, as well as NGC1569, SN2018COW, and GRB050826, is performed here. Instead of an on-phase rate, the FRB121102 rate is scaled from a total average from the aforementioned Effelsberg 7-beam survey of  $8 \pm 3$  bursts per day (Cruces et al., 2020). Again, an SEFD of 157 Jy and a bandwidth of 210 MHz is assumed. The luminosity distance, redshift, and inferred rates are given in Table 3.6.

The scaled rates of five PRSs are constrained by their 95% CL burst rate ULs (J1419+3940, J1622+3212, J2353+0758, J0927–0225, and J1025+1715). The hypothesis of an FRB121102-like source situated at each of these five PRSs and producing bursts above a fluence of  $1.9(w_{\text{ms}}/\text{ms})^{1/2}$  can thus be rejected at a 95% CL. One can see there is direct correlation between observing time and rejecting the scaled rate. All the PRSs are at similar redshifts, resulting in similar scaled rates. The observing time required to reject the scaled rates is therefore comparable between the PRSs, and based on the results here is roughly two hours.

The very high scaled rate of NGC1569 is also constrained by its burst rate UL. The reason for its scaled rate being so high arises from the luminosity distance scaling in Eq. 4.9. The difference in luminosity distance between FRB121102 and NGC1569 is roughly a factor of 400, resulting in a  $D_L$  factor of  $\sim 5 \times 10^4$  in Eq. 4.9. The FRB brightness distribution power-law index used here (and in §4.4) is  $\gamma = -0.91$  (James, 2019). With a flatter brightness distribution, i.e.  $\gamma$  closer to zero, the effects of the

<sup>3</sup>CHIME/FRB Public Database by the CHIME/FRB Collaboration: [chime-frb.ca](http://chime-frb.ca)

distance scaling would be drastically reduced. The burst rate of giant pulses (GPs) from the Crab pulsar (B0531+21) can also be scaled to NGC1569. Using survey values and  $\gamma = -2.8$  from Bera & Chengalur (2019) results in a PAF-scaled rate of  $\sim 10^{-12}$  GPs per day for a Crab-like pulsar in NGC1569. This shows that repeating FRBs are difficult to explain with Crab-like neutron stars, even when scaling to relatively nearby objects such as NGC1569. A flatter  $\gamma$  or a younger source with a higher absolute energy would be required in order to obtain more reasonable rates.

### 3.5.6 GC Pulsars

The observations of the GC magnetar J1745–2900 (Table 3.2) included observations of four other GC PSRs in the outer beams of the PAF: J1745–2910, J1746–2849, J1746–2850, and J1746–2856. The multi-beam data were folded at the period of each PSR using `dspsr` to see if a folded profile of any of the PSRs could be seen. None of the GC magnetar or PSRs were detected. The properties of the GC PSRs (Johnston et al., 2006; Deneva et al., 2009; Spitler et al., 2014b; Dexter et al., 2017a) can be used to estimate their expected S/N from the PAF observations. The scattering timescales of the GC PSRs are between 10–20% of their periods at the observed frequencies, and their scatter broadened widths result in an S/N of 24 for J1745–2900, 9–14 for J1746–2849, J1745–2850, and J1746–2856, and 4 for J1745–2910. The non-detection of the GC PSRs could thus be due to their expected low S/Ns and large scattering timescales in the PAF frequency band. Additionally, J1746–2850 is an intermittent source (Dexter et al., 2017b) and J1745–2910 has only been detected once (Deneva et al., 2009), so their non-detection is not surprising.

### 3.5.7 Future Outlook

Improvements can be made for future observations with the Effelsberg PAF. To be able to obtain polarisation data and to reveal burst structures at higher resolutions, a real-time search pipeline can be implemented to trigger baseband dumping. Efforts to reduce the system temperature, and consequently the SEFD, of the PAF will be important to improve its sensitivity.

Using the beamforming capabilities of the PAF to spatially reject RFI would vastly improve the observation data quality and reduce the number of false positive candidates. Another way to reduce false positive candidates would be to use the neural network candidate classifier `FETCH` (Agarwal et al., 2020), which bases its classification on frequency–time and DM–time images of candidates. `FETCH` can be implemented for both the real-time and offline searches. The beam mask value from `HEIMDALL`’s `coincider` can also be used in a more sophisticated way. From the beam mask one can tell from which beams a candidate was seen. Based on the beam setup, a list of allowed beam masks can be generated in order to reject candidates seen in distant beams.

Plenty of interesting observational possibilities exist for the Effelsberg PAF. FRB121102 and FRB180916.J0158+65 are probably the most clear examples (see §1.3

and §1.4). Their apparent periodicity can be investigated, and with baseband dumping their polarisation properties and burst structures can be scrutinised. The CHIME repeaters (CHIME/FRB Collaboration et al., 2019c) are poorly localised, but their localisation regions in most cases fit within the PAF FOV. These repeaters can thus be observed in order to further constrain their localisation regions, enabling further observations with more sensitive single-beam receivers or to localise them to their host galaxies with the European VLBI Network or the Karl G. Jansky Very Large Array. Galactic sources of interest are the GC PSRs. The beam pattern can be set in such a way that all of them can be observed simultaneously with the PAF, with one (or more) beam dedicated to each PSR. Of the GC PSRs, the most notable targets are the GC magnetar, PSR J1745-2900, to observe its rotation measure evolution (Eatough et al., 2013; Desvignes et al., 2018, see Chapter 5), and the elusive PSR J1745-2910, which has hardly been detected since its discovery (Deneva et al., 2009).

Continued commissioning work on the PAF is vital in order to have the infrastructure, knowledge, and software in place to provide a seamless transition to a cryogenically cooled PAF, should one be built for Effelsberg. Such a PAF will have a much higher sensitivity and SVS and could replace the 7-beam receiver at Effelsberg as the de facto 1.4 GHz receiver.



# Observing superluminous supernovae and long gamma ray bursts as potential birthplaces of repeating fast radio bursts

---

This chapter is based on an article titled “*Observing superluminous supernovae and long gamma ray bursts as potential birthplaces of repeating fast radio bursts*”, which is published in Monthly Notices of the Royal Astronomical Society, Volume 493, Issue 4, p.5170–5180, 2020<sup>1</sup>. The manuscript remains unchanged, but is formatted to fit the template of the thesis.

As the lead author of this publication, I have performed the Effelsberg observations, reduced and searched the entirety of the data, performed the analysis, and written the manuscript.

The full author list is **G. H. Hilmarsson**, L. G. Spitler, E. F. Keane, T. M. Athanasiadis, E. Barr, M. Cruces, X. Deng, S. Heyminck, R. Karuppusamy, M. Kramer, S. P. Sathyanarayanan, V. Ventakraman Krishnan, G. Wieching, J. Wu, and O. Wucknitz.

## 4.1 Abstract

Superluminous supernovae (SLSNe) and long gamma ray bursts (LGRBs) have been proposed as progenitors of repeating Fast Radio Bursts (FRBs). In this scenario, bursts originate from the interaction between a young magnetar and its surrounding supernova remnant (SNR). Such a model could explain the repeating, apparently non-Poissonian nature of FRB121102, which appears to display quiescent and active phases. This bursting behaviour is better explained with a Weibull distribution, which includes parametrisation for clustering. We observed 10 SLSNe/LGRBs for 63 hours, looking for repeating FRBs with the Effelsberg-100 m radio telescope, but have not detected any bursts. We scale the burst rate of FRB121102 to an FRB121102-like source inhabiting each of our observed targets, and compare this rate to our upper burst rate limit on a source by source basis. By adopting a fiducial beaming fraction of 0.6, we obtain 99.99% and 83.4% probabilities that at least one, and at least half of our observed sources are beamed towards us respectively. One of our SLSN targets, PTF10hgi, is coincident

---

<sup>1</sup>Available at [ui.adsabs.harvard.edu/abs/2020MNRAS.493.5170H/abstract](https://ui.adsabs.harvard.edu/abs/2020MNRAS.493.5170H/abstract)

with a persistent radio source, making it a possible analogue to FRB121102. We performed further observations on this source using the Effelsberg-100 m and Parkes-64 m radio telescopes. Assuming that PTF10hgi contains an FRB121102-like source, the probabilities of not detecting any bursts from a Weibull distribution during our observations are 14% and 16% for Effelsberg and Parkes respectively. We conclude by showing that a survey of many short observations increases burst detection probability for a source with Weibull distributed bursting activity.

## 4.2 Introduction

Fast Radio Bursts (FRBs) are bright, highly dispersed, millisecond-duration radio transients of unknown origin. Since their inaugural detection (Lorimer et al., 2007), close to 100 FRB discoveries have been published<sup>2</sup> (Petroff et al., 2016). FRBs are believed to be extragalactic due to their high dispersion measures (DM), which far exceed the expected Galactic DM contribution. This belief has strengthened as FRBs have been increasingly localized to host galaxies (Chatterjee et al., 2017; Bannister et al., 2019; Ravi et al., 2019; Prochaska et al., 2019; Marcote et al., 2020). While most FRBs detected so far have been single events, FRB121102 was the first to be seen to repeat (Spitler et al., 2016), and recently nine repeating FRBs have also been detected at CHIME (CHIME/FRB Collaboration et al., 2019a; The CHIME/FRB Collaboration et al., 2019). The repeating nature of some FRBs suggest that there are possibly two populations of FRBs, repeating and non-repeating.

FRB121102 has been localized to a host galaxy (Michilli et al., 2018a), and its host identified as a low-metallicity dwarf galaxy at a redshift of  $z = 0.1927$  (Tendulkar et al., 2017), with a stellar mass of  $M_* \sim 1.3 \times 10^8 M_\odot$  and a star formation rate of  $0.23 M_\odot$  per year (Bassa et al., 2017b). A compact persistent radio source with a projected size of  $< 0.7$  pc was detected alongside FRB121102 (Marcote et al., 2017) and was determined to be co-located to within a projected distance of  $< 40$  pc to the bursting source.

Evidence for coincidence between FRB121102 and the persistent radio source, along with the identification of the host galaxy, led to the suggestion of two types of progenitor models: a magnetar wind nebula containing a young magnetar, embedded within a supernova remnant (SNR) (Metzger et al., 2017); or a low luminosity active galactic nucleus (AGN) acting as the persistent radio source, with the bursting activity either originating from the AGN itself (Romero et al., 2016), or through interaction with a nearby neutron star (NS) (e.g. Zhang, 2018b). In the case of FRB121102, the AGN model was initially thought unlikely, as dwarf galaxies rarely contain AGNs, along with the fact that no evidence of an AGN in the optical spectrum was observed (Tendulkar et al., 2017). However, a recent survey has shown that AGNs can be found offset from the optical center of dwarf galaxies (Reines et al., 2020). Additionally, the recently observed large and decreasing rotation measures (RMs) of FRB121102 ( $\sim 10^5$  rad/m<sup>2</sup>) (Michilli et al., 2018a), have drawn analogies between the system and the Galactic

---

<sup>2</sup>[frbcat.org](http://frbcat.org)

center magnetar, J1745-2900 ( $\sim -65000$  rad/m<sup>2</sup>) and Sagittarius A\* system (Desvignes et al., 2018).

Supernovae occur from the collapse of massive stars into black holes (BHs) or NSs. In some rare cases the remnant BH or NS powers a relativistic jet into the circumstellar medium (Woosley, 1993), and internal shocks within these jets can produce long gamma-ray bursts (LGRBs) (Rees & Meszaros, 1994). Type-I superluminous supernovae (SLSNe) are a subclass of supernovae which are hydrogen poor, orders of magnitude more luminous, have shorter decay times than the typical Type-I supernovae, and have been postulated to be the precursor of LGRBs (Gal-Yam, 2019). The high luminosity is powered by a newly-born magnetar, where the magnetar spin-down rate is tied to the short decay time (Greiner et al., 2015). In addition to producing a fast-spinning NS with a strong magnetic field that could produce more luminous radio bursts than Galactic NSs, Type-I SLSNe and the resulting LGRBs also seem to occur more often in low-mass, low-metallicity galaxies (Fruchter et al., 2006; Perley et al., 2016). Type-I SLSNe and LGRBs can therefore explain the repeating nature of FRB121102 and its coincident persistent radio source. Note that throughout this paper, any mention of SLSNe is exclusively referring to Type-I SLSNe.

For FRB121102, the persistent radio source’s luminosity is consistent with a model of radio emission from an SNR which is powered by a young magnetar (Metzger et al., 2017). A radio burst could therefore originate from the magnetosphere of such a magnetar in a similar fashion to pulsar giant pulses (Cordes & Wasserman, 2016). Similarities in burst properties between FRB121102 and the Crab pulsar have been observed, although whether giant pulses from the Crab can be scaled to the energies of FRB121102 is unclear (see Hessels et al., 2019, and discussion therein). Alternatively, Metzger et al. (2019) have modelled FRBs as synchrotron maser emissions from within an SNR. In that scenario, a central engine releases ultrarelativistic particles which collide with a mildly relativistic magnetized ion-electron shell. The deceleration of the shell through forward shocks would then produce FRBs through a synchrotron maser mechanism. Metzger et al. (2019) illustrate both production of FRBs within a large frequency range, 0.1–10 GHz, and the apparently dormant and clustering phases of bursts observed from FRB121102.

Shortly after the explosion, an SNR is optically thick at radio frequencies, so radio bursts from an embedded magnetar cannot be detected. If the SNR is mainly ionized by the reverse shock, it can be probed at radio frequencies after a timescale of centuries (Piro, 2016). However, assuming that along with the reverse shock of the supernova ejecta, the SNR is photoionized from within by the magnetar, the SNR becomes optically thin at the frequency of the bursting emission after  $t \approx 10 \nu_{\text{GHz}}^{-2/5}$  yrs (Metzger et al., 2017). At 1.4 and 6 GHz,  $t$  is 8.7 and 4.9 yrs respectively, in the emitted frame.

In this work we have identified and observed nine SLSNe and LGRBs as suitable sources for a targeted repeating FRB search at high frequencies (5.3–9.3 GHz) with the Effelsberg 100-m Radio Telescope. The motivation for choosing this frequency range is that the SNR model allows for younger, and hence more, sources to be observable; and that FRB121102 has been observed to emit at these frequencies (Gajjar et al., 2018). We later added PTF10hgi to our 5.3–9.3 GHz survey and observed it during

commissioning time for the phased array feed (PAF) receiver at Effelsberg at 1.4 GHz and with the ultra wideband low (UWL) Parkes 64-m Radio Telescope receiver (0.7–4.0 GHz). This addition was made following the discovery of a radio source coincident with the SLSN PTF10hgi at 6 GHz with the VLA (Eftekhari et al., 2019). This is the first detection of a persistent radio source coincident with SLSNe/LGRBs, and it could be analogous to FRB121102’s persistent radio source. If an FRB were to be detected from PTF10hgi it would prove the theorised connection between FRBs and SLSNe/LGRBs. Additionally, the age of PTF10hgi was roughly nine years at the time of observing, so its SNR should be only recently optically thin at 1.4 GHz. With our wide range of frequencies we could potentially observe the optically thick-thin transition of the SNR.

Similar surveys have been performed recently: Law et al. (2019) observed 10 SLSN using the Karl G. Jansky Very Large Array (VLA) for 8.5 hrs at 3 GHz, where they managed to detect the persistent radio source of PTF10hgi in their radio image searching. Men et al. (2019) observed five LGRBs and one short GRB for 20 hrs using the Robert C. Byrd Green Bank Telescope (GBT) at 820 MHz and 2 GHz, and the Arecibo Radio Telescope at 1.4 GHz. Madison et al. (2019) observed six short GRBs, which originate from the merger of neutron stars and could leave behind a magnetar capable of producing repeating FRBs, for 20 hrs using the GBT at 2 GHz and Arecibo at 1.4 GHz. No FRBs were detected in these surveys.

### 4.3 Observations

Our observations were carried out using The Effelsberg 100-m Radio Telescope in Effelsberg, Germany; and The Parkes 64-m Radio Telescope in New South Wales, Australia. The receivers used at Effelsberg were the S45mm single pixel receiver, and the PAF; and at Parkes, the UWL receiver. These will be described in their respective subsections below.

The selection process for our targets was as follows. A list of SLSNe and LGRBs was gathered from the Open Supernova Catalog<sup>3</sup> (Guillochon et al., 2017) and the Swift GRB Catalog<sup>4</sup> with each source being older than five years, and at a maximum redshift of 0.4. The age cut-off was conservatively set to five years to include only SNRs which are optically thin in the observing band of the receiver. The redshift limit was set with respect to detections of FRB121102 at Effelsberg: By combining the radiometer equation (Dicke, 1946) and the brightness drop-off of the inverse square law, it follows that a detection with a signal to noise (S/N) of 40 at a redshift  $z = 0.2$  could be detected with a S/N of 10 at  $z = 0.4$  with the S45mm receiver.

The observed targets are listed in Table 4.1, and the complete list of observations can be found in Table 4.2. The range of our observations spans from June 2017 to September 2019. To reassure ourselves that the PAF system was working properly, we observed a test pulsar, B1612+07, for five minutes every hour during observations of

---

<sup>3</sup><https://sne.space>

<sup>4</sup>[https://swift.gsfc.nasa.gov/archive/grb\\_table.html](https://swift.gsfc.nasa.gov/archive/grb_table.html)

PTF10hgi. To detect it we folded the test pulsar data using `dspsr` from the pulsar analysis software library `psrchive`<sup>5</sup>. For 42.3 of our total 63 observing hours, we observed our original nine targets with the S45mm receiver for 1–2 hrs each time with a  $\sim 5$  month cadence. We observed PTF10hgi for 5.3 hrs, split into two observations of roughly 2.5 hrs each spaced a month apart with the S45mm receiver; for 13 hrs with the PAF receiver for 1.5–4 hrs each day for four days; and for 2.3 hours over three observations with the UWL spaced across six months. The strategy of multiple short observations was motivated by the apparent clustering of bursts from FRB121102 (Oppermann et al., 2018).

The total DMs of our potential radio sources can be broken down into individual contributions by various components

$$DM = DM_{\text{MW}} + DM_{\text{MWhalo}} + DM_{\text{IGM}} + DM_{\text{host}}, \quad (4.1)$$

where  $DM_{\text{MW}}$  and  $DM_{\text{MWhalo}}$  are the DM contribution of the Milky Way (MW) and its halo, respectively,  $DM_{\text{IGM}}$  is the contribution of the intergalactic medium (IGM), and  $DM_{\text{host}}$  is the contribution of the host galaxy and the local environment of the source. The  $DM_{\text{MW}}$  varies between different lines of sight (LoS), but in general does not exceed  $100 \text{ pc cm}^{-3}$  for LoSs away from the Galactic plane, which is the case for most of our targets. Using the Galactic electron density model YMW16 (Yao et al., 2017), we obtain  $DM_{\text{MW}}$  values between 22 and  $143 \text{ pc cm}^{-3}$  for our targets. We assume a  $DM_{\text{MWhalo}}$  value of  $50\text{--}80 \text{ pc cm}^{-3}$  (Prochaska & Zheng, 2019). To estimate the  $DM_{\text{IGM}}$  we use the relation  $z \sim DM/855 \text{ pc cm}^{-3}$  (Zhang, 2018a) resulting in a  $DM_{\text{IGM}}$  range of  $66\text{--}311 \text{ pc cm}^{-3}$ . The estimated  $DM_{\text{IGM}}$  from recent FRB localisations are in agreement with this relation (Bannister et al., 2019; Ravi et al., 2019). Note that LoS variations might vary from  $100$  to  $250 \text{ pc cm}^{-3}$  for  $DM_{\text{IGM}}$  for our redshift range depending on models for halos' gas profile of ionized baryons (McQuinn, 2014, Fig. 1, bottom panel). The  $DM_{\text{host}}$  component can vary between FRB progenitor models, types of host galaxies and local environments, orientation of the host galaxy, and the LoS to the source through its host (Walker et al., 2018). The  $DM_{\text{host}}$  estimate for FRB121102 is in the range of  $55\text{--}225 \text{ pc cm}^{-3}$  (Tendulkar et al., 2017). Using this range for our  $DM_{\text{host}}$ , the estimated total DM of our targets falls in the range of  $220\text{--}700 \text{ pc cm}^{-3}$ .

### 4.3.1 S45mm receiver

The S45mm receiver is located in the secondary focus of The Effelsberg Telescope, and yields 4 GHz of bandwidth between either 4–8 GHz or 5.3–9.3 GHz. The receiver has an SEFD of 18 Jy. All the observations made using this receiver in this work are in the 5.3–9.3 GHz mode, except for the observations of PTF10hgi, which were taken in the 4–8 GHz mode. The data are recorded with full Stokes using two ROACH2 backends, each capturing 2 GHz of the band, with a  $131 \mu\text{s}$  sampling rate, and a  $0.976562 \text{ MHz}$  channel bandwidth across 4096 channels. The resultant data are in a

<sup>5</sup><http://psrchive.sourceforge.net/>

Table 4.1: Properties of the observed SLSNe/LGRBs. *From left to right:* Source name, discovery date, right ascension (RA) and declination (DEC) in J2000 coordinates, sources redshift ( $z$ ), the type of source, i.e. whether it's an LGRB or SLSN, and the average estimated total DM ( $\text{pc cm}^{-3}$ ).

Source name	Discovery date	RA	DEC	$z$	Type	DM [ $\text{pc cm}^{-3}$ ]
GRB050826	2005/08/26	05 <sup>h</sup> 51 <sup>m</sup> 02.6 <sup>s</sup>	-02°39'28.8''	0.297	LGRB	600
GRB051109B	2005/11/09	23 <sup>h</sup> 01 <sup>m</sup> 52.6 <sup>s</sup>	+38°39'46.8''	0.080	LGRB	330
GRB111225A	2011/11/25	00 <sup>h</sup> 52 <sup>m</sup> 37.9 <sup>s</sup>	+51°34'22.8''	0.297	LGRB	590
PTF09cnd	2009/08/07	16 <sup>h</sup> 12 <sup>m</sup> 08.94 <sup>s</sup>	+51°29'16.1''	0.258	SLSN	450
PTF10uhf	2010/08/05	16 <sup>h</sup> 52 <sup>m</sup> 47 <sup>s</sup>	+47°36'21.76''	0.288	SLSN	480
PTF10bjp	2010/01/09	10 <sup>h</sup> 06 <sup>m</sup> 34 <sup>s</sup>	+67°59'19.0''	0.358	SLSN	550
SN2010gx	2010/03/13	11 <sup>h</sup> 25 <sup>m</sup> 46.71 <sup>s</sup>	-08°49'41.4''	0.230	SLSN	430
PTF12dam	2012/04/10	14 <sup>h</sup> 24 <sup>m</sup> 46.20 <sup>s</sup>	+46°13'48.3''	0.107	SLSN	320
LSQ12dlf	2012/07/10	01 <sup>h</sup> 50 <sup>m</sup> 29.8 <sup>s</sup>	-21°48'45''	0.250	SLSN	440
PTF10hgi	2010/05/15	16 <sup>h</sup> 37 <sup>m</sup> 47 <sup>s</sup>	+06°12'32.3''	0.099	SLSN	330

Table 4.2: List of observations in a chronological order for each source. *From left to right*: Source name, the dates and starting times for each observation (in UTC and MJD), observation duration, and the frequency range of the observation.

Source name	UT Date	UTC	MJD	Dur. [min]	Frequency [GHz]
GRB050826	20170630	11:18:41	57934.47131	58	5.3–9.3
GRB050826	20171128	22:21:04	58085.93130	147	5.3–9.3
GRB050826	20180330	16:31:30	58207.68854	120	5.3–9.3
GRB050826	20181023	00:46:50	58414.03252	60	4.6–5.1
GRB050826	20181023	04:08:30	58414.17257	60	4.6–5.1
GRB051109B	20171128	16:03:34	58085.66194	120	5.3–9.3
GRB051109B	20180330	09:23:50	58207.39155	90	5.3–9.3
GRB051109B	20181022	17:00:20	58413.70856	60	4.6–5.1
GRB111225A	20171128	18:12:54	58085.75896	120	5.3–9.3
GRB111225A	20180330	11:06:51	58207.46309	46	5.3–9.3
GRB111225A	20180330	18:35:50	58207.77488	51	5.3–9.3
GRB111225A	20181022	18:12:00	58413.75833	60	5.3–9.3
PTF09cnd	20170630	13:21:01	57934.55626	48	5.3–9.3
PTF09cnd	20180330	05:11:30	58207.21632	120	5.3–9.3
PTF09cnd	20181022	22:37:30	58413.94271	60	4.6–5.1
PTF10uhf	20170630	15:17:01	57934.63682	55	5.3–9.3
PTF10uhf	20180330	07:17:50	58207.30405	120	5.3–9.3
PTF10uhf	20181022	21:36:40	58413.90046	60	4.6–5.1
PTF10bjp	20170630	12:27:31	57934.51911	48	5.3–9.3
PTF10bjp	20171129	01:26:14	58086.05988	120	5.3–9.3
PTF10bjp	20180330	01:01:20	58207.04259	120	5.3–9.3
PTF10bjp	20180330	14:08:10	58207.58900	18	5.3–9.3
PTF10bjp	20181022	19:31:50	58413.81377	60	4.6–5.1
SN2010gx	20171129	04:41:44	58086.19565	14	5.3–9.3
SN2010gx	20180329	22:57:00	58206.95625	120	5.3–9.3
PTF12dam	20170630	14:23:11	57934.59943	50	5.3–9.3
PTF12dam	20171129	03:38:04	58086.15144	60	5.3–9.3
PTF12dam	20180330	03:09:40	58207.13171	120	5.3–9.3
PTF12dam	20181022	20:35:00	58413.85764	60	4.6–5.1
LSQ12dlf	20171128	20:17:54	58085.84576	120	5.3–9.3
LSQ12dlf	20180330	12:01:00	58207.50069	120	5.3–9.3
LSQ12dlf	20181022	23:43:40	58413.98866	60	4.6–5.1
PTF10hgi	20190205	18:48:31	58519.78369	42	0.7–4
PTF10hgi	20190210	02:24:52	58524.10060	155	4–8
PTF10hgi	20190220	20:15:55	58534.84439	44	0.7–4
PTF10hgi	20190308	01:14:42	58550.05187	160	4–8
PTF10hgi	20190323	23:54:29	58565.99618	216	1.222–1.452
PTF10hgi	20190324	22:54:32	58566.95454	236	1.222–1.452
PTF10hgi	20190325	23:18:01	58567.97085	90	1.222–1.452
PTF10hgi	20190326	23:11:26	58568.96627	236	1.222–1.452
PTF10hgi	20190830	05:05:15	58725.21198	55	0.7–4

Distributed Acquisition and Data Analysis (DADA) format<sup>6</sup>, from which Stokes  $I$  is extracted.

During the observaion on 22nd October 2018, a problem occurred with the S45mm receiver, resulting in poor attenuation levels making the receiver temporarily inoperable, and the use of a different receiver was needed. The S60mm receiver on Effelsberg was used instead, with 500 MHz of bandwidth at 4.6–5.1 GHz, 82  $\mu$ s sampling rate, 512 channels with 0.976562 MHz bandwidth, and an SEFD of 18 Jy. The data are recorded as sub-banded SIGPROC<sup>7</sup> filterbanks, which are a stream of n-bit numbers corresponding to multiple polarization and/or frequency channels over time, and are concatenated before processing.

### 4.3.2 PAF receiver

The Effelsberg PAF (Deng et al., 2018) is a dense array of antenna elements installed at the telescope’s primary focus, adapted from the models used by ASKAP (Hay & O’Sullivan, 2008; Johnston et al., 2008). Its 188 elements form a checkerboard shape over a 1.2 m diameter circle and the output of these elements are combined to form beams, controlled by varying the element weights.

In its current state, the Effelsberg PAF can produce 22 beams, with 230 MHz of bandwidth centered at 1337 MHz, and an SEFD of 34 Jy. Currently the data are recorded and stored on disk as total intensity DADA files with 512 channels of 0.449074 MHz bandwidth each, and a 216  $\mu$ s sampling time. The data can also be recorded as baseband data. This will be used in future surveys for real-time processing, where we will use the raw voltage data captured from a ring buffer to create full Stokes files with significantly higher frequency and time resolutions than our standard filterbanks.

### 4.3.3 UWL receiver

The UWL receiver (Dunning et al., 2015) is a wideband receiver at the Parkes telescope with an SEFD of 25 Jy. It has a bandwidth of 3.3 GHz, ranging from 0.7 to 4 GHz. The data were recorded in two different modes with the MEDUSA backend: full Stokes, with a sampling time of 1024  $\mu$ s and a channel bandwidth of 2 MHz across 1664 channels for the first observation; and Stokes  $I$ , with a sampling time of 256  $\mu$ s and 0.5 MHz channel bandwidth across 6656 channels for the latter two observations. The 256  $\mu$ s data were downsampled by a factor of four for consistency and to reduce computation time during analysis. The data are in a Pulsar Flexible Image Transport System (PSRFITS) format (Hotan et al., 2004).

### 4.3.4 Data processing

All data products are initially converted to SIGPROC filterbank format before being processed. For the S45mm, S60mm, and UWL data, the PRESTO<sup>8</sup> (Ransom, 2011)

---

<sup>6</sup><http://psrdada.sourceforge.net>

<sup>7</sup><http://sigproc.sourceforge.net>

<sup>8</sup>[github.com/scottransom/presto](https://github.com/scottransom/presto)

software package was used for single pulse searching. We used PRESTO’s `rfifind` to identify radio frequency interference (RFI) in the data and create an RFI mask to apply to the data. The data were dedispersed from 0–2000 pc cm<sup>−3</sup> in steps of 2 pc cm<sup>−3</sup> for the S45mm and S60mm data, and in steps of 1 pc cm<sup>−3</sup> for the UWL data, and subsequently searched for single pulses using PRESTO’s `single_pulse_search.py` with a S/N threshold of 7.

PRESTO searches for single pulses by dedispersing the data and convolving the dedispersed time series with boxcar filters of varying widths to optimise the S/N. PRESTO uses a pre-determined list of boxcar widths to use, so by setting a maximum candidate width, PRESTO will search using boxcars up to that width. We search up to the nearest boxcar width of 20 ms, which is 19.6 ms. We set this limit as FRBs tend not to have widths greater than a few ms at our observed frequencies, and 20 ms is roughly the DM sweep in the S45mm band for the lower limit of the estimated DMs of our targets.

We also compute the spectral modulation index of the candidates, which evaluates the fractional variation of a candidate across its spectrum and distinguishes narrowband RFI from broadband signals (Spitler et al., 2012). The candidate’s modulation index,  $m_I$ , is calculated as the normalized standard deviation of intensity across frequency, and must be below the modulation index threshold,

$$m_{I,\text{threshold}} = \frac{\sqrt{N_\nu}}{(S/N)_{\text{min}}}, \quad (4.2)$$

where  $N_\nu$  is the number of frequency channels, and  $(S/N)_{\text{min}}$  is the signal to noise threshold applied to the data. The candidates were then plotted and analysed by eye with a DM over time plot with marker sizes increasing with S/N. Promising candidates were further inspected using PRESTO’s `waterfall.py` plotting tool, which shows the the candidate’s dynamic spectrum and can be downsampled and subbanded at will.

For the PAF data, the GPU based single pulse search software HEIMDALL<sup>9</sup> was used. This was done to handle the vast amount of multibeam data taken, and to exploit HEIMDALL’s coincidenting capabilities. HEIMDALL’s single pulse searching uses the same convolution method as PRESTO, but achieves much greater processing speeds by utilising GPUs rather than CPUs. For the Effelsberg PAF, every frequency channel is calibrated independently, and channels affected by RFI stronger than the calibration source have undefined pointing positions, resulting in so-called badly beamformed channels. A considerable portion of the channels in the PAF data needed to be zapped during the processing due to both badly beamformed channels, and channels persistently contaminated with RFI. These channels amounted to 89 MHz, or 39% of the PAF band, and were flagged to be ignored by HEIMDALL. The data were dedispersed from 0–2000 pc cm<sup>−3</sup>. The DM steps in HEIMDALL are determined by the pulse broadening induced by the size of the DM step, so each DM trial is a function of the previous DM value and the data parameters (Levin, 2012). An initial detection threshold of S/N = 7 was applied. HEIMDALL groups candidates which are close in DM and time, and the group’s candidate with the highest S/N is the candidate given by HEIMDALL.

<sup>9</sup>[sourceforge.net/projects/heimdall-astro](https://sourceforge.net/projects/heimdall-astro)

This multi-beam data needed to be coincided in order to identify false candidates appearing across many beams simultaneously, so the single pulse candidates were ran through HEIMDALL’s coincidencer. The candidates were then sifted further in order to reduce the large number of false positives with low DMs and large widths: an increased S/N threshold of 8, a low DM threshold of 20 pc cm<sup>-3</sup>, and a maximum candidate width of 28 ms were applied. In addition, candidates detected in multiple beams go through further sifting. By taking the beam with the strongest S/N as the reference point, the other beam detections need to occur within the adjacent beams for the candidate to pass the sifting. The remaining candidates were then run through our own plotting tool<sup>10</sup> which plots dedispersed time series, dynamic spectrum, and a dedispersed dynamic spectrum. The dynamic spectra can also be downsampled and subbanded by factors of our choosing. These plots were then inspected by eye.

We are aware of potential difficulties due to the DM sweep across the 4–8 GHz band. For a DM of 500 pc cm<sup>-3</sup> the sweep is 50 ms, so a narrowband signal might be difficult to distinguish from zero-DM RFI. At the start of each observation we do however observe the pulsar B0355+54, which has a DM of 57 pc cm<sup>-3</sup>, and are able to detect its single pulses.

## 4.4 Results & Analysis

From the 63 hours of observational data, we have not detected any single pulses from any of the sources observed above our fluence limits of 0.04 ( $w_{\text{ms}}/\text{ms}$ )<sup>1/2</sup> Jy ms for the S45mm receiver, 0.53 ( $w_{\text{ms}}/\text{ms}$ )<sup>1/2</sup> Jy ms for the PAF receiver, and 0.07 ( $w_{\text{ms}}/\text{ms}$ )<sup>1/2</sup> Jy ms for the UWL receiver, for burst widths of  $w_{\text{ms}}$  ms.

Assuming Poissonian statistics, we can estimate the upper-limit to the rate of bursts emitted above our detection threshold on a source-by-source basis (Gehrels, 1986, Table 1). We also estimate the burst rate of an FRB121102-like source from each of the SLSNe/LGRBs observed. The C-band results from the observed SLSNe/LGRBs and the PTF10hgi results with the PAF and UWL receivers are shown in their respective following subsections.

To estimate the rate of an FRB121102-like source at different locations we make use of a brightness distribution power-law,

$$R = R_0 \left( \frac{E}{E_0} \right)^\gamma, \quad (4.3)$$

where  $R$  and  $E$  are the rate and energy, respectively,  $R_0$  and  $E_0$  are values for a reference source, and  $\gamma$  is the FRB brightness distribution power-law index. Here we use  $\gamma = -0.91 \pm 0.17$  as estimated by James (2019) independently of instrumental sensitivity by combining the multi-telescope observing campaign of FRB121102 (1.4 and 3 GHz, Law et al., 2017) and the GBT BL observations (6 GHz, Gajjar et al., 2018). An index of  $\gamma = -1.8 \pm 0.3$  was obtained by Gourdji et al. (2019) from 41 FRB121102 bursts at 1.4 GHz using Arecibo. These values of  $\gamma$  are inconsistent with each other, potentially

<sup>10</sup>[github.com/ghenning/PAFcode](https://github.com/ghenning/PAFcode)

due to Arecibo’s survey probing unprecedentedly low burst energies of FRB121102, or its high sensitivity (Gourdji et al., 2019). We choose  $\gamma = -0.91 \pm 0.17$  because the sensitivity of Effelsberg is closer to GTB and VLA than Arecibo, and this value is partially derived from detections in C-band.

The rate calculation also requires a relation between fluence and energy of a transient, considered specifically for the case of FRBs as Macquart & Ekers (2018)

$$F(\nu) = \frac{(1+z)^{2+\alpha}}{\Delta\nu_{\text{FRB}}} \frac{E}{4\pi D_L^2}, \quad (4.4)$$

where  $\Delta\nu_{\text{FRB}}$  is the intrinsic bandwidth of an FRB,  $z$  is the source’s redshift,  $\alpha$  is the spectral index,  $E$  is the total energy of a burst, and  $D_L$  is the luminosity distance to the bursting source. The spectral index for FRBs is not well constrained, and given the absence of information we assume a flat spectrum with  $\alpha = 0$  negating the need for a k-correction. James (2019) argues that Eq. 4.4 applies for bursts more broadband than the observing bandwidth. Bursts from FRB121102 have smaller fractional bandwidth (Hessels et al., 2019, Fig. 1), so Eq. 4.4 can be written as the observed fluence averaged across the observing band,  $\Delta\nu$ , (James, 2019, Eq. 8)

$$F = \frac{(1+z)}{\Delta\nu} \frac{E}{4\pi D_L^2}. \quad (4.5)$$

We can then estimate the rate of bursts from FRB121102-like sources located at different luminosity distances/redshifts, for surveys with different sensitivities by combining eqs. 4.3 and 4.5:

$$R = R_0 \left(\frac{F}{F_0}\right)^\gamma \left(\frac{1+z_0}{1+z}\right)^\gamma \left(\frac{D_L}{D_{L,0}}\right)^{2\gamma} \left(\frac{\Delta\nu}{\Delta\nu_0}\right)^\gamma, \quad (4.6)$$

with the subscripts of 0 being the values for FRB121102, and  $F_0$  being the fluence limit.

#### 4.4.1 C-band observations of SLSNe/LGRBs

The 95% confidence level (CL) upper-limit to the burst rates we obtain from our observations, assuming Poissonian statistics, are in the range of 0.4–1.4 bursts/hr and are shown in Table 4.3 and Fig. 4.1.

Observing campaigns of FRB121102 at high frequencies have reported various average burst rates. Gajjar et al. (2018) reported 21 detections in a single 6 hr observation at the Green Bank Telescope (GBT) using the 4–8 GHz Breakthrough Listen (BL) Digital Backend. Spitler et al. (2018) have three detections in 22 hrs with the 4.6–5.1 GHz, S60mm receiver at Effelsberg in an observing campaign spanning 4 months.

We also have obtained a rate of  $0.012_{-0.010}^{+0.027}$  bursts/hr ( $1\sigma$  error)<sup>11</sup> from an ongoing campaign using the 4–8 GHz, S45mm receiver at Effelsberg (Hilmarsson et al., 2020a). In that campaign, which yields a single detection from 86 hrs of observations spanning

<sup>11</sup>All uncertainties in burst rates reported here are  $1\sigma$  errors.

two years, FRB121102 is observed for 2–3 hours at a time with a roughly two week cadence (with gaps due to telescope/receiver maintenance). This rate is more robust than previously reported rates in the sense that it is a long-term average consisting of multiple observations, and does not depend on a single bursting phase. It is also obtained using the same observational setup as in this work.

Using the burst rate of FRB121102 from Hilmarrsson et al. (2020a) of  $0.012_{-0.010}^{+0.027}$  bursts/hr, we estimate the burst rate of an FRB121102-like source located at each of the SLSNe/LGRBs observed. Since we are working with the same observational setup and identical bursts at different locations, we can simplify Eq. 4.6 by setting  $(F/F_0)^\gamma$  and  $(\Delta\nu/\Delta\nu_0)^\gamma$  to 1:

$$R = R_0 \left( \frac{1+z_0}{1+z} \right)^\gamma \left( \frac{D_L}{D_{L,0}} \right)^{2\gamma}. \quad (4.7)$$

The hypothetical rate of an FRB121102-like source located at our sources of interest can be found in Table 4.3, and is shown in Fig. 4.1. There we have also estimated the number of bursts we would have expected to see from an FRB121102-like source during our observations, as well as how long we need to observe each source without a detection in order to constrain our estimated rates, i.e. the observation time required for the upper limit to the rate to reach the scaled rate.

The scaled rates from FRB121102 are influenced by the difference in luminosity distance between FRB121102 and the SLSNe/LGRBs, yet they do fall within the  $1\sigma$  range of FRB121102’s rate at C-band. This also implies that the time needed to constrain the scaled rates reaches impractical observation times for most of the sources (upwards of 300 hours). However, three of our sources, GRB051109B, PTF12dam, and PTF10hgi, have luminosity distances less than FRB121102, and therefore have a higher scaled rate than FRB121102. Since no bursts were detected in this work, constraining the scaled rates of these three sources is quite a feasible task for further surveys.

#### 4.4.2 PAF & UWL observations of PTF10hgi

We repeat the analysis from the previous section for the 13 hrs of PTF10hgi data taken with the PAF and the 2.3 hrs taken with the UWL. In order to do so, we use the rate from a recent FRB121102 survey (28 bursts in 116 hrs) performed at L-band using the P217mm 7-beam (SEFD = 17 Jy) receiver at the Effelsberg telescope. The average burst rate is  $0.24_{-0.05}^{+0.06}$  bursts/hr above a fluence of  $0.14 (w_{\text{ms}}/\text{ms})^{1/2}$  Jy ms (Cruces et al., 2020).

This rate must to be scaled to the PAF and UWL receivers, which we do using Eq. 4.6. For the factor of  $(F/F_0)^\gamma$  we use the radiometer equation (Dicke, 1946)

$$F = \frac{\text{SEFD S/N}}{\sqrt{n_p \Delta\nu}} \sqrt{w}, \quad (4.8)$$

where SEFD is the system equivalent flux density, S/N is the signal to noise,  $n_p$  is the number of polarizations,  $\Delta\nu$  is the receiver bandwidth, and  $w$  is the burst width. The

Table 4.3: Results from the burst rate analysis of the observed sources. *From left to right:* The observing band, source name, total observing time ( $T_{\text{obs.}}$ ), 95% confidence (CL) upper rate limit ( $R_{\text{UL}}$ ), luminosity distance ( $D_L$ ), the scaled burst rate from an FRB121102-like source ( $R_{\text{FRB121102}}$ ), the expected number of bursts from our observations based on the scaled rates ( $N_{\text{exp.}}$ ), and the observing time required to constrain the scaled rate ( $T_{\text{constr.}}$ ; i.e. the time needed for the 95% CL upper rate limit to reach the scaled rate). The luminosity distance and burst rate of FRB121102 are added for reference. *Top:* S45mm receiver results. *Center:* PAF receiver results. *Bottom:* Parkes UWL results.

Obs. band [GHz]	Source name	$T_{\text{obs}}$ [hr]	$R_{\text{UL}}$ [ $\text{hr}^{-1}$ ]	$D_L$ [Mpc]	$R_{\text{FRB121102}}$ [ $\text{hr}^{-1}$ ]	$N_{\text{exp}}$	$T_{\text{constr}}$ [hr]
	FRB121102	-	-	950	$0.012^{+0.027}_{-0.010}$	-	-
	GRB050826	7.4	0.41	1550	0.01	0.04	582
	GRB051109B	4.5	0.67	370	0.06	0.27	50
	GRB111225A	4.6	0.65	1550	0.01	0.02	582
	PTF09cnd	3.8	0.79	1320	0.01	0.03	447
4-8	PTF10uhf	3.9	0.77	1500	0.01	0.02	550
	PTF10bjp	6.1	0.49	1930	0.01	0.02	831
	SN2010gx	2.2	1.4	1150	0.01	0.02	358
	PTF12dam	4.8	0.62	500	0.03	0.17	85
	LSQ12dlf	5	0.60	1270	0.01	0.04	420
	PTF10hgi	5.3	0.57	460	0.04	0.21	73
1.2-1.4	FRB121102	-	-	950	$0.11^{+0.04}_{-0.03}$	-	-
	PTF10hgi	13.0	$0.41^{\text{a}}$	460	$0.4^{+0.1}_{-0.1}$	5	$14^{\text{a}}$
0.7-4.0	FRB121102	-	-	950	$0.62^{+0.33}_{-0.28}$	-	-
	PTF10hgi	2.3	$2.26^{\text{a}}$	460	$2.2^{+0.5}_{-0.5}$	5	$3^{\text{a}}$

<sup>a</sup>99.5% CL upper-limit.

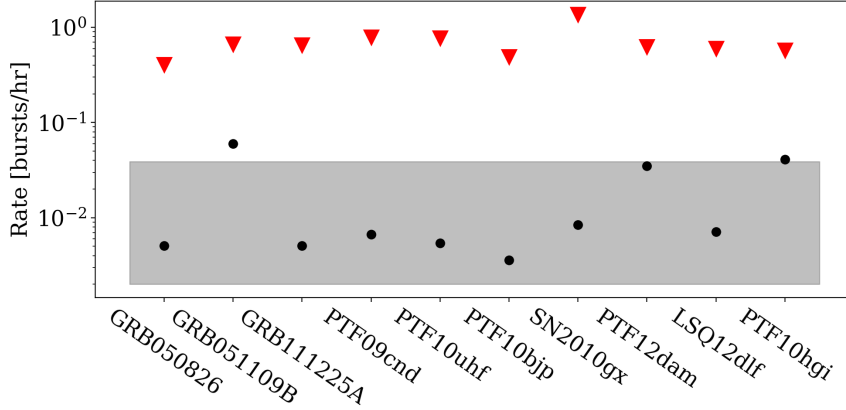


Figure 4.1: Scaled burst event rates of the observed sources at C-band. *Gray bar*:  $1\sigma$  burst event rate range of FRB121102 at C-band. *Black dots*: Scaled burst event rate of an FRB121102-like source located at our SLSNe/LGRBs targets. *Red arrows*: 95% CL upper limit rates based on the non-detection of our observations.

rate conversion from Eq. 4.6 then becomes

$$R = R_0 \left( \frac{\text{SEFD}}{\text{SEFD}_0} \right)^\gamma \left( \frac{\Delta\nu}{\Delta\nu_0} \right)^{\gamma/2} \left( \frac{1+z_0}{1+z} \right)^\gamma \left( \frac{D_L}{D_{L,0}} \right)^{2\gamma}, \quad (4.9)$$

where the last two bracketed terms are equal to 1 when converting rates for the same source. The FRB121102 burst rate scaled to the PAF and UWL receivers is  $0.11_{-0.03}^{+0.04}$  bursts/hr above  $0.53 (w_{\text{ms}}/\text{ms})^{1/2}$  Jy ms, and  $0.62_{-0.28}^{+0.33}$  bursts/hr above  $0.07 (w_{\text{ms}}/\text{ms})^{1/2}$  Jy ms respectively. Note that we are scaling burst energies to different observing bandwidths, so under the assumption that  $R(E)$  does not depend on the central frequency of the observing bandwidth we add an additional term of  $(\Delta\nu/\Delta\nu_0)$  to Eq. 4.9 when scaling from the P217mm receiver to the PAF and UWL receivers.

The resulting rate, obtained by using Eq. 4.9, for an FRB121102-like source located at PTF10hgi is  $0.4_{-0.1}^{+0.1}$  bursts/hr for the PAF receiver, and  $2.2_{-0.5}^{+0.5}$  bursts/hr for the UWL receiver. From the 13 hour observations with the PAF, we would have expected to detect 4–7 bursts on average by assuming this rate. We exclude this rate at the 99% confidence level for such a source inhabiting PTF10hgi. Likewise, for the 2.3 hour observations with the UWL receiver we would have expected 4–6 bursts on average, and exclude this rate at the 99% confidence level. The results are shown in the bottom section of Table 4.3 and in Fig. 4.2.

The fact that we do not detect any bursts and rule out the rate of an FRB121102-like source with a Poissonian distributed bursting activity inhabiting PTF10hgi can be interpreted in various ways: *i)* The most straightforward reason is that PTF10hgi simply does not contain a repeating FRB source, or at the very least not a source as active as FRB121102, as FRB121102 might be an abnormally active bursting source (e.g. Palaniswamy et al., 2018). *ii)* The assumption that FRBs are related to young magnetars within SNRs might not be correct. *iii)* The FRB121102-like source may

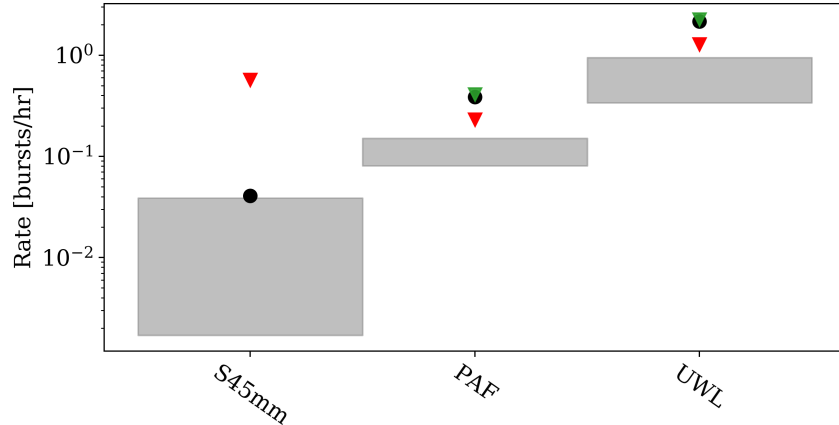


Figure 4.2: Scaled burst event rates of PTF10hgi for different receivers. *Gray bars*:  $1\sigma$  burst event rate range of FRB121102 at receiver. *Black dots*: Scaled burst event rate of an FRB121102-like source located at PTF10hgi. *Red/Green arrows*: 95/99.5% CL upper limits to the rates.

have been observed during a quiescent state, so no bursts were emitted during our observations. If this were the case, it would directly imply that the bursting activity of the source is non-Poissonian. *iv*) PTF10hgi’s age was roughly nine years at the time of the observations, so the SNR could be at the threshold of being optically thin at 1.4 GHz (Metzger et al., 2017). The SNR could simply still be opaque at 1.4 GHz, meaning that we cannot observe emitted bursts at that frequency, given that the emission has to travel through the SNR. *v*) The emission might be beamed and the bursts were not beamed towards us at the time of observing, so we were unable to detect bursts from the source.

#### 4.4.3 Beaming fraction

Emission mechanisms that generate luminous radio emissions are generally beamed, so a beaming fraction for our model should be taken into consideration. The beaming fraction,  $f$ , is the fraction of the celestial sky covered by the radio beam, and in the case of rotation it is how much is covered during a single rotation.

The coherent emission process by a single unit (particle or bunch of particles) has a beaming opening angle of  $1/\gamma_p$ , where  $\gamma_p$  is the Lorentz factor of the unit. Cordes & Chatterjee (2019) discuss three possibilities of FRB beaming geometries. First is a relativistic jet comprised of emission from multiple incoherent units, and whose beaming is thus much greater than from the coherent emission of a single unit. Second is a relativistic jet rotating around an axis, where the beam sweeps out an annulus shaped area during each revolution, similar to pulsars. Third is quasi-isotropic emission from a spherical shell.

Within the magnetar model framework, two distinct locations of emission have been discussed in the literature: a synchrotron maser mechanism from relativistic shocks in

the material surrounding the magnetar (Lyubarsky, 2014; Beloborodov, 2017), and pulsar-like emission in the magnetosphere (Kumar et al., 2017; Yang & Zhang, 2018). Metzger et al. (2019) model a synchrotron maser in a baryon-loaded shell that can produce bursts over the full area of the SNR, relating to the aforementioned third beaming geometry. The geometric probability of having a burst pointed towards an observer is therefore 1. Similarly, Beloborodov (2019) proposes that FRBs are produced in an electron-positron plasma in the helical-B winds of a rotating magnetar, where the geometric probability is on the order of  $\pi$  steradians over the celestial sphere. The lower limit to the beaming fraction of a burst is  $1/\gamma_p^2$  for a single emitting unit. If multiple units are emitting, then the beaming fraction of a single FRB follows the first beaming scenario previously described. The probability of a burst being directed towards an observer depends on the rate of burst generation and the beaming of each burst, but the details are beyond the scope of this paper.

However, we can estimate beaming fractions relating to the second, pulsar-like beaming geometry using the Crab pulsar, which has been used to model extragalactic FRBs (Cordes & Wasserman, 2016). We estimate the beaming fraction of the pulsar-like emission as a function of the opening angle of the emission beam,  $\rho$ , and the angle between the rotation and magnetic axes,  $\alpha$  (Tauris & Manchester, 1998, Eq. 7). For the Crab,  $\alpha$  is estimated to be between 45 and 70 degrees (Lyne et al., 2013), and  $\rho$  can be calculated from the pulsar’s period (Everett & Weisberg, 2001, Eq. 7). The period of the Crab is 33.3 ms<sup>12</sup> (Manchester et al., 2005), resulting in  $\rho = 20^\circ$ . Thus the beaming fraction of the Crab is between 0.5–0.7.

Assuming a fiducial beaming fraction value of 0.6, there is a 99.99% probability that at least one of our sources is beamed towards us and an 83.4% probability of at least half being beamed towards us. We also plot the probability that half or more of targeted sources are beamed towards us,  $P(>50\%)$ , as a function of various number of sources,  $N$ , and beaming fractions in Fig. 4.3. From this figure we see that  $P(>50\%)$  consistently reaches above 70% for  $f > 0.6$  and  $N > 10$ .

#### 4.4.4 Poisson & Weibull distributions

Repeating bursts from FRB121102 have hitherto been treated as if they follow the Poissonian process, which describes discrete, stochastically occurring events with a known average time between them. A Poisson distribution describes the probability to observe a number of events following the Poisson process for an certain time period (e.g. an observation).

FRB121102 does not appear to follow this process. FRB121102 goes through phases of quiescence and activity (Spitler et al., 2016; Law et al., 2017), i.e. observed bursts appear clustered together. A better way to describe bursts from FRB121102 might be with a Weibull distribution, which has a more complex parametrization than a Poissonian distribution. A Weibull distribution has a shape parameter,  $k$ , which describes the degree of clustering; a rate parameter  $r$ ; and is written as Oppermann et al. (2018,

<sup>12</sup>[atnf.csiro.au/research/pulsar/psrcat/](http://atnf.csiro.au/research/pulsar/psrcat/)

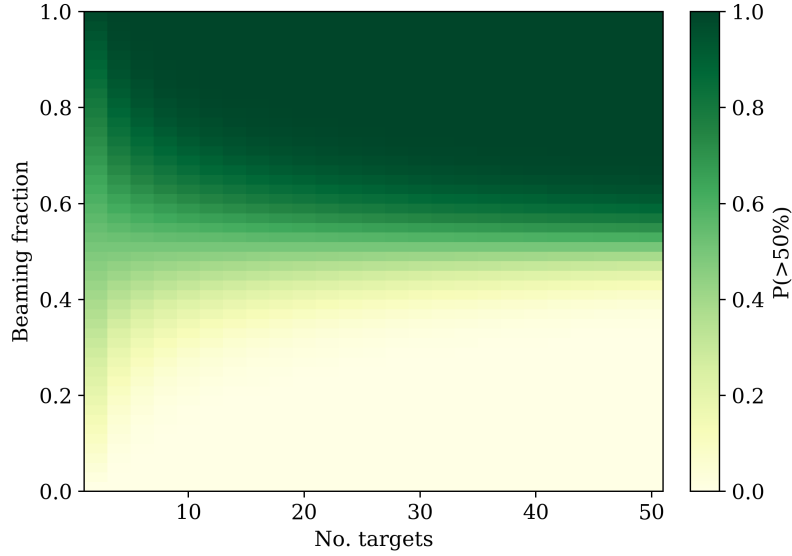


Figure 4.3: Probability that at least half of a list of observed sources would be beamed towards us ( $P > 50\%$ ) as a function of number of targets and beaming fraction.

Eq. 2):

$$\mathcal{W}(\delta | k, r) = k\delta^{-1} [\delta r \Gamma(1 + 1/k)]^\gamma e^{-[\delta r \Gamma(1 + 1/k)]^k}, \quad (4.10)$$

where  $\delta$  are the intervals between subsequent bursts and  $\Gamma$  is the gamma function. For  $k = 1$ , the Weibull distribution becomes a Poissonian distribution. If  $k < 1$ , a clustering with small intervals between bursts is favoured, so if a burst is detected, and observer is more likely to detect subsequent bursts on a short timescale afterwards. Oppermann et al. (2018) performed an analysis on L-band observations of FRB121102 in order to estimate  $k$  and  $r$ . They find that the posterior mean values of the shape parameter and rate are  $k = 0.34^{+0.06}_{-0.05}$  and  $r = 0.24^{+0.13}_{-0.08}$  bursts/hr, respectively. They also find that the Poissonian case of  $k = 1$  is strongly disfavored. Cruces et al. (2020) performed the same analysis on their aforementioned survey, and obtain a shape factor of  $k = 0.39^{+0.05}_{-0.03}$  and a rate of  $r = 0.27^{+0.09}_{-0.08}$  bursts/hr. These Weibull analysis rates are consistent with the Poissonian rate of  $0.24^{+0.06}_{-0.05}$  bursts/hr above  $0.14 (w_{\text{ms}} / \text{ms})^{1/2}$  Jy ms from Cruces et al. (2020).

We can estimate the probability of not detecting a burst from a source with Weibull-distributed bursting activity for an observation of duration  $\Delta_{\text{obs}}$  as Oppermann et al. (2018, Eq. 18):

$$P(N = 0 | k, r) = \frac{\Gamma(1/k) \Gamma_i(1/k, (\Delta_{\text{obs}} r \Gamma(1 + 1/k))^k)}{k \Gamma(1 + 1/k)}, \quad (4.11)$$

where  $r$  is the bursting rate,  $\Gamma$  is the gamma function, and  $\Gamma_i$  is the incomplete gamma function. The likelihood for multiple observations can be obtained by multiplying the

probabilities of each individual observation, given that the cadence of the observations is greater than the spacing between bursts.

We can estimate this probability for our 13 hr PAF observations at L-band of PTF10hgi (consisting of four separate observations of 1.5–4 hrs, see Table 4.2). We use the values from Cruces et al. (2020) of  $k = 0.39$  and  $r = 0.27$  bursts/hr. First we need to scale this rate from FRB121102 to PTF10hgi and from the P217mm receiver to the PAF receiver using Eq. 4.9, resulting in a rate of  $r = 0.43$  bursts/hr. The resulting probability of not detecting a burst from these observations, assuming that PTF10hgi contains an FRB121102-like source, is 14%.

We repeat this analysis for the UWL observations, which were three observations of 42, 44, and 55 minutes, using the same shape factor and rate. The scaled rate of PTF10hgi from the P217mm to the UWL receiver is 2.42 bursts/hr, and we obtain a 16% probability of not detecting a burst from these observations.

To perform the same calculations for the S45mm receiver observations, a burst event analysis for C-band observations of FRB121102 is needed in order to estimate the shape parameter  $k$  and rate  $r$ . This analysis is beyond the scope of this work, however we plot the probability of detecting zero bursts as a function of the shape parameter and rate. We illustrate two cases: the observations of PTF10hgi with the S45mm receiver presented here, and a hypothetical survey of 24 3-hr sessions (i.e. the time required to constrain the upper rate limit, see Table 4.3), shown in Fig. 4.4. There we see that the probability of not detecting any bursts rapidly decreases with increasing  $k$ , and that we can already exclude the L-band parameters from our observations. The lack of bursts detected from FRB121102 at C-band, compared to L-band detections, might lead one to believe that  $k$  and  $r$  are frequency dependent, with both being lower at higher frequencies. If we were to continue observing PTF10hgi at C-band in the same fashion until we have reached the time to constrain the Poisson rate, we could also place constraints on  $k$  and  $r$ . This hypothetical survey of 72 hrs shows that there is 0% chance of not detecting a burst for  $k \geq 0.2$  and  $r \geq 0.03$  burst/hr, and would constrain the upper-limit of  $k$  to  $\sim 0.2$  if no burst was detected.

## 4.5 Discussion & Conclusions

In this work we investigate the possibility of SLSNe/LGRBs hosting FRB121102-like progenitors. We have observed 10 targets for 63 hours using the S45mm (5.3–9.3 GHz) and PAF (1.2–1.5 GHz) receivers at Effelsberg and the UWL receiver (0.7–4 GHz) at Parkes, but have found no bursts.

By assuming an FRB121102-like source is located at our observed targets, we have estimated their scaled burst rates with respect to luminosity distance, redshift, and telescope sensitivity. We have also calculated the upper limit rate for each source, based on our non-detections. The rate upper limits do not constrain any of the scaled rates at C-band, but the scaled rates for three of our sources, GRB051109B, PTF12dam, and PTF10hgi, can be constrained with a reasonable amount of observing time.

PTF10hgi is a source of particular interest, as a persistent radio source which is

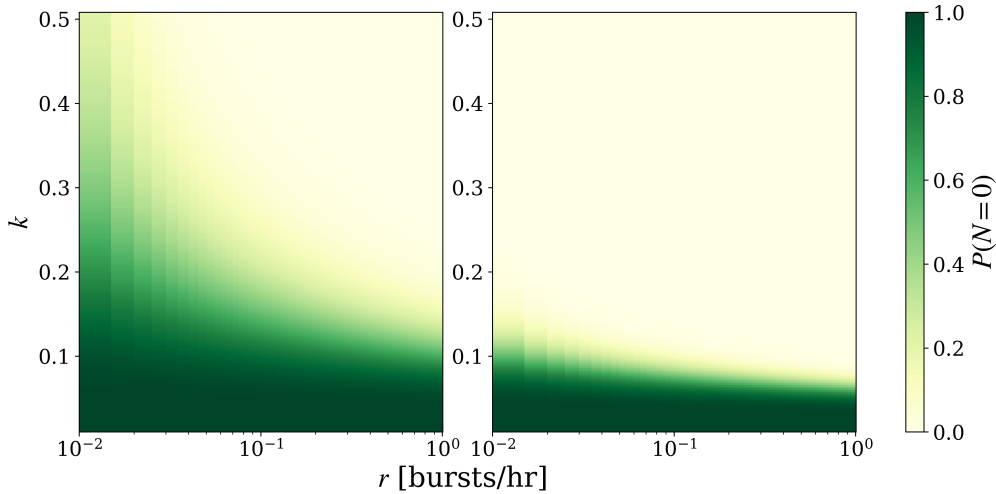


Figure 4.4: Probability of detecting zero bursts,  $P(N = 0)$ , for a Weibull distributed bursting activity of a source as a function of shape parameter,  $k$ , and rate  $r$ . *Left*: Probabilities from our two (5.3 hr in total) observations of PTF10hgi at C-band. *Right*: Probabilities from a hypothetical 72 hour observing campaign ( $24 \times 3$  hrs).

coincident with the SLSN was recently detected. This system could be analogous to FRB121102, and detecting an FRB originating from it could be instrumental in deciphering the enigmatic nature of these bursts. We have therefore spent 5.3 hrs observing PTF10hgi at 6 GHz with the S45mm receiver, 13 hrs at 1.4 GHz during the commissioning of the PAF receiver at Effelsberg, and 2.3 hrs at 2.4 GHz with the UWL receiver at Parkes. We did not detect any bursts from those observations, and rule out at the 99% CL the scaled PAF and UWL rates at L-band of an FRB121102-like source inhabiting PTF10hgi. There are several possibilities for why we have not detected any bursts: *i*) PTF10hgi does not contain an FRB121102-like source, *ii*) FRBs might not be related to young magnetars within SNRs, *iii*) the source was observed during a quiescent state, *iv*) PTF10hgi’s SNR might still be opaque at L-band, *v*) or bursts from the source are simply not beamed towards us,

When we adopt a beaming fraction of 0.6 for our sources we show there is 99.99% chance that at least one of our hypothetical targets would be beamed towards us, and an 83.4% probability that at least five of them are beamed towards us. From Fig. 4.3 we note that for beaming fractions larger than 0.6, at least half of the sources will consistently have a high probability of being beamed towards us.

The clustering of bursts from FRB121102 could be better explained with a Weibull rather than a Poissonian distribution (Oppermann et al., 2018). Using a shape factor of  $k = 0.39$  and a scaled rate of 0.43 bursts/hr for a Weibull distribution (Cruces et al., 2020) we estimate a 14% probability of not detecting a burst from our PAF receiver observations of PTF10hgi, assuming it contains an FRB121102-like source. By using the same shape factor and a rate of 2.42 bursts/hr for our UWL observations we

estimate a 16% probability of not detecting a burst. We do not have an estimate of the shape factor at C-band, however we plot the probability of not detecting a burst as a function of  $k$  and  $r$  for our S45mm receiver observations of PTF10hgi in Fig. 4.4, and show that the L-band rate and shape factor are already excluded.

We have several recommendations for future surveys which may follow up this work. By assuming that SLSNe/LGRBs contain FRB121102-like sources, we must expect that they also have clustering of emission, along with periods of dormancy. We should also assume that the bursts are beamed to some degree. Therefore we suggest that observing multiple sources for short periods of time on a regular basis would be ideal. The advantage of observing a source which has clustered burst phases across multiple short observations rather than a few (or one) long observations is shown in Fig. 4.5. There we plot the probability of detecting zero bursts for a survey totaling 73 hrs across different number of observations as a function of burst rate for a source with different shape factors. As we move further away from the Poissonian case of  $k = 1$ , it becomes increasingly important to split a survey into multiple observations in order to maximize the probability of detecting a burst. Since the rate scaling is dependent on distance, choosing sources closer than FRB121102 is advised. Finally, SLSNe/LGRBs with coincident persistent radio sources, like PTF10hgi, should be the primary sources to observe for future surveys of this kind; they should preferably be observed at higher frequencies, as we cannot be certain that the SNR is transparent at L-band. The UWL might be the ideal instrument for following up on this work for two reasons: *i)* The SNR of the targets observed here are most likely transparent in at least the upper part of UWL's band, making the optically thick-thin transition potentially observable with a single receiver. *ii)* The scaled FRB121102 UWL rates are higher than the ones for the S45mm receiver. This implies that the time needed to constrain the 95% CL upper rate limits of the targets observed in this work with the UWL is much less than for the S45mm receiver. We show in Table 4.4 that these times range between 1–16 hrs.

Recent localisations of FRBs (Bannister et al., 2019; Ravi et al., 2019; Prochaska et al., 2019; Marcote et al., 2020) have revealed host galaxies differing from FRB121102, with them being lenticular or spiral in shape, and more massive. The localisation of FRB180916.J1058+65 (Marcote et al., 2020) is of particular interest, as it is the only other localised repeating FRB. The host of FRB180916.J1058+65 is a spiral galaxy and is both more massive and has higher metallicity than the host of FRB121102, rendering it different to hosts of SLSNe/LGRBs as well. This bursting source also has no persistent radio counterpart, and the burst absolute RM value is roughly  $100 \text{ rad m}^{-2}$ , three orders of magnitude lower than FRB121102. The two bursting sources are however both localised within star forming regions of their respective host galaxies. FRB180916.J1058+65 still fits within the framework of a magnetar embedded in an SNR if the system is a few hundred years old (Marcote et al., 2020). By then the persistent radio source would have faded and the RM decreased to the observed value. This begs the question whether or not the host galaxy of FRB121102 is a typical host of repeating FRBs. Expanding future surveys like in this work to include galaxies similar to hosts of other localised FRBs could be more fruitful.

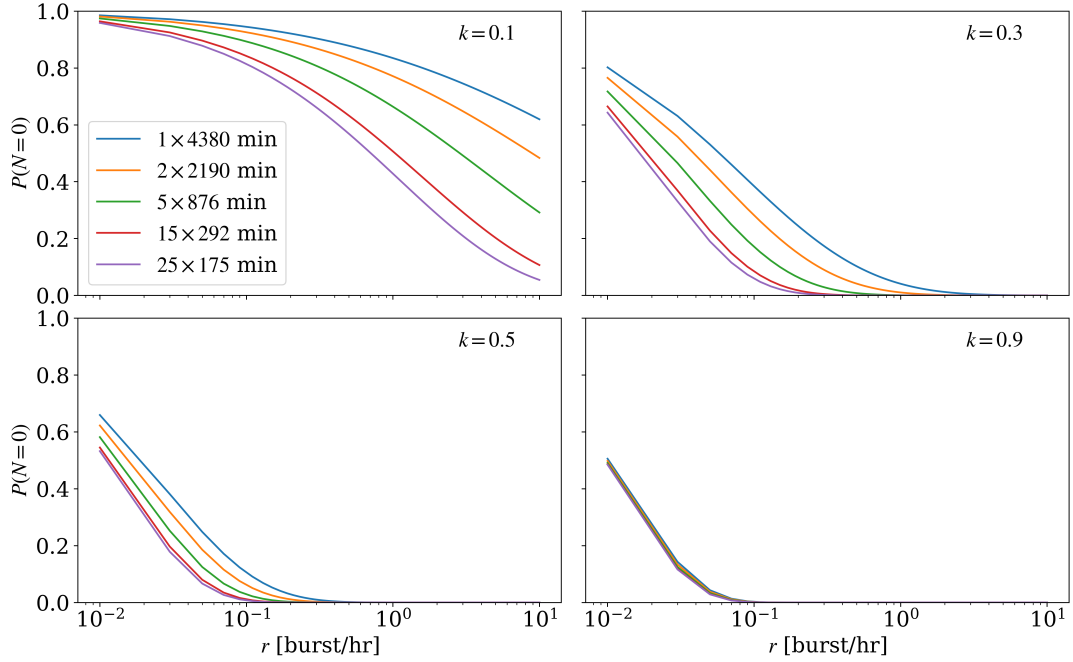


Figure 4.5: Probability of detecting zero bursts as a function of burst rate for hypothetical 73 hr surveys spanning different numbers of observations (colours). Different shape factors,  $k$ , are shown in each panel. As expected a single long observation has the highest probability of detecting zero bursts from a Weibull distribution, with the probability decreasing with number of observations.

Table 4.4: Burst rates of an FRB121102-like source located at the targets observed in this work. *From left to right*: Source name, burst rate of an FRB121102-like source scaled to the UWL receiver, and the observing time required to constrain those rates at the 95% confidence level.

Source name	$R_{\text{FRB121102}}$ [ $\text{hr}^{-1}$ ]	$T_{\text{constr}}$ [hr]
GRB050826	0.3	11
GRB051109B	3.2	1
GRB111225A	0.3	11
PTF09cnd	0.4	8
PTF10uhf	0.3	10
PTF10bjp	0.2	16
SN2010gx	0.4	7
PTF12dam	1.9	2
LSQ12dlf	0.4	8
PTF10hgi	2.2	1

## Acknowledgements

Based on observations with the 100-m telescope of the MPIfR (Max-Planck-Institut für Radioastronomie) at Effelsberg. Some of the results of this paper have been derived using the FRUITBAT package (Batten, 2019). The Parkes radio telescope is funded by the Commonwealth of Australia for operation as a National Facility managed by CSIRO. The time for this project was allocated from the Director’s Discretionary Time under the Project ID PX048. We thank Vincent Morello for assisting with our Parkes observations, and C. R. H. Walker for excellent comments and discussions. LGS is a Lise Meitner independent research group leader and acknowledges support from the Max Planck Society. We thank the referees for their comments which helped improving this manuscript.

# Rotation Measure Evolution of the Repeating Fast Radio Burst Source FRB 121102

---

This chapter is based on an article titled “*Rotation Measure Evolution of the Repeating Fast Radio Burst Source FRB 121102*”, which has been submitted for publication in the *Astrophysical Journal Letters*<sup>1</sup>. The manuscript remains unchanged, but is formatted to fit the template of the thesis.

As the lead author of this publication, I have performed the Effelsberg observations, reduced and searched the Effelsberg data, performed all the analysis, and written the manuscript.

The full author list is **G. H. Hilmarsson**, D. Michilli, L. G. Spitler, R. S. Wharton, P. Demorest, G. Desvignes, K. Gourdji, S. Hackstein, J. W. T. Hessels, K. Nimmo, A. D. Seymour, M. Kramer, and R. McKimven.

## 5.1 Abstract

The repeating fast radio burst source FRB 121102 has been shown to have an exceptionally high and variable Faraday rotation measure (RM), which must be imparted within its host galaxy and likely by or within its local environment. In the redshifted ( $z = 0.193$ ) source reference frame, the RM decreased from  $1.46 \times 10^5 \text{ rad m}^{-2}$  to  $1.33 \times 10^5 \text{ rad m}^{-2}$  between January and August 2017, showing day-timescale variations of  $\sim 200 \text{ rad m}^{-2}$ . Here we present sixteen FRB 121102 RMs from burst detections with the Arecibo 305-m radio telescope, the Effelsberg 100-m, and the Karl G. Jansky Very Large Array, providing a record of FRB 121102’s RM over a 2.5-year timespan. Our observations show a decreasing trend in RM, although the trend is not linear, dropping by an average of  $15\% \text{ year}^{-1}$  and is  $\sim 9.7 \times 10^4 \text{ rad m}^{-2}$  at the most recent epoch of August 2019. Erratic, short-term RM variations of  $\sim 10^3 \text{ rad m}^{-2} \text{ week}^{-1}$  were also observed between MJDs 58215–58247. A decades-old neutron star embedded within a still-compact supernova remnant or a neutron star near a massive black hole and its accretion torus have been proposed to explain the high RMs. We compare the observed RMs to theoretical models describing the RM evolution for FRBs originating within a supernova remnant. FRB 121102’s age is unknown, and we find that the models agree for source ages of  $\sim 6 - 17$  years at the time of the first available RM

---

<sup>1</sup>Pre-print available at [arxiv.org/abs/2009.12135](https://arxiv.org/abs/2009.12135)

measurements in 2017. We also draw comparisons to the decreasing RM of the Galactic center magnetar, PSR J1745–2900.

## 5.2 Introduction

Fast radio bursts (FRBs) are millisecond duration radio transients, whose origins are still unknown (Petroff et al., 2019). Of the roughly 100 FRBs published so far<sup>2</sup> (Petroff et al., 2016), around ten have been localised to a host galaxy (Chatterjee et al., 2017; Bannister et al., 2019; Ravi et al., 2019; Prochaska et al., 2019; Marcote et al., 2020; Macquart et al., 2020), confirming their extragalactic origins. Some FRBs have also been observed to repeat; the first discovered, and most observed so far, is FRB 121102 (Spitler et al., 2016), and more repeating FRBs have been detected by the Canadian Hydrogen Intensity Mapping Experiment (CHIME) radio telescope (CHIME/FRB Collaboration et al., 2019a,c; Fonseca et al., 2020b) and the Australian Square Kilometre Array Pathfinder (ASKAP, e.g. Kumar et al., 2019).

Polarisation properties of FRBs can reveal the nature of their local environment, as well as the FRB emission process and its geometry, thus adding constraints to progenitor theories. The rotation of the linearly polarised plane of a signal induced by the line of sight (LoS) magnetic field is called Faraday rotation. The rate of this rotation across frequency is quantified by the rotation measure (RM), calculated as the LoS integral of the product of the magnetic field strength and the electron density. Polarisation fractions and RMs have been determined for 20 FRBs (Petroff et al., 2016). Linear polarisation fractions ranging from  $\sim 0$  to  $\sim 100\%$  have been measured, and the absolute RM values are in the range  $\sim 10$ – $500 \text{ rad m}^{-2}$ , with the exception of FRB 121102, which has an exceptionally high RM of  $\sim 10^5 \text{ rad m}^{-2}$ . FRB 121102’s RM has also proven to be highly variable, with a decrease of  $\sim 10\%$  between epochs separated by seven months (Michilli et al., 2018a). To be able to observe such a high RM, a narrow channel bandwidth or a high observing frequency are required in order to avoid intra-channel depolarisation. Typical pulsar instrumentation have channel bandwidths of  $\sim 1 \text{ MHz}$ , so high frequency observations are required to observe high RMs.

In the original discovery of FRB 121102, the dispersion measure (DM) was found to be  $557 \pm 2 \text{ pc cm}^{-3}$  (Spitler et al., 2014a), where the DM is defined as the column density of free electrons along the LoS. In more recent observations, FRB 121102 has exhibited an increase in the measured DM,  $560.6 \pm 0.1 \text{ pc cm}^{-3}$  in Hessels et al. (2019) and  $563.6 \pm 0.5 \text{ pc cm}^{-3}$  in Josephy et al. (2019), revealing an average increase of roughly  $1 \text{ pc cm}^{-3}$  per year.

Bursts from FRB 121102 have been detected at frequencies spanning from  $\sim 0.3$ – $8 \text{ GHz}$  (Chawla et al., 2020b; Gajjar et al., 2018). The bursting activity of FRB 121102 does not seem to follow a Poissonian process, but rather goes through phases of bursting activity and quiescence which can be better explained with a Weibull distribution (Oppermann et al., 2018). This dichotomy in activity could also be explained by the

---

<sup>2</sup>frbcat.org

recently discovered apparent periodicity of FRB 121102 of 161 days with an active window of 54% (Rajwade et al., 2020b; Cruces et al., 2020), also detected in the repeating FRB 180916.J1058+65 with a period of 16 days and a 31% activity window (Chime/Frb Collaboration et al., 2020).

FRB 121102 is the first repeating FRB to be unambiguously localised to a host galaxy (Chatterjee et al., 2017), which is a low-metallicity dwarf galaxy at a redshift of  $z = 0.193$  (Tendulkar et al., 2017) with a stellar mass of  $M_* \sim 1.3 \times 10^8 M_\odot$  and a star formation rate of  $0.23 M_\odot$  per year (Bassa et al., 2017b). FRB 121102 is also coincident with a compact persistent radio source whose projected offset is  $< 40$  pc (Marcote et al., 2017).

The properties of FRB 121102 and its persistent radio source have motivated a number of FRB models. Among the leading scenarios, FRBs are generated by flaring magnetars within supernova remnants (SNRs). Here, the magnetar flares collide with the surrounding medium, producing shocks creating synchrotron maser emission, resulting in FRB generation. The main difference between these models lies in the nature of the shocked material, being dominated by either the magnetar wind nebula (e.g. Lyubarsky, 2014), or by previous magnetar flares (e.g. Beloborodov, 2017, 2019; Margalit & Metzger, 2018).

In this work we have observed FRB 121102 with the 305-m William E. Gordon Telescope at the Arecibo Observatory (AO), the Effelsberg 100-m Radio Telescope, and the Karl G. Jansky Very Large Array (VLA) to obtain RMs from its bursts in order to investigate its long-term RM evolution. In §5.3 we describe our observations, data acquisition and search analysis. In §5.4 we report sixteen new RM measurements of FRB 121102, a long-term average FRB 121102 burst rate from our Effelsberg observations, and discuss the properties of the detected bursts. §5.5 is dedicated to comparing our results to the theoretical prediction of the RM evolution of an SNR from the works of Piro & Gaensler (2018) and Margalit & Metzger (2018), as well as the Galactic center (GC) magnetar, PSR J1745–2900 (Desvignes et al., 2018), and in §5.6 we interpret those results. Finally, in §5.7 we summarise our findings.

## 5.3 Observations

The telescopes used for observations were the Arecibo Observatory 305-m William E. Gordon Telescope in Puerto Rico, USA; the Effelsberg 100-m Radio Telescope in Effelsberg, Germany; and the Karl G. Jansky Very Large Array in New Mexico, USA. The observational setup and data processing of each telescope is detailed in their respective subsections below.

We anticipated extremely high RM values from FRB 121102 bursts, and have thus observed at frequencies higher than the 1.4-GHz band in order to avoid intra-channel depolarisation.

### 5.3.1 Effelsberg

We have used the Effelsberg 100-m radio telescope to observe FRB 121102 at 4–8 GHz using the S45mm receiver with a roughly two-week cadence for 2–3 hours each session from late 2017 to early 2020, totaling 115 hours.

The data were recorded with full Stokes information using two ROACH2 backends with each one capturing 2 GHz of the band. The channel bandwidth is 0.976562 MHz across 4096 channels, with a 131  $\mu\text{s}$  sampling rate. The recorded data were in a Distributed Acquisition and Data Analysis (DADA) format<sup>3</sup>. Before processing, Stokes  $I$  was extracted from the data into a SIGPROC filterbank<sup>4</sup> format in order to perform the initial burst searching.

Observations on 22nd October 2018 encountered a receiver issue, forcing us to use the S60 mm receiver instead. The S60 mm receiver has an SEFD of 18 Jy, 500 MHz of bandwidth from 4.6 to 5.1 GHz, 0.976562 MHz channel bandwidth across 512 channels, and an 82  $\mu\text{s}$  sampling rate. The data were recorded as SIGPROC filterbanks.

The data were searched for single pulses using the PRESTO<sup>5</sup> software package (Ransom, 2011). We used `rfifind` to identify radio frequency interference (RFI) in the data over two-second intervals and to make an RFI mask which was applied to the data during searching. We used PRESTO to create dedispersed time-series of the data from 0–1000  $\text{pc cm}^{-3}$  in steps of 2  $\text{pc cm}^{-3}$ , which were searched for single pulses using `single_pulse_search.py` to convolve the time-series with boxcar filters of varying widths to optimise the signal-to-noise of a burst. A pre-determined list of boxcar widths from PRESTO was used, where the widths are multiples of the data sampling time. We searched for burst widths up to 19.6 ms and applied a signal-to-noise threshold of 7. DM-time and frequency-time plots of candidates were visually inspected to search for bursts.

For further RFI mitigation we calculated the modulation index of candidates. The modulation index assesses a candidate’s fractional variations across the frequency channels in order to discriminate between narrowband RFI and an actual broadband signal (Spitler et al., 2012). We applied this thresholding following Hilmarsson et al. (2020b).

If a burst was detected, we performed polarisation calibration in order to obtain the RM, polarisation angle (PA), and degree of polarisation of the burst. We used the `psrfits_utils` package<sup>6</sup> to create a `psrfits`<sup>7</sup> file containing the burst and used PSRCHIVE<sup>8</sup> (Hotan et al., 2004) to calibrate the data by first dedispersing the burst data using `pam`, then `pac` to polarise calibrate that data with noise diode observations. To get the RM value, we used `RMsyn.py`<sup>9</sup>, which fits a variation in Stokes  $Q$  and  $U$  as a function of frequency.

---

<sup>3</sup><http://psrdada.sourceforge.net>

<sup>4</sup><http://sigproc.sourceforge.net>

<sup>5</sup>[github.com/scottransom/presto](https://github.com/scottransom/presto)

<sup>6</sup>[github.com/demorest/psrfits\\_utils](https://github.com/demorest/psrfits_utils)

<sup>7</sup>[atnf.csiro.au/research/pulsar/psrfits\\_definition/Psrfits.html](http://atnf.csiro.au/research/pulsar/psrfits_definition/Psrfits.html)

<sup>8</sup><http://psrchive.sourceforge.net/>

<sup>9</sup>[github.com/gdesvignes/python-tools](https://github.com/gdesvignes/python-tools)

### 5.3.2 Arecibo

Data from the 305-m William E. Gordon Telescope at the Arecibo Observatory were acquired by using the C-band receiver at an observing frequency between 4.1 and 4.9 GHz. The Puerto Rican Ultimate Pulsar Processing Instrument (PUPPI) backend recorded dual-polarisation data every  $10.24 \mu\text{s}$  in 512 frequency channels, each coherently dedispersed to  $\text{DM} = 557 \text{ pc cm}^{-3}$  to reduce intra-channel dispersive smearing to  $< 2 \mu\text{s}$ . The time and frequency resolution were reduced to  $81.92 \mu\text{s}$  and 12.5 MHz, respectively, before searching for bursts. We used PRESTO to create 200 dedispersed time-series between 461 and  $661 \text{ pc cm}^{-3}$ , which were searched by `single_pulse_search.py` with box-car filters ranging from  $81.92 \mu\text{s}$  to 24.576 ms. A large fraction of detections due to noise and RFI were excluded by using dedicated software<sup>10</sup> (Michilli et al., 2018b). A ‘waterfall’ plot of signal intensity as a function of time and frequency was produced and visually inspected for the rest of the detections. The DSPSR package<sup>11</sup> (van Straten & Bailes, 2011) was used to create PSRCHIVE files containing the full resolution data recorded by PUPPI.

For each observation, PSRCHIVE utilities were used to calibrate the burst polarisation by using a scan of a noise diode. RM values and their uncertainties were calculated with the `RM-tools` package<sup>12</sup> by using rotation measure synthesis (Burn, 1966; Brentjens & de Bruyn, 2005) and a cleaning deconvolution algorithm (Heald, 2009). The resulting Faraday dispersion function for bursts detected on MJDs 58222 and 58712 (bursts 8, 19 and 20) shows signs of a poor polarisation calibration, namely symmetric peaks around the origin. We were not able to identify a cause for this and, while the RM measurements are still valid, the resulting polarisation fraction should be considered not reliable. PA curves were calculated by de-rotating the data with PSRCHIVE at the RM value obtained for each burst.

### 5.3.3 VLA

FRB 121102 was observed with the VLA as part of a monitoring project (VLA/17B-283) from 2017 November to 2018 January. Ten 1-hr observations were conducted at 2–4 GHz using the phased-array pulsar mode. Data were recorded with full Stokes information with  $8096 \times 0.25 \text{ MHz}$  channels and  $1024 \mu\text{s}$  time samples. Each observation had  $\approx 30$  min on-source. Data were dedispersed at 150 trial DMs from  $400 - 700 \text{ pc cm}^{-3}$  and the resulting time-series were searched for pulses using the PRESTO `single_pulse_search.py`.

Polarisation calibration was done using the 10-Hz injected noise calibrator signal. After polarisation calibration, the RMs were measured using the PSRCHIVE task `rmfit` which finds the RM that maximizes the linear polarisation fraction of the burst.

<sup>10</sup><http://asc1.net/1806.013> (Michilli & Hessels, 2018)

<sup>11</sup><http://dspsr.sourceforge.net/>

<sup>12</sup><https://github.com/CIRADA-Tools/RM-Tools>

## 5.4 Observational Results

From our observations we have sixteen new RM measurements from FRB 121102 bursts: 1 from Effelsberg, 2 from the VLA, and 13 from Arecibo. The details of our detections, along with previously reported RM values, are listed in Table 5.1. The previously reported RM values from Arecibo (Michilli et al., 2018a) and the GBT (Gajjar et al., 2018) listed in Table 5.1 are a global fit to multiple bursts from the same epoch. Each burst is also assigned a numerical value for clarity. The burst DMs in Table 5.1 are obtained through a linear interpolation of DMs from bursts detected at L-band with Arecibo (Seymour et al., in prep). The L-band burst DMs are determined by maximising the structure of the bursts and their sub-components<sup>13</sup>. That sample contains more bursts and shows more complex burst structures than the bursts presented here, resulting in more accurate and consistent DMs.

### 5.4.1 Long-term Burst Rate at C-band at Effelsberg

Previous surveys of FRB 121102 at frequencies between 4–8 GHz reported rates based on fewer observed hours (Spitler et al., 2018) and anomalously high burst rates (Gajjar et al., 2018). Spitler et al. (2018) detected three bursts from observing at 4.6–5.1 GHz for 22 hours consisting of 10 observing epochs spanning five months using the Effelsberg telescope. Gajjar et al. (2018) detected 21 bursts in a single six-hour observation, observing at 4–8 GHz at the Green Bank Telescope. Furthermore, Zhang et al. (2018) re-researched the data from Gajjar et al. (2018) using a convolutional neural network and detected an additional 72 bursts within the data.

Our Effelsberg survey spans over two years of observing FRB 121102 for 2–6 hrs at a time at 4–8 GHz with a two-week cadence, amounting to 115 hours of observations. Included here are 10 hours of observations presented in Caleb et al. (2020). We can therefore report a robust, long-term average burst rate of FRB 121102 in this frequency range of  $0.21_{-0.18}^{+0.49}$  bursts/day (1-sigma error) above a fluence of  $0.04 (w/\text{ms})^{1/2}$  Jy ms for a burst width of  $w$  ms. We list the details of the surveys discussed here in Table 5.2.

A caveat to our observed burst rate is the suspected periodic activity of FRB 121102 (Rajwade et al., 2020b). Roughly 40% of our Effelsberg observations were performed during suspected inactivity of FRB 121102, which if true would affect the observed burst rate. Including only observations while FRB 121102 is active, the average burst rate becomes  $0.35_{-0.29}^{+0.80}$  bursts/day above a fluence of  $0.04 (w/\text{ms})^{1/2}$  Jy ms.

The observed burst rates of FRB 121102 also seem to be frequency dependent, with the rate being lower at higher frequencies. At 1.4 GHz the FRB 121102 burst rate has been observed to be  $8 \pm 3$  bursts/day above a fluence of 0.08 Jy ms for 1 ms burst widths (Cruces et al., 2020).

<sup>13</sup><http://asc1.net/1910.004> (Seymour et al., 2019)

Table 5.1: Burst detections of FRB 121102 with measured RMs in chronological order. *From left to right:* Burst number, barycentric burst arrival time in MJD (referenced to infinite frequency), width ( $w$ , full-width at half-maximum), flux density ( $S$ ), fluence ( $F$ ), observed RM, DM, observing frequency, and telescope used. The burst DMs are obtained through linear interpolation of L-band bursts detected at Arecibo, whose DMs are determined by maximising their burst and sub-component structure. Sub-bursts of multi-component bursts are further labeled chronologically with lower-case letters. Previously reported bursts and bursts introduced in this work are separated by a horizontal line. Abbreviations are AO: Arecibo Observatory, Eff: Effelsberg, GBT: Green Bank Telescope, VLA: Very Large Array.

Burst	MJD	$w$ (ms)	$S$ (Jy)	$F$ (Jy ms)	RM <sub>obs</sub> (rad m <sup>-2</sup> )	DM (pc cm <sup>-3</sup> )	Freq. (GHz)	Telescope
1	57747.12956–57747.17597				102708 ± 4		4.1–4.9	AO <sup>a,c</sup>
2	57748.12564–57748.17570				102521 ± 4		4.1–4.9	AO <sup>a,c</sup>
3	57772.12903030				103039 ± 4		4.1–4.9	AO <sup>a</sup>
4	57991.58013–57991.58330				93573 ± 24		4–8	GBT <sup>a,b,c</sup>
5	58069.31853200	4.49 ± 0.09	0.38 ± 0.06	1.69	86850 ± 100	560.5	2–4	VLA
6a		1.65 ± 0.07	0.16 ± 0.02	0.26				
6b	58075.20058018	1.95 ± 0.08	0.32 ± 0.05	0.63	86550 ± 20	560.6	2–4	VLA
6c		3.62 ± 0.08	0.56 ± 0.08	2.03				
7	58215.86332798	0.34 ± 0.01	0.19 ± 0.03	0.06	70844 ± 50	561.5	4.1–4.9	AO
8a		0.59 ± 0.01	0.32 ± 0.05	0.19				
8b	58222.85751812	0.34 ± 0.04	0.05 ± 0.01	0.02	72039 ± 30	561.5	4.1–4.9	AO
9	58227.83201090	0.76 ± 0.04	0.08 ± 0.01	0.06	72038 ± 70	561.6	4.1–4.9	AO
10	58228.63801964	0.69 ± 0.08	0.35 ± 0.05	0.24	72300 ± 100	561.6	4–8	Eff
11	58234.81180934	0.39 ± 0.03	0.09 ± 0.01	0.04	73510 ± 80	561.6	4.1–4.9	AO
12	58234.81642918	0.35 ± 0.01	0.20 ± 0.03	0.07	73360 ± 40	561.6	4.1–4.9	AO
13	58243.77965432	0.52 ± 0.01	1.8 ± 0.3	0.96	71525 ± 3	561.7	4.1–4.9	AO
14a		0.92 ± 0.03	0.13 ± 0.02	0.12				
14b	58244.77641721	0.69 ± 0.03	0.12 ± 0.02	0.08	71160 ± 30	561.7	4.1–4.9	AO
15	58247.81273381	0.54 ± 0.02	0.13 ± 0.02	0.07	68940 ± 70	561.7	4.1–4.9	AO
16	58677.60475978	0.30 ± 0.02	0.13 ± 0.02	0.04	69380 ± 40	563.3	4.1–4.9	AO
17	58684.58367814	0.47 ± 0.03	0.09 ± 0.01	0.04	69520 ± 60	563.2	4.1–4.9	AO
18	58684.58990897	0.25 ± 0.02	0.09 ± 0.01	0.02	69410 ± 90	563.2	4.1–4.9	AO
19a		0.90 ± 0.03	0.27 ± 0.04	0.24				
19b	58712.47972031	0.207 ± 0.001	1.9 ± 0.3	0.40	66950 ± 10	563.1	4.1–4.9	AO
20	58712.48531398	1.89 ± 0.09	0.06 ± 0.01	0.11	67030 ± 90	563.1	4.1–4.9	AO

<sup>a</sup>Results presented in Michilli et al. (2018a).

<sup>b</sup>Results presented in Gajjar et al. (2018).

<sup>c</sup>Global fit to multiple bursts.

Table 5.2: FRB 121102 surveys at frequencies between 4–8 GHz. *From left to right:* Survey, number of bursts, number of hours observed, number of observing epochs, frequency range, and telescope used. All surveys except Spitler et al. (2018) recorded full Stokes data. Abbreviations are AO: Arecibo Observatory, Eff: Effelsberg, GBT: Green Bank Telescope.

Survey	No. bursts	No. hours	No. epochs	Freq. (GHz)	Telescope
Spitler et al. (2018)	3	22	10	4.6–5.1	Eff
Michilli et al. (2018a)	16	13	12	4.1–4.9	AO
Gajjar et al. (2018)	21	6	1	4–8	GBT
Zhang et al. (2018) <sup>a</sup>	93	6	1	4–8	GBT
This work	1	115	35	4–8	Eff

<sup>a</sup>Re-searching of data from Gajjar et al. (2018)

### 5.4.2 Burst Properties

We plot the dynamic spectra, polarisation profile, and polarisation angles (PAs) of our detected bursts in Fig. 5.1. The PA is equal to  $\text{RM}\lambda^2 + \text{PA}_{\text{ref}}$ , where  $\lambda$  is the observing wavelength, and  $\text{PA}_{\text{ref}}$  is a reference angle at a specific frequency (central observing frequency in our case). The bursts are mostly  $\sim 100\%$  linearly polarised, with no circular polarisation detected. Bursts from FRB 121102 have been consistently  $\sim 100\%$  linearly polarised since its first polarisation measurement in late 2016 (Michilli et al., 2018a), which suggests a stability in its emission process. The Arecibo bursts at MJD 58222, 58247, and 58712 (bursts 8, 15, 19, and 20) are not fully linearly polarised, which is uncharacteristic for FRB 121102, and can be attributed to polarisation calibration issues (see §5.3.2). The lack of circular polarisation indicates that no Faraday rotation conversion occurs at our observing frequencies, where linear polarisation is converted to circular in a magneto-ionic environment (Vedantham & Ravi, 2019; Gruzinov & Levin, 2019).

The PAs are flat across each burst, as has been seen previously from FRB 121102 (Michilli et al., 2018a; Gajjar et al., 2018). The flat PAs indicate the burst timescales are intrinsic, and not from a beam sweeping the LoS of an observer. We do not discuss PA changes over time, as we did not observe an absolute calibrator for polarisation. In the absence of an absolute calibrator we cannot compare PAs across multiple telescopes. This discussion is outside the scope this work.

The VLA burst on MJD 58075 (burst 6) exhibits a triple component profile. The second and third components exhibit a downward drift in frequency, a feature predominantly observed from repeating FRBs (e.g. Hessels et al., 2019; The CHIME/FRB Collaboration et al., 2020a). The first component has an apparent upward drift in frequency, which is rarely seen, and a different PA than the two other components. While the temporal spacing between the components is not large, the difference in PAs between the first component and the other two might suggest that these are in fact two separate bursts.

The Effelsberg burst at MJD 58228 (burst 10) was only detected between 4–5.2 GHz of the 4–8 GHz bandwidth. We were affected by strong edge effects in the bandpass,

resulting in an uneven frequency response across the bandwidth. Thus we are uncertain of whether the burst frequency envelope is inherent to the burst or due to the bandpass.

### 5.4.3 Dispersion and Rotation Measures of FRB 121102

The RMs we obtained from our bursts are listed in Table 5.1. We plot the RMs over time in Fig. 5.2. The observed RM of FRB 121102 has dropped by 34% over 2.6 years from  $\sim 10^5 \text{ rad m}^{-2}$  to  $\sim 6.7 \times 10^4 \text{ rad m}^{-2}$ . As Fig. 5.2 shows, the drop in RM has not been steady over time. From MJD 57757 to MJD 58215 (bursts 1–7), the RM decreased rapidly to  $\sim 7 \times 10^4 \text{ rad m}^{-2}$  and has declined only slightly ( $\sim 5000 \text{ rad m}^{-2}$ ) since then.

Within a 32-day timespan the observed RM of FRB 121102 exhibited significant short-timescale variations (bursts 7–15). At epochs separated by a week, the RM increased by  $\sim 1000 \text{ rad m}^{-2}$  (bursts 7–8). For three epochs during the following week, the RM remained stable between bursts 8–10, before increasing again by  $\sim 1000 \text{ rad m}^{-2}$  a week later (bursts 11–12). During three epochs in the following two weeks, the RM was observed to drop rapidly by a total of  $\sim 4500 \text{ rad m}^{-2}$  (bursts 12–15). This short-timescale behaviour can be seen in the inset of Fig 5.2. No RM measurement is available between MJDs 58247 and 58677 (430 days), but the RMs are consistent with each other at these dates (bursts 15–16). Another drop in RM of  $\sim 2000 \text{ rad m}^{-2}$  can be seen between bursts 18 and 19, separated by 28 days.

Only minor changes in DM have been observed during the observed RM evolution of FRB 121102. While the RM decreased significantly, the DM has increased by  $\sim 4 \text{ pc cm}^{-3}$ , from  $559.7 \pm 0.1 \text{ pc cm}^{-3}$  (Michilli et al., 2018a) up to  $563.3 \text{ pc cm}^{-3}$  from the aforementioned linear interpolation of L-band burst DMs used in this work.

An increase in DM means an increase in the LoS electron density. There are many contributing factors to the DM along the LoS, so a smaller fractional change in DM is not surprising. The Faraday rotating medium contributes only a fraction of the total DM and its amount is unknown. A decrease in RM implies either a decrease in the magnetic field strength or the electron density along the LoS, or both. The opposing RM and DM evolution thus has two possible scenarios: the changes in RM and DM arise from different media; or the changes arise from the same medium, implying that the LoS magnetic field strength must be decreasing.

Michilli et al. (2018a) constrained the average magnetic field along the LoS in the region which Faraday rotation occurs,  $\langle B_{\parallel} \rangle$ , between 0.6 mG and 2.4 mG using their measured FRB 121102 RM in the source frame of  $\text{RM}_{\text{src}} \sim 1.4 \times 10^5 \text{ rad m}^{-2}$  and the estimated host DM contribution of  $\text{DM}_{\text{host}} 70 - 270 \text{ pc cm}^{-3}$  (Tendulkar et al., 2017). From a measured DM and RM,  $\langle B_{\parallel} \rangle$  can be calculated, ignoring sign reversals, as

$$\langle B_{\parallel} \rangle = 1.23 \text{ RM}_{\text{src}} / \text{DM}_{\text{host}} \mu\text{G}. \quad (5.1)$$

The most recent DM and RM values in our sample yield  $\langle B_{\parallel} \rangle = 0.4\text{--}1.6 \text{ mG}$ . This is a lower limit as the DM in the Faraday rotating region could be much lower.

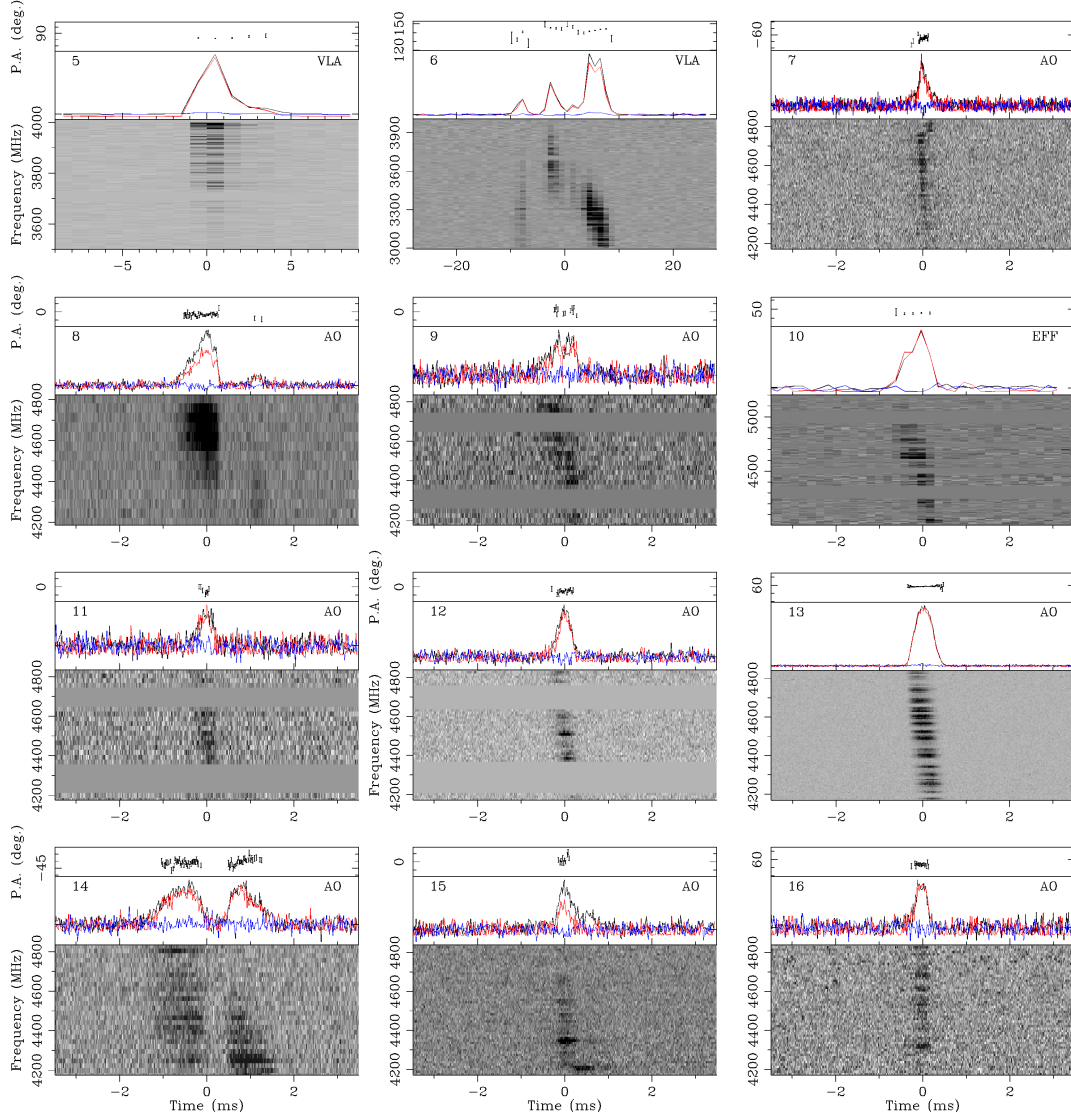


Figure 5.1: Dynamic spectra of the bursts detected with Arecibo, VLA, and Effelsberg in a chronological order, dedispersed to their respective DMs listed in Table 5.1. On top of each spectrum is plotted the profile of the burst (in black), linear polarisation (in red), and circular polarisation (blue), as well as the polarisation angle (PA). Each panel is labeled with the corresponding burst number from Table 5.1 and the telescope at which the burst was detected. Bursts 8, 15, 19, and 20 suffer from poor polarisation calibration, resulting in unreliable polarisation fractions (see §5.3.2). Figure continued on next page.

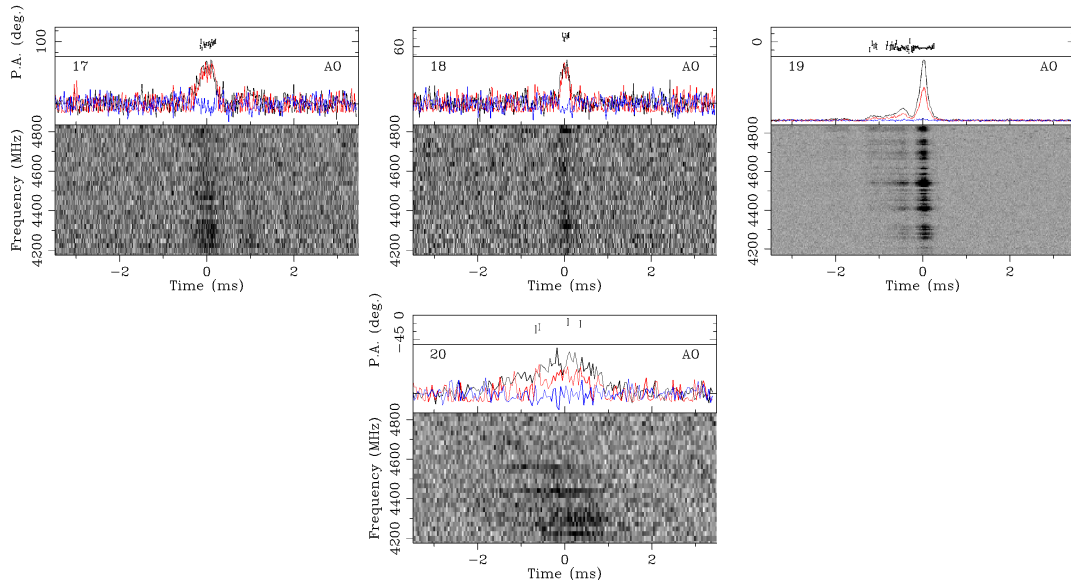


Figure 5.1 continued.

## 5.5 Implications for source scenarios

We explore two models which estimate the RM evolution over time within an SNR. First is a model from Piro & Gaensler (2018) which estimates both the RM and DM evolution for three different scenarios: a supernova expanding into a constant density ISM, a progenitor wind affecting the circumstellar medium, solely contributing to the RM, and a supernova expanding into wind affected ISM. The second model is a one-zone magnetar nebula expanding spherically at a constant radial velocity (Margalit & Metzger, 2018).

Additionally, we consider an environment near a massive black hole by comparing to the GC magnetar, PSR J1745–2900. The RM magnitude and trend of FRB 121102 seems to be analogous to PSR J1745–2900, which has undergone rapid changes in RM in recent times (Desvignes et al., 2018).

Using Bayesian inference, we fit the RM evolution prediction from the aforementioned SNR models to the observed RM of FRB 121102. A Markov–chain Monte Carlo (MCMC) method is used to estimate the posterior of the model parameters and the age of the FRB 121102 bursting source,  $t_{\text{age}}$ , at the time of its first RM measurement. The models considered here predict that DM decreases over time, while the observed DM is increasing. We therefore do not perform a similar analysis on the DM evolution. To perform an MCMC we used the `emcee`<sup>14</sup> Python package (Foreman-Mackey et al., 2013). MCMC deploys random walkers around the initial estimates of the parameters, where the walkers explore the parameter space in order to reconstruct the posterior probability of the parameters.

To obtain an initial estimate for our parameters we used the `scipy` (Virtanen et al.,

<sup>14</sup>[emcee.readthedocs.io](https://emcee.readthedocs.io)

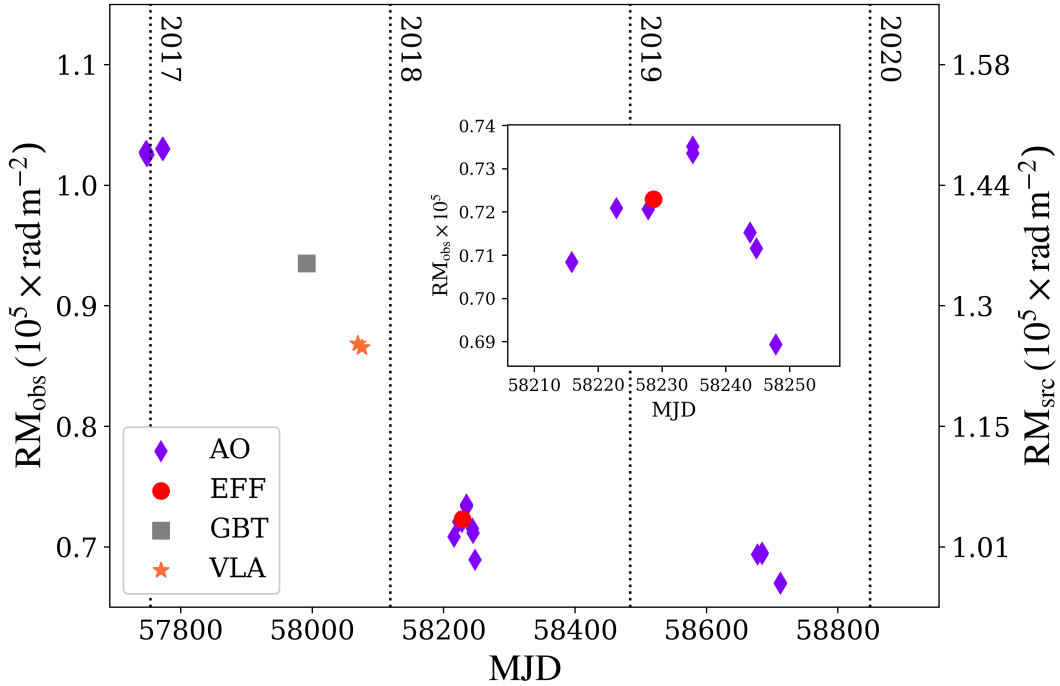


Figure 5.2: RMs of FRB 121102 as a function of time in MJD. The left y-axis shows the observed RM and the right y-axis shows the RM in the source frame of FRB 121102. Different markers indicate at which telescope the burst was detected. The horizontal dotted lines show the start of each calendar year. The inset gives a closer look at the cluster of bursts around MJD  $\sim 58230$  (when a high-cadence observing campaign was performed). The observed rotation measure uncertainties are not large enough to exceed the boundaries of the markers. Abbreviations are AO: Arecibo Observatory, Eff: Effelsberg, GBT: Green Bank Telescope, VLA: Very Large Array. The points near MJD 57800 and 58000 are data from Michilli et al. (2018a) and Gajjar et al. (2018) respectively.

2020) stochastic least squares module `differential_evolution`. An initial guess is also required for `differential_evolution`, where we used the parameters of each model variety in Piro & Gaensler (2018) and Margalit & Metzger (2018). For our MCMC we randomly scattered 10 walkers around each parameter (up to 10% away), where each walker was made to walk  $1.5 \times 10^3$  steps. We used uninformative uniform priors for all our model parameters.

The observed RMs can be affected by instrumental or other kinds of noise processes, which are unaccounted for in the observed uncertainties. We introduced an error added in quadrature,  $\Sigma$ , in order to account for underestimation of the uncertainties of the observed RMs.  $\Sigma$  enters our Gaussian likelihood function as an underestimation of the variance  $\sigma$  (observed RM uncertainties in this case) as

$$s^2 = \sigma^2 + \Sigma^2. \quad (5.2)$$

The measured RM uncertainties,  $\sigma$ , are on the order of  $\lesssim 10^2$  rad m<sup>-2</sup>.

Henceforth, all values mentioned will be in the reference frame of the source, unless otherwise stated. This requires a conversion of the observed values to the source frame. The conversions are  $DM_{\text{source}} = DM_{\text{obs}}(1 + z)$ ,  $RM_{\text{source}} = RM_{\text{obs}}(1 + z)^2$ , and  $t_{\text{source}} = t_{\text{obs}}(1 + z)^{-1}$ , where  $z \sim 0.2$  is the redshift of FRB 121102. This means that the minimum  $t_{\text{age}}$  possible in the source frame is just over 3 years due to the time elapsed from the first detection of FRB 121102 (Spitler et al., 2014a) and its first RM measurement (Michilli et al., 2018a). In the case of DM, we will only consider the contribution local to the source, i. e. local to the bursting source and the host galaxy. For each model we first describe it in more detail before comparing it to our results.

### 5.5.1 Piro & Gaensler (2018)

#### 5.5.1.1 Model Description

Piro & Gaensler (2018) model the temporal evolution of both RM and DM of an expanding SNR. They consider three cases of evolutionary environments, which we expand upon below.

The first evolutionary case is an SNR that expands into an ISM of constant density. The shocked, ionized regions of the SN ejecta and ISM, as well as ionized material from the pulsar wind nebula close to the SNR center, provide sufficient free electrons to disperse an FRB. The Faraday rotation arises from the magnetic fields generated by the forward and reverse shocks during the SNR expansion. The SNR dominates both the DM and RM contributions at early times until the ISM takes over on a timescale of  $\sim 10^2 - 10^3$  years. The free parameters in this model are the number density of the uniform ISM,  $n$ , and the SN ejecta mass,  $M$ . The energy of the explosion is kept constant as  $E = 10^{51}$  erg for all cases.

The second case is where the stellar wind of the massive progenitor affects the circumstellar environment. The magnetized wind provides another source of magnetic field as well as altering the DM evolution. The DM is much higher initially compared to the previous scenario due to high density for the wind adjacent to the SN, but

the DM decreases more rapidly because of the wind’s decreasing density. The wind environment produces an ordered magnetic field, which is swept up by the SNR. This is the focal point of RM generation in this scenario as opposed to the shock generation of magnetic fields in the previous scenario. The RM also drops rapidly due to the steep decline with time of the wind’s density and magnetic field. Here the free parameters are the ejecta mass,  $M$ , and the wind mass loading parameter,  $K$ , which is a function of the mass loss rate,  $\dot{M}$ , and wind velocity,  $v_w$ , and is given in units of  $\text{g cm}^{-1}$ .

The third is a mixture of the first two scenarios; an SNR expands into an ISM affected by a constant velocity wind, with  $M$  and  $K$  as free parameters. For all three cases they assume supernova ejecta masses of  $10 M_\odot$  (red supergiant progenitor) and  $2 M_\odot$  (stripped-envelope SN).

### 5.5.1.2 Results

Using an MCMC we can estimate the posterior of  $n$ ,  $K$ ,  $t_{\text{age}}$ , and  $\Sigma$  of each model variety (Piro & Gaensler, 2018, Eqs. 26, 57, and Appendix) using the measured RM values of FRB 121102 (Table 5.1). Our initial guesses are the median values of  $n$  ( $1 \text{ cm}^{-3}$ ) and  $K$  ( $10^{13} \text{ g cm}^{-1}$ ) from Piro & Gaensler (2018),  $t_{\text{age}} = 5$  years, and  $\Sigma = 10^3 \text{ rad m}^{-2}$  (roughly 1% of the observed RM magnitude). We plot our 2D posterior corner plots in Fig. 5.3 and list our results in Table 5.3.

For the constant ISM model we obtain a  $t_{\text{age}}$  of 1.4 years at the time of the first RM detection. For the wind and wind plus SNR evolution models we obtain  $t_{\text{age}}$  between  $\sim 6$ –8 years. The range of RM from our results (1-sigma error) for each model and mass is plotted as a function of time in Fig. 5.4, and overplotted with the observed RM values of FRB 121102.

We also plot the local DM versus RM for the models in Piro & Gaensler (2018) in Fig. 5.5, showing how the DM changes as RM decreases over time. The estimated source frame local DM (up to  $270 \text{ pc cm}^{-3}$ , Tendulkar et al., 2017) and the source frame RM values of FRB 121102 are overplotted on the figure.

## 5.5.2 Margalit & Metzger (2018)

### 5.5.2.1 Model Description

Margalit & Metzger (2018) consider a magnetar surrounded by a magnetar nebula. Flares and winds from the magnetar inject particles and magnetic energy into the nebula that is in turn responsible for the large observed RM. Their model is a one-zone magnetar nebula model, where they assume a spherical, freely expanding nebula with a constant radial velocity,  $v_n$ . The free magnetic energy of the magnetar,  $E_{B_*}$  is released into the nebula at a rate following a power-law in time,  $\dot{E} \propto t^{-\alpha}$  (Margalit & Metzger, 2018, Eq. 4), where  $\alpha \gtrsim 1$ . The Faraday rotation occurs in non-relativistic electrons ejected earlier in the nebula’s history and cooled from radiation and adiabatic expansion.

In this model, the RM can be approximated as (Margalit & Metzger, 2018, Eq. 19,

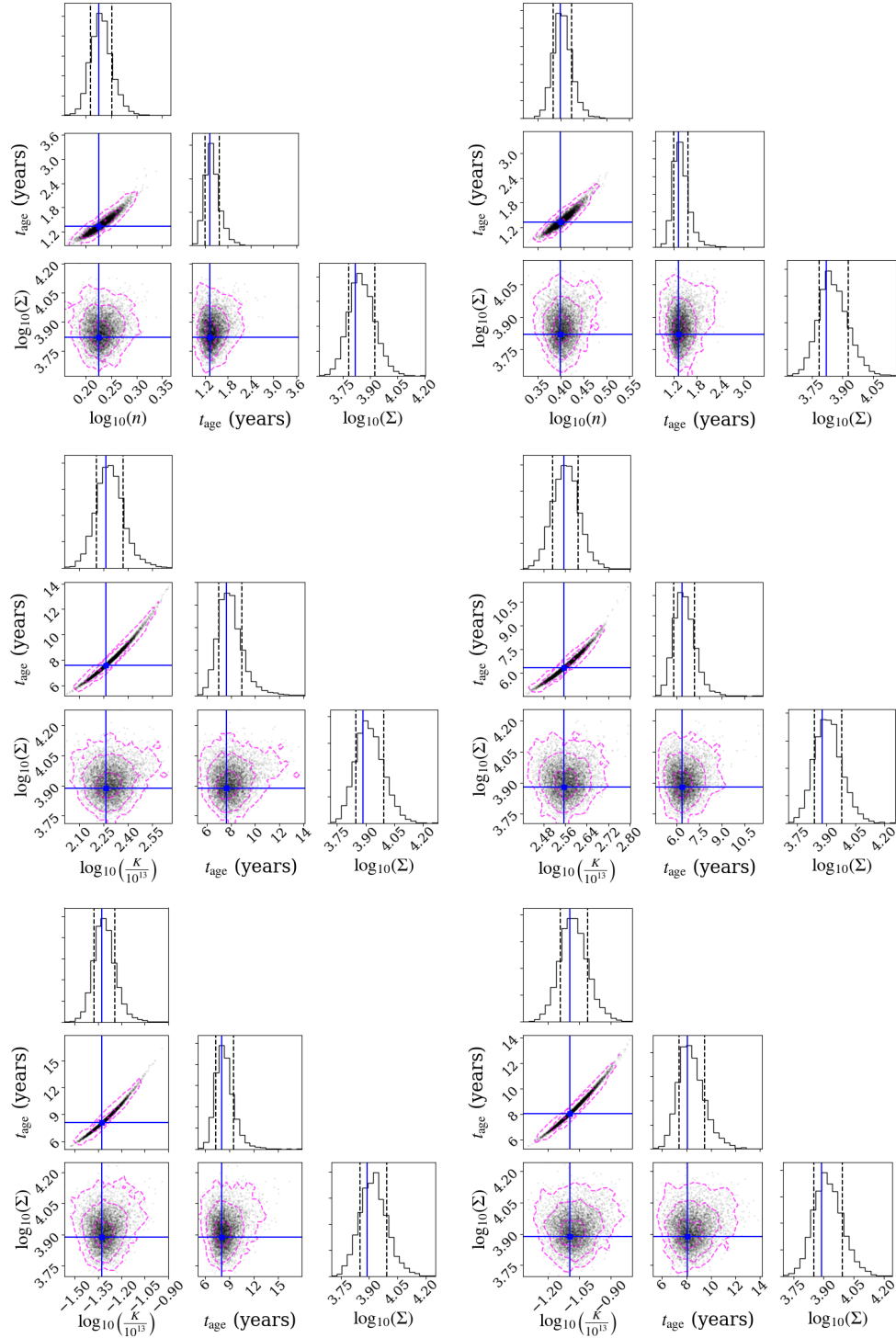


Figure 5.3: 2D posterior corner plot for the parameters ( $n$ ,  $K$ ,  $t_{\text{age}}$ , and  $\Sigma$ ) of the models in Piro & Gaensler (2018). The histograms indicate the posterior probability of each parameter, with the dashed vertical lines denoting the 1-sigma range. The plots show the explored parameter space, with 1, 2, and 3 sigma dashed contours. The crosses indicate the prior used for each parameter, obtained with a stochastic least squares method. The left column shows the results for a  $10 M_{\odot}$  ejecta, and the right column for a  $2 M_{\odot}$  ejecta. *Top row*: Uniform ISM model. *Middle row*: Progenitor wind model. *Bottom row*: Progenitor wind and evolving supernova remnant model.

Table 5.3: Model parameters of Piro & Gaensler (2018) for each scenario. *From left to right:* Model scenario, supernova explosion energy ( $E$ ), supernova ejecta mass ( $M$ ), number density of surrounding uniform ISM ( $n$ ), wind mass loading parameter ( $K$ ), age of bursting source ( $t_{\text{age}}$ ), and the underestimation factor of the measured rotation measure,  $\Sigma$ . The parameters  $n$ ,  $K$ ,  $t_{\text{age}}$ , and  $\Sigma$  were obtained in this work (§5.5.1.2). Uncertainties are 1-sigma.

Model	E (erg)	$M$ ( $M_{\odot}$ )	$n$ ( $\text{cm}^{-3}$ )	$\log_{10}(K)$ ( $\text{g cm}^{-2}$ )	$t_{\text{age}}$ (years)	$\log_{10}(\Sigma)$ ( $\text{rad m}^{-2}$ )
Const. ISM	$10^{51}$	10	$1.7^{+0.1}_{-0.1}$	-	$1.4^{+0.2}_{-0.2}$	$3.9^{+0.1}_{-0.1}$
	$10^{51}$	2	$2.5^{+0.1}_{-0.1}$	-	$1.4^{+0.2}_{-0.2}$	$3.8^{+0.1}_{-0.1}$
Wind	$10^{51}$	10	-	$15.3^{+0.1}_{-0.1}$	$7.8^{+0.9}_{-1.1}$	$3.9^{+0.1}_{-0.1}$
	$10^{51}$	2	-	$15.6^{+0.1}_{-0.1}$	$6.4^{+0.6}_{-0.7}$	$3.9^{+0.1}_{-0.1}$
Wind + SNR	$10^{51}$	10	-	$11.7^{+0.1}_{-0.1}$	$8.3^{+1.0}_{-1.2}$	$3.9^{+0.1}_{-0.1}$
	$10^{51}$	2	-	$11.9^{+0.1}_{-0.1}$	$8.3^{+1.0}_{-1.1}$	$3.9^{+0.1}_{-0.1}$

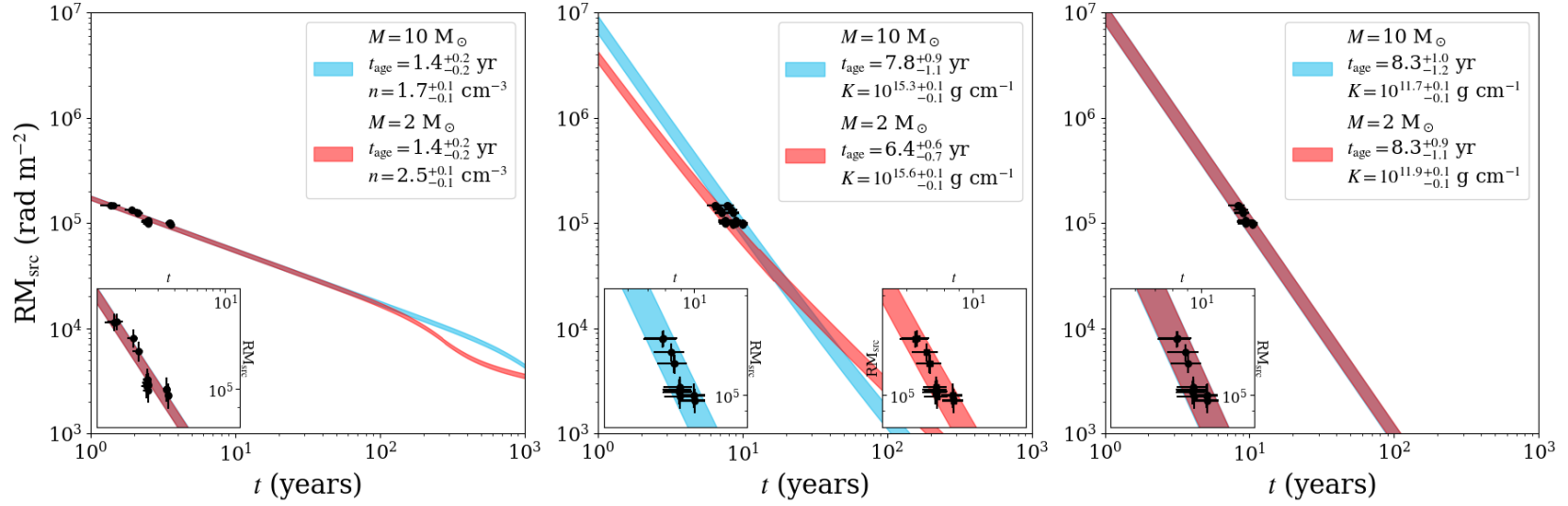


Figure 5.4: Source frame RM as a function of time for each model and ejecta mass in Piro & Gaensler (2018). The ranges show the possible RMs from the parameters obtained in this work with 1-sigma uncertainties (Table 5.3). The black dots are the source frame RMs of FRB 121102, starting at the obtained  $t_{\text{age}}$  for each model variation. The RM uncertainties are calculated from Eq. 5.2. The insets are zoomed in to the RM-time space around each  $t_{\text{age}}$ . *Left*: Uniform ISM model. *Center*: Progenitor wind model. *Right*: Progenitor wind and evolving supernova remnant model.

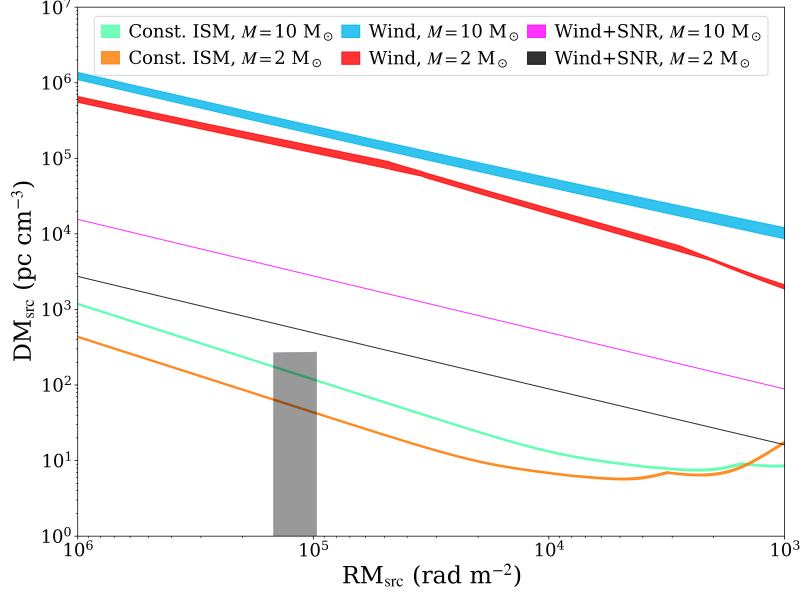


Figure 5.5: Source frame DM versus RM of each model scenario presented in Piro & Gaensler (2018). Shown are the ranges of the predicted DMs and RMs of each scenario using the parameters obtained in this work with 1-sigma uncertainties (Table 5.3). The grey shaded area shows the RM and estimated local source DM contribution of FRB 121102 in the reference frame of the bursting source.

values normalised to 1 are omitted for clarity)

$$\begin{aligned} \text{RM}_5 \approx & 6 \left( \frac{E_{B_*}}{10^{50} \text{ erg}} \right)^{3/2} \left( \frac{v_n}{10^{17} \text{ cm/s}} \right)^{-7/2} \\ & \times (\alpha - 1)^{3/2} t_0^{(\alpha-1)/2} t^{-(6+\alpha)/2} \text{ rad m}^{-2}, \end{aligned} \quad (5.3)$$

where  $\text{RM}_5 \equiv \text{RM}/10^5 \text{ rad m}^{-2}$ ,  $E_{B_*}$  is in erg,  $v_n$  in  $\text{cm s}^{-1}$ ,  $t$  is seconds since the SN explosion, and  $t_0$  is the time in seconds since the onset of the active period of the magnetar's energy release into the nebula. We extract  $t_{\text{age}}$  from Eq. 5.3 by replacing  $t$  with  $t_{\text{age}} + t'$ , where  $t'$  is the time elapsed in seconds of each RM measurement since the first one.

For completeness, the estimated DM contribution from the Faraday-rotating medium is given by

$$\begin{aligned} \text{DM} \sim & 3 \times 10^{18} \left( \frac{E_{B_*}}{10^{50}} \right) \left( \frac{v_n}{10^8} \right)^{-2} \\ & \times (\alpha - 1) t^{-2} \text{ pc cm}^{-3} \end{aligned} \quad (5.4)$$

In their analysis, Margalit & Metzger (2018) consider three variations of their model with each having its own set of values for  $E_{B_*}$ ,  $t_0$ ,  $v_n$ , and  $\alpha$ . They call these variations 'model A, B, and C', and we keep the same notation to avoid confusion.

Margalit & Metzger (2018) use models A, B, and C to estimate  $t_{\text{age}}$  of FRB 121102 from Eq. 5.3 using the RM measurements from Michilli et al. (2018a) and Gajjar et al. (2018). Their choice of parameters and their results are shown in Table 5.4.

### 5.5.2.2 Results

Again, we used MCMC to estimate the posterior of  $\alpha$ ,  $t_{\text{age}}$ , and  $\Sigma$ . The initial guesses are the parameters of models A, B, and C and  $t_{\text{age}}$  in Margalit & Metzger (2018), and like before  $\Sigma = 10^3 \text{ rad m}^{-2}$ . We plot our 2D posterior corner plots in Fig. 5.6, and list our results in Table 5.4.

A similar  $t_{\text{age}}$  of  $\sim 15\text{--}17$  years was obtained for all the models. Our obtained  $\alpha$  values lie in the range of 1.1–1.6 and are consistent with the values in Margalit & Metzger (2018). The resulting RM range (1-sigma error), overplotted with observed FRB 121102 RM values is plotted in Fig. 5.7.

### 5.5.3 Galactic Center Magnetar PSR J1745–2900

The GC magnetar PSR J1745–2900 has exhibited similar behaviour as FRB 121102 regarding changes in RM. Since its first RM measurements of  $-67000 \text{ rad m}^{-2}$  (Eatough et al., 2013), it showed some variations in RM of a few hundred  $\text{rad m}^{-2}$  per year for a few years until its RM suddenly exhibited a steep drop in absolute magnitude (Desvignes et al., 2018). This drop in RM is similar to FRB 121102, albeit not as intense, as PSR J1745–2900 had a drop of 5% in RM over the course of a year while the RM of FRB 121102 has dropped by an average of  $15\% \text{ yr}^{-1}$  over roughly two years. Both PSR J1745–2900 and FRB 121102 exhibit short-term variations in their observed RMs. Although somewhat similar, the magnitude of the FRB 121102 variations is greater. Desvignes et al. (2018) also report a constant DM and attribute the RM evolution to the changing line of sight towards the moving magnetar where either the projected magnetic field or the GC free electron content varies.

Desvignes et al. (2018) use the measured proper motion of PSR J1745–2900 to estimate the characteristic size of magneto-ionic fluctuations to be  $\sim 2$  astronomical units (AU). Assuming the bursts from FRB 121102 originate from the magnetosphere of a neutron star with a speed of  $\sim 100 \text{ km s}^{-1}$ , the source moves a distance of 20 AU per year. The observations of PSR J1745–2900 show that spatial variations on the scale of a few to 10s of AUs are possible in the vicinity of a massive black hole. If the host of FRB 121102 also harbors a massive black hole, the variations seen in the RM of FRB 121102 could be caused by the changing medium in its accretion disk. The velocity of the medium could be much higher than in the Galactic center, contributing to the observed fluctuation.

## 5.6 Discussion

We compared our measured RM sample to the theoretical RM predictions of Piro & Gaensler (2018) and Margalit & Metzger (2018) by obtaining MCMC posteriors of the

Table 5.4: Model parameters of Margalit & Metzger (2018). *From left to right:* Model, free magnetic energy of the magnetar ( $E_{B^*}$ ), onset of magnetar’s active period ( $t_0$ ), radial velocity of expanding nebula ( $v_n$ ), power-law parameter ( $\alpha$ ) and age of bursting source ( $t_{\text{age}}$ ) used in Margalit & Metzger (2018), and  $\alpha$ ,  $t_{\text{age}}$ , and underestimation factor of the measured rotation measure,  $\Sigma$ , obtained in this work (§5.5.2.2). Uncertainties are 1-sigma.

Model	$E_{B^*}$ (erg)	$t_0$ (years)	$v_n$ (cm s <sup>-1</sup> )	$\alpha^{\text{a}}$	$t_{\text{age}}$ (years) <sup>a</sup>	$\alpha^{\text{b}}$	$t_{\text{age}}$ (years) <sup>b</sup>	$\log_{10}(\Sigma)$ (rad m <sup>-2</sup> )
A	$5 \times 10^{50}$	0.2	$3 \times 10^8$	1.3	12.4	$1.6_{-0.4}^{+0.3}$	$16.8_{-0.6}^{+2.0}$	$3.9_{-0.1}^{+0.1}$
B	$5 \times 10^{50}$	0.6	$10^8$	1.3	37.8	$1.1_{-0.1}^{+0.1}$	$16.2_{-2.6}^{+2.0}$	$3.9_{-0.1}^{+0.1}$
C	$4.9 \times 10^{51}$	0.2	$9 \times 10^8$	1.83	13.1	$1.6_{-0.3}^{+0.3}$	$15.3_{-0.3}^{+0.8}$	$3.9_{-0.1}^{+0.1}$

<sup>a</sup>In Margalit & Metzger (2018)

<sup>b</sup>This work

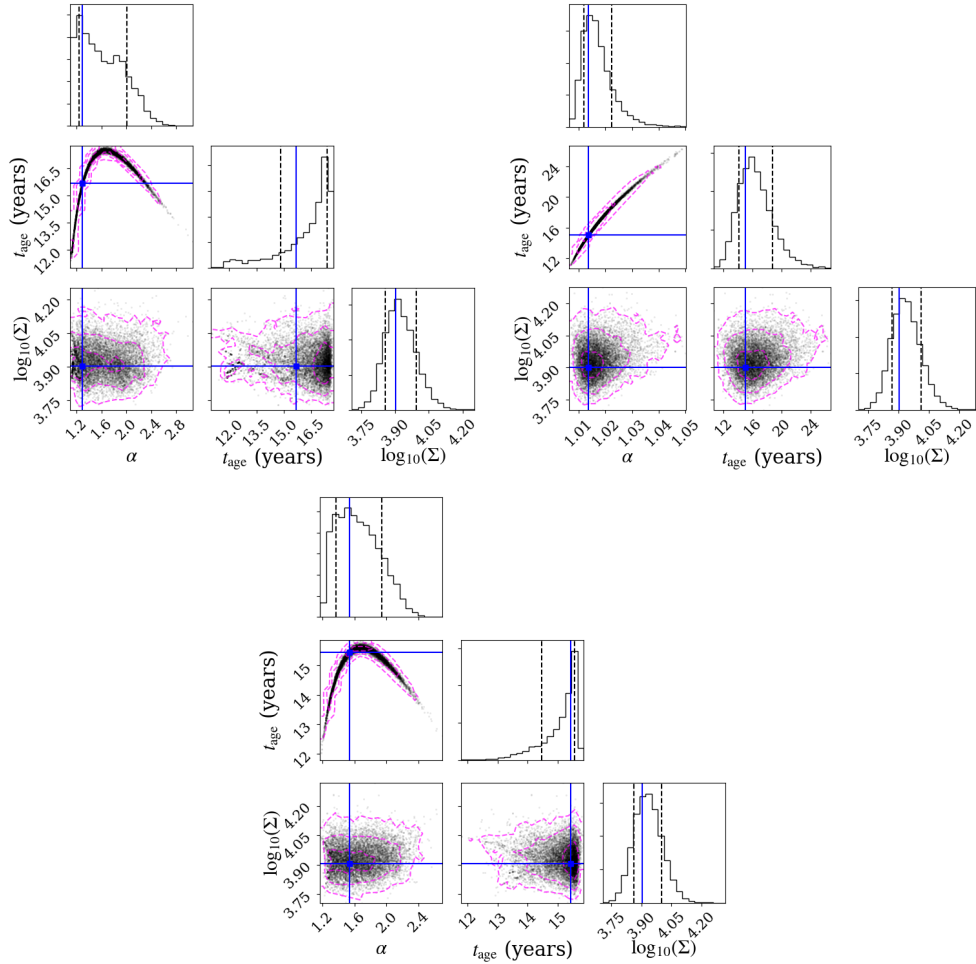


Figure 5.6: 2D posterior corner plot for the parameters ( $\alpha$ ,  $t_{\text{age}}$ , and  $\Sigma$ ) of the models in Margalit & Metzger (2018). The histograms indicate the posterior probability of each parameter, with the dashed vertical lines denoting the 1-sigma range. The plots show the explored parameter space, with 1, 2, and 3 sigma dashed contours. The crosses indicate the prior used for each parameter, obtained with a stochastic least squares method. *Top left:* Model A. *Top right:* Model B. *Bottom:* Model C.

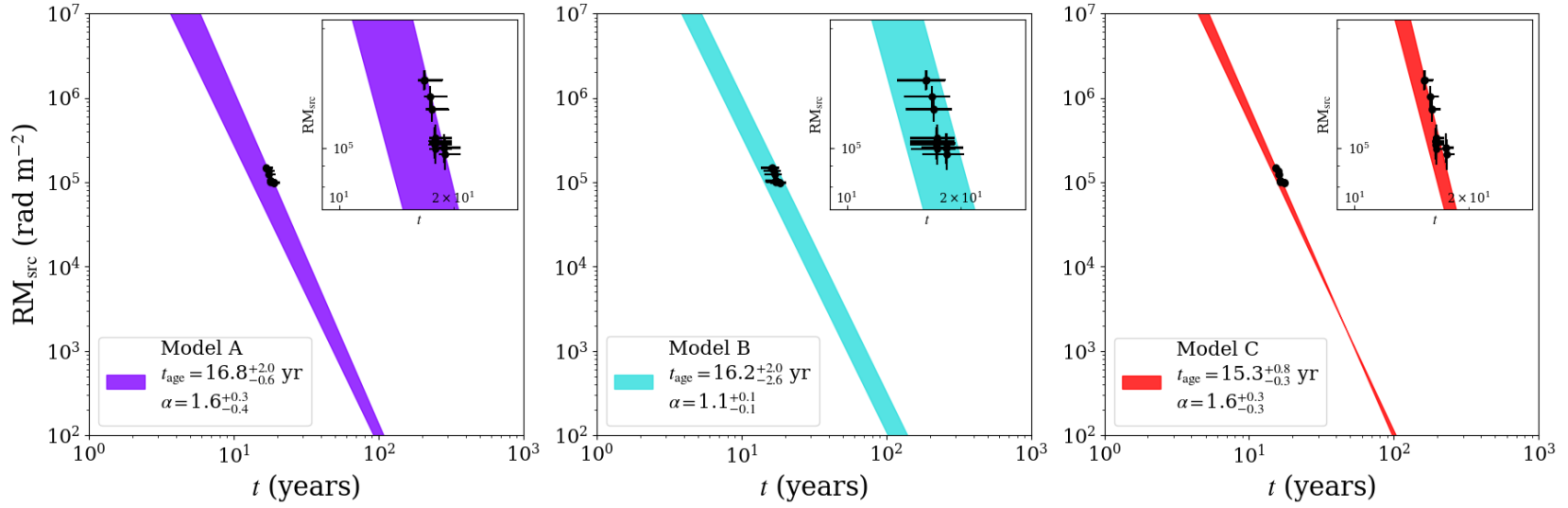


Figure 5.7: Source frame RM as a function of time for each model in Margalit & Metzger (2018). The ranges show the possible RMs from the parameters obtained in this work with 1-sigma uncertainties (Table 5.4). The black dots are the source frame RMs of FRB 121102, starting at the obtained  $t_{\text{age}}$  for each model. The RM uncertainties calculated from Eq. 5.2. The insets are zoomed in to the RM-time space around each  $t_{\text{age}}$ . *Left:* Model A. *Center:* Model B. *Right:* Model C.

model parameters and the age of the FRB 121102 bursting source at the time of its first RM measurement,  $t_{\text{age}}$ .

For the model variations in Piro & Gaensler (2018), we obtain a  $t_{\text{age}} \sim 1.5$  years for the uniform ISM scenario, and 6 – 9 years for the progenitor wind and progenitor wind plus SNR evolution scenarios. Based on observations, the minimum possible  $t_{\text{age}}$  is  $\gtrsim 3$  years, so we exclude the uniform ISM scenario. A drawback for the wind-only scenario is that it requires a high wind mass loading parameter ( $K > 10^{15} \text{ g cm}^{-1}$ ) to be consistent with the data.

We also compare our sample to the predicted DM vs RM evolution in Piro & Gaensler (2018). The excluded uniform ISM scenario predicts DM values consistent with FRB 121102, but both wind scenarios predict much higher DMs than is observed. However, all the model variations predict a decrease rather than increase in DM at the observed source frame RMs of FRB 121102.

Our results here show that origin scenarios with standard supernovae have difficulties explaining both the RM and DM of FRB 121102. A caveat is that the models assume uniform media, while the ISM, SNR, and wind environments most likely have spatial structures such as filaments.

For the models in Margalit & Metzger (2018) we obtain a  $t_{\text{age}}$  of  $\sim 15$ – $17$  years and  $\alpha$  of 1.1–1.6. Our results show that the observed RM evolution of FRB 121102 is consistent with these models. The estimated DM contribution from the nebula in Margalit & Metzger (2018) is  $\sim 2$ – $20 \text{ pc cm}^{-3}$  for models A, B, and C (Eq. 5.4). The measured increase in DM of  $\sim 4 \text{ pc cm}^{-3}$  is difficult to reconcile with the RM decrease if it originates from the same electrons.

The DM and RM might not necessarily be coupled. Metzger et al. (2019) estimate that photoionization just outside the propagating outward shock could contribute on the order of  $10 \text{ pc cm}^{-3}$  with an increase of a few  $\text{pc cm}^{-3}$  possible over several years. Therefore, the RM decrease and DM increase are likely occurring in different regions.

The SNR is initially optically thick at radio frequencies due to free-free absorption. According to Piro (2016), the SNR becomes optically thin at radio frequencies on a timescale of centuries if the SNR is solely ionised by the reverse shock. However, if the SNR is also photoionised from within by the magnetar wind nebula the SNR becomes optically thin at our observed frequencies on a timescale of  $\lesssim 10$  years (Metzger et al., 2017).

A by-product of our MCMC calculations is the error added in quadrature,  $\Sigma$ , which characterises the underestimation of the observed RM uncertainties. We find  $\Sigma$  to be consistent with  $\sim 10^{3.9} \text{ rad m}^{-2}$  for all models and their variations, or roughly 10% of the observed RMs. This underestimation could be due to unaccounted noise processes. Alternatively, the large  $\Sigma$  could be explained by deviations of the observed RMs from the RM evolution models considered in this work, which are inherently power-laws. These deviations could be due to LoS variations across observing epochs as is seen for PSR J1745–2900 (Desvignes et al., 2018).

PSR J1745–2900 has exhibited similarly drastic changes in RM over time (Desvignes et al., 2018). This change is attributed to variations in the projected magnetic field or the GC free electron content due to line of sight changes of the moving magnetar.

FRB 121102 is located outside of its host dwarf galaxy center (Tendulkar et al., 2017), but we cannot exclude a similar scenario due to the fact that AGNs can be found offset from the optical center of dwarf galaxies (Reines et al., 2020).

A comparison can be made between FRB 121102 and another localised, repeating FRB, FRB 180916.J1058+65, which has no discernable associated persistent radio source, and its RM is three orders of magnitude less than the RM of FRB 121102. However, it can still fit within the SNR framework where the persistent radio source has faded and the RM dropped to its observed levels due to the source being a few hundred years old (Marcote et al., 2020).

The observed RMs of FRB 121102 show large-scale variations of  $\sim 10^4$  rad m<sup>-2</sup> over year-timescales and small-scale variations of  $\sim 10^3$  rad m<sup>-2</sup> over week-timescales. There is no obvious periodicity in the observed RM variations at the proposed FRB 121102 periodicity of 161 days (Cruces et al., 2020).

Future polarisation measurements will show whether the RM of FRB 121102 has “leveled-off” at its current magnitude or will continue to vary. If the RM continues to decrease, the parameters of the SNR models considered in this work can be constrained further. On the other hand, if the RM will stay the same, the models can be rejected or will require adjustments. If the RM increases significantly, it would strongly challenge the SNR models.

Investigating the RM and DM evolution of repeating FRBs is certainly helpful in constraining source models. If FRBs, especially repeating ones, continue exhibiting vast differences from FRB 121102, such as host galaxy type, RM magnitude, and DM evolution, one must consider the possibility that FRB 121102 is a unique FRB source, likely residing locally to an AGN.

## 5.7 Conclusions

We present sixteen new RMs from bursts of FRB 121102 using observations taken with Arecibo, Effelsberg, and VLA.

Our Effelsberg survey consists of over 100 observing hours spanning over two years at 4 – 8 GHz (Table 5.2). An FRB 121102 survey of this magnitude in this frequency range is unprecedented, and thus enables us to present a robust, long-term average burst rate of  $0.21_{-0.18}^{+0.49}$  bursts/day above a fluence of  $0.04 (w/ms)^{1/2}$  Jy ms.

Along with previously reported RM values of FRB 121102 (Michilli et al., 2018a; Gajjar et al., 2018), we have an RM sample spanning roughly 2.5 years. During that time, the source frame RM has decreased significantly. From the first RM measurement at MJD 57747 to MJD 58215, the RM declined rapidly from  $1.4 \times 10^5$  rad m<sup>-2</sup> to  $1.0 \times 10^5$  rad m<sup>-2</sup>. From that point onward, the RM has stayed relatively constant, with only a slight decrease down to  $9.7 \times 10^4$  rad m<sup>-2</sup>. However, short-term RM variations of  $\sim 1000$  rad m<sup>-2</sup> per week have been observed during that period.

We fit the observed RM of FRB 121102 to theoretical models of RM evolution from within SNRs from Piro & Gaensler (2018) and Margalit & Metzger (2018). The results yield a source age estimate of 6–17 years for FRB 121102 at the time of its first RM

measurement in late 2016. Conventional SNRs do not agree with our data, but the inclusion of a pulsar wind nebula is compatible with our data.

## Acknowledgements

GHH thanks Dr. Ben Margalit for useful discussions and Dr. Nataliya K. Porayko for help with the MCMC implementation. The Arecibo Observatory is a facility of the National Science Foundation operated under cooperative agreement (#AST-1744119) by the University of Central Florida in alliance with Universidad Ana G. Méndez (UAGM) and Yang Enterprises (YEI), Inc. Based on observations with the 100-m telescope of the MPIfR (Max-Planck-Institut für Radioastronomie) at Effelsberg. The National Radio Astronomy Observatory is a facility of the National Science Foundation operated under cooperative agreement by Associated Universities, Inc. DM is a Banting Fellow. LGS is a Lise Meitner Independent Research Group leader and acknowledges support from the Max Planck Society. SH acknowledges financial support from the Deutsche Forschungsgemeinschaft (DFG) under grant BR2026/25. RSW acknowledges financial support by the European Research Council (ERC) for the ERC Synergy Grant BlackHoleCam under contract no. 610058. R.M. recognizes support from the Queen Elizabeth II Graduate Scholarship and the Lachlan Gilchrist Fellowship. J.W.T.H. acknowledges funding from an NWO Vici grant (“AstroFlash”). This publication has received funding from the European Union’s Horizon 2020 research and innovation programme under grant agreement No 730562 [RadioNet].



# Conclusions

---

The overarching topic of the work in this thesis is targeted searches of FRBs, an enigmatic phenomenon of cosmological origins whose properties and propagation effects were introduced in Chapter 1. How FRB data are acquired and searched was described in detail in Chapter 2.

The targeted searches conducted here have been twofold: observing potential locations of FRBs based on theoretical source models or similar environments of known FRBs to search for new FRBs (e.g. PRSs and SLSN/LGRBs), and observing known repeating FRBs in order to study them further. Both approaches focus on small areas of the celestial sky and are thus well suited for single-dish telescopes with high sensitivities and wide-band receivers. The former approach enables the validity of theoretical source models to be scrutinised. If an FRB were to be detected then the FRB origin problem would be solved. With non-detections, constraints can be placed on models. The latter approach of observing known repeating FRBs allows for detailed FRB studies, such as studying burst morphology to help reveal the emission process of FRBs, or investigating periodic activity and the RM and DM evolution to unveil the local environment of FRB bursting sources.

The following sections provide concluding remarks and future outlook for each of the science chapters of this thesis, followed by a section on a general future outlook of the FRB field.

## 6.1 PAF at Effelsberg

In Chapter 3, the commissioning observations of a PAF receiver at Effelsberg were described, which took place in March, June, and August 2018, and in March 2019. The observed targets were categorised into test PSRs, FRBs, PRSs, and miscellaneous sources.

No FRBs were detected during the PAF observations. However, the sensitivity of the PAF could be estimated based on the test PSR observations, resulting in a median SEFD of 254 Jy in August 2018 and 157 Jy in March 2019. Such a high SEFD results in a fluence detection threshold of  $\sim 2(w_{\text{ms}}/\text{ms})^{1/2}$  Jy ms. The non-detection of FRBs is therefore not surprising, as extremely bright bursts are required to surpass this fluence threshold. As an example, none of the FRB121102 bursts presented in Chapter 5 could have been detected with the PAF.

It is therefore vital for future observations to improve the sensitivity of the PAF. Badly beamformed channels, artificially reducing the observing bandwidth, are suspected to be one of the causes of the high estimated SEFD.

The commissioning of the PAF at Effelsberg is ongoing. Efforts have been made to improve the beamforming process, thus reducing the number of badly beamformed channels. Utilising the PAF beamforming in order to spatially reject RFI will undoubtedly improve the data quality and reduce the number of false positives while searching the data. Implementing a candidate classifier, such as `FETCH`, would improve the currently used false positive candidate rejection during post-processing.

The PAF commissioning observations provide an opportunity for long-exposure, high-cadence observations. This enables a detailed study of the apparent periodicities of FRB121102 and FRB180916.J0158+65. During active phases, investigation of whether bursts are uniformly distributed across the phase can be performed. On the other hand, the validity of the activity phases can be explored while observing during an inactive phase. Another observing opportunity is to observe repeating FRBs detected with CHIME, which have large localisation regions. The PAF FOV can cover each region in a single observation, and is therefore an ideal tool to further constrain the localisation regions. The improved localisation by PAF can be followed up by the likes of the EVN and the VLA in order to identify a host galaxy, or by more sensitive single-beam receivers for burst morphology and polarisation studies. Carrying out real-time searches with the PAF to trigger a baseband dump of burst detections will enable polarisation properties to be measured.

A cryogenically cooled PAF is under development based on experience with the current Effelsberg PAF. Such a PAF will have lower system temperature than the current PAF, and will thus be more sensitive. Continued commissioning of the Effelsberg PAF will provide a smooth transition to using the cooled PAF.

## 6.2 SLSNe/LGRBs

Chapter 4 describes the observations of ten SLSNe and LGRBs with Effelsberg at 4.6–9.3 GHz in order to search for repeating FRB sources. SLSNe and LGRBs were targeted due to their host galaxies sharing similarities with the host galaxy of FRB121102, and these transient events may produce magnetars that could generate FRBs.

As no FRBs were detected, UL burst rates and a scaled FRB121102 burst rate to each target were calculated. For nine of the targets the scaled rates were not constrained by the ULs. An FRB121102-like source associated with the SLSNe/LGRBs can therefore not be excluded at a 95% CL.

The scaled FRB121102 rate of the SLSN PTF10hgi, observed with the PAF at Effelsberg and the UWL at Parkes, is excluded at the 99% CL by the ULs. Assuming an FRB121102-like source residing within PTF10hgi and following a Weibull distributed bursting activity, the non-detection probability was estimated to be 14% and 16% from the PAF and UWL observations, respectively. These results show that an FRB121102-like source at PTF10hgi is unlikely. Other interpretations of non-detections from PTF10hgi are that the bursting source was observed during an “off-state” of either a Weibull distributed or periodic bursting activity, the SNR of PTF10hgi was still opaque at the observed frequencies, or that the bursting emission was beamed away

from Earth during the observations.

The recommendations made in §4.5 for future surveys of SLSNe/LGRBs were made under the assumption that FRB121102 bursts were clustered in time, i.e. following a Weibull distribution. At the time, the periodicity of FRB121102 was yet to be discovered. Assuming SLSNe/LGRBs contain FRB121102-like sources, surveys should be split into multiple, short observations on a regular basis. This is also a suitable strategy for periodic sources.

The burst rate of FRB121102 appears to be frequency dependent, with a rate of  $\sim 0.2$  bursts per day at 6 GHz (Hilmarsson et al., 2020a) and  $\sim 8$  bursts per day at 1.4 GHz (Cruces et al., 2020). For future surveys it is therefore recommended to observe at lower frequencies. The SNR is expected to become optically thin after  $\sim 9$  years at 1.4 GHz and  $\sim 5$  years at 6 GHz (Piro, 2016; Metzger et al., 2017). Therefore, SLSNe/LGRBs older than the ones observed in Chapter 4 must be targeted.

### 6.3 FRB121102 RM

The RM evolution of FRB121102 is investigated in Chapter 5. The first RM measurement of FRB121102 of  $1.46 \times 10^5$  rad m $^{-2}$  in the source reference frame was exceptionally high, and decreased down to  $1.33 \times 10^5$  rad m $^{-2}$  in seven months (Michilli et al., 2018a). In Chapter 5, sixteen FRB121102 RMs detected over roughly two years are presented, showing a continued decreasing trend in RM, dropping by an average of 15% per year down to  $9.7 \times 10^4$  rad m $^{-2}$  at the latest epoch of August 2019. However, the trend is not linear, as the relative decrease in RM since 2018 is only slight ( $\sim 10^4$  rad m $^{-2}$ ). Additionally, erratic, short-term RM variations of  $\sim 10^3$  rad m $^{-2}$  per week were observed.

The high RM of FRB121102 has been suggested to originate from the environment around a neutron star within an SNR, or a neutron star in the vicinity of a black hole. The RM evolution of FRB121102 is compared to theoretical RM evolution models of magnetars within SNRs (Piro & Gaensler, 2018; Margalit & Metzger, 2018), as well as the RM evolution of PSR J1745-2900 (Desvignes et al., 2018).

The varieties of the SNR RM models where the remnant magnetar is surrounded by a constant density ISM is inconsistent with observations. On the other hand, model varieties where a magnetar wind nebula is considered are consistent with our data. The model fitting also allows for an estimate of the source age of FRB121102 at the time of the first RM measurement, yielding an age of 6–17 years.

PSR J1745-2900's RM has exhibited similar variations as FRB121102, although to a lesser degree. For a few years, variations of  $\sim 100$  rad m $^{-2}$  per year were seen, until its absolute RM dropped by 5% over a timescale of a year (Desvignes et al., 2018). These RM fluctuations were attributed to variations in either the projected magnetic field or the GC free electron content due to the changing line of sight towards the moving magnetar.

The theoretical RM evolution models are essentially power-laws in nature. If future RM measurements of FRB121102 reveal an ongoing stable and relatively flat evolution,

the models can be excluded or will require considerable adjustments. If the SNR models can be rejected, the most likely scenario of FRB121102 is that it is a bursting source residing locally to an AGN.

No obvious periodicity in the RM of FRB121102 is seen at its proposed bursting periodicity of 161 days (Cruces et al., 2020). With more FRB121102 RMs covering multiple activity phases, preferably with multiple RM detections per phase, short-term and long-term periodicities in RM can be explored in more detail. Changes or trends between and within active phases could also help solve the mystery behind FRB121102.

## 6.4 Future Outlook

FRBs are being detected in droves with the recent large FOV radio telescopes ASKAP and CHIME, rendering blind surveys with single-dish telescopes obsolete. This provides an excellent opportunity to solely utilise single-dish telescopes for targeted searches and follow-up of known FRBs, which includes localising poorly localised FRBs to host galaxies with the likes of the EVN. While discovering more FRBs is important, studying them over a wider frequency range with more sensitive telescopes is necessary to further study their nature. Cryogenically cooled PAFs and ultra-wide-band receivers are the next generation of receivers. The versatility of PAFs on single-dish telescopes has been demonstrated in Chapter 3, and the large instantaneous bandwidth of ultra-wide-band receivers is greatly advantageous over the current generation of receivers. Installing these kind of receivers at single-dish telescopes will result in excellent follow-up facilities for current and upcoming radio facilities.

Upcoming radio telescope facilities and improved technologies will surely spell exciting times for radio astronomy in coming years. The MeerKAT array in South Africa, the planned expansion of CHIME, and the monumental Square Kilometre Array in the Southern Hemisphere will bring unrivaled FOVs and sensitivities, capable of detecting and localising FRBs at an unprecedented rate.

# Bibliography

- Agarwal, D., Aggarwal, K., Burke-Spolaor, S., Lorimer, D. R., & Garver-Daniels, N. 2020, MNRAS, 497, 1661, doi: 10.1093/mnras/staa1856 (Cited on page 72.)
- Akahori, T., Ryu, D., & Gaensler, B. M. 2016, ApJ, 824, 105, doi: 10.3847/0004-637X/824/2/105 (Cited on page 14.)
- Bannister, K. W., Shannon, R. M., Macquart, J. P., et al. 2017, ApJ, 841, L12, doi: 10.3847/2041-8213/aa71ff (Cited on pages 4, 57 and 58.)
- Bannister, K. W., Deller, A. T., Phillips, C., et al. 2019, Science, 365, 565, doi: 10.1126/science.aaw5903 (Cited on pages 11, 55, 57 and 58.)
- Bannister, K. W., Deller, A. T., Phillips, C., et al. 2019, Science, doi: 10.1126/science.aaw5903 (Cited on pages 76, 79, 94 and 98.)
- Barrau, A., Rovelli, C., & Vidotto, F. 2014, Phys. Rev. D, 90, 127503, doi: 10.1103/PhysRevD.90.127503 (Cited on page 25.)
- Barsdell, B. R., Bailes, M., Barnes, D. G., & Fluke, C. J. 2012, in Astronomical Society of the Pacific Conference Series, Vol. 461, Astronomical Data Analysis Software and Systems XXI, ed. P. Ballester, D. Egret, & N. P. F. Lorente, 37. <https://arxiv.org/abs/1112.0065> (Cited on page 42.)
- Bassa, C. G., Pleunis, Z., & Hessels, J. W. T. 2017a, Astronomy and Computing, 18, 40, doi: 10.1016/j.ascom.2017.01.004 (Cited on page 40.)
- Bassa, C. G., Tendulkar, S. P., Adams, E. A. K., et al. 2017b, ApJ, 843, L8, doi: 10.3847/2041-8213/aa7a0c (Cited on pages 19, 76 and 99.)
- Batten, A. 2019, The Journal of Open Source Software, 4, 1399, doi: 10.21105/joss.01399 (Cited on page 96.)
- Beloborodov, A. M. 2017, ApJ, 843, L26, doi: 10.3847/2041-8213/aa78f3 (Cited on pages 23, 90 and 99.)
- . 2019, arXiv e-prints, arXiv:1908.07743. <https://arxiv.org/abs/1908.07743> (Cited on pages 90 and 99.)
- Bera, A., & Chengalur, J. N. 2019, MNRAS, 490, L12, doi: 10.1093/mnrasl/slz140 (Cited on page 72.)
- Bhandari, S., Bannister, K. W., James, C. W., et al. 2019, MNRAS, 486, 70, doi: 10.1093/mnras/stz804 (Cited on page 55.)
- Bhandari, S., Keane, E. F., Barr, E. D., et al. 2018, MNRAS, 475, 1427, doi: 10.1093/mnras/stx3074 (Cited on pages 3, 5 and 56.)

- Bhandari, S., Sadler, E. M., Prochaska, J. X., et al. 2020, *ApJ*, 895, L37, doi: 10.3847/2041-8213/ab672e (Cited on page 24.)
- Bird, R., & VERITAS Collaboration. 2017, in *International Cosmic Ray Conference*, Vol. 301, 35th International Cosmic Ray Conference (ICRC2017), 621. <https://arxiv.org/abs/1708.04717> (Cited on page 27.)
- Bochenek, C. D., Ravi, V., Belov, K. V., et al. 2020, arXiv e-prints, arXiv:2005.10828. <https://arxiv.org/abs/2005.10828> (Cited on page 21.)
- Bonetti, L., Ellis, J., Mavromatos, N. E., et al. 2017, *Physics Letters B*, 768, 326, doi: 10.1016/j.physletb.2017.03.014 (Cited on page 28.)
- Brentjens, M. A., & de Bruyn, A. G. 2005, *A&A*, 441, 1217, doi: 10.1051/0004-6361:20052990 (Cited on pages 46 and 101.)
- Burke-Spolaor, S., & Bannister, K. W. 2014, *ApJ*, 792, 19, doi: 10.1088/0004-637X/792/1/19 (Cited on page 3.)
- Burn, B. J. 1966, *MNRAS*, 133, 67, doi: 10.1093/mnras/133.1.67 (Cited on page 101.)
- Caleb, M., Stappers, B., Barr, E., et al. 2019, *The Astronomer's Telegram*, 13098, 1 (Cited on page 18.)
- Caleb, M., Stappers, B. W., Abbott, T. D., et al. 2020, *MNRAS*, 496, 4565, doi: 10.1093/mnras/staa1791 (Cited on page 102.)
- Cao, X.-F., Yu, Y.-W., & Zhou, X. 2018, *ApJ*, 858, 89, doi: 10.3847/1538-4357/aabadd (Cited on page 6.)
- Champion, D. J., Petroff, E., Kramer, M., et al. 2016, *MNRAS*, 460, L30, doi: 10.1093/mnrasl/slw069 (Cited on pages 3, 5 and 60.)
- Chatterjee, S., Law, C. J., Wharton, R. S., et al. 2017, *Nature*, 541, 58, doi: 10.1038/nature20797 (Cited on pages 18, 19, 76, 98 and 99.)
- Chawla, P., Andersen, B. C., Bhardwaj, M., et al. 2020a, arXiv e-prints, arXiv:2004.02862. <https://arxiv.org/abs/2004.02862> (Cited on page 6.)
- . 2020b, *ApJ*, 896, L41, doi: 10.3847/2041-8213/ab96bf (Cited on page 98.)
- CHIME/FRB Collaboration, Amiri, M., Bandura, K., et al. 2019a, *Nature*, 566, 235, doi: 10.1038/s41586-018-0864-x (Cited on pages 4, 19, 63, 76 and 98.)
- . 2019b, *Nature*, 566, 230, doi: 10.1038/s41586-018-0867-7 (Cited on page 4.)
- CHIME/FRB Collaboration, Andersen, B. C., Bandura, K., et al. 2019c, *ApJ*, 885, L24, doi: 10.3847/2041-8213/ab4a80 (Cited on pages 19, 20, 71, 73 and 98.)
- Chime/Frb Collaboration, Amiri, M., Andersen, B. C., et al. 2020, *Nature*, 582, 351, doi: 10.1038/s41586-020-2398-2 (Cited on page 99.)

- Chippendale, A. P., Beresford, R. J., Deng, X., et al. 2016, in 2016 International Conference on Electromagnetics in Advanced Applications (ICEAA), 909–912, doi: 10.1109/ICEAA.2016.7731550 (Cited on page 59.)
- Chippendale, A. P., & Hellbourg, G. 2017, arXiv e-prints, arXiv:1706.04292. <https://arxiv.org/abs/1706.04292> (Cited on page 58.)
- Chippendale, A. P., Brown, A. J., Beresford, R. J., et al. 2015, in 2015 International Conference on Electromagnetics in Advanced Applications (ICEAA), 541–544, doi: 10.1109/ICEAA.2015.7297174 (Cited on page 55.)
- Connor, L., Lin, H.-H., Masui, K., et al. 2016, MNRAS, 460, 1054, doi: 10.1093/mnras/stw907 (Cited on page 5.)
- Connor, L., van Leeuwen, J., Oostrum, L. C., et al. 2020, arXiv e-prints, arXiv:2002.01399. <https://arxiv.org/abs/2002.01399> (Cited on page 55.)
- Cordes, J. M. 2002, Astronomical Society of the Pacific Conference Series, Vol. 278, Pulsar Observations I. – Propagation Effects, Searching Distance Estimates, Scintillations and VLBI, ed. S. Stanimirovic, D. Altschuler, P. Goldsmith, & C. Salter, 227–250 (Cited on pages 9 and 15.)
- Cordes, J. M., & Chatterjee, S. 2019, ARA&A, 57, 417, doi: 10.1146/annurev-astro-091918-104501 (Cited on pages 8 and 89.)
- Cordes, J. M., & Lazio, T. J. W. 2002, arXiv e-prints, astro. <https://arxiv.org/abs/astro-ph/0207156> (Cited on page 11.)
- Cordes, J. M., & McLaughlin, M. A. 2003, ApJ, 596, 1142, doi: 10.1086/378231 (Cited on page 41.)
- Cordes, J. M., & Wasserman, I. 2016, MNRAS, 457, 232, doi: 10.1093/mnras/stv2948 (Cited on pages 23, 77 and 90.)
- Crawford, D. F., Jauncey, D. L., & Murdoch, H. S. 1970, ApJ, 162, 405, doi: 10.1086/150672 (Cited on page 6.)
- Cruces, M., Spitler, L. G., Scholz, P., et al. 2020, arXiv e-prints, arXiv:2008.03461. <https://arxiv.org/abs/2008.03461> (Cited on pages 68, 69, 71, 86, 91, 92, 93, 99, 102, 120, 125 and 126.)
- Cunningham, V., Cenko, S. B., Burns, E., et al. 2019, ApJ, 879, 40, doi: 10.3847/1538-4357/ab2235 (Cited on page 26.)
- Deneva, J. S., Cordes, J. M., & Lazio, T. J. W. 2009, ApJ, 702, L177, doi: 10.1088/0004-637X/702/2/L177 (Cited on pages 72 and 73.)
- Deng, W., & Zhang, B. 2014, ApJ, 783, L35, doi: 10.1088/2041-8205/783/2/L35 (Cited on page 11.)

- Deng, X., Chippendale, A. P., Hobbs, G., et al. 2017, *PASA*, 34, e026, doi: 10.1017/pasa.2017.20 (Cited on page 59.)
- Deng, X., Chippendale, A., Barr, E., et al. 2018, in *IAU Symposium*, Vol. 337, *Pulsar Astrophysics the Next Fifty Years*, ed. P. Weltevrede, B. B. P. Perera, L. L. Preston, & S. Sanidas, 330–331, doi: 10.1017/S1743921317009899 (Cited on pages 55, 59 and 82.)
- Desvignes, G., Eatough, R. P., Pen, U. L., et al. 2018, *ApJ*, 852, L12, doi: 10.3847/2041-8213/aaa2f8 (Cited on pages 24, 63, 73, 77, 99, 107, 115, 119 and 125.)
- Dexter, J., Deller, A., Bower, G. C., et al. 2017a, *MNRAS*, 471, 3563, doi: 10.1093/mnras/stx1777 (Cited on page 72.)
- Dexter, J., Degenaar, N., Kerr, M., et al. 2017b, *MNRAS*, 468, 1486, doi: 10.1093/mnras/stx583 (Cited on page 72.)
- Dicke, R. H. 1946, *Review of Scientific Instruments*, 17, 268, doi: 10.1063/1.1770483 (Cited on pages 78 and 86.)
- Dunning, A., Bowen, M., Bourne, M., Hayman, D., & Smith, S. L. 2015, in *2015 IEEE-APS Topical Conference on Antennas and Propagation in Wireless Communications (APWC)*, 787–790, doi: 10.1109/APWC.2015.7300180 (Cited on page 82.)
- Dunning, A., Bowen, M. A., Hayman, D. B., et al. 2016, in *2016 46th European Microwave Conference (EuMC)*, 1568–1571 (Cited on page 55.)
- Eatough, R. P., Falcke, H., Karuppusamy, R., et al. 2013, *Nature*, 501, 391, doi: 10.1038/nature12499 (Cited on pages 73 and 115.)
- Eftekhari, T., Berger, E., Margalit, B., et al. 2019, *ApJ*, 876, L10, doi: 10.3847/2041-8213/ab18a5 (Cited on pages 63 and 78.)
- Everett, J. E., & Weisberg, J. M. 2001, *ApJ*, 553, 341, doi: 10.1086/320652 (Cited on pages 13 and 90.)
- Falcke, H., & Rezzolla, L. 2014, *A&A*, 562, A137, doi: 10.1051/0004-6361/201321996 (Cited on page 24.)
- Farah, W., Flynn, C., Bailes, M., et al. 2018, *MNRAS*, 478, 1209, doi: 10.1093/mnras/sty1122 (Cited on pages 4 and 40.)
- . 2019, *MNRAS*, 488, 2989, doi: 10.1093/mnras/stz1748 (Cited on page 4.)
- Fisher, J. R., Bradley, R. F., Briskin, W. F., et al. 2009, in *astro2010: The Astronomy and Astrophysics Decadal Survey*, Vol. 2010, 39 (Cited on page 56.)
- Fonseca, E., Andersen, B. C., Bhardwaj, M., et al. 2020a, *ApJ*, 891, L6, doi: 10.3847/2041-8213/ab7208 (Cited on page 19.)

- . 2020b, arXiv e-prints, arXiv:2001.03595. <https://arxiv.org/abs/2001.03595> (Cited on page 98.)
- Foreman-Mackey, D., Hogg, D. W., Lang, D., & Goodman, J. 2013, *PASP*, 125, 306, doi: 10.1086/670067 (Cited on page 107.)
- Fruchter, A. S., Levan, A. J., Strolger, L., et al. 2006, *Nature*, 441, 463, doi: 10.1038/nature04787 (Cited on page 77.)
- Gaensler, B. M. 2014, *GRB Coordinates Network*, 16533, 1 (Cited on page 21.)
- Gajjar, V., Siemion, A. P. V., Price, D. C., et al. 2018, *ApJ*, 863, 2, doi: 10.3847/1538-4357/aad005 (Cited on pages 7, 18, 19, 77, 84, 85, 98, 102, 103, 104, 108, 115 and 120.)
- Gal-Yam, A. 2019, *ARA&A*, 57, 305, doi: 10.1146/annurev-astro-081817-051819 (Cited on page 77.)
- Gehrels, N. 1986, *ApJ*, 303, 336, doi: 10.1086/164079 (Cited on page 84.)
- Gourdji, K., Michilli, D., Spitler, L. G., et al. 2019, *ApJ*, 877, L19, doi: 10.3847/2041-8213/ab1f8a (Cited on pages 6, 8, 19, 84 and 85.)
- Greiner, J., Mazzali, P. A., Kann, D. A., et al. 2015, *Nature*, 523, 189, doi: 10.1038/nature14579 (Cited on pages 23 and 77.)
- Gruzinov, A., & Levin, Y. 2019, *ApJ*, 876, 74, doi: 10.3847/1538-4357/ab0fa3 (Cited on page 104.)
- Guillochon, J., Parrent, J., Kelley, L. Z., & Margutti, R. 2017, *The Astrophysical Journal*, 835, 64, doi: 10.3847/1538-4357/835/1/64 (Cited on page 78.)
- Hackstein, S., Brüggén, M., Vazza, F., Gaensler, B. M., & Heesen, V. 2019, *MNRAS*, 488, 4220, doi: 10.1093/mnras/stz2033 (Cited on page 14.)
- Han, J., Wang, C., Xu, J., & Han, J.-L. 2016, *Research in Astronomy and Astrophysics*, 16, 159, doi: 10.1088/1674-4527/16/10/159 (Cited on page 6.)
- Hardy, L. K., Dhillon, V. S., Spitler, L. G., et al. 2017, *MNRAS*, 472, 2800, doi: 10.1093/mnras/stx2153 (Cited on page 27.)
- Hay, S. G., & O’Sullivan, J. D. 2008, *Radio Science*, 43, RS6S04, doi: 10.1029/2007RS003798 (Cited on page 82.)
- Heald, G. 2009, in *IAU Symposium*, Vol. 259, *Cosmic Magnetic Fields: From Planets, to Stars and Galaxies*, ed. K. G. Strassmeier, A. G. Kosovichev, & J. E. Beckman, 591–602, doi: 10.1017/S1743921309031421 (Cited on page 101.)
- Hessels, J. W. T., Spitler, L. G., Seymour, A. D., et al. 2019, *ApJ*, 876, L23, doi: 10.3847/2041-8213/ab13ae (Cited on pages 6, 18, 19, 20, 77, 85, 98 and 104.)

- Hilmarsson, G. H., Michilli, D., Spitler, L. G., et al. 2020a, arXiv e-prints, arXiv:2009.12135. <https://arxiv.org/abs/2009.12135> (Cited on pages 18, 19, 85, 86 and 125.)
- Hilmarsson, G. H., Spitler, L. G., Keane, E. F., et al. 2020b, MNRAS, 493, 5170, doi: 10.1093/mnras/staa701 (Cited on page 100.)
- Hotan, A. W., van Straten, W., & Manchester, R. N. 2004, PASA, 21, 302, doi: 10.1071/AS04022 (Cited on pages 45, 82 and 100.)
- Houben, L. J. M., Spitler, L. G., ter Veen, S., et al. 2019, A&A, 623, A42, doi: 10.1051/0004-6361/201833875 (Cited on pages 7, 18 and 27.)
- Ioka, K., & Zhang, B. 2020, ApJ, 893, L26, doi: 10.3847/2041-8213/ab83fb (Cited on page 24.)
- Jackson, J. D. 1962, Classical Electrodynamics (Cited on page 12.)
- James, C. W. 2019, MNRAS, 486, 5934, doi: 10.1093/mnras/stz1224 (Cited on pages 6, 71, 84 and 85.)
- James, C. W., Ekers, R. D., Macquart, J. P., Bannister, K. W., & Shannon, R. M. 2019, MNRAS, 483, 1342, doi: 10.1093/mnras/sty3031 (Cited on page 6.)
- Jankowski, F., van Straten, W., Keane, E. F., et al. 2018, MNRAS, 473, 4436, doi: 10.1093/mnras/stx2476 (Cited on pages 6 and 7.)
- Jansson, R., & Farrar, G. R. 2012, ApJ, 761, L11, doi: 10.1088/2041-8205/761/1/L11 (Cited on page 14.)
- Johnston, S., Kramer, M., Lorimer, D. R., et al. 2006, MNRAS, 373, L6, doi: 10.1111/j.1745-3933.2006.00232.x (Cited on page 72.)
- Johnston, S., Taylor, R., Bailes, M., et al. 2008, Experimental Astronomy, 22, 151, doi: 10.1007/s10686-008-9124-7 (Cited on page 82.)
- Josephy, A., Chawla, P., Fonseca, E., et al. 2019, ApJ, 882, L18, doi: 10.3847/2041-8213/ab2c00 (Cited on pages 18 and 98.)
- Karuppusamy, R., Stappers, B. W., & Lee, K. J. 2012, A&A, 538, A7, doi: 10.1051/0004-6361/201117667 (Cited on page 6.)
- Keane, E. F., & Petroff, E. 2015, MNRAS, 447, 2852, doi: 10.1093/mnras/stu2650 (Cited on page 8.)
- Keane, E. F., Stappers, B. W., Kramer, M., & Lyne, A. G. 2012, MNRAS, 425, L71, doi: 10.1111/j.1745-3933.2012.01306.x (Cited on page 3.)
- Kulkarni, S. R. 2018, Nature Astronomy, 2, 832, doi: 10.1038/s41550-018-0621-y (Cited on page 22.)

- Kumar, P., Lu, W., & Bhattacharya, M. 2017, *MNRAS*, 468, 2726, doi: 10.1093/mnras/stx665 (Cited on pages 23 and 90.)
- Kumar, P., Shannon, R. M., Osłowski, S., et al. 2019, *ApJ*, 887, L30, doi: 10.3847/2041-8213/ab5b08 (Cited on page 98.)
- Law, C. J., Gaensler, B. M., Metzger, B. D., Ofek, E. O., & Sironi, L. 2018, *ApJ*, 866, L22, doi: 10.3847/2041-8213/aae5f3 (Cited on page 63.)
- Law, C. J., Abruzzo, M. W., Bassa, C. G., et al. 2017, *ApJ*, 850, 76, doi: 10.3847/1538-4357/aa9700 (Cited on pages 7, 84 and 90.)
- Law, C. J., Omand, C. M. B., Kashiyama, K., et al. 2019, arXiv e-prints, arXiv:1910.02036. <https://arxiv.org/abs/1910.02036> (Cited on page 78.)
- Levin, L. 2012, PhD thesis, Swinburne University of Technology (Cited on pages 51 and 83.)
- Levin, Y., Beloborodov, A. M., & Bransgrove, A. 2020, arXiv e-prints, arXiv:2002.04595. <https://arxiv.org/abs/2002.04595> (Cited on page 24.)
- Li, Z.-X., Gao, H., Ding, X.-H., Wang, G.-J., & Zhang, B. 2018, *Nature Communications*, 9, 3833, doi: 10.1038/s41467-018-06303-0 (Cited on page 29.)
- Lingam, M., & Loeb, A. 2017, *ApJ*, 837, L23, doi: 10.3847/2041-8213/aa633e (Cited on page 25.)
- Liu, B., Li, Z., Gao, H., & Zhu, Z.-H. 2019, *Phys. Rev. D*, 99, 123517, doi: 10.1103/PhysRevD.99.123517 (Cited on page 29.)
- Lorimer, D. R., Bailes, M., McLaughlin, M. A., Narkevic, D. J., & Crawford, F. 2007, *Science*, 318, 777, doi: 10.1126/science.1147532 (Cited on pages 3 and 76.)
- Lorimer, D. R., & Kramer, M. 2012, *Handbook of Pulsar Astronomy* (Cited on pages 8, 9, 12, 13, 14, 15, 17, 18, 32, 36, 40 and 63.)
- Luo, R., Lee, K., Lorimer, D. R., & Zhang, B. 2018, *MNRAS*, 481, 2320, doi: 10.1093/mnras/sty2364 (Cited on page 6.)
- Lyne, A., & Graham-Smith, F. 2012, *Pulsar Astronomy* (Cited on page 8.)
- Lyne, A., Graham-Smith, F., Weltevrede, P., et al. 2013, *Science*, 342, 598, doi: 10.1126/science.1243254 (Cited on page 90.)
- Lyubarsky, Y. 2014, *MNRAS*, 442, L9, doi: 10.1093/mnrasl/slu046 (Cited on pages 23, 90 and 99.)
- Macquart, J. P., & Ekers, R. 2018, *MNRAS*, 480, 4211, doi: 10.1093/mnras/sty2083 (Cited on pages 8 and 85.)

- Macquart, J.-P., & Koay, J. Y. 2013, *ApJ*, 776, 125, doi: 10.1088/0004-637X/776/2/125 (Cited on pages 15, 16 and 17.)
- Macquart, J. P., Shannon, R. M., Bannister, K. W., et al. 2019, *ApJ*, 872, L19, doi: 10.3847/2041-8213/ab03d6 (Cited on page 7.)
- Macquart, J. P., Prochaska, J. X., McQuinn, M., et al. 2020, *Nature*, 581, 391, doi: 10.1038/s41586-020-2300-2 (Cited on pages 28, 55, 57 and 98.)
- Madison, D. R., Agarwal, D., Aggarwal, K., et al. 2019, arXiv e-prints, arXiv:1909.11682. <https://arxiv.org/abs/1909.11682> (Cited on page 78.)
- MAGIC Collaboration, Acciari, V. A., Ansoldi, S., et al. 2018, *MNRAS*, 481, 2479, doi: 10.1093/mnras/sty2422 (Cited on page 27.)
- Malenta, M. 2018, PhD thesis, University of Manchester (Cited on page 60.)
- Manchester, R. N., Hobbs, G. B., Teoh, A., & Hobbs, M. 2005, *AJ*, 129, 1993, doi: 10.1086/428488 (Cited on pages 65 and 90.)
- Marcote, B., Nimmo, K., Salafia, O. S., et al. 2019, *ApJ*, 876, L14, doi: 10.3847/2041-8213/ab1aad (Cited on page 63.)
- Marcote, B., Paragi, Z., Hessels, J. W. T., et al. 2017, *ApJ*, 834, L8, doi: 10.3847/2041-8213/834/2/L8 (Cited on pages 19, 76 and 99.)
- Marcote, B., Nimmo, K., Hessels, J. W. T., et al. 2020, *Nature*, 577, 190, doi: 10.1038/s41586-019-1866-z (Cited on pages 20, 21, 76, 94, 98 and 120.)
- Margalit, B., Beniamini, P., Sridhar, N., & Metzger, B. D. 2020, arXiv e-prints, arXiv:2005.05283. <https://arxiv.org/abs/2005.05283> (Cited on page 21.)
- Margalit, B., Berger, E., & Metzger, B. D. 2019, *ApJ*, 886, 110, doi: 10.3847/1538-4357/ab4c31 (Cited on page 25.)
- Margalit, B., & Metzger, B. D. 2018, *ApJ*, 868, L4, doi: 10.3847/2041-8213/aaedad (Cited on pages vii, x, xi, 99, 107, 109, 110, 114, 115, 116, 117, 118, 119, 120 and 125.)
- Masui, K., Lin, H.-H., Sievers, J., et al. 2015, *Nature*, 528, 523, doi: 10.1038/nature15769 (Cited on pages 3, 7 and 60.)
- Masui, K. W., & Sigurdson, K. 2015, *Phys. Rev. Lett.*, 115, 121301, doi: 10.1103/PhysRevLett.115.121301 (Cited on page 28.)
- McQuinn, M. 2014, *ApJ*, 780, L33, doi: 10.1088/2041-8205/780/2/L33 (Cited on pages 12, 28 and 79.)
- Men, Y., Aggarwal, K., Li, Y., et al. 2019, *MNRAS*, 489, 3643, doi: 10.1093/mnras/stz2386 (Cited on page 78.)

- Metzger, B. D., Berger, E., & Margalit, B. 2017, *ApJ*, 841, 14, doi: 10.3847/1538-4357/aa633d (Cited on pages 22, 23, 76, 77, 89, 119 and 125.)
- Metzger, B. D., Margalit, B., & Sironi, L. 2019, *MNRAS*, 485, 4091, doi: 10.1093/mnras/stz700 (Cited on pages 23, 77, 90 and 119.)
- Michilli, D., & Hessels, J. W. T. 2018, *SpS: Single-pulse Searcher*. <http://ascl.net/1806.013> (Cited on page 101.)
- Michilli, D., Seymour, A., Hessels, J. W. T., et al. 2018a, *Nature*, 553, 182, doi: 10.1038/nature25149 (Cited on pages 6, 7, 19, 76, 98, 102, 103, 104, 105, 108, 109, 115, 120 and 125.)
- Michilli, D., Hessels, J. W. T., Lyon, R. J., et al. 2018b, *MNRAS*, 480, 3457, doi: 10.1093/mnras/sty2072 (Cited on page 101.)
- Mitra, D., Wielebinski, R., Kramer, M., & Jessner, A. 2003, *A&A*, 398, 993, doi: 10.1051/0004-6361:20021702 (Cited on page 13.)
- Most, E. R., Nathanael, A., & Rezzolla, L. 2018, *ApJ*, 864, 117, doi: 10.3847/1538-4357/aad6ef (Cited on page 24.)
- Nimmo, K., Marcote, B., Hessels, J. W. T., et al. 2020, *The Astronomer's Telegram*, 13786, 1 (Cited on page 21.)
- Ofek, E. O. 2017, *ApJ*, 846, 44, doi: 10.3847/1538-4357/aa8310 (Cited on page 63.)
- Oosterloo, T., Verheijen, M., & van Cappellen, W. 2010, in *ISKAF2010 Science Meeting*, 43. <https://arxiv.org/abs/1007.5141> (Cited on page 55.)
- Oostrum, L. C., Maan, Y., van Leeuwen, J., et al. 2020, *A&A*, 635, A61, doi: 10.1051/0004-6361/201937422 (Cited on pages 6 and 55.)
- Oppermann, N., Yu, H.-R., & Pen, U.-L. 2018, *MNRAS*, 475, 5109, doi: 10.1093/mnras/sty004 (Cited on pages 20, 79, 90, 91, 93 and 98.)
- Palaniswamy, D., Li, Y., & Zhang, B. 2018, *ApJ*, 854, L12, doi: 10.3847/2041-8213/aaaa63 (Cited on page 88.)
- Palmer, D. M., & BAT Team. 2020, *GRB Coordinates Network*, 27665, 1 (Cited on page 21.)
- Patel, C., Agarwal, D., Bhardwaj, M., et al. 2018, *ApJ*, 869, 181, doi: 10.3847/1538-4357/aaee65 (Cited on page 5.)
- Perley, D. A., Quimby, R. M., Yan, L., et al. 2016, *ApJ*, 830, 13, doi: 10.3847/0004-637X/830/1/13 (Cited on page 77.)
- Pescalli, A., Ghirlanda, G., Salvaterra, R., et al. 2016, *A&A*, 587, A40, doi: 10.1051/0004-6361/201526760 (Cited on page 6.)

- Petroff, E., Hessels, J. W. T., & Lorimer, D. R. 2019, *A&A Rev.*, 27, 4, doi: 10.1007/s00159-019-0116-6 (Cited on pages 3, 8 and 98.)
- Petroff, E., Keane, E. F., Barr, E. D., et al. 2015a, *MNRAS*, 451, 3933, doi: 10.1093/mnras/stv1242 (Cited on page 3.)
- Petroff, E., Bailes, M., Barr, E. D., et al. 2015b, *MNRAS*, 447, 246, doi: 10.1093/mnras/stu2419 (Cited on pages 3 and 26.)
- Petroff, E., Barr, E. D., Jameson, A., et al. 2016, *PASA*, 33, e045, doi: 10.1017/pasa.2016.35 (Cited on pages 3, 6, 7, 8, 76 and 98.)
- Pietka, M., Fender, R. P., & Keane, E. F. 2015, *MNRAS*, 446, 3687, doi: 10.1093/mnras/stu2335 (Cited on page 3.)
- Pilia, M., Burgay, M., Possenti, A., et al. 2020, arXiv e-prints, arXiv:2003.12748. <https://arxiv.org/abs/2003.12748> (Cited on page 6.)
- Piro, A. L. 2016, *ApJ*, 824, L32, doi: 10.3847/2041-8205/824/2/L32 (Cited on pages 22, 77, 119 and 125.)
- Piro, A. L., & Gaensler, B. M. 2018, *ApJ*, 861, 150, doi: 10.3847/1538-4357/aac9bc (Cited on pages vii, ix, xi, 99, 107, 109, 110, 111, 112, 113, 114, 115, 119, 120 and 125.)
- Planck Collaboration, Ade, P. A. R., Aghanim, N., et al. 2016, *A&A*, 594, A13, doi: 10.1051/0004-6361/201525830 (Cited on page 11.)
- Platts, E., Weltman, A., Walters, A., et al. 2019, *Phys. Rep.*, 821, 1, doi: 10.1016/j.physrep.2019.06.003 (Cited on page 22.)
- Prochaska, J. X., & Zheng, Y. 2019, *MNRAS*, 485, 648, doi: 10.1093/mnras/stz261 (Cited on pages 11 and 79.)
- Prochaska, J. X., Macquart, J.-P., McQuinn, M., et al. 2019, *Science*, 366, 231, doi: 10.1126/science.aay0073 (Cited on pages 76, 94 and 98.)
- Qiu, H., Bannister, K. W., Shannon, R. M., et al. 2019, *MNRAS*, 486, 166, doi: 10.1093/mnras/stz748 (Cited on page 55.)
- Rajwade, K. M., Mickaliger, M. B., Stappers, B. W., et al. 2020a, *MNRAS*, doi: 10.1093/mnras/staa1237 (Cited on page 20.)
- . 2020b, arXiv e-prints, arXiv:2003.03596. <https://arxiv.org/abs/2003.03596> (Cited on pages 99 and 102.)
- Ransom, S. 2011, PRESTO: PulsAR Exploration and Search TOOLkit. <http://ascl.net/1107.017> (Cited on pages 46, 82 and 100.)

- Ravi, V., Shannon, R. M., & Jameson, A. 2015, *ApJ*, 799, L5, doi: 10.1088/2041-8205/799/1/L5 (Cited on page 3.)
- Ravi, V., Catha, M., D'Addario, L., et al. 2019, *Nature*, 572, 352, doi: 10.1038/s41586-019-1389-7 (Cited on pages 4, 11, 76, 79, 94 and 98.)
- Readhead, A. C. S. 1994, *ApJ*, 426, 51, doi: 10.1086/174038 (Cited on page 8.)
- Rees, M. J., & Meszaros, P. 1994, *ApJ*, 430, L93, doi: 10.1086/187446 (Cited on page 77.)
- Reines, A. E., Condon, J. J., Darling, J., & Greene, J. E. 2020, *ApJ*, 888, 36, doi: 10.3847/1538-4357/ab4999 (Cited on pages 24, 76 and 120.)
- Rickett, B. J. 1977, *ARA&A*, 15, 479, doi: 10.1146/annurev.aa.15.090177.002403 (Cited on page 17.)
- . 1990, *ARA&A*, 28, 561, doi: 10.1146/annurev.aa.28.090190.003021 (Cited on pages 12 and 18.)
- Romero, G. E., del Valle, M. V., & Vieyro, F. L. 2016, *Phys. Rev. D*, 93, 023001, doi: 10.1103/PhysRevD.93.023001 (Cited on pages 23 and 76.)
- Roshi, D. A., Shillue, W., Simon, B., et al. 2018, *AJ*, 155, 202, doi: 10.3847/1538-3881/aab965 (Cited on page 55.)
- Schechter, P. 1976, *ApJ*, 203, 297, doi: 10.1086/154079 (Cited on page 6.)
- Schnitzeler, D. H. F. M., & Lee, K. J. 2017, *MNRAS*, 466, 378, doi: 10.1093/mnras/stw3104 (Cited on page 46.)
- Scholz, P., Spitler, L. G., Hessels, J. W. T., et al. 2016, *ApJ*, 833, 177, doi: 10.3847/1538-4357/833/2/177 (Cited on page 18.)
- Scholz, P., Bogdanov, S., Hessels, J. W. T., et al. 2017, *ApJ*, 846, 80, doi: 10.3847/1538-4357/aa8456 (Cited on page 27.)
- Seymour, A., Michilli, D., & Pleunis, Z. 2019, *DM\_phase*: Algorithm for correcting dispersion of radio signals. <http://ascl.net/1910.004> (Cited on page 102.)
- Shannon, R. M., Macquart, J. P., Bannister, K. W., et al. 2018, *Nature*, 562, 386, doi: 10.1038/s41586-018-0588-y (Cited on pages 4 and 55.)
- Smith, S. W. 1997, *The Scientist and Engineer's Guide to Digital Signal Processing* (California Technical Publishing). <http://www.dspguide.com> (Cited on page 44.)
- Sokolowski, M., Bhat, N. D. R., Macquart, J. P., et al. 2018, *ApJ*, 867, L12, doi: 10.3847/2041-8213/aae58d (Cited on page 26.)
- Spitler, L. G., Cordes, J. M., Chatterjee, S., & Stone, J. 2012, *ApJ*, 748, 73, doi: 10.1088/0004-637X/748/2/73 (Cited on pages 51, 83 and 100.)

- Spitler, L. G., Cordes, J. M., Hessels, J. W. T., et al. 2014a, *ApJ*, 790, 101, doi: 10.1088/0004-637X/790/2/101 (Cited on pages 3, 4, 18, 19, 98 and 109.)
- Spitler, L. G., Lee, K. J., Eatough, R. P., et al. 2014b, *ApJ*, 780, L3, doi: 10.1088/2041-8205/780/1/L3 (Cited on page 72.)
- Spitler, L. G., Scholz, P., Hessels, J. W. T., et al. 2016, *Nature*, 531, 202, doi: 10.1038/nature17168 (Cited on pages 4, 18, 76, 90 and 98.)
- Spitler, L. G., Herrmann, W., Bower, G. C., et al. 2018, *ApJ*, 863, 150, doi: 10.3847/1538-4357/aad332 (Cited on pages 18, 85, 102 and 104.)
- Sun, H., Zhang, B., & Li, Z. 2015, *ApJ*, 812, 33, doi: 10.1088/0004-637X/812/1/33 (Cited on page 6.)
- Suresh, A., & Cordes, J. M. 2019, *ApJ*, 870, 29, doi: 10.3847/1538-4357/aaf004 (Cited on page 12.)
- Tauris, T. M., & Manchester, R. N. 1998, *MNRAS*, 298, 625, doi: 10.1046/j.1365-8711.1998.01369.x (Cited on page 90.)
- Tavani, M., Ursi, A., Verrecchia, F., et al. 2020, *The Astronomer's Telegram*, 13686, 1 (Cited on page 21.)
- Tendulkar, S. P., Bassa, C. G., Cordes, J. M., et al. 2017, *ApJ*, 834, L7, doi: 10.3847/2041-8213/834/2/L7 (Cited on pages 19, 24, 76, 79, 99, 105, 110 and 120.)
- The CHIME/FRB Collaboration, :, Andersen, B. C., et al. 2019, arXiv e-prints, arXiv:1908.03507. <https://arxiv.org/abs/1908.03507> (Cited on page 76.)
- The CHIME/FRB Collaboration, Amiri, M., Andersen, B. C., et al. 2020a, arXiv e-prints, arXiv:2001.10275. <https://arxiv.org/abs/2001.10275> (Cited on pages 6, 21 and 104.)
- The CHIME/FRB Collaboration, :, Andersen, B. C., et al. 2020b, arXiv e-prints, arXiv:2005.10324. <https://arxiv.org/abs/2005.10324> (Cited on page 21.)
- Thompson, A. R., Moran, J. M., & Swenson, George W., J. 2017, *Interferometry and Synthesis in Radio Astronomy*, 3rd Edition, doi: 10.1007/978-3-319-44431-4 (Cited on page 36.)
- Thornton, D., Stappers, B., Bailes, M., et al. 2013, *Science*, 341, 53, doi: 10.1126/science.1236789 (Cited on pages 3, 5 and 8.)
- Totani, T. 2013, *PASJ*, 65, L12, doi: 10.1093/pasj/65.5.L12 (Cited on page 25.)
- Tuthill, J., Hampson, G., Bunton, J., et al. 2012, 1067–1070, doi: 10.1109/ICEAA.2012.6328788 (Cited on page 59.)

- van Straten, W., & Bailes, M. 2011, *PASA*, 28, 1, doi: 10.1071/AS10021 (Cited on pages 65 and 101.)
- Vazza, F., Brüggén, M., Hinz, P. M., et al. 2018, *MNRAS*, 480, 3907, doi: 10.1093/mnras/sty1968 (Cited on page 28.)
- Vedantham, H. K., & Ravi, V. 2019, *MNRAS*, 485, L78, doi: 10.1093/mnrasl/slz038 (Cited on page 104.)
- Virtanen, P., Gommers, R., Oliphant, T. E., et al. 2020, *Nature Methods*, 17, 261, doi: <https://doi.org/10.1038/s41592-019-0686-2> (Cited on page 107.)
- Walker, C. R. H., Ma, Y. Z., & Breton, R. P. 2018, arXiv e-prints, arXiv:1804.01548. <https://arxiv.org/abs/1804.01548> (Cited on pages 12 and 79.)
- Wang, J.-S., Yang, Y.-P., Wu, X.-F., Dai, Z.-G., & Wang, F.-Y. 2016, *ApJ*, 822, L7, doi: 10.3847/2041-8205/822/1/L7 (Cited on page 25.)
- Williamson, I. P. 1972, *MNRAS*, 157, 55, doi: 10.1093/mnras/157.1.55 (Cited on page 14.)
- Wilson, T. L., Rohlf, K., & Hüttemeister, S. 2013, *Tools of Radio Astronomy*, doi: 10.1007/978-3-642-39950-3 (Cited on pages 31, 32 and 35.)
- Woosley, S. E. 1993, *ApJ*, 405, 273, doi: 10.1086/172359 (Cited on page 77.)
- Wright, E. L. 2006, *PASP*, 118, 1711, doi: 10.1086/510102 (Cited on page 7.)
- Xu, S., & Zhang, B. 2016, *ApJ*, 832, 199, doi: 10.3847/0004-637X/832/2/199 (Cited on page 16.)
- Yamasaki, S., Totani, T., & Kiuchi, K. 2018, *PASJ*, 70, 39, doi: 10.1093/pasj/psy029 (Cited on page 25.)
- Yang, Y.-P., & Zhang, B. 2018, *ApJ*, 868, 31, doi: 10.3847/1538-4357/aae685 (Cited on pages 23 and 90.)
- Yao, J. M., Manchester, R. N., & Wang, N. 2017, *ApJ*, 835, 29, doi: 10.3847/1538-4357/835/1/29 (Cited on pages 11 and 79.)
- Yu, Y.-W., Cheng, K.-S., Shiu, G., & Tye, H. 2014, *J. Cosmology Astropart. Phys.*, 2014, 040, doi: 10.1088/1475-7516/2014/11/040 (Cited on page 25.)
- Zhang, B. 2017, *ApJ*, 836, L32, doi: 10.3847/2041-8213/aa5ded (Cited on page 23.)
- . 2018a, *ApJ*, 867, L21, doi: 10.3847/2041-8213/aae8e3 (Cited on pages 11 and 79.)
- . 2018b, *ApJ*, 854, L21, doi: 10.3847/2041-8213/aaadba (Cited on pages 23 and 76.)
- Zhang, C. F., Jiang, J. C., Men, Y. P., et al. 2020, *The Astronomer's Telegram*, 13699, 1 (Cited on page 21.)

- 
- Zhang, Y. G., Gajjar, V., Foster, G., et al. 2018, *ApJ*, 866, 149, doi: 10.3847/1538-4357/aadf31 (Cited on pages 6, 7, 102 and 104.)
- Zhou, B., Li, X., Wang, T., Fan, Y.-Z., & Wei, D.-M. 2014, *Phys. Rev. D*, 89, 107303, doi: 10.1103/PhysRevD.89.107303 (Cited on page 28.)

# Publications that account for major parts of the thesis

## Refereed:

**G. H. Hilmarsson**, L. G. Spitler, E. F. Keane, T. M. Athanasiadis, E. Barr, M. Cruces, X. Deng, S. Heyminck, R. Karuppusamy, M. Kramer, S. P. Sathyanarayanan, V. Ventakraman Krishnan, G. Wieching, J. Wu, O. Wucknitz. “*Observing superluminous supernovae and long gamma ray bursts as potential birthplaces of repeating fast radio bursts*”, 2020, MNRAS,493,4.

## Submitted:

**G. H. Hilmarsson**, D. Michilli, L. G. Spitler, R. S. Wharton, P. Demorest, G. Desvignes, K. Gourdji, S. Hackstein, J. W. T. Hessels, K. Nimmo, A. D. Seymour, M. Kramer, R. McKimven. “*Rotation Measure Evolution of the Repeating Fast Radio Burst Source FRB 121102*”, submitted to ApJL, 2020.

